

# Quantum chemical and microkinetic modeling of the Fischer-Tropsch reaction

**Citation for published version (APA):**

Filot, I. A. W. (2015). *Quantum chemical and microkinetic modeling of the Fischer-Tropsch reaction*. [Phd Thesis 1 (Research TU/e / Graduation TU/e), Chemical Engineering and Chemistry]. Technische Universiteit Eindhoven.

**Document status and date:**

Published: 01/01/2015

**Document Version:**

Publisher's PDF, also known as Version of Record (includes final page, issue and volume numbers)

**Please check the document version of this publication:**

- A submitted manuscript is the version of the article upon submission and before peer-review. There can be important differences between the submitted version and the official published version of record. People interested in the research are advised to contact the author for the final version of the publication, or visit the DOI to the publisher's website.
- The final author version and the galley proof are versions of the publication after peer review.
- The final published version features the final layout of the paper including the volume, issue and page numbers.

[Link to publication](#)

**General rights**

Copyright and moral rights for the publications made accessible in the public portal are retained by the authors and/or other copyright owners and it is a condition of accessing publications that users recognise and abide by the legal requirements associated with these rights.

- Users may download and print one copy of any publication from the public portal for the purpose of private study or research.
- You may not further distribute the material or use it for any profit-making activity or commercial gain
- You may freely distribute the URL identifying the publication in the public portal.

If the publication is distributed under the terms of Article 25fa of the Dutch Copyright Act, indicated by the "Taverne" license above, please follow below link for the End User Agreement:

[www.tue.nl/taverne](http://www.tue.nl/taverne)

**Take down policy**

If you believe that this document breaches copyright please contact us at:

[openaccess@tue.nl](mailto:openaccess@tue.nl)

providing details and we will investigate your claim.

# Quantum Chemical and Microkinetic Modeling of the Fischer-Tropsch Reaction

## PROEFSCHRIFT

ter verkrijging van de graad van doctor aan de Technische  
Universiteit Eindhoven, op gezag van de rector magnificus,  
prof.dr.ir. C.J. van Duijn, voor een commissie aangewezen  
door het College voor Promoties, in het openbaar te verdedigen  
op maandag 16 maart 2015 om 14:00 uur

door

Ivo Antonius Wilhelmus Filot

geboren te Sittard

Dit proefschrift is goedgekeurd door de promotoren en de samenstelling van de promotiecommissie is als volgt:

|                          |                            |                                    |
|--------------------------|----------------------------|------------------------------------|
| Voorzitter:              | prof.dr.ir. J.C. Schouten  |                                    |
| 1 <sup>e</sup> promotor: | prof.dr.ir. E.J.M. Hensen  |                                    |
| 2 <sup>e</sup> promotor: | prof.dr. R.A. van Santen   |                                    |
| Leden:                   | dr.ir. T.A. Nijhuis        |                                    |
|                          | prof.dr.ir. K. de Jong     | (Universiteit Utrecht)             |
|                          | prof.dr. P. Sautet         | (Ecole Normale Supérieure de Lyon) |
|                          | prof.dr.ir. J.A.M. Kuipers |                                    |

*To Sandra*

« ἵνα παρακληθῶσιν αἱ καρδίαι αὐτῶν, συμβιβασθέντες ἐν ἀγάπῃ καὶ εἰς πᾶν πλοῦτος τῆς πληροφορίας τῆς συνέσεως, εἰς ἐπίγνωσιν τοῦ μυστηρίου τοῦ θεοῦ, Χριστοῦ, ἐν ᾧ εἰσιν πάντες οἱ θησαυροὶ τῆς σοφίας καὶ γνώσεως ἀπόκρυφοι. »

ΠΡΟΣ ΚΟΛΟΣΣΑΕΙΣ 2:2-3



Additional information regarding this dissertation is available online at <http://www.ivofilot.nl/thesis>

Filot, I.A.W.

*Quantum Chemical and Microkinetic Modeling of the Fischer-Tropsch Reaction*

Technische Universiteit Eindhoven

A catalogue record is available from the Eindhoven University of Technology Library

ISBN: 978-90-386-3793-8

Subject headings: density functional theory, microkinetic modeling, Fischer-Tropsch, reaction mechanism, heterogeneous catalysis, computational catalysis

Copyright © 2015 by Ivo Filot



Printer by: Gildeprint Drukkerijen - The Netherlands

Cover design: Ivo Filot



*The work described in this thesis has been carried out at the Schuit Institute of Catalysis within the Inorganic Materials Chemistry group at the Eindhoven University of Technology*



**Catalysis Controlled  
by Chemical Design**

*This work was made with financial support of NRSC-Catalysis.*



*NWO is acknowledged for funding computational resources.*



*This work was carried out on the Dutch national e-infrastructure with the support of SURF Foundation.*

# CONTENTS

|           |   |           |
|-----------|---|-----------|
| <b>1.</b> | <b>INTRODUCTION AND OUTLINE</b>   | <b>1</b>  |
| 1.1.      | THE WORLD ENERGY CHALLENGE  | 3         |
| 1.2.      | CATALYSIS   | 5         |
| 1.2.1     | THE CATALYTIC PROCESS   | 5         |
| 1.2.2     | THE ACTIVE SITE   | 8         |
| 1.2.3     | REACTIVITY TRENDS   | 9         |
| 1.3       | FISCHER-TROPSCH SYNTHESIS   | 10        |
| 1.4       | SCOPE OF THIS THESIS  | 13        |
| 1.5       | REFERENCES  | 15        |
| <b>2.</b> | <b>COMPUTATIONAL METHODS</b>  | <b>17</b> |
| 2.1       | INTRODUCTION  | 19        |
| 2.2       | QUANTUM-CHEMICAL METHODS  | 21        |
| 2.2.1     | THE ELECTRONIC STRUCTURE PROBLEM  | 21        |
| 2.2.2     | THE HARTREE-FOCK APPROXIMATION  | 22        |
| 2.2.3     | DENSITY FUNCTIONAL THEORY   | 22        |
| 2.2.3.1   | THOMAS-FERMI THEORY   | 23        |
| 2.2.3.2   | HOHENBERG-KOHN THEOREM  | 24        |
| 2.2.3.3   | EXCHANGE-CORRELATION FUNCTIONS  | 25        |
| 2.2.3.4   | PLANE-WAVES AND PSEUDOPOTENTIALS  | 26        |
| 2.3       | MICROKINETIC MODELING   | 27        |
| 2.3.1     | PARAMETER EVALUATION USING DFT  | 28        |
| 2.3.2     | CONSTRUCTION AND SOLVING OF THE SET OF<br>ORDINARY DIFFERENTIAL EQUATIONS   | 31        |
| 2.3.3     | STABLE-POINT ANALYSIS   | 34        |
| 2.4       | REFERENCES  | 35        |
| <b>3.</b> | <b>SIZE AND TOPOLOGICAL EFFECTS OF RHODIUM<br/>SURFACES, CLUSTERS AND NANOPARTICLES<br/>ON THE DISSOCIATION OF CO</b> | <b>37</b> |
| 3.1       | INTRODUCTION  | 39        |
| 3.2       | MODEL AND COMPUTATIONAL METHODS   | 40        |
| 3.3       | RESULTS   | 41        |
| 3.3.1     | RH13 CLUSTER  | 42        |
| 3.3.2     | RH57 NANOPARTICLE   | 44        |
| 3.3.3     | RH SURFACES   | 48        |
| 3.4       | DISCUSSION  | 51        |
| 3.5       | CONCLUSION  | 53        |
| 3.6       | REFERENCES  | 54        |

## **4. QUANTUM CHEMISTRY OF CO HYDROGENATION ON STEPPED RHODIUM SURFACES 57**

|        |   |    |
|--------|---|----|
| 4.1    | INTRODUCTION                                  | 59 |
| 4.2    | COMPUTATIONAL METHOD                          | 61 |
| 4.3    | RESULTS AND DISCUSSION                        | 61 |
| 4.3.1. | ADSORPTION SITES                              | 62 |
| 4.3.2  | DIRECT AND HYDROGEN-MEDIATED CO DISSOCIATION  | 65 |
| 4.3.3  | C HYDROGENATION TO CH <sub>4</sub>            | 65 |
| 4.3.4  | CO HYDROGENATION TO FORMALDEHYDE AND METHANOL | 66 |
| 4.3.5  | CH <sub>x</sub> + OH <sub>y</sub> COUPLING    | 68 |
| 4.3.6  | CH <sub>x</sub> + CH <sub>y</sub> COUPLING    | 69 |
| 4.3.7  | CH <sub>x</sub> + CO COUPLING                 | 70 |
| 4.3.9  | CHXCHYOZ HYDROGENATION                        | 74 |
| 4.3.10 | WATER FORMATION                               | 74 |
| 4.4    | CONCLUSION                                    | 74 |
| 4.5    | REFERENCES                                    | 75 |

## **5. FIRST-PRINCIPLES-BASED MICROKINETICS SIMULATIONS OF CO HYDROGENATION ON RHODIUM 77**

|       |   |    |
|-------|---|----|
| 5.1   | INTRODUCTION  | 79 |
| 5.2   | COMPUTATIONAL METHOD                                    | 80 |
| 5.3   | RESULTS   | 82 |
| 5.3.1 | OVERALL KINETICS  | 82 |
| 5.3.2 | REACTION NETWORK ANALYSIS: RATE AND SELECTIVITY CONTROL | 84 |
| 5.3.3 | GENERAL DISCUSSION                                      | 96 |
| 5.4   | CONCLUSIONS   | 97 |
| 5.5   | REFERENCES  | 98 |

## **6. PROBING THE ACTIVE SITES FOR CO DISSOCIATION BY N<sub>2</sub> IR SPECTROSCOPY 101**

|       |  |     |
|-------|--|-----|
| 6.1   | INTRODUCTION   | 103 |
| 6.2   | COMPUTATIONAL METHOD   | 104 |
| 6.3   | RESULTS  | 105 |
| 6.3.1 | FISCHER-TROPSCH CATALYSIS OVER ZIRCONIA-SUPPORTED RH NANOPARTICLES | 106 |
| 6.3.2 | DFT CALCULATIONS   | 108 |
| 6.4   | DISCUSSION   | 112 |
| 6.5   | CONCLUSION   | 116 |
| 6.6   | REFERENCES   | 116 |

## **7. QUANTUM CHEMISTRY OF THE FISCHER-TROPSCH REACTION CATALYZED BY A STEPPED RUTHENIUM SURFACE 119**

|         |   |     |
|---------|---|-----|
| 7.1     | INTRODUCTION  | 120 |
| 7.2     | METHOD  | 121 |
| 7.3     | RESULTS AND DISCUSSION                                  | 123 |
| 7.3.1   | DFT CALCULATIONS  | 125 |
| 7.3.1.1 | CO DISSOCIATION   | 125 |
| 7.3.1.2 | C HYDROGENATION TO CH <sub>4</sub>                      | 125 |
| 7.3.1.3 | CH <sub>x</sub> +CH <sub>y</sub> COUPLING REACTIONS     | 125 |
| 7.3.1.4 | CH <sub>x</sub> CH <sub>y</sub> HYDROGENATION REACTIONS | 126 |
| 7.3.1.5 | CH <sub>x</sub> +CO COUPLING                            | 128 |
| 7.3.1.6 | CH <sub>x</sub> -CO HYDROGENATION                       | 130 |
| 7.3.1.7 | CH <sub>x</sub> CH <sub>y</sub> -O BOND SCISSION        | 130 |
| 7.3.1.8 | WATER FORMATION   | 131 |
| 7.3.2   | ELECTRON DENSITY DIFFERENCE ANALYSIS                    | 132 |
| 7.3.2.1 | CH+CH COUPLING  | 132 |
| 7.3.2.2 | CH+CH VS. CH+CCH <sub>3</sub> COUPLING                  | 134 |
| 7.3.2.4 | ETHYLENE VS. PROPYLENE DESORPTION                       | 134 |
| 7.3.3   | REACTION ENERGY DIAGRAMS                                | 135 |
| 7.3.4   | CARBIDE VS. CO INSERTION MECHANISM                      | 139 |
| 7.4     | CONCLUSIONS   | 141 |
| 7.5     | REFERENCES  | 142 |

## **8. THE OPTIMALLY PERFORMING FISCHER-TROPSCH CATALYST 145**

|     |                        |     |
|-----|------------------------|-----|
| 8.1 | INTRODUCTION           | 147 |
| 8.2 | METHOD                 | 148 |
| 8.3 | RESULTS AND DISCUSSION | 149 |
| 8.4 | CONCLUSION             | 157 |
| 8.5 | REFERENCES             | 159 |

## **9. REACTIVITY OF CO ON CARBON-COVERED COBALT SURFACES IN FISCHER-TROPSCH SYNTHESIS 161**

|         |  |     |
|---------|--|-----|
| 9.1     | INTRODUCTION                                   | 162 |
| 9.2     | COMPUTATIONAL METHOD                           | 163 |
| 9.3     | RESULTS AND DISCUSSION                         | 165 |
| 9.3.1   | FLAT SURFACE                                   | 167 |
| 9.3.1.1 | CARBON DIFFUSION                               | 168 |
| 9.3.1.2 | EFFECT OF CARBON DEPOSITION ON CO DISSOCIATION | 169 |
| 9.3.2   | CORRUGATED SURFACE                             | 173 |
| 9.3.2.1 | CARBON DEPOSITION                              | 174 |
| 9.3.2.2 | EFFECT OF CARBON DEPOSITION ON CO DISSOCIATION | 176 |
| 9.4     | CONCLUSIONS                                    | 181 |
| 9.5     | REFERENCES                                     | 182 |

**SUMMARY AND OUTLOOK 185**

|            |     |
|------------|-----|
| SUMMARY    | 185 |
| OUTLOOK    | 187 |
| REFERENCES | 190 |

**APPENDIX A 191**

GEOMETRIES OF ELEMENTARY REACTION STEPS ON RH(211)

**APPENDIX B 199**

GEOMETRIES OF ELEMENTARY REACTION STEPS ON RU(1121)

**CURRICULUM VITAE 203**

**LIST OF PUBLICATIONS 204**

**ACKNOWLEDGEMENTS 209**

## Abstract

In this chapter we will sketch a general background of the research described in this thesis. The basics of catalysis are sketched, and the goals of our research is placed in a wide context.

★ *Chemistry without catalysis would be a sword without a handle, a light without brilliance, a bell without sound.* ★ Alwin Mittasch

# INTRODUCTION AND OUTLINE



# 1

## 1.1. THE WORLD ENERGY CHALLENGE

The societal challenges we are confronted with are growing on a global scale. Cross-continental food shortages, economic recessions, climate change and oil depletion are issues that affect us all. Over the last years, we saw a significant increase in the energy demand and our annual energy consumption is projected to double in 2050. Furthermore, the do-

minant part of the annual energy consumption relies on fossil fuels (Figure 1.1) of which the reserves are slowly dwindling. Regrettably, less than 10 percent of the world's total energy production is based on renewable energy sources such as solar, wind, geothermal and hydro-electrical energy.<sup>1</sup>

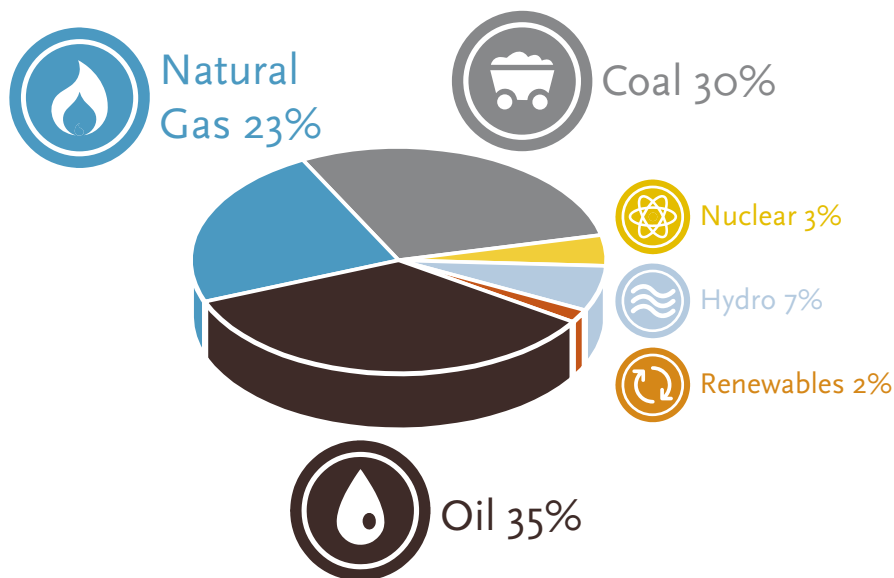


**Figure 1.1:** Pie-chart showing the ratio of the energy source of the global annual energy consumption in 2012.<sup>1</sup>

The finite size of the fossil reserves is highlighted in Figure 1.2. This analysis only provides a rough estimate. Global energy demand is expected to increase significantly because of increasing world population and increasing per capita energy demand, new oil and gas reserves

are being discovered and recovery methods are improved. Nevertheless, Figure 1.2 serves to make the point that the fossil reserves are finite and that conventional oil will become more and more scarce in the upcoming years. It is therefore unrealistic to solely rely on the refining and

catalytic conversion of crude oil to meet the soaring energy demand. In the last few decades, a significant amount of research and investment has been made to reduce the world's dependence on crude oil. One possible solution to address the

concern for diminishing oil reserves and soaring oil price is to utilize other carbon sources for energy. In fact, recently attempts have been made to explore the extraction of energy from unconventional sources, such as shale gas and methane

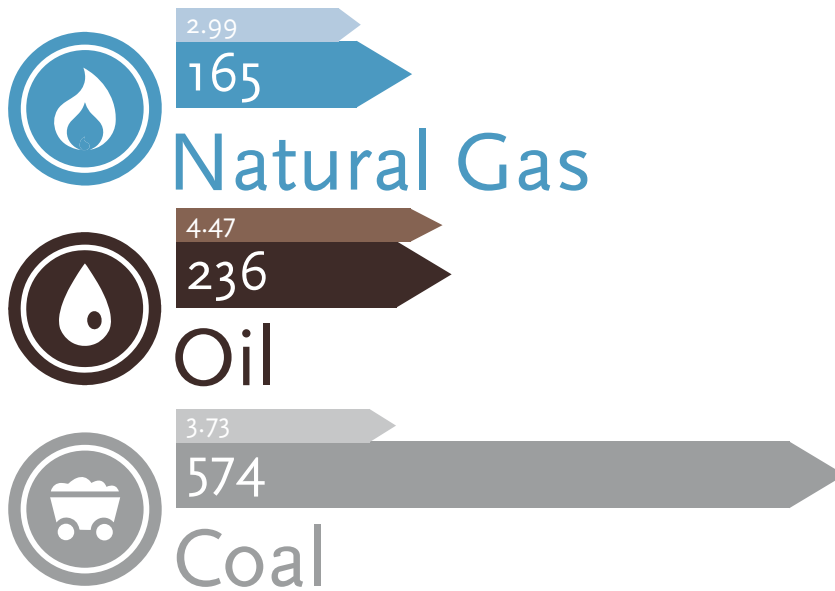


**Figure 1.2:** Fossil fuel reserves (darker arrow) and annual consumption (lighter arrow) in 2012 for the three major fossil fuels. The values are in billion (10<sup>9</sup>) metric tons of oil equivalents.<sup>1</sup>

hydrates. Although these unconventional carbon sources provide an alternative to the direct utilization of crude oil, many technological and environmental challenges arise from switching from crude oil to natural gas or coal. The exploitation of fossil fuels results in the release of high amounts of carbon dioxide (CO<sub>2</sub>) in the atmosphere, resulting in a green-

house effect. Although attempts were made to mitigate the accumulation of greenhouse gases in the atmosphere by carbon capture and sequestration, there is a huge imbalance in the carbon cycle, due to the continuous burning of fossil fuels for energy. Despite that direct usage of natural gas is relatively clean, many locations where natural gas can be exploited

are remote from where it can be utilized. Transportation is thus needed and the low density of natural gas leads to very high transportation costs. Coal on the other hand is considered as an extremely “dirty” source of energy due to the high carbon to hydrogen ratio and high sulfur content. As such, the usage of coal is very detrimental to the environment.

Various alternatives to the non-renewable fossil fuels exist, such as nuclear fission and fusion, solar power or biomass conversion, which all have their own drawbacks. Energy extraction from nuclear fission is far from feasible at the moment, whereas nuclear fission generates large amounts of highly radioactive waste, that has to be carefully stored. Solar power on the other hand is at the moment too costly<sup>1</sup> and biomass is in addition to the high transportation costs also

incompatible with the current infrastructure. Therefore, with gas and biomass too expensive, coal too dirty, nuclear too risky and the development of advanced renewables such as nuclear fusion too slow, what are our alternatives?

Instead of the direct utilization of biomass, coal or natural gas, a feasible alternative is the conversion of these carbon sources to chemicals more suitable for transportation and/or utilization. In comparison to crude oil, the conversion of these carbon sources is much more difficult due to the higher stability of the reacting molecules and/or the presence of extensive polymeric carbon networks containing functional groups with oxygen, sulfur or nitrogen. Hence, catalysts play a pivotal role in the conversion of these complex molecules to the desired products.

## 1.2. CATALYSIS

### 1.2.1 THE CATALYTIC PROCESS

The use of catalysts is well-known to the public. They are for instance being used in cars for the clean-up of the exhaust gases. Nearly 90% of all chemical processes use catalysts and as such catalysts have a considerable impact on the gross domestic product (GDP) of most developed countries. Without catalysts,

the large-scale production of ammonia required for intensive agriculture would not be feasible and we would not be able to sustain the current global population. Even in our bodies, catalysts (typically called enzymes) are responsible for almost all biological processes. Clearly, catalysts are ubiquitous in life and society.

A catalyst is a compound that accelerates reactions, where chemical bonds are being dissociated or formed. Catalysts

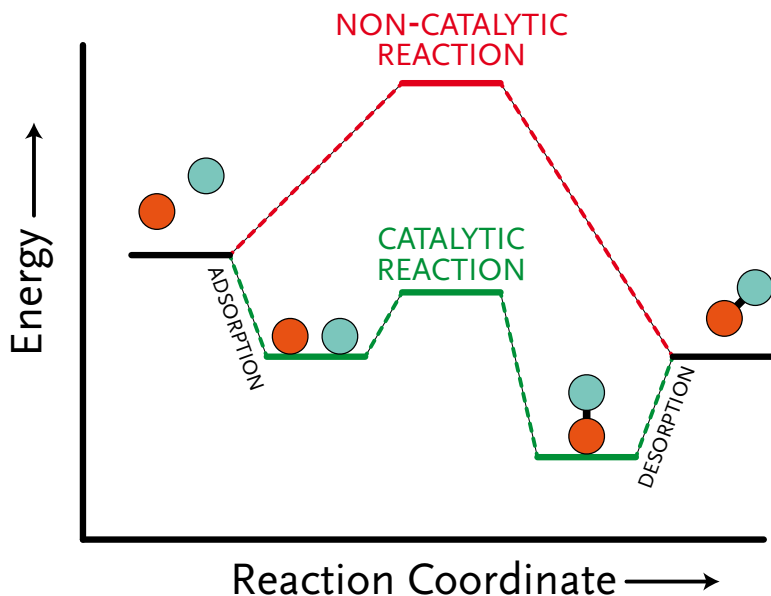


**Figure 1.3:** Cartoon representation of a reaction energy diagram (RED) of the association reaction of two arbitrary compounds. The lower line shows the catalyzed pathway and the top line shows the un-catalyzed reaction.

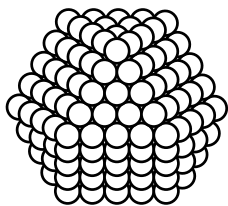
function by forming bonds with the reactants, intermediates and products to lower the energy barriers of the dissociation and association reaction steps (Figure 1.3). This lowers the overall activation energy of a particular chemical reaction and implies that the same reaction can be carried out at a lower temperature than the non-catalyzed reaction. Importantly, a catalyst never affects the overall energy of a reaction as this would be violation of the first law of thermodynamics. Although the formal definition<sup>2</sup> states that a catalyst is both a reactant as well as a product of the same reaction, this could imply that a catalyst is never spent. In reality,

catalysts tend to deactivate via various mechanisms and they have to be regenerated or removed from the process.

The interaction of a catalyst with the reactants in terms of the catalytic activity fulfills the Goldilocks' principle: If the bond between catalyst and reactants is too weak, the reactant is insufficiently activated and there will be little to no conversion. If on the other hand the interaction is too strong, the product will not desorb from the catalyst and the catalyst will be poisoned. This requirement for an optimal catalyst is known as the Sabatier's principle.

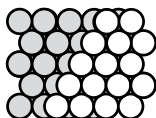
A successful implementation of a

## NANOPARTICLE



1-10 nm

## CATALYTIC SURFACE



1-2 nm

## ACTIVE SITE



0.1-0.5 nm

**Figure 1.4:** Typical length-scales involved in catalysis.

catalyst requires understanding of the reaction mechanism and its relation to the catalyst structure and topology at the molecular scale. Catalyst behavior on the molecular scale is typically modelled using a variety of length scales. Phenomenon occurring in one particular length scale determine processes in the other length scales. To exemplify, in Figure 1.4, three typical of such length scales of a catalytic particle are shown. On the left, the catalytic nanoparticle is depicted. The chemical environment, the adlayer coverage as well as the type of support determine the size, shape and stability of this nanoparticle. Especially the shape of the particle plays an important role, as the shape of the particle determines the type of crystal facets exposed for the chemical reaction.

For instance, the very stable cuboctahedral shape (left image in Figure 1.4) exposes  $\text{fcc}(111)$  and  $\text{fcc}(100)$  facets. Neither of these facets give rise to a facile CO dissociation. On the other hand, a nanopar-

ticle could be envisioned in which a step-edge (middle image in Figure 1.4) is exposed. The number of these step-edge sites depends on the particle size and shape as suggested by an early treatment of Van Harvelde and coworkers.<sup>3,4</sup> He coined these step-edge sites as  $B_5$  sites (right image in Figure 1.4). From theoretical investigations it is known that these sites facilitate a facile CO dissociation. This reasoning shows the important role of catalyst topology and structure, and size-dependency, on the overall reaction.

It is worthwhile to note that this type of reasoning goes both ways. In other words, the catalytic reaction can alter the particle shape and size, as well. If the catalytic nanoparticle contains a sufficient amount of active sites, this could lead to a high coverage of a particular adsorbate, say carbon, on the catalyst. This high carbon coverage can lead to surface reconstruction, resulting in the re-shaping of the nanoparticle and perhaps even in agglomeration (sintering) or disinte-

gration of the nanoparticle. Clearly, the processes happening on these different length scales are strongly correlated.

This strong correlation of catalyst performance and topology leads to the hypothesis that catalysis is a complex and emergent phenomenon. The dynamic nature and interplay of the catalytic material and the reacting species gives rise to the phenomenon of catalysis. To say this in other words, a catalytic material facilitates catalysis in the same way that the catalyzed species influences the topology of the catalyst.

### 1.2.2 THE ACTIVE SITE

Central in the atom-scale interpretation of heterogeneous catalysis is the active site. In 1925, it was already suggested by Taylor that special "active sites" associated with low-coordinated surface atoms or defects control the surface chemical reactivity. Boudart<sup>5</sup> was among the first to systematically investigate the catalytic activity as a function of particle size and he introduced the terms structure sensitivity.

Subsequently, Somorjai and Yates used the surface science approach to study the surface reactivity of well-defined surfaces.<sup>6</sup> In special, they investigated the importance of step sites to the catalytic reactivity. The breakthrough in this field came with the contribution of

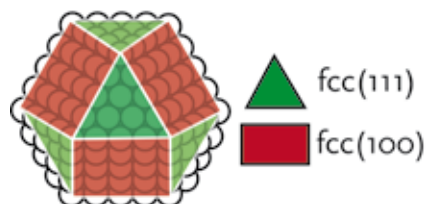
Nobel Laureate Ertl, who showed that the active sites in the dissociative chemisorption of NO on a Ru(0001) surface are the step-edge sites.<sup>7</sup> Computational chemistry gave a tremendous boost to the elucidation of the effect of step sites. In particular, the advance of DFT should be mentioned.

Several key concepts determine the properties of a catalytic site. These are the coordination numbers (the numbers of next-nearest neighbors), the orientation or topology and the type of metal. The first two concepts are conceptually depicted in Figure 1.5.

The type of crystal facet, and in particular the orientation of the crystal facets with respect to each other, determines the surface topology of a catalytic nanoparticle. Layering of crystal facets results in the formation of step-edge sites and is a form of surface corrugation. The coordination number (CN) of a metal atom is linked to its coordinative (un)saturation, where a lower CN leads to a stronger interaction with an adsorbate. This stronger interaction with the adsorbate often leads to more pronounced activation of the molecular bonds of said adsorbate, thereby facilitating cleavage or formation of those bonds.

From the right hand side image in Figure 1.5, we see that there is a correlation between the type of atom (terrace, (step-)edge or corner) and the coordina-

## CRYSTAL SURFACES



## COORDINATION NUMBERS

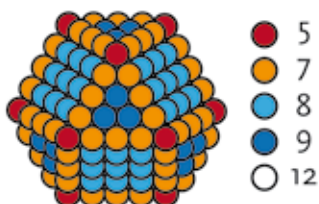


**Figure 1.5:** (left) Crystal surfaces exposed by a face centered cubic (fcc) cuboctahedral catalytic nanoparticle. The triangular shaped orientation (green triangles) are fcc(111) facets, whereas the square orientation (red rectangles) are fcc(100) sites. (right) The coordination number (CN) of terrace sites (light and dark blue, CN=8, CN=9, respectively), (step-)edge sites (orange, CN=7) and corner sites (red, CN=5). The atoms in the center (not visualized) have coordination number 12.

tion number. Terrace sites tend to have higher coordination numbers and thus lower reactivity as compared to (step-) edge and corner sites. Certain configurations of atoms tend to activate particular type of bonds. For example, for the activation of a s-bond such as in  $\text{CH}_4$  a low-coordinated corner atom is required. In contrast, for the activation of a p-bond such as in CO, a concave step-edge site is necessary. This understanding has been confirmed both by experimental means by investigation of the turn-over frequency as a function of particle size as well as by theoretical means using density functional theory calculations.<sup>8-10</sup>

### 1.2.3 REACTIVITY TRENDS

To interpret chemical reactivity and investigate periodic trends, many scaling laws have been proposed. The Brønsted-Evans-Polanyi (BEP) relationship correlates the activation energy with the reaction energy for an elementary surface reaction.<sup>11</sup> The Nørskov scaling laws<sup>12</sup> on the other hand provide a relation between the adsorption strength with respect to the gas phase of reaction intermediates on the one hand and the metal-carbon and metal-oxygen interaction energy on the other hand. Combining these two relationships enables us to study current catalytic systems and provides a guide for the search of optimal catalytic systems.

In the Brønsted-Evans-Polanyi relationship the change in activation energy

scales linearly with the change in reaction enthalpy as given by

$$\partial E_{\text{act}} = \alpha \cdot \partial E_{\text{R}} \quad (1.1)$$

where  $E_{\text{act}}$  denotes the activation energy,  $E_{\text{R}}$  the reaction enthalpy and  $\alpha$  the proportionality constant. The value for  $\alpha$  lies between 0 and 1 and is a measure for the lateness of the transition state. In other words, when the geometry of the transition state resembles that of the final state, the transition state is termed late and consequently the value for  $\alpha$  is close to unity. On the basis of microscopic reversibility it is easily seen that the proportionality constant  $\alpha$  in the reverse direction is  $1-\alpha$ . Consequently, for many dissociation reactions  $\alpha$  is around 0.8, whereas for association reactions, a value

of 0.2 is found.

Once the reaction enthalpy and activation energy in one particular situation is known, the BEP relationship enables us to express the activation energy in another situation once the reaction enthalpy for the latter situation is known. As such, the BEP relationship saves us the effort of performing another transition state search. There are however limits to what extend the BEP relationship can be successfully employed. The underlying assumption of the relation is that the curvature in the direction of reaction coordinate in the initial and transition state between the two situations used for the relation are similar. In simpler terms, the topology of the active site between the different metals has to be very similar.<sup>9</sup>

### 1.3. FISCHER-TROPSCH SYNTHESIS

Fischer-Tropsch (FT) synthesis is the process that converts synthesis gas ( $\text{CO} + \text{H}_2$ ), into a wide range of long-chain hydrocarbons and oxygenates.<sup>13</sup> The Fischer-Tropsch synthesis is a route for the chemical liquefaction of coal and natural gas. With regard to the classic refining of crude oil, it provides an interesting alternative to the production of transportation fuels and chemical feedstock (see Figure 1.6). Moreover, as the synthesis gas can be derived from  $\text{CO}_2$  or

biomass, it may serve a role in the strife towards sustainability. The FT reaction is of increasing commercial interest and several large scale commercial plants have been constructed in recent years by major energy companies such as Chevron, Sasol and Shell.

Although the FT reaction is over 100 years old, its underlying mechanism is still heavily debated in the literature.<sup>14-21</sup> Fischer-Tropsch synthesis is basically a polymerization reaction, consisting of an

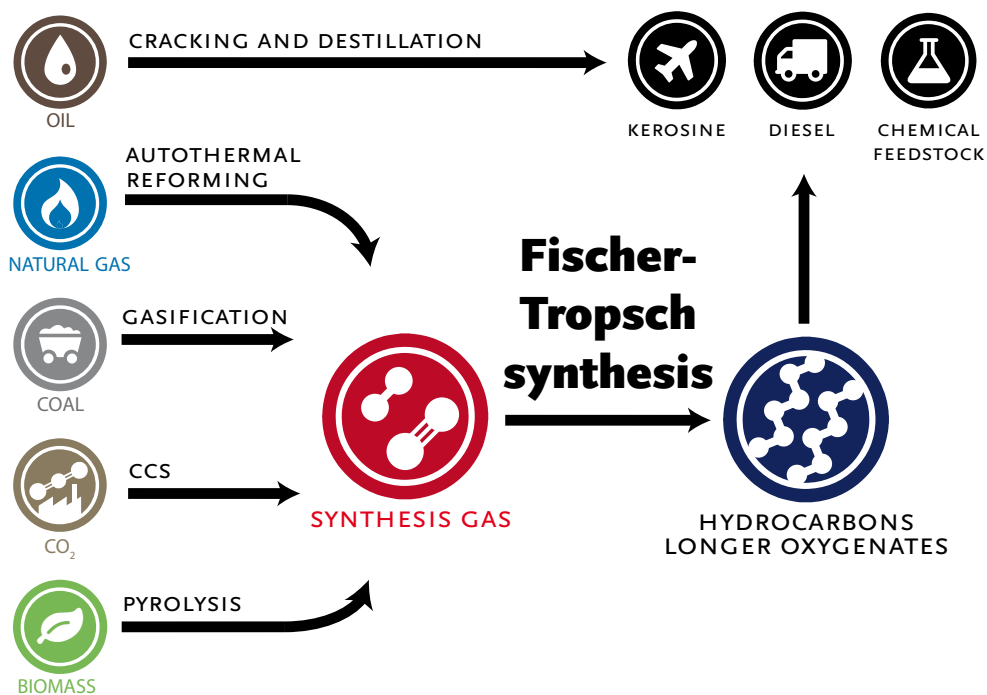


**Figure 1.6:** Transportation fuels and chemical feedstock are mainly obtained from the refining of crude oil. Fischer-Tropsch synthesis provides an alternative pathway for the synthesis of hydrocarbons from natural gas, coal, CO<sub>2</sub> or biomass.

initiation, several propagation and finally a termination step. Among the various mechanisms proposed, in general two types of mechanisms are possible, that differ in the nature of the propagation step. Either the propagation step proceeds by the insertion of a CH<sub>x</sub> monomer in the growing chain, henceforth termed the carbide mechanism (see Figure 1.7), or by insertion of a CO species in the growing chain, from here on called the CO-insertion mechanism (see Figure 1.8).

In the carbide mechanism, the adsorbed CO dissociates. The resulting carbon adatom is hydrogenated to a CH<sub>x</sub>

building block, that is inserted into the growing hydrocarbon chain. This chain reaction is terminated by desorption of the hydrocarbon chain from the surface as an alkene or alkane. The oxygen is removed from the surface as water by two hydrogenation steps. In the CO-insertion mechanism on the other hand, CO is not dissociated and is readily inserted into the growing hydrocarbon chain. Only after the insertion, the oxygen atom is dissociated. Currently, the carbide mechanism has the most support in the literature.<sup>22,23</sup>

Based on extensive DFT studies on

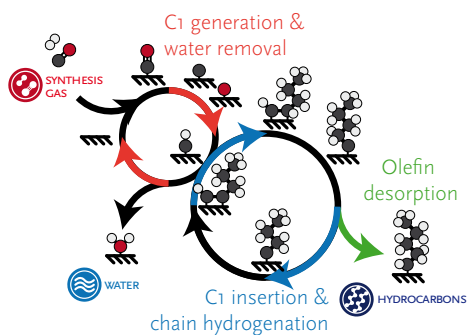


**Figure 1.7:** *The carbide mechanism. The initiation reaction consists of the adsorption of CO, its dissociation and the hydrogenation of the resulting carbon adatom. Hence, a  $\text{CH}_x$  building block is formed, that can be inserted in the growing hydrocarbon chain. By several (de-)hydrogenation steps, the growing hydrocarbon chain can accept another  $\text{C}_1$  building block or alternatively is hydrogenated to an alkene or alkane, that leaves the surface.*

the FT mechanism, it was concluded in a recent review that the carbide mechanism is the most probable mechanism for FT chain growth.<sup>13</sup> Within this mechanism, in order to form long chain products the rate of CO dissociation has to be fast and the rate of methane formation slow to provide sufficient  $\text{CH}_x$  intermediates to maintain a high rate of chain growth. Also, the formation of long chain products requires the rate of termination to be slow compared to the rate of chain growth.<sup>22</sup> These simple set of principles already elucidate the experimentally

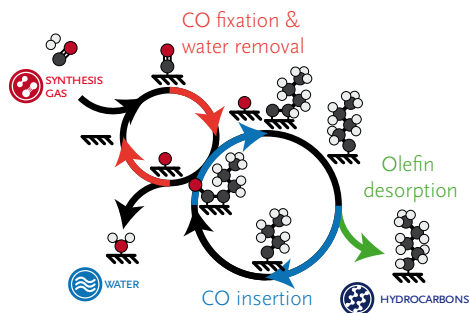


**Figure 1.8:** *The CO-insertion mechanism: This mechanism differs from the carbide mechanism in the way that the C-O bond is broken. CO does not readily dissociate on the surface, but is first inserted into the growing hydrocarbon chain. After C-C bond formation, the C-O bond scission occurs. By several (de-)hydrogenation steps, the growing hydrocarbon chain can accept another CO moiety or alternatively is hydrogenated to an alkene or alkane, that leaves the surface.*

found product selectivities as depicted in Figure 1.9. Fe, Co and Ru tend to have a high rate of CO dissociation and a high rate of  $\text{CH}_x$  insertion. These metals yield longer hydrocarbons. Although the rate of chain growth is reasonable on Ni, the CO dissociation is much too slow compared to the rate of methane formation, by which on Ni only methane is formed. Pd, Os, Ir, and Pt have no facile CO dissociation. This results in the formation of methanol as the CO can only be hydrogenated. Finally, Rh provides an interesting case as it has a moderate rate of CO



**Figure 1.9:** Typical FT product selectivity. Fe, Co and Ru tend to produce longer hydrocarbons, whereas Pd, Os, Ir and Pt mainly produce methanol. Rh provides an interesting position as it lies in between these two extremes, therefore mainly producing longer oxygenates. On Ni only methane is produced.

dissociation and a relatively slow rate of methane formation. Therefore, on Rh the

production of longer oxygenates is found.

## 1.4. SCOPE OF THIS THESIS

The goal of this work is to understand the kinetics and mechanism of the Fischer-Tropsch reaction. The Fischer-Tropsch reaction is a very complex reaction involving many elementary reaction steps. The rate of these steps depends in a sensitive manner on the type of transition metal, the surface metal atom topology and the composition of the adsorbed layer. While density functional theory methods provide accurate data for

the rate constants for these elementary reaction steps, microkinetics simulations allow to predict the composition of the adsorbed layer on the surface as well as the rates of all elementary reaction steps. In this manner, important issues can be resolved that pertain to the mechanism of the Fischer-Tropsch reaction such as the dominant reaction pathway from reactants (CO and H<sub>2</sub>) to products (alkanes, alkenes, oxygenates and water). Pertinent

questions relevant to the Fischer-Tropsch reaction relate to the manner of CO dissociation, which of the two main proposed mechanisms for chain growth - the carbide mechanism and the CO insertion mechanism – dominates, what the rate-controlling steps are and which elementary reaction steps influence the product selectivity.

**CHAPTER 2** of this thesis describes the computational methods employed in this study, namely quantum chemical calculation to obtain activation barriers and pre-exponential factors for the elementary reaction steps and microkinetics modeling to predict steady state surface coverages and macroscopic reaction rates and related kinetic parameters.

**CHAPTER 3** investigates the influence of surface topology and particle size on the CO dissociation reaction, which is one of the principle reactions in FT catalysis. The electronic effect of particle size and the influence of surface topology, i.e. fcc(111), fcc(211) and fcc(100), are investigated.

**CHAPTER 4** gives the results of an extensive DFT study of all relevant elementary reaction steps in Rh-catalyzed CO hydrogenation on a stepped Rh(211) surface. These steps include (hydrogen-mediated) CO dissociation, C hydrogenation,  $\text{CH}_x + \text{CH}_y$  coupling and  $\text{CH}_x + \text{CO}$  coupling,  $\text{C}_2$  hydrocarbon/oxygenate hydrogenation, and water removal. The results of these

quantum chemical calculations will be used to construct a database of reaction barriers and pre-exponential factors in order to construct a microkinetics model for the FT reaction.

**CHAPTER 5** discusses the results of microkinetics simulations of CO hydrogenation on Rh(211) surfaces. By kinetic analysis of the CO hydrogenation reaction network, the rate-controlling elementary reaction steps are identified. To study the influence of these elementary reaction steps on the selectivity, an extension of the degree of rate control (DRC) methodology of Campbell is presented. Uniquely, we have determined which elementary reaction steps favor the formation of ethanol, whilst inhibiting the production of unwanted side products such as methane.

In **CHAPTER 6**, a computational study is carried out to calculate the spectra of adsorbed  $\text{N}_2$  on various Rh surfaces and clusters with the aim to establish whether IR spectroscopy of  $\text{N}_2$  adsorbed on Rh nanoparticles can help to identify step-edge sites. This work is combined with catalytic performance data of zirconia-supported Rh nanoparticles that display structure sensitive behavior in CO hydrogenation with the purpose to evidence the importance of step-edge sites for the CO dissociation reaction on Rh.

**CHAPTER 7** provides the results of extensive DFT calculations to study Ru-catalyzed FT synthesis. In this chapter, a

database is constructed of elementary reaction steps to perform microkinetics simulations in Chapter 8. A comparison is made between the carbide mechanism and the CO insertion mechanism. It is established that the carbide mechanism provides a more favorable pathway to long-chain hydrocarbons than the CO insertion mechanism. The experimentally observed C<sub>2</sub> anomaly in the Anderson-Schulz-Flory distribution is rationalized by analysis of the electron density of the involved complexes. A cooperative effect for CH insertion is found that facilitates efficient chain propagation.

In **CHAPTER 8**, a detailed analysis of the extensive reaction energy diagram was conducted to explore the kinetic regimes of FT synthesis using reactivity descriptors. We have extrapolated the results obtained for corrugated Ru surfaces (chapter 7) to simulate FT synthesis on different metals by employing surface stability linear scaling relations as well as

Brønsted-Evans-Polanyi relations. This approach enabled us to identify three kinetic regimes, that are the monomer formation limiting regime, the chain-growth limiting regime and the water removal limiting regime. At the intersection of these three regimes lies the kinetic optimum. Current-generation industrial catalysts were found to be suboptimal in terms of CO conversion rate.

In **CHAPTER 9**, the effect of carbon deposition on the adsorption and dissociation of CO is studied for the flat Co(0001) and corrugated Co(11 $\bar{1}$ 1) surface using DFT calculations. It was found that the topology of the surface has a much more pronounced influence on the CO dissociation barrier than the effect of co-adsorbed carbon. The favorable surface topology of Co(11 $\bar{1}$ 1) enables a significantly lower dissociation barrier for CO dissociation as compared to the barrier on Co(0001). ■

## 1.5 REFERENCES

- (1) *Levelized Cost of New Generation Resources in the Annual Energy Outlook 2013*, U.S. Energy Information Administration, 2013.
- (2) McNaught, A. D.; Wilkinson, A.; Blackwell Scientific Publications: 1997.
- (3) Van Hardeveld, R.; Hartog, F. *Surf. Sci.* **1969**, *15*, 189
- (4) van Hardeveld, R.; Hartog, F. In *Adv. Catal.*; D.D. Eley, H. P., Paul, B. W., Eds.; Academic Press: 1972; Vol. Volume 22, p 75.
- (5) Boudart, M.; McDonald, M. A. *J. Phys. Chem.* **1984**, *88*, 2185.
- (6) Somorjai, G. A. *Introduction to Surface Chemistry and Catalysis*; Wiley: New York, 1994.

- (7) Zambelli, T.; Wintterlin, J.; Trost, J.; Ertl, G. *Science* **1996**, *273*, 1688.
- (8) Ligthart, D. A. J. M.; van Santen, R. A.; Hensen, E. J. M. *J. Catal.* **2011**, *280*, 206.
- (9) van Santen, R. A.; Ghouri, M. M.; Shetty, S.; Hensen, E. J. M. *Catal. Sci. Technol.* **2011**, *1*, 891.
- (10) van Santen, R. A.; Neurock, M. *Molecular Heterogeneous Catalysis*; Wiley-VCH Verlag GmbH & Co. KGaA: Weinheim, 2006.
- (11) Santen, R. A. v.; Neurock, M.; Shetty, S. G. *Chem. Rev.* **2009**, *110*, 2005.
- (12) Abild-Pedersen, F.; Greeley, J.; Studt, F.; Rossmeisl, J.; Munter, T. R.; Moses, P. G.; Skúlason, E.; Bligaard, T.; Nørskov, J. K. *Phys. Rev. Lett.* **2007**, *99*, 016105.
- (13) van Santen, R. A.; Ciobica, I. M.; van Steen, E.; Ghouri, M. M. In *Adv. Catal.*; Bruce, C. G., Helmut, K., Eds.; Academic Press: 2011; Vol. Volume 54, p 127.
- (14) Bell, A. T. *Catal. Rev.* **1981**, *23*, 203.
- (15) Ponec, V. *Catal. Rev.* **1978**, *18*, 151.
- (16) Anderson, R. B. *The Fischer-Tropsch Synthesis*; Academic Press: New York, 1984.
- (17) Hindermann, J. P.; Hutchings, G. J.; Kiennemann, A. *Catal. Rev.* **1993**, *35*, 1.
- (18) Claeys, M.; van Steen, E. In *Stud. Surf. Sci. Catal.*; André, S., Mark, D., Eds.; Elsevier: 2004; Vol. Volume 152, p 601.
- (19) Dry, M. E. *Appl. Catal. A* **1996**, *138*, 319.
- (20) Adesina, A. A. *Appl. Catal. A* **1996**, *138*, 345.
- (21) Van Der Laan, G. P.; Beenackers, A. A. C. M. *Catal. Rev.* **1999**, *41*, 255.
- (22) van Santen, R. A.; Markvoort, A. J.; Ghouri, M. M.; Hilbers, P. A. J.; Hensen, E. J. M. *J. Phys. Chem. C* **2013**, *117*, 4488.
- (23) van Santen, R. A.; Markvoort, A. J. *ChemCatChem* **2013**, *5*, 3384.

## Abstract

A formal description of the methods used in this study is given. Density functional theory (DFT) is the key quantum-chemical method to compute kinetic parameters of the elementary reaction steps that make up the catalytic mechanism. The basic principles of quantum chemistry and the assumptions made in DFT are discussed. The theoretical background of microkinetics simulations and its implementation in the study of surface reactions is given.

★ *This isn't right. This isn't even wrong.* ★

Wolfgang Pauli

# COMPUTATIONAL METHODS



2

## 2.1 INTRODUCTION

Computational modeling is nowadays widely used in the chemical, physical and engineering sciences in assisting in the interpretation of experimental data and, increasingly, as a predictive tool for instance for materials selection. The methodologies used are becoming increasingly more accurate in the prediction of the behavior of matter at the atomic level due to the development of better models and the availability of ever faster computers. Modeling methodologies have typically been applied in the field of solid state and materials science with the aim to understand bulk and surface properties of solids. In catalysis, a main objective is to predict the macroscopic rate of a chemical reaction occurring on the surface of solids of heterogeneous catalysts or in homogeneous catalytic complexes. The pivotal prerequisite is that the rate constants of the elementary reaction steps that make up the mechanism of a catalytic reaction can be accurately predicted. Based on these data, one can then predict the composition of the surface adlayer as a function of temperature and partial pressure and, with this, the overall reaction rate.

To model chemical reactivity, detailed understanding of its underlying processes, such as adsorption/desorption, surface reaction and diffusion, is re-

quired. These processes are “multiscale” in nature, both with respect to time and space. Typical time scales involved in catalysis are vibrations in molecules ( $10^{-12}$  s), electronic motion ( $10^{-15}$  s) and chemical bond-breaking and -making steps ( $10^{-5}$  s). The corresponding length scales for molecular vibrations, electronic motion and elementary reaction steps are  $10^{-11}$ ,  $10^{-14}$  and  $10^{-10}$  Å, respectively. Given a list of reaction events and their rate constants, adsorbates arrange themselves in spatial configurations or patterns, as a result of the collective behavior of the ensemble of all species. At this mesoscopic scale, the collective behavior has to be averaged over length and time scales that are much larger than the characteristic length and time scale of the underlying pattern – or what is known as the correlation length – in order to compute the reaction rate. This can be achieved via non-equilibrium statistical mechanics techniques, such as microkinetics or Monte Carlo. Due to the fast vibrations of adsorbates with respect to the reaction time scales, adsorbates are typically thermally equilibrated, and reaction events can be thought of as rare events.

In this work, we make use of multi-scale modeling to predict chemical reactivity of heterogeneous reactions. First, *ab initio* modeling using Density Functional

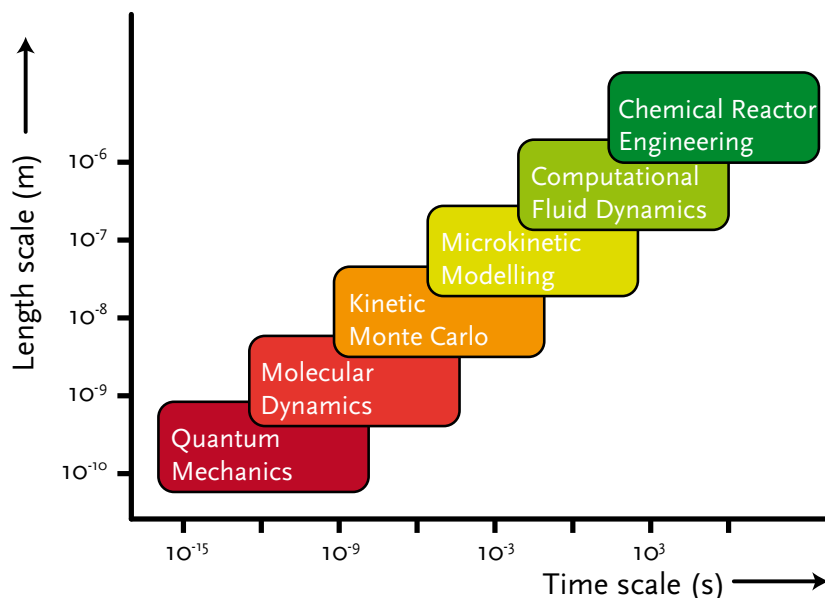


**Figure 2.1:** Computer simulations can be done at different length and time scales depending on the purpose. Usually, the time scale by which events can be described correlates to the length scale. Very accurate determination of rate constants requiring quantum-mechanics and the time evolution of a molecular system as done in molecular dynamics can only be done for small systems. Combining methods at different length and time scales is termed multi-scale modelling.

Theory (DFT) is employed to calculate the electronic structure of the chemical system in order to construct the reaction energy surface for calculating rate constants and energetics. Second, this dataset is used to construct a chemical reaction network, which serves as the parameters for a microkinetic model (MKM) that is made up of all relevant elementary reaction steps in the mechanism of the reaction under study. With this, we can predict surface coverages, reaction rates of individual steps and, also, the overall macroscopic reaction rate. It also enables

us to compute selectivity when more than one product can be formed in the chemical reaction. Furthermore, methods are employed to understand which individual steps are controlling the reaction rate the most. In section 2.2 we will discuss density functional theory (DFT) and in section 2.3 we will elaborate on how a connection is made between DFT and microkinetics simulations by means of statistical thermodynamics. Furthermore, we will discuss the algorithm employed in microkinetics simulations.

## 2.2 QUANTUM-CHEMICAL METHODS

### 2.2.1 THE ELECTRONIC STRUCTURE PROBLEM

The main purpose of electronic structure calculations is to solve the non-relativistic time-independent Schrödinger equation:

$$\hat{H}\psi_i(\vec{x}_1, \vec{x}_2, \dots, \vec{x}_M, \vec{R}_1, \vec{R}_2, \dots, \vec{R}_N) = E_i\psi_i(\vec{x}_1, \vec{x}_2, \dots, \vec{x}_M, \vec{R}_1, \vec{R}_2, \dots, \vec{R}_N) \quad (2.1)$$

Herein,  $\mathbf{H}$  is the Hamiltonian for a system consisting of  $M$  nuclei and  $N$  electrons which are described by the position vectors and  $\mathbf{R}_j, \mathbf{r}_i$  respectively. In atomic units<sup>1</sup>, the Hamiltonian can be expressed as:

$$\hat{H} = -\frac{1}{2} \sum_{i=1}^N \nabla_i^2 - \frac{1}{2} \sum_{j=1}^M \frac{1}{M_j} \nabla_j^2 - \sum_{i=1}^N \sum_{j=1}^M \frac{Z_j}{r_{i,j}} + \sum_{i=1}^N \sum_{k>i}^N \frac{1}{R_{i,k}} + \sum_{j=1}^M \sum_{l>j}^M \frac{Z_j Z_l}{R_{j,l}} \quad (2.2)$$

$M_j$  is here the ratio of the mass of the nucleus  $j$  to the mass of an electron and  $Z_j$  is the atomic number of nucleus  $j$ . The first two terms in equation 2.2 are for the kinetic energy of the electrons and nuclei, respectively. The third term represents the Coulomb attraction between electrons and nuclei. The fourth and fifth terms

represent the repulsion between electrons and between nuclei, respectively.

Vital to many electronic structure calculations is the Born-Oppenheimer approximation<sup>2</sup>, which neglects the motion of the nuclei, as these are much heavier than the electrons. Even for the lightest nucleus, a proton, its mass is approximately 1836 times larger than the electron. Thus, in most cases, electron motion can be described by its motion in an electrostatic field produced by the nuclei. With this approximation, the second term in equation 2.2 can be neglected and the final term, the repulsion between the nuclei, can be treated as a constant for a fixed configuration of the nuclei. Henceforth, we obtain equation 2.3, which is termed the electronic Hamiltonian.

$$\hat{H}_{\text{elec}} = -\frac{1}{2} \sum_{i=1}^N \nabla_i^2 - \sum_{i=1}^N \sum_{j=1}^M \frac{Z_j}{r_{i,j}} + \sum_{i=1}^N \sum_{k>i}^N \frac{1}{r_{i,k}} \quad (2.3)$$

Obtaining the solution to the Schrödinger equation involving the electronic Hamiltonian (eq. 2.3) is the main focus in electronic structure calculations. As electrons are fermions and obey the Pauli exclusion principle, their wavefunction should be anti-symmetric with respect to the interchange of the spin-space

coordinates of any two electrons. Slater determinants satisfy this antisymmetry condition through an appropriate linear combination of Hartree products, which are the non-interacting electron wave functions.

### 2.2.2 THE HARTREE-FOCK APPROXIMATION

Among the approximate ways to solve the electronic Schrödinger equation (eq. 2.3), the Hartree-Fock (HF) approximation<sup>1</sup> has a central role. It is one of the earliest methodologies in solving the electronic structure problem. In addition, it functions as a stepping-stone for explaining more advanced and accurate methodologies in modern quantum chemistry. The Hartree-Fock method uses a single Slater Determinant as an approximation to the wave function of the ground state of the N-electron system:

$$\text{To find the best approximate wave } |\Phi\rangle = |\chi_1, \chi_2, \dots, \chi_A, \chi_B, \dots, \chi_N\rangle \quad (2.4)$$

function, the variational principle is employed, which systematically varies the spin orbitals, while constraining that they remain orthogonal until the electronic minimum  $E_0$  is reached. This leads to the HF energy expression,

$$E = \frac{\int \langle \Phi(x) | \hat{H} | \Phi(x) \rangle d\bar{x}}{\int \langle \Phi(x) | \Phi(x) \rangle d\bar{x}} \quad \text{The major} \quad (2.5)$$

drawback in the Hartree-Fock approximation is that the correlation of the movement of the electrons is neglected. Many post-Hartree-Fock methods have been developed that incorporate the electron-correlation. Configuration Interaction (CI) uses a linear combination of Slater determinants instead of a single one. Møller-Plesset perturbation theory treats electron correlation using perturbation theory. In the Coupled Cluster method, the electron correlation is handled through use of a so-called cluster operation.<sup>1</sup> Although these post-Hartree-Fock methods provide a very accurate description of the electronic structure, they are computationally too demanding to be employed to problems in catalysis as these methods can only be applied to systems with less than 50 atoms at the current level of computational power.

### 2.2.3 DENSITY FUNCTIONAL THEORY

Hartree-Fock, Møller-Plesset Perturbation Theory and Coupled Cluster methods have in common that they rely on the many body wave function as a central quantity. In contrast, in density functional theory the electron density is used

as the central quantity. The many-body wavefunction depends on  $3N$  spatial variables together with a spin variable, where  $N$  is the number of electrons, limiting its applicability to relatively small systems. Density functional theory can effectively treat significantly larger systems as the dimensionality of the problem is severely reduced. The electron density is always three-dimensional regardless of the number of electrons. Partly for this reason, DFT has become the most widely used method in electronic structure calculations, particularly in the field of computational catalysis. Comprehensive discussions of DFT can be found in a range of excellent review articles<sup>3-6</sup> and textbooks<sup>7,8</sup>.

### 2.2.3.1 THOMAS-FERMI THEORY

Interestingly, the first article employing the electron density as the central quantity precedes that of the Hartree-Fock approximation. The early work of Thomas and Fermi<sup>9,10</sup> describes a method to calculate the kinetic energy of electrons derived from the quantum statistical theory based on the uniform electron gas. In this theory, the electron density is defined as

$$\rho(\vec{r}) = N \int \dots \int |\vec{x}_1, \vec{x}_2, \dots, \vec{x}_N|^2 \mathrm{d}\vec{x}_1 \mathrm{d}\vec{x}_2 \dots \mathrm{d}\vec{x}_N \quad (2.6)$$

where  $\rho$  determines the chance of finding any of the  $N$  electrons within the volume  $d\mathbf{r}$  arbitrarily of the position and spin of the other  $N-1$  electrons. Obviously, the electron density integrated over all space should be equal to the number of electrons in the system as given by

$$\int \rho(\vec{r}) \mathrm{d}\vec{r} = N \quad (2.7)$$

The kinetic energy is then defined as

$$T[\rho] = C_F \int \rho^{\frac{5}{3}}(\vec{r}) \mathrm{d}\vec{r} \quad (2.8)$$

where the constant  $C_F$  is based on the exact solution of the uniform electron gas.

$$C_F = \frac{3}{10} (3\pi^2)^{\frac{2}{3}} = 2.871 \quad (2.9)$$

Finally, the total energy of the system can then be expressed by combining the approximation of the kinetic energy using the electron density with a classical approach to calculate the electron-nucleus and electron-electron interactions.

$$E[\rho] = C_F \int \rho^{\frac{5}{3}}(\vec{r}) \mathrm{d}\vec{r} \quad (2.10)$$

$$- Z \int \frac{\rho(\vec{r})}{r} \mathrm{d}\vec{r}$$

$$+ \frac{1}{2} \iint \frac{\rho(\vec{r}_1)\rho(\vec{r}_2)}{|\vec{r}_1 - \vec{r}_2|} \mathrm{d}\vec{r}_1 \mathrm{d}\vec{r}_2$$

Irrespective of the simplicity and the lack of accuracy of the method, it

illustrates two very important principles. Firstly, it is possible to determine the kinetic energy purely on the basis of the spatial distribution of the electron density. Secondly, the constant required for this expression can be derived from the ideal case of the homogenous electron gas.

### 2.2.3.2 HOHENBERG-KOHN THEOREM

The next step in the development of modern density functional theory was made in 1964 with the publication of the paper of Hohenberg and Kohn.<sup>11</sup> Herein, two key principles were postulated. Firstly, a one-to-one mapping between the external potential (from the nuclei) and the electron density was established. Secondly, it was shown that the ground-state energy can be found using the variational principle.

The first principle can be proved by a *reductio ad absurdum* kind of reasoning. Suppose there is a collection of electrons enclosed in a box influenced by an external potential  $V(\mathbf{r})$ . If we know the electron density of this system,  $V(\mathbf{r})$  is fixed and, accordingly, also all properties. Imagine another external potential  $V'(\mathbf{r})$  which differs from  $V(\mathbf{r})$  by more than a constant, that can also give the same electron density  $\rho(\mathbf{r})$  for the ground state. We then have two different Hamiltonians  $H$  and

$H'$  whose ground state electron density is the same, but where the normalized wave function  $\Phi$  and  $\Phi'$  would be different. This would give rise to the following equation,

$$\begin{aligned} E_0 &< \langle \Phi' | \hat{H}' | \Phi' \rangle \quad (2.11) \\ &= \langle \Phi' | \hat{H}' | \Phi' \rangle + \langle \Phi' | \hat{H} - \hat{H}' | \Phi' \rangle \\ &= E'_0 + \int \rho(\vec{r}) [v(\vec{r}) - v'(\vec{r})] d\vec{r} \end{aligned}$$

and similarly we get,

$$\begin{aligned} E'_0 &< \langle \Phi | \hat{H} | \Phi \rangle \quad (2.12) \\ &= \langle \Phi | \hat{H} | \Phi \rangle + \langle \Phi | \hat{H}' - H | \Phi \rangle \\ &= E_0 + \int \rho(\vec{r}) [v(\vec{r}) - v'(\vec{r})] d\vec{r} \end{aligned}$$

Combining these two definitions yields the contradiction:

$$E_0 - E'_0 < E'_0 - E_0 \quad (2.13)$$

This result reveals that there can be no two different external potentials that can give the same  $\rho(\mathbf{r})$ . Thus  $\rho(\mathbf{r})$  uniquely determines  $v(\mathbf{r})$  and all ground-state properties.

As such, we can write down the energy  $E$  explicitly as a functional of the electron density :

$$E[\rho] = T[\rho] + T_{\text{NE}}[\rho] + V_{\text{EE}}[\rho] = \int \rho(\vec{r}) v(\vec{r}) d\vec{r} + F_{\text{HK}}[\rho] \quad (2.14)$$

where

$$F_{\text{HK}}[\rho] = T[\rho] + V_{\text{EE}}[\rho] \quad (2.15)$$

Note here that  $F_{\text{HK}}[\rho]$  is a universal functional of  $\rho(\mathbf{r})$ .

The second Hohenberg-Kohn theorem demonstrates that the ground state energy can be obtained using a variational principle, where the density that gives the lowest energy is the exact ground state density. Using the first theorem, suppose the ground state wave function is  $\Phi$  and its related electron density is  $\rho(\mathbf{r})$ . Thus the density  $\rho(\mathbf{r})$  uniquely defines the external potential  $v(\mathbf{r})$ . If there is another wave function  $\Phi'$  with an arbitrary variation from  $\Phi$  and its electron density is  $\rho'(\mathbf{r})$ , then we can obtain:

$$\begin{aligned} \langle \Phi' | \hat{H} | \Phi' \rangle &= \int \rho'(\bar{\mathbf{r}}) v(\bar{\mathbf{r}}) + \\ &F_{\text{HK}}[\rho'] \\ &= E[\rho'] \geq E[\rho] \end{aligned} \quad (2.16)$$

Conclusively, the lowest energy found given a certain electron density corresponds to the ground-state electron density.

Although these two principles provide a proof that the total ground-state energy can be obtained from the ground-state density, the exact description to obtain  $\rho(\mathbf{r})$  or  $F_{\text{HK}}[\rho]$  was not clear until Hohenberg and Kohn released another paper in 1965.<sup>12</sup> Herein, similar to the Hartree-Fock approximation, they (re-)introduced the idea of one-electron orbitals and the

approximation of the kinetic energy of the system by the kinetic energy of the non-interacting orbitals. This yields the following expression for the total energy

$$\begin{aligned} E &= \sum_i^N \varepsilon_i - \frac{1}{2} \iint \frac{\rho(\bar{\mathbf{r}})\rho(\bar{\mathbf{r}}')}{|\bar{\mathbf{r}} - \bar{\mathbf{r}}'|} d\bar{\mathbf{r}}d\bar{\mathbf{r}}' \quad (2.17) \\ &+ E_{\text{XC}}[\rho] - \int v_{\text{XC}}\rho(\bar{\mathbf{r}}) d\bar{\mathbf{r}} \end{aligned}$$

Unfortunately, there is one unknown term in this equation: the exchange-correlation energy  $E_{\text{XC}}$ .  $E_{\text{XC}}$  includes the non-classical aspects of the electron-electron interaction along with the component of the kinetic energy of the real system different from the fictitious non-interacting system. The latter term needs to be included, as the kinetic energy of non-interacting electrons is obviously different from interacting electrons. Since  $E_{\text{XC}}$  is not known exactly, many approximations have been introduced to calculate this term.

### 2.2.3.3 EXCHANGE-CORRELATION FUNCTIONS

To use the Kohn-Sham equations, the form of the exchange-correlation function has to be known. The simplest variant of the exchange-correlation approximations is the local density approximation (LDA). This local density approximation is exact for the ideal case of a uniform electronic system. The kinetic and exchange en-

ergies of such a system are easily evaluated and the correlation energy can be established using accurate Monte-Carlo simulations. The LDA approximation for the exchange-correlation energy can be written as

$$E_{\text{XC-LDA}}[\rho(\vec{r})] = \int \rho(\vec{r}) \varepsilon_{\text{XC-unif}}(\rho(\vec{r})) d\rho(\vec{r}) \quad (2.18)$$

where  $\varepsilon_{\text{XC-unif}}$  is the exchange-correlation energy per particle of the homogeneous electron gas of density  $\rho(\mathbf{r})$ . In other words, to calculate the exchange-correlation energy of an inhomogeneous electron gas, the correlation energy of a uniform electron gas of the same density is used. The LDA is an oversimplification of the actual density distribution and leads to an overestimation of bond energies. Strictly, the LDA is only valid for slowly varying densities, which is obviously not the case for many chemical systems. It was therefore a surprise that it works relatively well and much of the current understanding of metals and semiconductors is based on LDA simulations. Partly, the successful application of LDA was attributed to upholding so-called sum-rules.

The obvious improvement to the local density approximation is not only taking into account the local electronic density in the evaluation of the exchange-correla-

tion energy, but including the gradient as well. The general expression is then written as

$$E_{\text{XC-GGA}}[\rho(\vec{r})] = \int \rho(\vec{r}) \varepsilon_{\text{XC-unif}}(\rho(\vec{r}), \nabla\rho(\vec{r})) d\rho(\vec{r}) \quad (2.19)$$

Thus, generalized gradient approximations (GGA) are semi-local, comprised of corrections to the LDA while, like LDA, ensuring consistency with the sum rules. For many properties such as geometries and ground state energies of molecules, GGAs yield better results than their LDA counterparts. The most widely used GGAs for chemical applications are the PW91 and PBE functionals. The latter version has several offspring, such as revPBE<sup>13</sup>, RPBE<sup>14</sup>, PBE-WC<sup>15</sup> and PBE-sol<sup>16</sup>. The most widely used flavor is PBE, which has been used in all of the reported DFT calculations within this thesis.

### 2.2.3.4 PLANE-WAVES AND PSEUDOPOTENTIALS

For many practical applications of DFT, a particular choice in the type of basis set has to be made. Within this thesis, we are mainly investigating catalysis on large extended (periodic) surfaces. Henceforth, planewaves are used as our basis-set. Based on Bloch's theorem<sup>17</sup>, the eigenstates  $\Phi$  of the one-electron Hamiltonian,  $H = -\frac{1}{2}\nabla^2 + U(\vec{r})$ , can be

written as

$$\phi_{nk}(\vec{r}) = \exp(i\vec{k} \cdot \vec{r}) \mu_{nk}(\vec{r}) \quad (2.20)$$

where  $\mu_{nk}$  is a function with the same periodicity as the potential  $U(\mathbf{r})$  in such a way that

$$\mu_{nk}(\vec{r} + \vec{R}) = \mu_{nk}(\vec{r}) \quad (2.21)$$

The size of the planewave basis set is given by stating the highest energy of the planewave in a given set. This is termed the cutoff energy.

For typical chemical properties of interest, it is known that the valence electrons play a more important role than the core electrons. Given the fact that the core electrons within a plane-wave basis set require a fairly large amount of basis functions for their description due to their highly oscillatory behavior, this leads to the contradiction that the least important electrons require the largest part of the computational effort. One common way to resolve this discrepancy

is the use of pseudopotentials in which core electrons and nuclei are described by a smooth effective potential. In such a method however, all the information about the real wavefunction close to the nuclei is lost. Furthermore, there is no systematic way to generate good pseudopotentials.

A more general approach is the Projector-Augmented-Wave method (PAW) as introduced by Blöchl<sup>18</sup> in 1994 as an extension of both the augmented-wave and pseudopotential method. This approach is schematically depicted in Figure 2.2. Herein, the wavefunction is divided into two parts: a partial expansion within an atom-centered sphere, and an envelope function outside. The two parts are then matched smoothly at the sphere edge. The wavefunction within the sphere is linked onto a local basis of auxiliary functions. This linkage ensures that the kinks and strong oscillations near the nucleus are attached to a numerically smooth auxiliary wave function, which is expanded into planewaves.

## 2.3 MICROKINETIC MODELING

Microkinetic modeling is the modeling of reactions in terms of elementary reaction steps that occur on the catalytic surface. A requirement for the construction of a microkinetic model is a detailed

analysis of the chemical reaction network. The transient behavior of the chemical system can then be studied by solving a series of ordinary differential equations (ODE) over time. The parameters for the

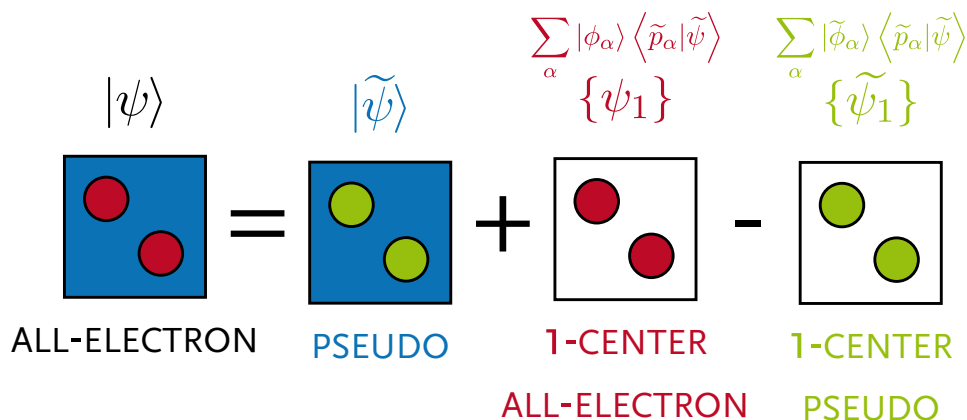


**Figure 2.2:** Schematic representation of the Projector-Augmented-Wave method. The pseudo wavefunction consists of a part that approximates the free electrons in the solid using plane-waves, and a part that approximates the electron density near the core using pseudopotentials. There is a correction term for the difference between the two regions.

microkinetic model can be obtained from *ab initio* methods such as DFT, or from experimental means.

### 2.3.1 PARAMETER EVALUATION USING DFT

For a microkinetic simulation, the rate constants of all the elementary reaction steps need to be known. These can be obtained from DFT calculations in the following way (as schematically depicted in Figure 2.3).

By performing electronic structure calculations, the absolute electronic energies (i.e. the bonding energy with respect to all electrons and nuclei infinitely far apart) are calculated for the initial, transition and final state of all relevant elementary reaction steps. From these,

the electronic activation energies in the forward and backward direction of the elementary reaction step are obtained.

The complete set of activation energies and all elementary reaction steps yield an electronic reaction energy surface (RES). By performing a frequency analysis on all these states, in other words, probing the curvature in all configurational directions for these states, the vibrational degrees of freedom are inventoried from which the zero-point energy correction to the electronic activation energies can be calculated.

The zero point energy (ZPE) correction to the electronic activation energy can be as large as 10-15 kJ/mol. Although this correction may not seem much, especially given that the accuracy of a typical DFT calculation is in the same

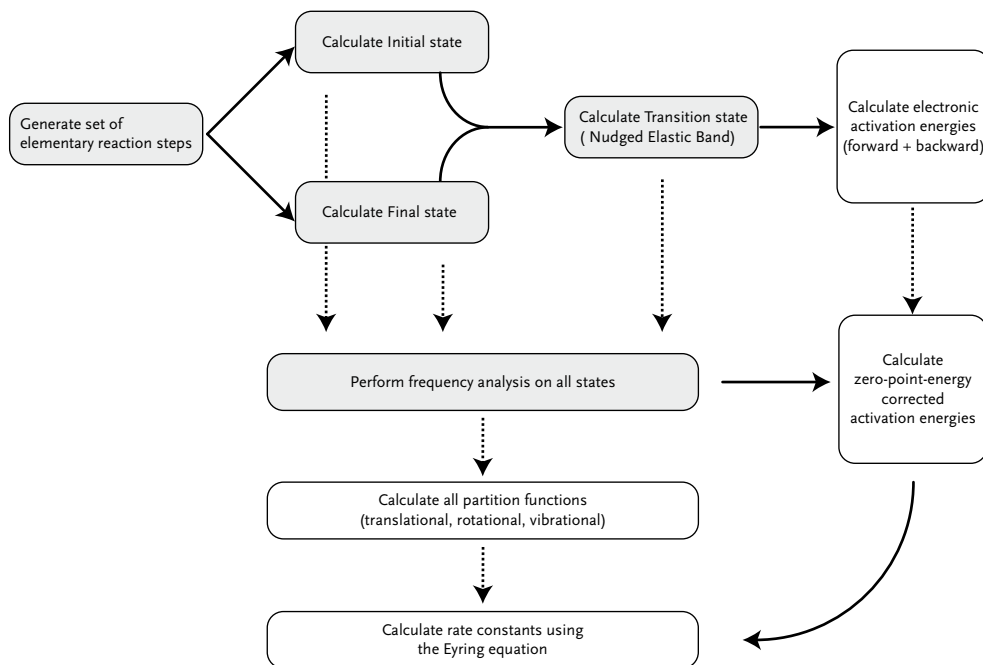


**Figure 2.3:** Schematic representation of the Projector-Augmented-Wave method. The pseudo wavefunction consists of a part that approximates the free electrons in the solid using plane-waves, and a part that approximates the electron density near the core using pseudopotentials. There is a correction term for the difference between the two regions.

range, neglecting the ZPE correction yields erroneous results. For instance, not taking ZPE corrections into account gives an overestimation of the reaction enthalpy of methane and water formation from carbon monoxide and hydrogen by roughly 100 kJ/mol.

So far, we have explained how to calculate the ZPE-corrected energy differences between the states. To calculate the rate constants used in microkinetics modeling, the partition functions corresponding to the configurational degrees of freedom in these states are needed as

well. To compute the rate constant for a particular elementary reaction step, the Eyring equation<sup>19</sup> is used:

$$k = \frac{k_b T}{h} \frac{Q^\ddagger}{Q} \exp\left(\frac{-\Delta E_{\text{act}}^{\text{zpe-corr}}}{k_b T}\right) \quad (2.22)$$

Here  $k$  is the reaction rate of a single elementary reaction step.  $Q^\ddagger$  and  $Q$  are the total partition function of the transition and initial state, respectively.  $\Delta E_{\text{act}}^{\text{zpe-corr}}$  is the ZPE corrected activation energy in J per particle,  $k_b$  the Boltzmann's constant,  $h$  Planck's constant and  $T$  the temperature in Kelvin.

Typically, we distinguish three types of elementary reaction steps: adsorption, surface reaction and desorption. The difference in the change of the configurational degrees of freedom between these three types of reaction is significant and consequently, their corresponding formulas for the rate constants differ.

For a catalytic reaction on a surface,  $Q^{\ddagger}$  and  $Q$  are composed of the partition functions corresponding to  $3N-1$  and  $3N$  vibrational degrees of freedom, respectively. The values for the partition functions can be calculated using a frequency analysis employing the following formula

$$f_{\text{vib}} = \frac{1}{1 - \exp\left(-\frac{h\omega}{k_b T}\right)} \quad (2.23)$$

Herein,  $\omega$  is the frequency of the vibrational mode,  $k_b$  the Boltzmann's constant and  $T$  the temperature in Kelvin. For surface reactions, there is not a significant change in the entropy and consequently the pre-exponential factor of the rate constants is typically in the order of  $10^{13}$ .

In contrast, for adsorption and desorption reactions there is a profound change in entropy. Typically, a gaseous compound has several rotational and translational degrees of freedom of which the partition function is given by the following formulas.

For the translational partition function, the formula is

$$f_{\text{trans}} = \frac{L\sqrt{2\pi mk_b T}}{h} \quad (2.24)$$

where  $L$  denotes the characteristic length of the translation and  $m$  the mass of the particle.

The rotational partition function in three directions is given by

$$f_{\text{rot}} = \frac{8\pi^2 I k_b T}{h^2} \quad (2.25)$$

where  $I$  denotes the rotational moment of inertia in three directions.

In an adsorption reaction, we assume that the surface is a plane far from the side where the adsorption takes place and on which the potential energy is constant and equal to its value in the gas phase. In such a case, one translational degree of freedom (perpendicular to the direction of the catalytic surface) is converted to a vibrational mode (as a consequence of bonding). Furthermore, chemisorption is a non-activated process and hence the activation energy equals zero. Inserting equation (2.24) into the Eyring equation (2.22) yields

$$k_u = \frac{k_b T}{h} \frac{L^2 (2\pi m k_b T) h^3}{L^3 (2\pi m k_b T)^{3/2}} \quad (2.26)$$

Rearranging the above equation

and using the ideal gas approximation ( $PV=nRT$ ) gives the rate constant for adsorption.

$$k_{\text{ads}} = \frac{PA}{\sqrt{2\pi mk_{\text{b}}T}} \quad (2.27)$$

where  $P$  is the pressure in Pascal and  $A$  is the surface area for adsorption (i.e. the area of a surface site).

For a desorption process, we assume that the desorbing compound gains two translational degrees of freedom and three rotational degrees of freedom in the transition state. This gives the following expression when plugging in the formula for the rotational degrees of freedom in three dimensions (eq. 2.25) together with the formula for the translational degree of freedom (eq. 2.24) into the Eyring equation (eq. 2.22)

$$k_{\text{ads}} = \frac{k_{\text{b}}T}{h} \frac{A(2\pi mk_{\text{b}}T)}{h^2} \frac{8\pi I k_{\text{b}}T}{\sigma h^2} \cdot \exp\left(\frac{-\Delta E_{\text{des}}}{k_{\text{b}}T}\right) \quad (2.28)$$

which upon rearranging yields

$$k_{\text{ads}} = \frac{k_{\text{b}}T^3}{h^3} \frac{A(2\pi mk_{\text{b}})}{\sigma \theta_{\text{rot}}} \cdot \exp\left(\frac{-\Delta E_{\text{des}}}{k_{\text{b}}T}\right) \quad (2.29)$$

Herein,  $\theta_{\text{rot}}$ , is the characteristic temperature for rotation and  $\sigma$  the symmetry

number to properly account for the number of indistinguishable orientations as a result of the rotation of the molecule.

It should be noted that if the transition state for desorption is rigid (for instance in  $\text{CH}_3$  hydrogenation that leads directly to desorption), the same kinetic expression as for a surface reaction is used.

To summarize, from the DFT calculations all the kinetic parameters can be obtained. By investigating the curvature of the electronic energy surface by a frequency analysis, the configurational degrees of freedom can be calculated necessary to compute the partition function. Finally, by insertion of these partition functions into the Eyring equation, the rate constants for the reaction can be calculated.

### 2.3.2 CONSTRUCTION AND SOLVING OF THE SET OF ORDINARY DIFFERENTIAL EQUATIONS

The construction of the ordinary differential equations is fairly straightforward. The initial step is to construct a library of elementary reaction steps and corresponding rate constants. This gives a set of  $2R$  elementary reaction equations (forward and backward) and  $N$  compounds. For each unique compound, an ODE is obtained of the form

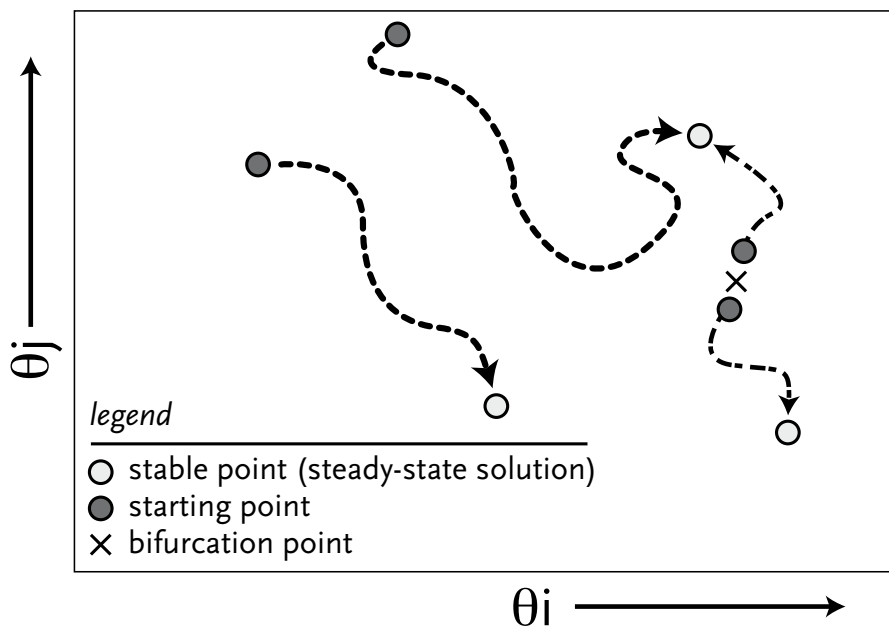


**Figure 2.4:** Schematic representation of phase space. The light circles are stable points in phase space (i.e. steady-state solutions to the set of ODEs). The dark circles are starting points (i.e. initial values of the concentrations in the set of ODEs) and the crosses are marked as crosses. The dotted lines are trajectories in phase space, which depend on the initial values as well as the set of ODEs.

$$\frac{\partial \theta_i}{\partial t} = \sum_j^{2R} \left( \nu_{j,i} k_j \prod_q^{N_j} \theta_{q,j}^{\nu_{q,j}} \right) \quad (2.30)$$

for all  $q$ , where  $\nu_{q,j} < 0$ .

where  $\theta_i$  is the concentration of species  $i$  on the surface,  $\nu_{j,i}$  is the stoichiometric coefficient of compound  $i$  in reaction  $j$ ,  $k_j$  is the rate constant of reaction  $j$ ,  $\theta_{q,j}$  is the concentration of compound  $q$  in reaction  $j$  and  $\nu_{q,j}$  is the stoichiometric coefficient of compound  $q$  in reaction  $j$ .

Loosely speaking, this formula tells us that the concentration of each compound

changes over time depending on whether the compound is a reactant or a product in the elementary reaction step. The rate at which the compound changes over time in a given elementary reaction step then depends on the reaction constant  $k_j$  and the product of the concentration of species involved in the elementary reaction step. Note that  $\nu_{j,i}$  has a negative value if compound  $i$  is a reactant in reaction  $j$  and a positive value when it is a product of the reaction.

The set of  $2R$  ordinary differential equations is then solved, meaning that

the ODEs are integrated over time until a steady state solution is reached given by

$$\left\{ \frac{\partial \theta_i}{\partial t} = 0 \right\}, \text{ for all } i \quad (2.31)$$

The set of all possible values of  $\{\theta_i\}$  is termed the phase space (see Figure 2.4). Integrating in time can be seen as moving through phase space and the path taken is termed the trajectory. Obviously, this trajectory depends on the set of ODEs and thus on the chemical network. The point where equation 2.31 is fulfilled, is termed a stable-point in phase space. In theory, several such stable points can exist in phase space, meaning that given a fixed set of ODEs, purely on the basis of the initial settings, i.e. the starting point in phase space, a different steady-state solution can be found. In practice, a good methodology is therefore to start with an empty catalytic surface in the simulation. The existence of multiple stable points in phase space leads to the concept of bifurcation points. These special points in phase space have the characteristic that if the system is on one side of this point, it converges to a different stable point as when it is on the other side of that point. It is not very difficult to imagine that probing the curvature in phase space very close to such a bifurcation point can lead to chaotic behavior. Such problems sometimes occur in the calculations and are often resolved by marginally changing

the temperature in the simulation.

Solving a set of ordinary differential equations is no trivial task and the algorithm or routine for integrating a set of ODEs in time is termed an ODE solver. Many such solvers exist and depending on the nature of the ODEs a particular type of ODE solver performs better than any other. Several excellent articles exist treating ODE solvers.<sup>20-22</sup> Here we would like to emphasize that the set of ODEs involved in a chemical network are a so-called stiff set of ODEs. Although there is no clear mathematical definition as to what stiffness entails, it is sufficient to know that for a stiff system the values of the differential equations tend to differ over several orders of magnitude. This is not very hard to realize considering that the reaction rates depend on the activation energy by an exponential relationship.

Specialist solvers dealing with stiff systems of ODEs often use the  $N \times N$  Jacobian matrix in which each element is given by

$$J_{i,j} = \frac{\partial^2 \theta_j}{\partial \theta_i \partial t} \quad (2.32)$$

to efficiently integrate the set of ODEs. Using this matrix, the solver is able to approximate the direction in which the system needs to be integrated, thus minimizing the number of function

calls and therefore the computational effort.

A nice analogy to explain this principle is the following: Imagine you are in the mountains and want to find the way to the nearest village. An unintelligent solver would let you bounce from one side of the mountain to the other in order to find the village. An efficient solver using the Jacobian matrix would follow the mountain trail.

### 2.3.3 STABLE-POINT ANALYSIS

Several important quantities of interest exist in order to analyze a chemical reaction network using microkinetic modeling. In principle one probes the curvature in hyper phase space around a stable point in phase space, either by changing the partial pressures, reaction temperature or the height of the transition state.

In order to compare a microkinetics simulation with experimental observables, the reaction order is such an important quantity of interest. This quantity is given by

$$n_i = \frac{\partial \ln(r_j^+)}{\partial p_i} \quad (2.33)$$

where  $r_j$  is the reaction order in compound  $j$ ,  $p_i$  the partial pressure in compound  $i$  and  $r_j^+$  the forward rate based on given key-compound  $j$ .

In this thesis, we use a linear-fitting procedure to calculate the abovementioned differential. The forward rate is probed by varying the partial pressure of compound  $i$  in the range of  $\pm 0.2\%$  around the default value. For the linear fitting, five datapoints are used. We found that five datapoints is sufficient for obtaining a proper linear fit ( $R^2 > 0.98$ ), whereas increasing this value does not lead to significantly better results. Furthermore, we found that if the steady-solution of the ODEs is far away from any bifurcation points in phase space, varying the partial pressure by any value in the range from  $0.1-10\%$  yields accurate linear fits.

Another experimentally probed quantity is the apparent activation energy. To calculate this observable, one solves

$$E_{\text{act}}^{\text{app}} = RT^2 \frac{\partial \ln(r_j^+)}{\partial T} \quad (2.34)$$

Similarly to the procedure employed for obtaining the reaction order, for calculating the apparent activation energy a linear fitting procedure is used as well. Herein, the reaction rate in the forward direction is calculated using five datapoints and performing a linear fit from which the slope is used to calculate the differential given in eq. 2.34. For a proper linear fit, the interval used between the five datapoints should not be too large and on the basis of many test runs it was

found that a 1K interval provides good results in almost all cases.

Pivotal in the analysis of a chemical reaction network is the identification of the rate-controlling steps.<sup>23</sup> The amount of rate-control of a particular elementary reaction step is expressed as

$$\chi_i = \left( \frac{\partial \ln(r_j^+)}{\partial \ln(k_i^\pm)} \right) \Bigg|_{k_{i \neq j}, K_i} \quad (2.35)$$

where  $\chi_i$  is the degree of rate-control of elementary reaction step  $i$  and  $k_i$  the rate constant of elementary reaction step  $i$  in both the forward and backward direction. In words, this means that the effect of increasing both the forward and the backward rate of a particular elementary reaction step with regard to the forward reaction rate of the key-compound is probed. If the value of  $\chi_i$  is positive, this means that the elementary reaction step is a rate-limiting step. Decreasing the

transition state would then result in an increase of the overall reaction rate. If on the other hand the value of  $\chi_i$  is negative, this means that the particular elementary reaction step is rate-inhibiting. In other words, decreasing the activation energy in both directions would result in a decrease of the overall reaction rate.

For any stable point in phase space, sufficiently far removed from a bifurcation point in hyper-space, the following relationship seems to hold

$$\sum_i \chi_i = 1 \quad (2.36)$$

For complex reaction networks, equation 2.36 provides a useful test to check whether the calculation has converged and whether the post-analysis was successful. ■

## 2.4 REFERENCES

- (1) Szabo, A.; Ostlund, N. S. *Modern Quantum Chemistry - Introduction to Advanced Electronic Structure Theory*; Dover Publications, Inc.: Mineola, 1996.
- (2) Born, M.; Oppenheimer, R. *Annalen der Physik* **1927**, *389*, 457.
- (3) Geerlings, P.; De Proft, F.; Langenaeker, W. *Chem. Rev.* **2003**, *103*, 1793.
- (4) Jones, R. O.; Gunnarsson, O. *Rev. Mod. Phys.* **1989**, *61*, 689.
- (5) Parr, R. G. *Annu. Rev. Phys. Chem.* **1983**, *34*, 631.
- (6) Ziegler, T. *Chem. Rev.* **1991**, *91*, 651.
- (7) Dreizler, M. R.; Gross, E. K. U. *Density Functional Theory: An Approach to the Quantum Many-Body Problem*; Springer: Berlin, 1990.
- (8) Parr, R. G.; Yang, W. *Density-Functional Theory of Atoms and Molecules*; Oxford University Press: New-York, 1989.
- (9) Fermi, E. *Rend. Accad. Naz. Lincei* **1927**, *6*, 602.

- (10) Thomas, L. H. *Proc. Cambridge Phil. Soc.* **1927**, 23, 542.
- (11) Hohenberg, P.; Kohn, W. *Phys. Rev.* **1964**, 136, B864.
- (12) Kohn, W.; Sham, L. J. *Phys. Rev.* **1965**, 140, A1133.
- (13) Zhang, Y.; Yang, W. *Phys. Rev. Lett.* **1998**, 80, 890.
- (14) Hammer, B.; Hansen, L. B.; Nørskov, J. K. *Phys. Rev. B* **1999**, 59, 7413.
- (15) Wu, Z.; Cohen, R. E. *Phys. Rev. B* **2006**, 73, 235116.
- (16) Perdew, J. P.; Ruzsinszky, A.; Csonka, G. I.; Vydrov, O. A.; Scuseria, G. E.; Constantin, L. A.; Zhou, X.; Burke, K. *Phys. Rev. Lett.* **2008**, 100, 136406.
- (17) Bloch, F. Z. *Physik* **1929**, 52, 555.
- (18) Blöchl, P. E. *Phys. Rev. B* **1994**, 50, 17953.
- (19) Eyring, H. J. *Chem. Phys.* **1935**, 3, 107.
- (20) Brown, P. N.; Byrne, G. D.; Hindmarsh, A. C. *SIAM J. Sci. and Stat. Comput.* **1989**, 10, 1038.
- (21) Byrne, G. D.; Hindmarsh, A. C. *ACM Trans. Mat. Soft.* **1975**, 1, 71.
- (22) Byrne, G. D.; Hindmarsh, A. C. *J. Comput. Phys.* **1987**, 70, 1.
- (23) Stegelmann, C.; Andreasen, A.; Campbell, C. T. *J. Am. Chem. Soc.* **2009**, 131, 8077.

## Abstract

The present density functional theory study provides insight into the reactivity of the surface metal atoms of extended/periodic Rh surfaces, clusters and nanoparticles toward CO adsorption and dissociation. Our results demonstrate that the defect site in a  $B_5$  configuration is the most active one for CO dissociation on all three considered systems. However, the reactivity of the  $B_5$  site for CO dissociation depends critically on the size of the system. It was found that the smaller system sizes lead to an increase of the CO dissociation barrier on the  $B_5$  site. The barrier for CO dissociation on the  $B_5$  site on a stepped Rh (211) surface is significantly lower as compared to all other pathways that were investigated. Moreover, this site was the only site where the TS energy was below the CO desorption energy.

---

THIS CHAPTER HAS BEEN PUBLISHED AS:

Filot, I.A.W., Shetty, S., van Santen, R.A., Hensen, E.J.M.,

*J. Phys. Chem. C*, 2011, 115, 14204-14212.

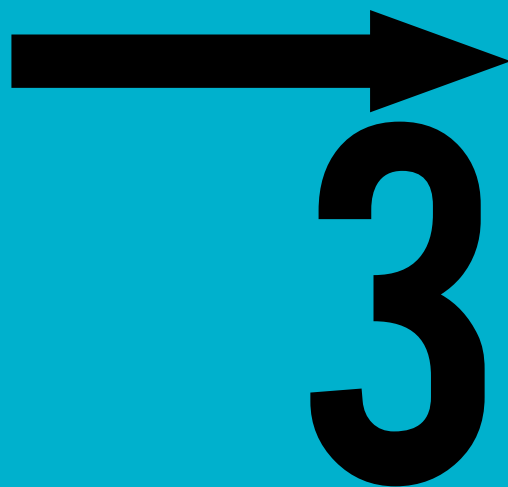


---

★ *"Venezuelan Beaver Cheese" is fictitious but, despite this, recipes for it have since been published. ★*

Wikipedia article about the Cheese Shop sketch of Monty Python

**SIZE AND  
TOPOLOGICAL  
EFFECTS OF  
RHODIUM  
SURFACES,  
CLUSTERS AND  
NANOPARTICLES  
ON THE  
DISSOCIATION OF  
CO**



## 3.1 INTRODUCTION

The limited resources of fossil fuels along with environmental concerns have stimulated a broad intensive search for alternative energy sources.<sup>1</sup> Due to its abundance, the importance of natural gas as a feedstock for the synthesis of fuels and chemicals continues to grow. Synthesis gas, derived from natural gas by steam reforming, can be used to synthesize higher aliphatic hydrocarbons as well as olefins and other oxygenates via the Fischer-Tropsch (FT) reaction.<sup>2-4</sup>

The synthesis of hydrocarbons and their oxygenated derivatives requires active catalysts with high selectivity to the desired product. Rhodium catalysts are known for their reasonable selectivity toward oxygenates because of their ability to dissociate CO while ensuring an appreciable rate of CO insertion.<sup>5</sup> It is not surprising that Rh is studied for the production of olefins and other (longer) oxygenates, since it occupies a position in the periodic table that lies between Fe and Co, which both are able to dissociate CO to form (long) hydrocarbons and Pd, Pt and Ir, which mainly produce alcohols and other oxygenates.<sup>5-8</sup> The initial step in the Fischer-Tropsch reaction is CO dissociation and is of crucial importance to understanding of the Fischer-Tropsch mechanism.

Based on density functional theory

(DFT) calculations and experimental observations, the optimum site for dissociation of molecules with  $\pi$  bonds such as CO and NO has been proposed to be the  $B_5$  site present on stepped or corrugated surfaces.<sup>9-11</sup> This site represents a particular geometry of at least five surface Rh atoms arranged in such manner that a step is created. Mavrikakis *et al.* showed that the barrier for CO dissociation is lower by 120 kJ/mol on the  $B_5$  site than on the terrace.<sup>12</sup> This is supported by experimental work of Ren *et al.*, who found that CO adsorbs only molecularly on Rh(111) and (001) surface planes as compared to stepped sites, where CO dissociates significantly.<sup>13</sup> Stroppa *et al.* proposed that the activation barrier for CO dissociation on Rh(553) is approximately 100 kJ/mol lower than on Rh(111).<sup>14</sup> In a similar case, Lofreda *et al.* reported an activation barrier of 0.95 eV for NO dissociation on step sites of the Rh(511) surface in comparison to 1.61 eV on a flat Rh(111) surface.<sup>15</sup>

Experimentally, it has been shown that the catalytic performance in Fischer-Tropsch is dependent on the size and shape of the metal nanoparticles. Xiao *et al.* showed a strong particle size dependency for the aqueous phase FT synthesis by small Ru clusters with dimensions between 1.5 and 4.5 nm.<sup>16</sup> The group of De Jong<sup>17, 18</sup> have shown that

the optimal Co particle size lies around 6 nm with a strong decrease of the FTS activity with decreasing particle size. These authors suggested that the rate of CO dissociation decreases when the Co particles become smaller.

These considerations imply that the rate of CO dissociation will strongly depend on the particle size and the geometry of the surface ensemble involved in the dissociation reaction. The catalytic properties of very small particles may differ from larger ones because of a lower extent of electron delocalization. The influence of the structure of the site over which CO dissociates is also to be taken into account. It may be argued that the ability to stabilize  $B_5$  sites will also depend on the particle size.<sup>9</sup> To the best of our knowledge, there has been only one study of CO dissociation over nanosized clusters by Lanzani *et al.*, who computed a reaction barrier of 0.77 eV for CO dissociation on the facets of a  $Fe_{55}$  icosahedron particle.<sup>19</sup>

In the present theoretical study we employed DFT to investigate the role of  $B_5$  sites for CO dissociation. In order to understand the influence of electron (de) localization, we computed barriers for CO dissociation on  $B_5$  sites stabilized on small metal clusters and extended periodic surfaces. Moreover, whereas on one side extended surfaces are characterized by their strong electron delocalization

and on the other side small metallic clusters exhibit quantum confinement, the electronic properties of nanoparticles lies in between these two extremes. Furthermore, in comparison to periodic surfaces, small metal clusters (or nanoparticles) contain a larger variety of adsorption sites for CO (terraces, facets) that can potentially facilitate its dissociation. Therefore, a number of mechanisms for CO dissociation on small metal clusters with 13 and 57 Rh atoms was included.

By our knowledge, this is one of the few articles<sup>19</sup> that discusses the Rh particle size effect for CO dissociation by DFT.

## 3.2 MODEL AND COMPUTATIONAL METHODS

All calculations were performed using a plane-wave density functional theory approach with the projector-augmented wave (PAW) method<sup>20,21</sup> as implemented in the Vienna ab initio simulation package (VASP).<sup>22,23</sup> The Perdew-Becke-Ernzerhof (PBE) exchange-correlation functional was used.<sup>24</sup> The kinetic energy cutoff for the plane wave basis set was 500 eV. We applied Monkhorst-Pack mesh k-points of (5x5x1) for the Rh(100) and (111) surface, (3x3x1) for the Rh(211) surface and the  $\gamma$ -point for the  $Rh_{13}$  cluster and the  $Rh_{57}$  nanoparticle. For the surfaces, the dipole-dipole interaction between the super cells has been avoided

by adsorption on both sides of the surface retaining a center of inversion. In the calculations all the degrees of freedom of the system have been optimized using the conjugate-gradient technique. The reaction paths have been generated by the nudged elastic band (NEB) as implemented in VASP.<sup>25</sup> The transition states (TS) have been confirmed by the saddle points obtained from frequency calculations. Frequencies have been calculated using the finite displacement technique. The bulk Rh-Rh distance from our calculations corresponds to 2.71 Å with a binding energy of -5.91 eV/atom, which is in good agreement with the experimental reported value for the binding energy of -5.75 eV/atom and the Rh-Rh distance of 2.69 Å.<sup>26</sup>

Three different models have been used to carry out quantum chemical calculations of the active B<sub>5</sub> site: (1) A Rh<sub>13</sub> system for the cluster, (2) a Rh<sub>57</sub> system for the nanoparticle and (3) Rh(100) and Rh(111) slabs and Rh(211) steps for the periodic/extended surface. The optimized Rh<sub>13</sub> cluster is shown in Figure 3.1a. In a recent theoretical study it was shown that this cluster shows relatively high stability among clusters between 3-13 atoms.<sup>27</sup>

The cluster was placed in a cubic supercell maintaining a vacuum gap of at

least 10 Å between the neighboring images. The binding energy of the Rh atoms in the clusters is -4.02 eV/atom and the magnetic moment is 0.69 μ/atom. These values are very similar to those reported by Shetty *et al.*, that is a binding energy of -3.66 eV/atom and a magnetic moment of 0.7 μ/atom using the PW-91 functional in combination with ultra-soft pseudopotentials.<sup>27</sup>

In the case of the nanoparticle, a semi-cuboctahedron consisting of 57 rhodium atoms was constructed (Figure 3.1b). The cuboctahedron has six (100) facets and eight (111) facets. On one of the (100) facets rhodium atoms were adsorbed on two adjacent fourfold sites. The cluster was placed in a cubic supercell maintaining a vacuum gap of at least 15 Å between the neighboring images. The binding energy is -4.70 eV/atom and the magnetic moment is 0.47 μ/atom.

For the (100) open and (111) terrace, a 3 x 3 supercell consisting of 5 layered slabs was considered, while for the (211) stepped surface was constructed a 2 x 3 supercell consisting of 8 layered slabs. The vacuum layer for all three surfaces was at least 15 Å. The CO coverages were 0.11 ML, 0.11 ML and 0.056 ML for the (100), (111) and (211) surfaces, respectively.

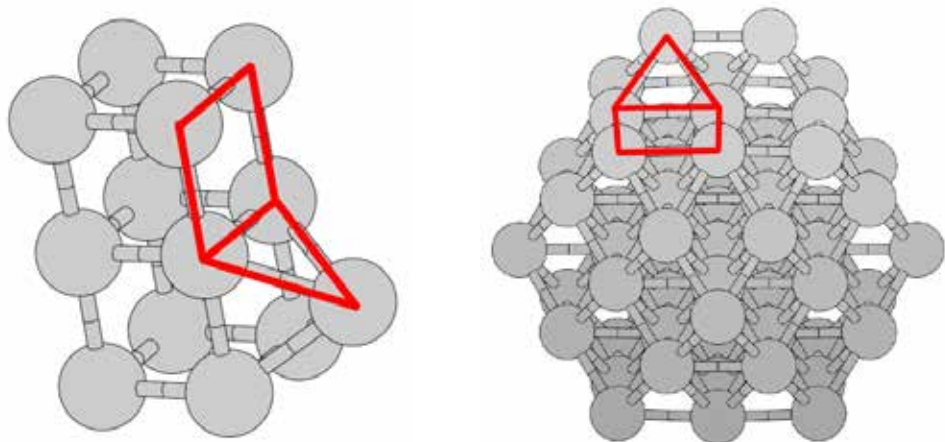


**Figure 3.1:** The optimized  $Rh_{13}$  and  $Rh_{57}$  systems. The red lines represent the  $B_5$  site, which consists of four atoms in a square formation and one atom in a fourfold coordination on a neighboring square site.

## 3.3 RESULTS

In this section we discuss the adsorption and dissociation of CO on  $Rh(111)$ ,  $Rh(100)$ , and  $Rh(211)$  surfaces, the  $Rh_{13}$  cluster and the  $Rh_{57}$  nanoparticle.

### 3.3.1 $Rh_{13}$ CLUSTER

For CO dissociation on the  $Rh_{13}$  cluster, the geometries and the potential energy diagrams are presented in Figures 3.2 and 3.3, respectively. Four different pathways for CO dissociation were considered, i.e. one on the  $B_5$  site, two on the face and one on the side of the particle.

We will briefly elaborate on the CO dissociation mechanism for each of these sites (Figure 3.2). For the  $B_5$  site CO preferentially adsorbs on a threefold site in

the initial state (IS). In the transition state (TS) the C atom stays in the threefold site, while the O atom moves to a bridge site. The final state (FS) leaves the C and O located in threefold and bridge sites, respectively. Importantly, the TS does not involve sharing of metal atoms between C and O. In contrast to the dissociation mechanism on the  $B_5$  site, the other sites involve sharing of metal atoms between C and O. For the  $fi$  site CO initially adsorbs on a bridge site. During the reaction C and O move to threefold and bridge sites, respectively. In this case, two metal atoms are shared in the TS by C and O. In the FS, C remains in the threefold site, while O moves to another bridge site. On the side of the  $Rh_{13}$  particle, CO adsorbs in

**Table 3.1:** The preferred adsorption site, coordination numbers (CN) of the metal atoms involved in the Rh-C bonding in the IS, energy of adsorption ( $E_{ads}$ ) and C-O bond distances for each of the four different pathways studied on the  $Rh_{13}$  particle.

|            | Adsorption site | CN         | Eads [eV] | C---O Bond distance [Å] |      |      |
|------------|-----------------|------------|-----------|-------------------------|------|------|
|            |                 |            |           | IS                      | TS   | FS   |
| $B_5$ site | Threefold       | 4, 5, 5    | 1.47      | 1.20                    | 2.22 | 3.70 |
| f1         | Bridge          | 4, 5       | 1.93      | 1.19                    | 1.94 | 4.22 |
| f2         | Bridge          | 4, 5       | 1.93      | 1.19                    | 2.02 | 4.72 |
| side       | Fourfold        | 3, 3, 4, 5 | 0.92      | 1.22                    | 2.11 | 4.85 |

a fourfold site. In the TS, C remains in the fourfold site and O moves to a bridge site. As was the case for the f1 site, also here the TS involves two metal atoms being shared by C and O. Finally, similar to the f1 site, CO adsorbs on a bridge site for the f2 site. Dissociation proceeds by moving C to a threefold site, while O moves “upward” to a bridge site. In this case, one metal atom is shared between C and O in the TS. In the FS, C remains in the threefold site, while O moves to a bridge site.

From inspection of Figure 3.3 it follows that CO adsorbs strongest on bridge sites (f1 and f2: 1.93 eV), followed by adsorption on a threefold coordinated site ( $B_5$ : 1.47 eV) and a fourfold coordinated site (side: 0.92 eV). To investigate the influence of the relaxation of the metal atoms upon adsorption of CO, deformation energies of the cluster were calculated. The deformation energy of the cluster is

defined as the single point energy of the cluster with CO minus the energy of the cluster without CO with an optimized geometry. The deformation energies were found to be very similar for the various adsorption sites and were 0.16, 0.29, 0.29 and 0.23 eV, for  $B_5$ , f1, f2 and side, respectively.

The coordination numbers of the metal atoms involved in binding of carbon in the IS are reported in Table 3.1. It is seen that lower coordination numbers result in lower adsorption energies. This trend contrasts the tendency to have strong adsorption associated when CO is bound to metal surface atoms with a lower coordination number as follows from the Bond Order Conservation (BOC) principle.<sup>28</sup> We will elaborate on this peculiarity in the Discussion section.

The activation barriers for CO dissociation on the f1, f2, side and  $B_5$  sites were calculated to be 3.56, 3.23, 3.11 and 2.58

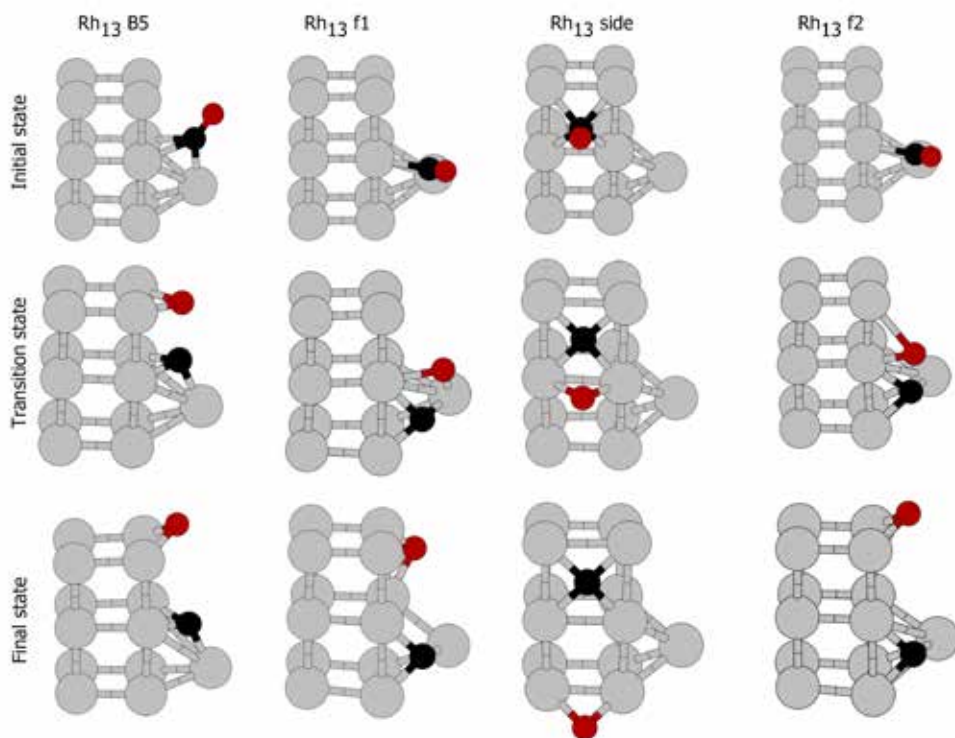


**Figure 3.2:** The four different CO dissociation pathways on the  $Rh_{13}$  cluster.

eV, respectively. The three highest TS energies for f1, f2 and “side” sites involve a TS in which one or more metal atoms are shared between the C and O atoms. The C-O distances are also listed in Table 3.1. Although there is considerable variation among the TS barriers of the four different pathways, there seems to be little correlation between the CO distances and these energies. One may furthermore note that none of the CO dissociation barriers lies below the gas phase energy.

### 3.3.2 $Rh_{57}$ NANOPARTICLE

Next, we will discuss the dissociation

pathways of CO on a  $Rh_{57}$  semi-cuboctahedron nanoparticle. In contrast to the  $Rh_{13}$  cluster, the  $Rh_{57}$  nanoparticle shows an electronic band structure more similar to that of extended surfaces as follows from the density of states (not shown here). The considered reaction pathways were chosen similar to those investigated for the  $Rh_{13}$  cluster. Two of these pathways proceed on (100) and (111) facets of the nanoparticle and the other two on the  $B_3$  site. The geometries and energy pathways are shown in Figures 3.4 and 3.5, respectively.

CO dissociation on the (100) facet is very similar to that of the ‘side’ site for

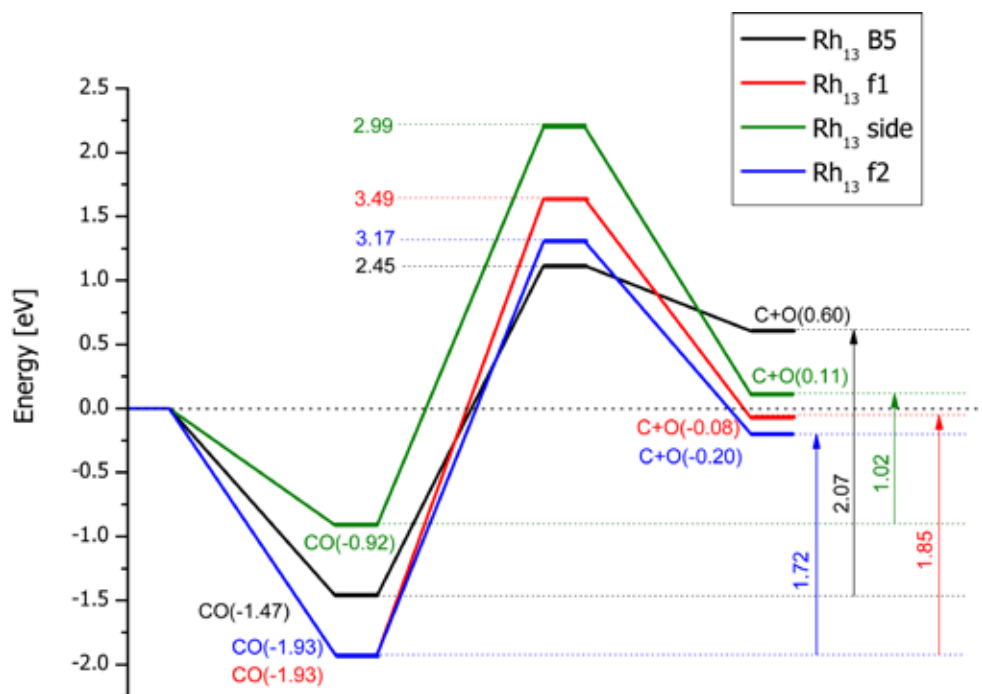


**Figure 3.3:** Potential energy diagram of CO dissociation of four different adsorption sites on a  $Rh_{13}$  nanoparticle. The values in brackets are the adsorption energies with respect to gas phase CO (left), the activation barrier with respect to adsorbed CO adsorbed (middle) and the reaction energy (right).

the  $Rh_{13}$  particle with CO initially adsorbed in the fourfold site. In the TS, C and O share two metal atoms. In the FS, C occupies a fourfold site, while O moves to a bridge site. CO is threefold coordinated on the (111) facet. In the TS, C and O share one metal atom. The FS has C in the initial threefold site with O moving to an adjacent threefold site. Two different mechanisms were studied for CO dissociation over a  $B_5$  site. The first one ( $B_5$  mechanism 1) starts from CO adsorption on a bridge site with the C moving to a

fourfold site in the TS, whilst O moves toward the top metal of the  $B_5$  site. In the TS no metal atoms are shared between C and O. In the FS, O moves to the top bridge site with C remaining in the fourfold site. The other mechanism involves CO initially adsorbed on the threefold site. In the TS, O moves to the bridge site below the step and C remains in the threefold site. The final state involves O in the threefold site of the (111) facet and C in its initial position. As in the other cases considered here the TS does not involve

**Table 3.2:** The preferred adsorption site, coordination numbers (CN) of the metal atoms involved in the Rh-C bonding in the IS, energy of adsorption ( $E_{ads}$ ) and C-O bond distances for each of the four different pathways studied on the  $Rh_{57}$  particle.

|                   | Adsorption site | CN         | $E_{ads}$ [eV] | C---O Bond distance [Å] |      |      |
|-------------------|-----------------|------------|----------------|-------------------------|------|------|
|                   |                 |            |                | IS                      | TS   | FS   |
| (100) facet       | Fourfold        | 5, 7, 7, 8 | 1.95           | 1.22                    | 1.92 | 5.07 |
| (111) facet       | Threefold       | 5, 7, 7    | 2.15           | 1.21                    | 1.89 | 3.25 |
| $B_5$ mechanism 1 | Bridge          | 5, 7       | 2.11           | 1.19                    | 2.13 | 4.41 |
| $B_5$ mechanism 2 | Threefold       | 5, 8, 10   | 1.76           | 1.21                    | 1.98 | 4.85 |

metal atom sharing between C and O.

The CO adsorption energy on the (111) and (100) facets and  $B_5$  site with mechanism 1 were 2.15, 2.11 and 1.95 eV respectively. The CO adsorption energy on the  $B_5$  site with mechanism 2 was significantly lower with a value of 1.76 eV. Interestingly, the activation barrier for CO dissociation for mechanism 2 on the  $B_5$  site was much lower (1.85 eV) than the barriers for the (111) and (100) pathway and  $B_5$  site with mechanism 1, which amounted to 2.48, 2.14 and 2.51 eV, respectively. The coordination numbers (CN) of the metal atoms involved in the Rh-C bonding are collected in Table 3.2.

The higher the metal-metal CN of

the metals involved in CO adsorption, the lower the CO adsorption energy. For example, the two adsorption sites (100) and the  $B_5$  site with mechanism 2 have the lowest CO adsorption energies and contain one or more metal atoms with a CN of 8 or more. On the contrary, the two sites with the highest CO adsorption energies, (111) and the  $B_5$  site with mechanism 1, have no metal atoms with such a high CN. Similar to the  $Rh_{13}$  cluster, deformation energies were calculated and were found to be 0.07, 0.12, 0.12 and 0.20 eV for the (100), (111) and the  $B_5$  sites with mechanisms 1 and 2, respectively.

In general, the sharing of metal atoms results in higher activation energies, as

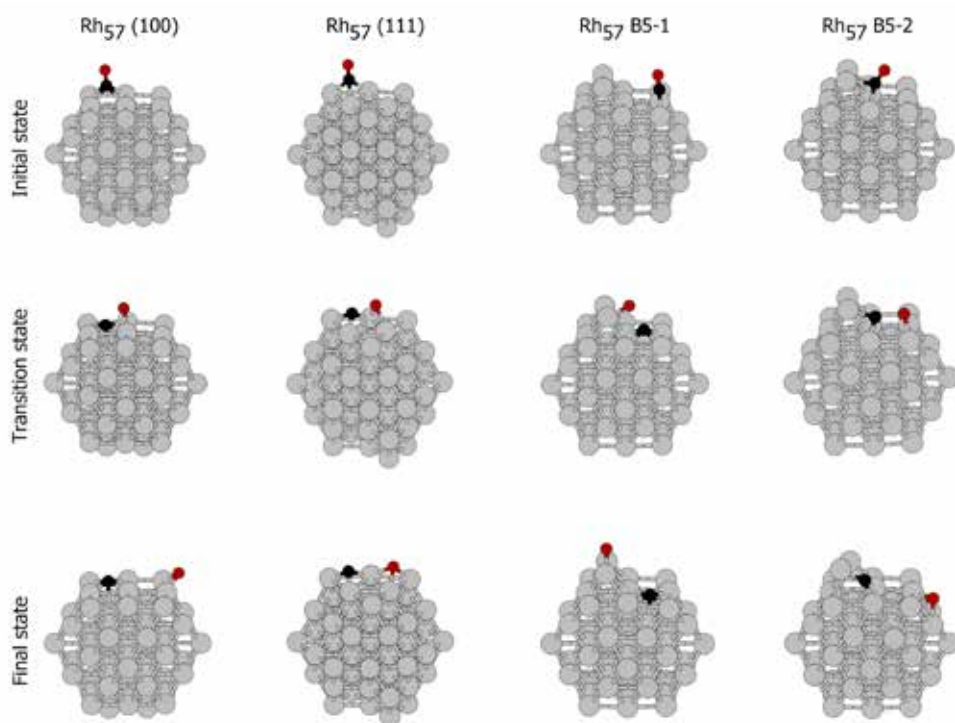


**Figure 3.4:** The four different CO dissociation pathways on the  $Rh_{57}$  nanoparticle.

can be derived from Figure 3.5. For example, the activation barriers for the CO dissociation on the (111) facets (2.48 eV), where one metal atom is shared, is significantly higher as compared to the  $B_5$  site with mechanism 2 (1.85 eV), which does not involve surface metal atom sharing of C and O in the TS. Moreover, upon comparison of the CO distance in the IS and FS between the two mechanism on the  $B_5$  site (no metal atom sharing), it can be deduced that when the transition state lies further away from the initial state, this results in a high activation energy. To elaborate: the CO distance in the IS

for the  $B_5$  site with mechanism 1 is 1.19 Å as compared to 2.13 in the TS, giving a difference of 0.94 Å. This is significantly larger than the difference in CO distance between IS and TS for mechanism 2 on the  $B_5$  site which is only 0.77 Å.

The C-O distances for the IS, TS and FS for each of the four different pathways are presented in Table 3.2. From Table 3.4 and Figure 3.5 it can be seen that the CO distance in the FS on the (100) facet is significantly longer with respect to the other sites. In contrast, the CO distance in the FS of the (111) facet is considerably shorter as compared to the other sites.

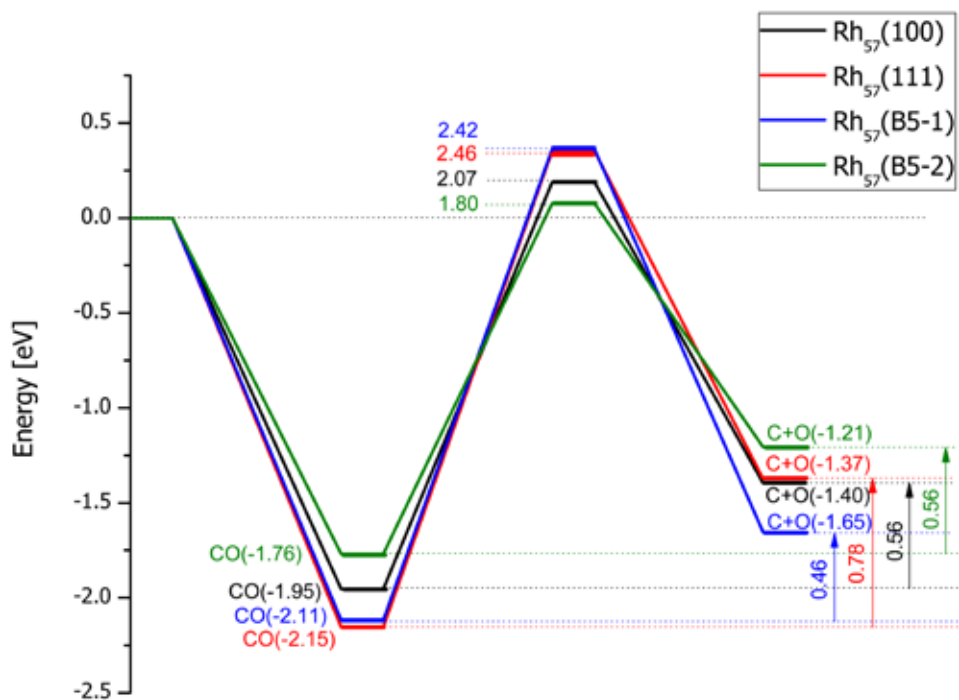


**Figure 3.5:** The energies corresponding to the initial, transition and FS of the four different CO dissociation pathways on a  $Rh_{57}$  nanoparticle. The reported values on the left, middle and right of the graph represent the adsorption energy with respect to gas phase CO, the activation barrier with respect to CO adsorbed and the reaction energy respectively.

This is reflected in the dissociation energies, which is higher for the (111) facet (-0.78 eV) as opposed to the (100) facet (-0.56 eV).

Finally, note that none of the CO dissociation barriers lie below the gas phase energy.

### 3.3.3 RH SURFACES

In this section, we discuss the dissociation of CO on the flat (111) surface, the open (100) surface and the stepped (211)

surface. Four different CO dissociation mechanisms were studied. The geometries and the energies are presented in Figures 3.6 and 3.7, respectively.

On the (100) flat surface, CO adsorbs on a fourfold coordination site. In the TS, O and C share two metals atoms. The C atom resides in a fourfold site, while O occupies the bridge site. In the FS, O has moved to another bridge site. CO adsorption on the (111) surface is similar to the (111) facet on the  $Rh_{57}$  nanoparticle and proceeds from a threefold site.

**Table 3.3:** The preferred adsorption site, coordination numbers (CN) of the metal atoms involved in the Rh-C bonding in the IS, energy of adsorption ( $E_{ads}$ ) and C-O bond distances for each of the four different pathways studied on the Rh surfaces.

|                            | Adsorption site | CN         | Eads [eV] | C---O Bond distance [Å] |      |      |
|----------------------------|-----------------|------------|-----------|-------------------------|------|------|
|                            |                 |            |           | IS                      | TS   | FS   |
| (100)                      | Fourfold        | 8, 8, 8, 8 | 1.91      | 1.21                    | 1.91 | 4.23 |
| (111)                      | Threefold       | 9, 9, 9, 9 | 1.81      | 1.19                    | 1.90 | 3.01 |
| B <sub>5</sub> mechanism 1 | Bridge          | 7, 7       | 2.11      | 1.18                    | 1.95 | 4.12 |
| B <sub>5</sub> mechanism 2 | Threefold       | 9, 9, 9    | 1.76      | 1.26                    | 2.09 | 3.09 |

During the reaction the C atom remains in the threefold site, while O moves to a bridge site. One metal atom is shared in the TS. The final geometry has the O atom moved to another threefold site. Similar to the B<sub>5</sub> site on the Rh<sub>57</sub> nanoparticle, there exist two different mechanisms on the (211) surface. In the first mechanism, CO adsorbs on a bridge site. During the reaction, C moves to a threefold site, while O moves to a bridge site. In the FS the C remains in a semi threefold site, while the O moves to another threefold site. In the TS one metal atom is shared. In the second mechanism on the (211) surface, CO adsorbs on a threefold site. In the TS, C remains in the threefold site,

while O moves to a bridge site. In the TS no metal atoms are shared. In the FS both C and O remain at the same site as in the TS.

From Figure 3.6 and 3.7 it can be seen that CO binds strongest on the bridge site of the (211) stepped surface (2.11 eV), followed by the fourfold site on the (100) surface (1.91 eV), the threefold site of the (111) surface (1.81 eV) and finally on a threefold site of the (211) surface (1.76) eV. Similar to the Rh<sub>57</sub> nanoparticle, an analysis of the CN of the metal atoms involved in the Rh-C bonding is performed. The results are collected in Table 3.3.

Similar to the case of the Rh<sub>57</sub> nanoparticle, the sites with the lowest adsorption energy are the threefold sites.

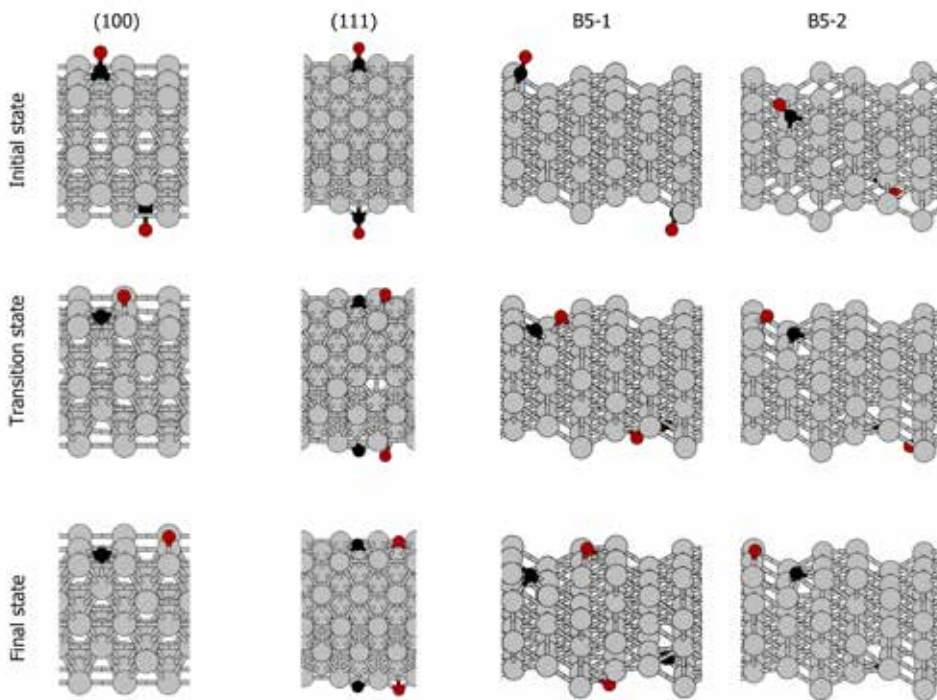


**Figure 3.6:** The four different pathways on the Rh surfaces. Variation barrier with respect to CO adsorbed and the reaction energy respectively.

orption energy correspond to sites where the metal atoms have high coordination numbers, whereas the adsorption sites of the highest adsorption energy contain metal atoms with a coordination number smaller than 8. Indeed, both the (111) as well as the  $B_5$  (mechanism 2) site contain three Rh atoms with  $CN = 9$  and the adsorption energies of these sites are very similar, that is 1.76 and 1.81 eV, respectively.

From Figure 3.6 it can be seen that for the (100), (111) and  $B_5$  (mechanism 1) site, one or more metal atoms are shared

between C and O atom in the TS, while for the  $B_5$  (mechanism 2) site, no metal atoms are shared. As is the case for the  $Rh_{57}$  particles also here the absence of the sharing of metal atoms among C and O atom lowers the activation energies. Moreover, the sharing of metal atoms with a higher CN results in higher activation energies as compared to the sharing of metal atoms with a low(er) CN. On the (111) site one metal atom with  $CN = 9$  is being shared between C and O, while for the (100) site two metal atoms with  $CN = 8$  are shared. The activation energy for

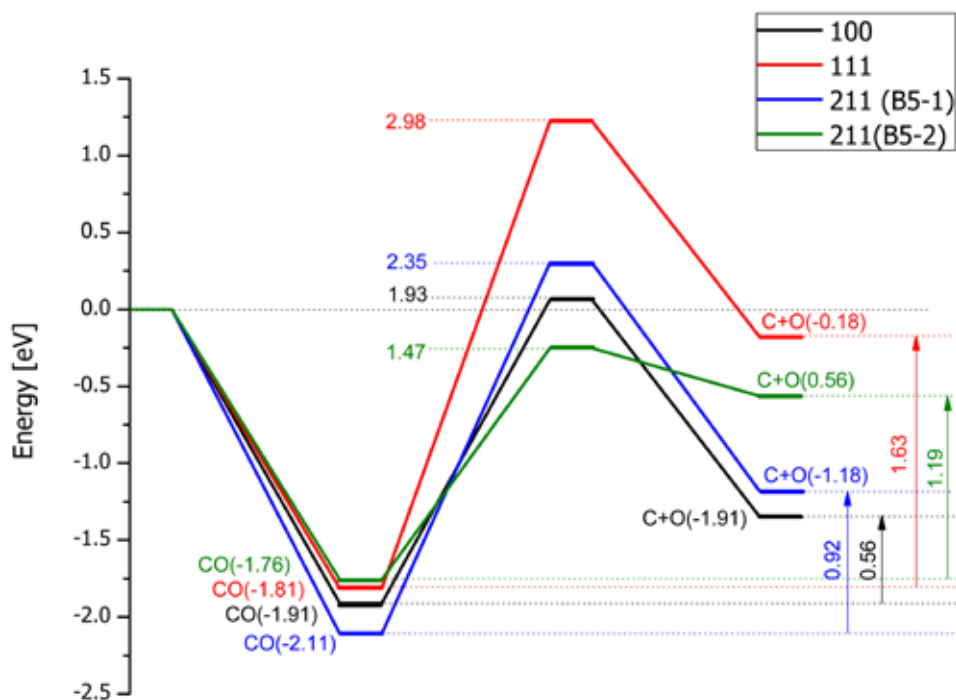


**Figure 3.7:** The energies corresponding to the initial, transition and FS of the four different CO dissociation pathways on different surfaces. The reported values on the left, middle and right of the graph represent the adsorption energy with respect to gas phase CO, the activation barrier with respect to CO adsorbed and the reaction energy respectively.

CO dissociation on the (111) site (3.04 eV) is significantly higher as compared to the activation energy on the (100) site (1.97 eV).

The C-O distances for the IS, TS and FS for each of the four different pathways are presented in Table 3.3. Similar to the reaction pathways for  $\text{Rh}_{13}$  and  $\text{Rh}_{57}$  particles, the cases involving a final state with large  $d_{\text{C}\cdots\text{O}}$  distances represents a

less endothermic reaction energies. For example, the (100) pathway has a  $d_{\text{C}\cdots\text{O}}$  distance of 4.23 Å and a reaction energy of 0.56 eV, whereas the (111) pathway has a  $d_{\text{C}\cdots\text{O}}$  distance of 3.01 Å and a reaction energy of 1.63 eV. Finally, note that only the CO dissociation barrier of mechanism 2 on the  $\text{B}_5$  site lies below the gas phase energy.

## 3.4 DISCUSSION

We have carried out a theoretical study to quantify the role of active  $B_5$  sites for CO dissociation on a Rh cluster, a nanoparticle and extended surfaces. In this section, we will discuss the three different features (adsorption, transition state and reaction energy) of CO dissociation on the different systems that were studied.

From the adsorption energies with respect to the CN of the Rh atoms involved in the Rh-C bonds, a clear trend is visible for the  $Rh_{37}$  nanoparticle and the Rh surfaces. CO interaction with Rh atoms with lower CN result in stronger bonds, because these metal surfaces have an upward shift of the d-band center, resulting in a better overlap with the CO  $5\sigma$  and  $2\pi^*$  orbitals.<sup>4,29-31</sup> This trend does not hold for CO adsorption on the  $Rh_{13}$  cluster. Besides the effect of the CN of the surface atoms, which obviously does not explain the lower adsorption energy for  $Rh_{13}$ , the effect of the more substantial deformation of the small cluster or the mode of CO adsorption may explain this deviant behavior.

Concerning the former, it is indeed noticed that the  $Rh_{13}$  cluster deforms more substantially upon CO adsorption than the  $Rh_{37}$  nanoparticle does. Thus,

one may hypothesize that the CO adsorption energies on small clusters are lower because of the relaxation of the metal-metal bonds that occurs upon adsorption of CO or, alternatively, to the coordination of the Rh-C bond due to the strong delocalization of the electron density. However, by close inspection of the deformation energies, it can be seen that the deformation energy for the  $f_1$  and  $f_2$  sites on the  $Rh_{13}$  cluster are both 0.29 eV, whereas these sites have the highest CO adsorption energy (1.93 eV, Figure 3.3). This indicates that the effect of deformation is not explaining the different CO adsorption energy for the smallest cluster. Thus, although we cannot give a very clear explanation to the deviant behavior, our results show a preference for CO adsorption on the bridge site, followed by a threefold and fourfold coordination, for very small clusters. This different order of stable adsorption geometries is analogous for the Rh clusters investigated by Shetty *et al.*<sup>27</sup>

Upon comparison of the  $Rh_{13}$  cluster (Figure 3.3),  $Rh_{37}$  nanoparticle (Figure 3.5) and extended Rh surfaces (Figure 3.7), it can be concluded that the activation energies decrease with an increasing particle size. Our results show that there

occurs more relaxation of the metal atoms to accommodate the CO in the TS for smaller system sizes, which could explain the higher activation energies of these systems.

In all cases, CO dissociation is most favorable on the  $B_5$  site. The two most important explanations for the low barrier are the absence of metal sharing between C and O in the TS and the different binding site of CO in the initial state and of C in the TS.<sup>9</sup> Indeed, in all three cases of the  $B_5$  pathway via mechanism 2, no metal atoms are shared in the TS, whereas CO dissociation on the (100) and (111) facets of the  $Rh_{57}$  nanoparticle and the f1, f2 and “side” pathways on the  $Rh_{13}$  cluster involves one or more metal atoms being shared between the C and O atoms. Although this explains why the activation barrier for the  $B_5$  pathway via mechanism 2 is significantly lower as compared to the other pathways, it does not explain why the activation barrier on the same  $B_5$  site via mechanism 1 on the  $Rh_{57}$  nanoparticle and the stepped (211) surface is significantly higher as compared to mechanism 2 on the  $B_5$  site. Indeed, the activation barrier for CO dissociation on the (100) facet of  $Rh_{57}$  is lower than the one of the

$B_5$  site with mechanism 1, despite the metal atom sharing in the former case.

In the case where the CN of the Rh atoms involved in the Rh-C bonds is lower for the IS as compared to CN numbers of the Rh atoms involved in the Rh-C bonds in the TS, this increases the activation energy for CO dissociation. For example, for the Rh atoms involved in the Rh-C bonds for the  $B_5$  site with mechanism 1, the CN are 5 and 7 for the  $Rh_{57}$  particles and 7 and 7 for the (211) surface. Their corresponding CNs in the TS are 5, 7, 8 and 9 for the  $Rh_{57}$  particles and 7, 7, 9 and 9 for the (211) stepped surface. In other words, the accommodation of the C atom in the TS requires bonding with less Rh atoms with higher CN. This phenomenon does not occur for the pathway on the  $B_5$  site via mechanism 2, because the C atoms remains in the TS in the same threefold coordination as in the IS.

If we compare the different energy pathways on each of the three system sizes, it can be seen that only the  $B_5$  mechanism 2 pathway on the (211) surface shows a TS below the CO gas phase energy. Therefore, only on this system CO dissociation is favored, while in all the other cases, the desorption of CO is more likely.

### 3.5 CONCLUSION

The present work describes 12 different CO dissociation pathways on three

different system sizes (13 atom cluster, 57 atom nanoparticle and extended surfa-

ces) using DFT. It was found that for the nanoparticle and the extended surfaces the CO adsorption energy correlates with the CN of the Rh atoms. This trend does not hold for the smallest cluster and, in this case, the coordination mode of the CO adsorption (bridge, threefold or fourfold) appears to be of overriding importance in determining the adsorption energy.

The major factors governing the TS energies for CO dissociation are (i) the sharing of metal atoms by the C and O in the TS and (ii) the coordination of the metal atoms involved in the Rh-C bond in the TS versus their coordination in the IS. Sharing of the C and O fragments with surface metal atoms in the TS leads to an increase in the dissociation barrier. Conversely, a lower CN of the metal atoms involved in the Rh-C bond in the

TS as compared to the CN of the metal atoms involved in the Rh-C bond in the IS lowers the dissociation barrier.

In all but one case the energy barrier for CO dissociation is higher than the desorption energy for CO: CO dissociation is possible over a  $B_3$  site on the (211) surface, where CO is initially adsorbed on a threefold site and carbon remains in this threefold site, while the oxygen moves to a bridge site.

The present data show that CO dissociation becomes more likely for larger particles. The results suggest that the decrease in activation energy for CO dissociation is an effect of the site topology rather than an electronic effect. The reported optimum in the particle size in experimental data should be due to an optimum density of  $B_3$  sites as a function of the particle size. ■

## 3.6 REFERENCES

- (1) Song, C. *Catal. Today* **2006**, *115*, 2.
- (2) Fischer, F.; Tropsch, H. *Brennst.-Chem* **1923**, *4*, 276.
- (3) Anderson, R. B. *The Fischer-Tropsch Synthesis*; Academic Press: New York, 1984, 1<sup>st</sup> Ed.
- (4) Somorjai, G. A. *Introduction to Surface Chemistry and Catalysis*; Wiley: New York, 1994.
- (5) Spivey, J. J.; Egbeki, A. *Chem. Soc. Rev.* **2007**, *36*, 1514.
- (6) Choi, Y.; Liu, P. J. *Am. Chem. Soc.* **2009**, *131*, 13054.
- (7) Shetty, S.; van Santen, R. A.; Stevens, P. A.; Raman, S. J. *Mol. Catal. A: Chem.* **2010**, *330*, 73.
- (8) Subramani, V.; Gangwal, S. K. *Energy & Fuels* **2008**, *22*, 814.
- (9) Santen, R. A. v.; Neurock, M.; Shetty, S. G. *Chem. Rev.* **2009**, *110*, 2005.
- (10) Shetty, S. G.; Jansen, A. P. J.; van Santen, R. A. J. *Phys. Chem. C* **2008**, *112*, 14027.
- (11) Ciobica, I. M.; van Santen, R. A. J. *Phys. Chem. B* **2003**, *107*, 3808.
- (12) Mavrikakis, M.; Bäumer, M.; Freund, H. J.; Nørskov, J. K. *Catal. Lett.* **2002**, *81*, 153.
- (13) Ren, D. M.; Liu, W. *Surf. Sci.* **1990**, *232*, 316.

- (14) Stroppa, A.; Mittendorfer, F.; Andersen, J. N.; Parteder, G.; Allegretti, F.; Surnev, S.; Netzer, F. P. *J. Phys. Chem. C* **2009**, *113*, 942.
- (15) Loffreda, D.; Simon, D.; Sautet, P. *J. Catal.* **2003**, *213*, 211.
- (16) Xiao, C. X.; Cai, Z.; Wang, T.; Kou, Y.; Yan, N. *Angew. Chem. Int. Ed.* **2008**, *47*, 746.
- (17) Bezemer, G. L.; Bitter, J. H.; Kuipers, H. P. C. E.; Oosterbeek, H.; Holewijn, J. E.; Xu, X.; Kapteijn, F.; van Dillen, A. J.; de Jong, K. *P. J. Am. Chem. Soc.* **2006**, *128*, 3956.
- (18) den Breejen, J. P.; Radstake, P. B.; Bezemer, G. L.; Bitter, J. H.; Frøseth, V.; Holmen, A.; Jong, K. P. d. *J. Am. Chem. Soc.* **2009**, *131*, 7197.
- (19) Lanzani, G.; Nasibulin, A. G.; Laasonen, K.; Kauppinen, E. L. *Nano Res.* **2009**, *2*, 660.
- (20) Blöchl, P. E. *Phys. Rev. B* **1994**, *50*, 17953.
- (21) Kresse, G.; Joubert, J. *Phys. Rev. B* **1999**, *59*, 1758.
- (22) Kresse, G.; Furthmüller, J. *J. Comput. Mater. Sci.* **1996**, *6*, 15.
- (23) Kresse, G.; Hafner, J. *Phys. Rev. B* **1994**, *49*, 14251.
- (24) Perdew, J. P.; Burke, K.; Ernzerhof, M. *Phys. Rev. Lett.* **1996**, *77*, 3865.
- (25) Henkelman, G.; Jónsson, H. *J. Chem. Phys.* **2000**, *113*, 9978.
- (26) Kittel, C. *Introduction to solid state physics*; John Wiley and Sons Inc.: Newyork, London, Sydney, 1966; Vol. 3rd ed.
- (27) Shetty, S. G.; Strych, S.; Jansen, A. P. J.; van Santen, R. A. *Can. J. Chem.* **2009**, *87*, 1.
- (28) van Santen, R. A. *Recl. Trav. Chim. Pays-Bas* **2010**, *109*, 59.
- (29) Nilsson, A.; Pettersson, L. G. M.; Nørskov, J. K. *Chemical Bonding at Surfaces and Interfaces*; Elsevier: Amsterdam, 2008.
- (30) Jorgensen, W. L.; Salem, L. *The Organic Chemist's Book of Orbitals*; Academic Press, Inc.: New York and London, 1973.
- (31) Sung, S.-S.; Hoffman, R. J. *Am. Chem. Soc.* **1984**, *107*, 578.



## Abstract

All relevant elementary reaction steps relevant to CO hydrogenation into methane, ethylene, formaldehyde, methanol, and ethanol on Rh(211) were studied using density functional theory. The calculations show that CO dissociation proceeds in a direct fashion without hydrogen assistance. For C-C bond forming reactions, the most facile CO insertion step is C+CO coupling and the most facile  $\text{CH}_x + \text{CH}_y$  reaction is C+C coupling. Water formation proceeds by proton migration between two hydroxyl species. The kinetic parameters from this study form the basis for a microkinetics model to compute rates and selectivities of CO hydrogenation.

★ *The major difference between a thing that might go wrong and a thing that cannot possibly go wrong is that when a thing that cannot possibly go wrong goes wrong it usually turns out to be impossible to get at and repair.* ★

Douglas Adams

**QUANTUM  
CHEMISTRY  
OF CO  
HYDROGENATION  
ON STEPPED  
RHODIUM  
SURFACES**



**4**

## 4.1 INTRODUCTION

The decline in readily available fossil fuel resources has motivated the search for alternative sources of fuels and chemicals.<sup>1</sup> The valorization of abundant and cheap natural gas into liquid transportation fuels by the Fischer–Tropsch reaction is increasingly practiced at the industrial scale as an economically viable alternative to crude oil refining. The Fischer–Tropsch reaction converts synthesis gas into long-chain hydrocarbons. The active phase in industrial Fischer–Tropsch catalysts is usually composed of Fe or Co.<sup>2–6</sup> Ruthenium is one of the most active Fischer–Tropsch metals, but it is too expensive to be used in commercial settings. Co, Fe, and Ru can catalyze the Fischer–Tropsch reaction, because these transition metals can dissociate CO at sufficiently high rates.

When less reactive transition metals that dissociate CO at lower rates are used to hydrogenate carbon monoxide, products other than long-chain hydrocarbons are obtained. For instance, Ni mainly produces methane and Cu methanol, while Pd, Ir, and Pt predominantly convert CO into methanol.<sup>7–10</sup> The use of Rh is notable because of its high selectivity for the production of ethanol.<sup>7,10,11</sup> Among other uses, ethanol is an attractive intermediate for the production of light olefins.<sup>12</sup> Many experimental works have focused

on optimizing the ethanol yield of Rh catalysts.<sup>13–23</sup> In addition to methanol and ethanol, small amounts of olefins (primarily ethylene) and oxygenates such as acetaldehyde and acetic acid are obtained with these catalysts. The formation of C<sub>2</sub>-oxygenates by Rh catalysts is usually explained by its intermediate activity in CO dissociation.<sup>7,24</sup>

Quantum chemical modeling based on density functional theory (DFT) can predict the kinetic parameters for the elementary reaction steps that underlie the mechanisms of heterogeneous reactions with good accuracy. The use of first principles kinetic parameters in microkinetics simulations provides insight into the dependence of catalyst sensitivity on the structure of the catalytic surface and the composition of the adsorbed layer under reaction conditions.<sup>25–27</sup> With advances in computing power, it is currently possible to carry out comprehensive studies for increasingly complex catalytic reactions such as the Fischer–Tropsch reaction.<sup>28,29</sup> In our recent work, we resolved important issues related to the Fischer–Tropsch reaction involving catalytic site requirements, the nature of chain propagation, and the effect of the reactivity of the transition metal.<sup>29</sup> The active sites for the Fischer–Tropsch reaction are step-edge sites on the surfaces of

sufficiently reactive transition metals that catalyze long-chain hydrocarbon formation.

Pertinent questions concerning CO hydrogenation on Rh catalysts relate to the optimum site for CO dissociation, the mode of CO dissociation and the dominant C-C coupling mechanism. Several theoretical studies have been carried out to study some of the elementary reaction steps relevant to these issues; planar Rh(111) and stepped Rh(211) surfaces have been the subjects of most of these investigations.<sup>8,25,26,30-36</sup> However, a complete mechanistic study of CO hydrogenation on Rh that clarifies the abovementioned issues for Rh catalysts is lacking.

The activation energy for CO dissociation on the Rh(111) terrace surface is known to be very high ( $E_{\text{act}} > 250$  kJ/mol).<sup>8,25,30,34,35,37</sup> Choi and Liu showed that hydrogen-assisted CO dissociation via HCO is more favorable on the close-packed surface than direct CO dissociation.<sup>8</sup> We reported that CO dissociation is preferred on stepped surfaces compared with the terraced (111) and (100) surfaces of Rh.<sup>30</sup> In line with these results, Kapur and co-workers concluded that hydrogen-assisted CO dissociation via CHO is the preferred route on Rh(111), while the most favorable path on Rh(211) is direct CO dissociation.<sup>24</sup> DFT calculations combined with microkinetics simulations of the steam reforming reaction of

methane showed that CO formation via HCO competes with direct CO formation.<sup>26,30-32</sup> C-C coupling reactions on Rh surfaces have also been investigated by quantum-chemical modeling.<sup>8,24,33,38</sup> Choi and Liu concluded that  $\text{CH}_3 + \text{CO}$  coupling is the main reaction pathway to  $\text{C}_2$ -oxygenates.<sup>8</sup> Alternatively, Kapur *et al.* found that  $\text{CH}_2 + \text{CO}$  coupling is the most feasible route for  $\text{C}_2$ -oxygenate formation on Rh(211) surfaces.<sup>24</sup> The reverse ethanol decomposition reaction has been studied more frequently in the past;<sup>33,39-42</sup> for instance, Zhang *et al.* found that ethanol decomposition proceeds via  $\text{CH}_3\text{CO}$  dissociation on Rh(111) and Rh(211) surfaces, with the barrier being the lowest on the stepped surface.<sup>33</sup>

In the present study, we have investigated the relevant elementary reaction steps for the hydrogenation of CO to methane, ethylene, formaldehyde, methanol, and ethanol on the stepped Rh(211) surface using quantum chemical DFT calculations. This choice was motivated by the very high barrier for CO dissociation on terraced surfaces;<sup>30</sup> under typical reaction conditions, the rate of CO dissociation on these surfaces is extremely low. All relevant coupling reactions between  $\text{CH}_x$  and CO were taken into account in this study, and the oxygen atoms originating from CO dissociation were removed as water.

The calculated reaction barriers are used to construct a microkinetics model

(see chapter 5) for CO hydrogenation on Rh(211).

## 4.2 COMPUTATIONAL METHOD

All DFT calculations were performed using the plane-wave approach with the projector-augmented wave (PAW) method<sup>43,44</sup> implemented in the Vienna Ab Initio Simulation Package (VASP).<sup>45,46</sup> The Perdew–Burke–Ernzerhof (PBE) exchange correlation functional was used.<sup>47</sup> The kinetic energy cutoff for the plane-wave basis set was 400 eV, and a Brillouin zone sampling of  $5 \times 5 \times 1$   $k$ -points was used. We modeled the surface using the Rh(211) termination of fcc Rh (Figure 4.1) in a  $3 \times 2$  supercell with periodic boundary conditions. In order to avoid spurious interactions between system images, a vacuum layer of at least 10 Å was added perpendicular to the surface. To confirm that the vacuum layer was large enough, we verified that the electron density approached zero at the border of the supercell. To avoid dipole-dipole interactions between supercells, we placed the adsorbates on both sides of the surface

to retain an inversion center. Electronic convergence was set to  $10^{-5}$  eV, and geometries were converged to  $10^{-4}$  eV using a conjugate-gradient algorithm that employs trial and corrector steps to converge both the energy of the structure as well as the forces on the ions. To determine transition states, we employed the nudged elastic band (NEB) method developed by Jónsson *et al.*<sup>48</sup> All optimized transition geometries corresponded to a first-order saddle point on the potential energy surface, as determined by frequency analysis. The vibrational frequencies of local minima and transition states were computed using the finite displacement method. These frequencies were then used to determine the zero-point energy (ZPE) correction to the electronic energy. The computed Rh–Rh bulk distance of 2.71 Å and the cohesive energy of -5.91 eV/atom correspond well to experimental values of 2.69 Å and -5.75 eV/atom.<sup>49</sup>

## 4.3 RESULTS AND DISCUSSION

DFT calculations were performed for all elementary reaction steps relevant to the formation of hydrocarbons (methane,

ethylene, and ethane) and oxygenates (formaldehyde, methanol, acetaldehyde, and ethanol). These reaction steps were

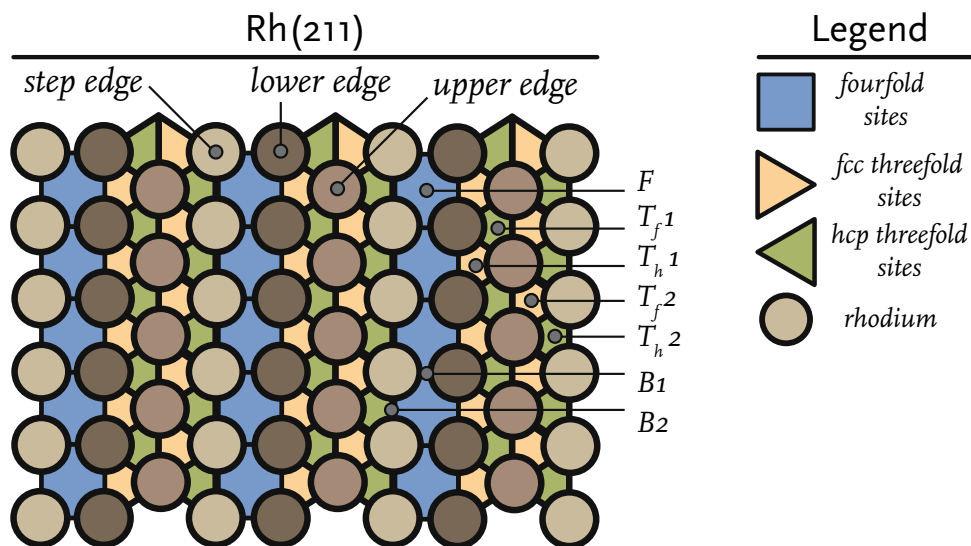


**Figure 4.1:** Schematic representation of the stepped Rh(211) surface. The coordination number (CN) of the surface atoms are CN = 7 for the step-edge, CN = 9 for the upper edge, and CN = 10 for the lower edge. Adsorption sites include one four-fold (F), two three-fold fcc (T<sub>f</sub>), two three-fold hcp sites (T<sub>h</sub>), and two bridge (B) sites.

grouped into the following categories: (i) direct and hydrogen-assisted CO dissociation reactions; (ii) C hydrogenation reactions to CH<sub>x</sub> intermediates and CH<sub>4</sub>; (iii) CO hydrogenation reactions to methanol; (iv) CH<sub>x</sub> + OH<sub>y</sub>; (v) CH<sub>x</sub> + CH<sub>y</sub> and (vi) CH<sub>x</sub> + CO coupling reactions; (vii) CH<sub>x</sub>CH<sub>y</sub> and (viii) CH<sub>x</sub>CH<sub>y</sub>OH<sub>z</sub> hydrogenation reactions; and (ix) O hydrogenation reactions that remove oxygen from the surface as water. The activation barrier values are given in the form of reaction networks that convert CO and H<sub>2</sub> into C<sub>1</sub> products (methane, formaldehyde, and methanol; Figure 4.3) and C<sub>2</sub> products (ethylene, ethane, acetaldehyde, and ethanol; Figure 4.5). The activation energies

are given with respect to the most stable adsorbed state for each intermediate. First, we discuss the different adsorption sites and geometries of the intermediates. Second, we briefly discuss the individual elementary reaction steps and highlight the main trends in activation energies and transition state structures.

### 4.3.1. ADSORPTION SITES

Figure 1 shows the two-, three-, and four-fold bridge and top adsorption sites on the Rh(211) surface. Table 4.1 lists the most stable adsorption sites identified for the surface intermediates. It is worthwhile to point out some general trends.

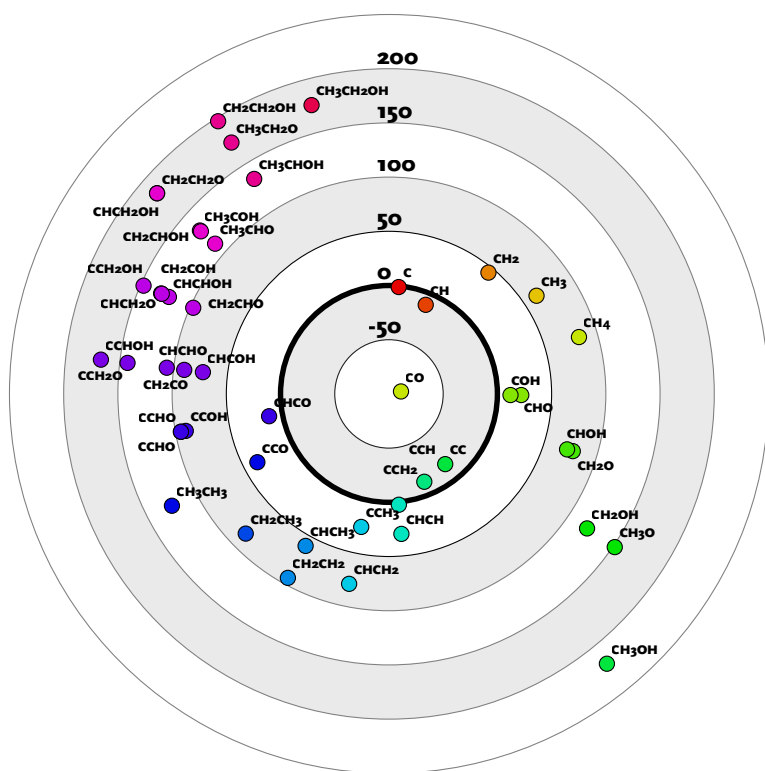


**Figure 4.2:** Stability plot of all surface reaction intermediates. Intermediates located closer to the center are more stable. The energy of each compound is calculated using atomic carbon, oxygen, and/or hydrogen adsorbed on the surface at infinite distance as the reference state (all energies are in kJ/mol).

Adsorbates that are saturated in terms of coordination tend to adsorb on bridge and top sites, whereas more reactive adsorbates tend to favor three- and four-fold coordination sites. For instance,  $\text{CH}_3$  favors top adsorption on the step-edge atom, while atomic C favors four-fold coordination on the (100) facet below the step. We found that  $\text{C}_2$  and oxygenated  $\text{C}_1$  and  $\text{C}_2$  adsorbates adsorb on the surface in a bidentate and, in some cases, in a tridentate manner.

To analyze the relative stabilities of the surface intermediates, a stability plot was constructed (Figure 4.2). All reported energies are given with respect to adsorbed atomic C, O, and H. Lateral interactions between adsorbates are ignored. From this plot, it is immediately clear that CO is very stable on the surface. The dissociation of CO into the  $\text{C}_1$  monomer is endothermic, which is consistent with the less reactive nature of Rh compared with Ru and Co, on which the CO dissoci-

**Table 4.1:** The preferred adsorption site, coordination numbers (CN) of the metal atoms involved in the Rh-C bonding in the IS, energy of adsorption ( $E_{ads}$ ) and C-O bond distances for each of the four different pathways studied on the Rh surfaces.

| Adsorbate                          | Site           | Geometry   |
|------------------------------------|----------------|--|
| CO                                 | $T_h^1$        | Threefold  |
| C                                  | F <sup>h</sup> | Fourfold   |
| CH                                 | F              | Fourfold   |
| CH <sub>2</sub>                    | B2             | Bridged  |
| CH <sub>3</sub>                    | T              | Top site, step-edge  |
| CH <sub>4</sub>                    | Gas phase      | Gas phase  |
| CHO                                | B2             | Bridged  |
| CH <sub>2</sub> O                  | B2, T          | Bridged C, Top O   |
| CH <sub>3</sub> O                  | T              | Top O  |
| CH <sub>2</sub> OH                 | T              | Top O  |
| COH                                | B2             | Bridged C  |
| CHOH                               | B2             | Bridged C  |
| CH <sub>2</sub> OH                 | B2             | Bridged C  |
| CC                                 | F, $T_h^1$     | C <sup>1</sup> fourfold, C <sup>2</sup> threefold            |
| CCH                                | F, $T_h^1$     | C <sup>1</sup> fourfold, C <sup>2</sup> threefold            |
| CCH <sub>2</sub>                   | F, $T_h^1$     | C <sup>1</sup> fourfold, C <sup>2</sup> threefold            |
| CCH <sub>3</sub>                   | F              | C <sup>1</sup> fourfold, methyl towards gas phase            |
| CHCH                               | $T_h^1, T_f^1$ | C <sup>1</sup> threefold, C <sup>2</sup> threefold           |
| CHCH <sub>2</sub>                  | B2             | C <sup>1</sup> bridged                                       |
| CHCH <sub>3</sub>                  | B2             | C <sup>1</sup> bridged                                       |
| CH <sub>2</sub> CH <sub>2</sub>    | T, T           | C <sup>1</sup> top, C <sup>2</sup> top                       |
| CH <sub>2</sub> CH <sub>3</sub>    | B2             | C <sup>1</sup> bridged                                       |
| CH <sub>3</sub> CH <sub>3</sub>    | Gas phase      | Gas phase (eclipsed)   |
| CCO                                | $T_f^2, T_h^2$ | C <sup>1</sup> threefold, C <sup>2</sup> threefold, O on top |
| CHCO                               | $T_f^1$        | C <sup>1</sup> bridged, C <sup>2</sup> top                   |
| CH <sub>2</sub> CO                 | $T_f^2, T_h^2$ | C <sup>1</sup> threefold, C <sup>2</sup> bridged, O top      |
| CCOH                               | $T_f^2, T_h^2$ | C <sup>1</sup> threefold, C <sup>2</sup> threefold           |
| CHCOH                              | $T_f^2, T_h^2$ | C <sup>1</sup> threefold, C <sup>2</sup> threefold           |
| CH <sub>2</sub> COH                | $T_f^2, T_h^2$ | C <sup>1</sup> bridged, C <sup>2</sup> bridged, O top        |
| CH <sub>3</sub> COH                | $T_f^2$        | C <sup>2</sup> bridged, O top                                |
| CCHO                               | $T_h^2$        | C <sup>1</sup> threefold                                     |
| CHCHO                              | $T_h^2$        | C <sup>1</sup> threefold                                     |
| CH <sub>2</sub> CHO                | $T_h^2, T_f^2$ | C <sup>1</sup> bridged, C <sup>2</sup> top, O top            |
| CH <sub>3</sub> CHO                | B2             | C <sup>2</sup> top, O top                                    |
| CCHOH                              | $T_h^1$        | C <sup>1</sup> threefold                                     |
| CHCHOH                             | $T_h^2, T_f^2$ | C <sup>1</sup> bridged, C <sup>2</sup> bridged               |
| CH <sub>2</sub> CHOH               | $T_h^2, T_f^2$ | C <sup>1</sup> top, C <sup>2</sup> bridged                   |
| CH <sub>3</sub> CHOH               | $T_h^2, T_f^2$ | C <sup>2</sup> bridged                                       |
| CCH <sub>2</sub> O                 | $T_h^2$        | C <sup>1</sup> threefold, O top                              |
| CHCH <sub>2</sub> O                | $T_h^2$        | C <sup>1</sup> bridged, O top                                |
| CH <sub>2</sub> CH <sub>2</sub> O  | $T_h^2, T_f^2$ | C <sup>1</sup> top, C <sup>2</sup> top, O bridged            |
| CH <sub>3</sub> CH <sub>2</sub> O  | B2             | C <sup>2</sup> -H top, O top                                 |
| CCH <sub>2</sub> OH                | $T_h^2$        | C <sup>1</sup> bridged                                       |
| CHCH <sub>2</sub> OH               | $T_h^2, T_f^2$ | C <sup>1</sup> bridged                                       |
| CH <sub>2</sub> CH <sub>2</sub> OH | $T_f^2$        | C <sup>2</sup> bridged, O top                                |
| CH <sub>3</sub> CH <sub>2</sub> OH | Gas phase      | Gas phase  |

ation reaction on similar stepped surfaces is exothermic. There is a substantial difference in energy between C or CH and CH<sub>2</sub> or CH<sub>3</sub>; this implies that C and CH species are the dominant CH<sub>x</sub> surface species under reaction conditions. Oxygenated species tend to be less stable on the surface than their oxygen-free counterparts (e.g., CC is about 50 kJ/mol more stable than CCO). This difference relates to the relatively strong stability of atomic oxygen on the Rh(211) surface.

### 4.3.2 DIRECT AND HYDROGEN-MEDIATED CO DISSOCIATION

Direct and hydrogen-assisted CO dissociation on the stepped Rh(211) surface have been extensively studied before by us<sup>26,30,31</sup> and other groups<sup>24,38,50</sup>. To construct a consistent database of kinetic parameters for the complete chemical network, we computed these elementary reaction steps at the same computational accuracy as employed for the other reaction steps. The activation barriers of the various CO dissociation reaction steps are tabulated in Table 4.2. Direct dissociation of CO, which has an activation barrier of 173 kJ/mol, is preferred over H-assisted alternatives. The latter steps involve HCO and COH intermediates, whose formations are highly endothermic (93 and 103 kJ/mol, respectively). The consecutive C–O bond scission step is as difficult as

direct CO dissociation, with barriers of 170 and 172 kJ/mol, respectively. Accordingly, H-assisted CO dissociation has a much higher overall barrier compared with direct CO dissociation. Although direct CO dissociation is the most favorable pathway, the forward activation energy of 173 kJ/mol is substantially higher than values computed for the stepped surfaces of typical Fischer–Tropsch metals such as Ru (65 kJ/mol)<sup>28,51,52</sup> and Co (92 kJ/mol)<sup>51,53</sup>.

### 4.3.3 C HYDROGENATION TO CH<sub>4</sub>

The forward and backward activation energies for the consecutive hydrogenation steps of adsorbed carbon to gaseous methane are given in Figure 4.3 and Table 4.3. The results are consistent with available data in the literature,<sup>26,31,32</sup> which are reported here for comparison. The hydrogenations of C to CH and of CH to CH<sub>2</sub> have relatively high activation energies of 80 and 78 kJ/mol, respectively. The hydrogenation of CH to CH<sub>2</sub> is endothermic by 55 kJ/mol. Consecutive hydrogenation steps from adsorbed CH<sub>2</sub> to CH<sub>3</sub> and CH<sub>3</sub> to CH<sub>4</sub> have activation barriers of 33 and 50 kJ/mol, respectively. The former two hydrogenation steps occur along the stepped surface, whereas the latter two take place at the step-edge. The reaction pathway of C hydrogenation

**Table 4.2:** Direct and hydrogen-mediated CO dissociation on Rh(211). The reported forward and reverse energies are in relation to the most stable states found for the reactants and products and include zero-point-energy corrections.

| Index | Elementary reaction                                     | Forward $E_{\text{act}}$<br>(kJ/mol) | Backward $E_{\text{act}}$<br>(kJ/mol) |
|-------|---|--------------------------------------|---------------------------------------|
| 1     | $\text{CO}^* + * \rightarrow \text{C}^* + \text{O}^*$   | 173                                  | 92                                    |
| 2     | $\text{CO}^* + \text{H}^* \rightarrow \text{COH}^*$     | 161                                  | 68                                    |
| 3     | $\text{CO}^* + \text{H}^* \rightarrow \text{CHO}^*$     | 120                                  | 17                                    |
| 4     | $\text{COH}^* + * \rightarrow \text{C}^* + \text{OH}^*$ | 170                                  | 168                                   |
| 5     | $\text{CHO}^* + * \rightarrow \text{CH}^* + \text{O}^*$ | 172                                  | 140                                   |

**Table 4.3:** Methanation pathway from adsorbed carbon on Rh(211). The reported forward and reverse energies are in relation to the most stable states found for the reactants and products and include zero-point-energy corrections.

| Index | Elementary reaction  | Forward $E_{\text{act}}$<br>(kJ/mol) | Backward $E_{\text{act}}$<br>(kJ/mol) |
|-------|--|--------------------------------------|---------------------------------------|
| 6     | $\text{C}^* + \text{H}^* \rightarrow \text{CH}^* + *$      | 80                                   | 91                                    |
| 7     | $\text{CH}^* + \text{H}^* \rightarrow \text{CH}_2^* + *$   | 78                                   | 23                                    |
| 8     | $\text{CH}_2^* + \text{H}^* \rightarrow \text{CH}_3^* + *$ | 33                                   | 15                                    |
| 9     | $\text{CH}_3^* + \text{H}^* \rightarrow \text{CH}_4 + 2^*$ | 50                                   | 36                                    |

to  $\text{CH}_4$  is different from the pathway identified for the stepped Ru(111) surface, where only the first hydrogenation step to CH occurs along the step, and the other hydrogenation steps occur at the step-edge site.<sup>28</sup>

#### 4.3.4 CO HYDROGENATION TO FORMALDEHYDE AND METHANOL

Adsorbed CO can be hydrogenated to formaldehyde and methanol by a sequence of hydrogenation steps. In total, we considered ten different direct CO hydrogenation steps. These reactions include hydrogenation reactions of the carbon or the oxygen atom. The two reac-

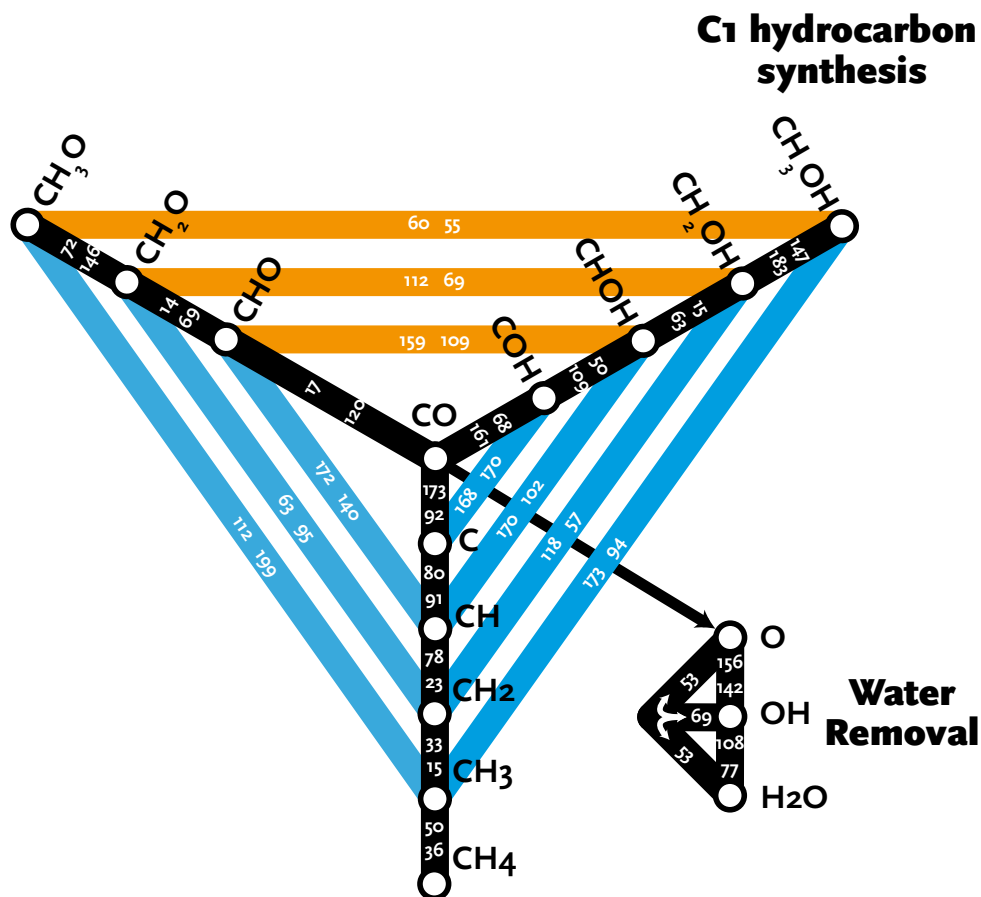


**Figure 4.3:** Forward and backward activation energies (kJ/mol) for the conversion of CO to CH<sub>2</sub>O, CH<sub>3</sub>OH, CH<sub>4</sub>, and H<sub>2</sub>O.

tions that lead to the formation of HCO and COH have already been discussed in section 4.3.2. The barriers for all of these elementary reaction steps are given in Figure 4.3; all CO hydrogenation steps are endothermic. The hydrogenation of HCO to methanol proceeds as follows. HCO that is initially bound in a bridged fashion by its C atom is hydrogenated at the step-edge with a relatively low barrier of 69 kJ/mol. The resulting H<sub>2</sub>CO

adsorbate migrates to the bottom of the step and is bound to the surface by the C and O atoms. The forward barrier for hydrogenation to CH<sub>3</sub>O is high (146 kJ/mol). Compared with the hydrogenation of CH<sub>2</sub>O to CH<sub>3</sub>O, CH<sub>2</sub>O desorption is more favorable at 99 kJ/mol.

For the CH<sub>3</sub>O intermediate, the octet rule is fulfilled for the C atom; thus, the binding of CH<sub>3</sub>O occurs only via the O atom at the step-edge to take advantage of

**Table 4.4:**  $CH_x-OH_y$  hydrogenation reactions on Rh(211). The reported forward and reverse energies are in relation to the most stable states found for the reactants and products and include zero-point-energy corrections.

| Index | Elementary reaction                        | Forward $E_{act}$<br>(kJ/mol) | Backward $E_{act}$<br>(kJ/mol) |
|-------|--|-------------------------------|--------------------------------|
| 10    | $CHO^* + H^* \rightarrow CHOH^* + ^*$      | 159                           | 109                            |
| 11    | $CH_2O^* + H^* \rightarrow CH_2OH^* + ^*$  | 112                           | 69                             |
| 12    | $CH_3O^* + H^* \rightarrow CH_3OH^* + ^*$  | 60                            | 55                             |
| 13    | $CHO^* + H^* \rightarrow CH_2O^* + ^*$     | 69                            | 14                             |
| 14    | $CH_2O^* + H^* \rightarrow CH_3O^* + ^*$   | 146                           | 72                             |
| 15    | $COH^* + H^* \rightarrow CHOH^* + ^*$      | 109                           | 50                             |
| 16    | $CHOH^* + H^* \rightarrow CH_2OH^* + ^*$   | 63                            | 15                             |
| 17    | $CH_2OH^* + H^* \rightarrow CH_3OH^* + ^*$ | 183                           | 147                            |

the lower coordination number of the Rh step-edge atom. The final hydrogenation step to form methanol takes place with a forward reaction barrier of 60 kJ/mol, and the methanol desorption energy is 25 kJ/mol.

The alternative hydrogenation pathway to methanol proceeds by the hydrogenation of COH. The reactions of this pathway occur at the step-edge site. COH is adsorbed on a fcc site prior to hydrogenation. The hydrogenation of COH to HCOH has a forward barrier of 109 kJ/mol. The hydrogenation of CHOH to  $CH_2OH$  proceeds in a manner comparable to the hydrogenation of HCO to  $H_2CO$ ; the respective forward barriers are 63 kJ/mol and 60 kJ/mol. The final hydrogenation step to form methanol is very difficult ( $E_{act} = 183$  kJ/mol). Overall,

the pathway that proceeds through C hydrogenation via  $CH_3O$  is more favorable than the hydrogenation of the COH intermediate.

### 4.3.5 $CH_x + OH_y$ COUPLING

A total of seven  $CH_x + OH_y$  coupling reactions were considered. Three of these coupling reactions are the reverse reactions of C–O bond cleavage reactions, namely those for CO, HCO, and COH intermediates. The other coupling reactions are given in Table 4.5. All coupling reactions take place at the step-edge with the C atom bound to an Rh atom with a low coordination number of seven. The coupling proceeds via the migration of the  $OH_x$  adsorbate to the adjacent edge to form the C–O bond (see Figure 4.4).

**Table 4.5:**  $CH_x+OH_y$  coupling reactions on Rh(211). The reported forward and reverse energies are in relation to the most stable states found for the reactants and products and include zero-point-energy corrections.

| Index | Elementary reaction                       | Forward $E_{act}$<br>(kJ/mol) | Backward $E_{act}$<br>(kJ/mol) |
|-------|---|-------------------------------|--------------------------------|
| 18    | $CH^* + OH^* \rightarrow CHOH^* + ^*$     | 170                           | 102                            |
| 19    | $CH_2^* + OH^* \rightarrow CH_2OH^* + ^*$ | 118                           | 57                             |
| 20    | $CH_3^* + OH^* \rightarrow CH_3OH^* + ^*$ | 173                           | 94                             |
| 21    | $CH_2^* + O^* \rightarrow CH_2O^* + ^*$   | 95                            | 63                             |
| 22    | $CH_3^* + O^* \rightarrow CH_3O^* + ^*$   | 112                           | 199                            |

**Table 4.6:**  $CH_x-CH_y$  coupling reactions on Rh(211). The reported forward and reverse energies are in relation to the most stable states found for the reactants and products and include zero-point-energy corrections.

| Index | Elementary reaction                      | Forward $E_{act}$<br>(kJ/mol) | Backward $E_{act}$<br>(kJ/mol) |
|-------|--|-------------------------------|--------------------------------|
| 23    | $C^* + C^* \rightarrow CC^* + ^*$        | 91                            | 86                             |
| 24    | $C^* + CH^* \rightarrow CCH^* + ^*$      | 93                            | 103                            |
| 25    | $C^* + CH_3^* \rightarrow CCH_3^* + ^*$  | 119                           | 144                            |
| 26    | $CH^* + CH^* \rightarrow CHCH^* + ^*$    | 94                            | 156                            |
| 27    | $CH^* + CH_3^* \rightarrow CHCH_3^*$     | 38                            | 20                             |
| 28    | $CH_2^* + CH_2^* \rightarrow CH_2CH_2^*$ | 136                           | 75                             |

With the exception of  $CH + O$  coupling, all of the  $CH_x + OH_y$  coupling reactions are endothermic. The most facile coupling reaction is that between  $CH_2$  and  $O$  to form formaldehyde

( $E_{act} = 95$  kJ/mol; reaction 21), followed by  $CH_2 + OH$  coupling ( $E_{act} = 118$  kJ/mol; reaction 11). The result that  $CH_2 + O$  cou-

pling is the most facile is in agreement with the literature.<sup>24</sup>

### 4.3.6 $CH_x + CH_y$ COUPLING

$C_2$  hydrocarbon formation by the coupling of two  $C_1$  species can proceed in ten different ways. We were able to identify

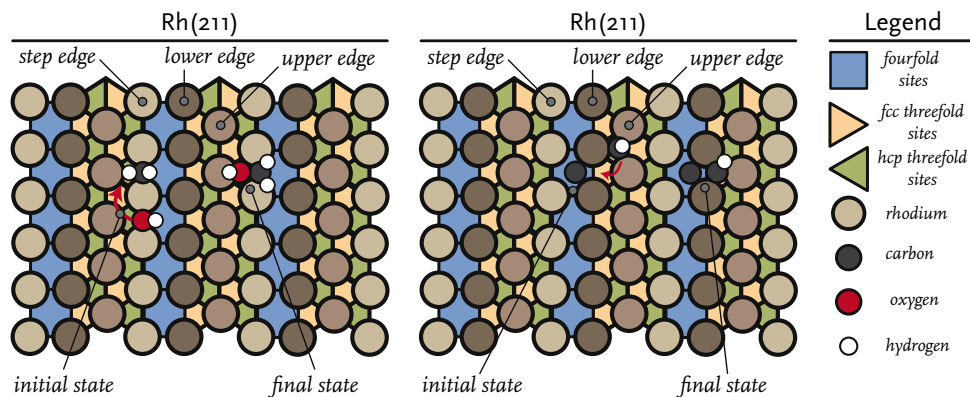


**Figure 4.4:** (left) schematic representation of  $\text{CH}_x + \text{OH}_y$  coupling. The  $\text{CH}_x$  moiety resides at the step-edge.  $\text{OH}_y$  insertion proceeds by migrating the  $\text{OH}_y$  moiety to the upper-edge, thus enabling the formation of an  $\text{C}-\text{O}$  bond. (right) Schematic representation of  $\text{CH}_x + \text{CH}_y$  coupling. One of the  $\text{CH}_x$  moieties resides in the step.  $\text{CH}_y$  insertion proceeds by migrating the  $\text{CH}_y$  moiety to the lower-edge, thus facilitating the formation of an  $\text{C}-\text{C}$  bond.

the transition states of six of these coupling steps, and they are shown in Table 6. All  $\text{CH}_x + \text{CH}_y$  coupling reactions take place at the step. To form a  $\text{C}-\text{C}$  bond, one of the two  $\text{C}_i$  intermediates is adsorbed on the step at a four-fold site, and the other  $\text{C}_i$  species moves to an adjacent site (see Figure 4.4). In the case of  $\text{CH}_3$  coupling, the  $\text{CH}_3$  fragment is no longer bound to the surface after coupling. The most facile of these coupling reactions is  $\text{CH} + \text{CH}_3$ , which has a barrier of only 38 kJ/mol. All the other coupling pathways have substantially higher activation barriers. Chen and Liu indicated that  $\text{C} + \text{CH}$  and  $\text{CH}_2 + \text{CH}_2$  coupling reactions are preferred for  $\text{C}-\text{C}$  bond formation on the  $\text{Rh}(322)$

surface, that is similar to the  $\text{Rh}(211)$  surface.<sup>38</sup>

### 4.3.7 $\text{CH}_x + \text{CO}$ COUPLING

$\text{CO}$  insertion into  $\text{CH}_x$  surface intermediates was studied in order to identify the pathways that lead to  $\text{C}_2$  oxygenate formation. Table 4.7 lists the three relevant coupling reactions.  $\text{CO}$  coupling occurs either at the step-edge ( $\text{C} + \text{CO}$  coupling and  $\text{CH}_2 + \text{CO}$  coupling) or at the upper terrace ( $\text{CO} + \text{CH}$  coupling). The most facile  $\text{CO}$  insertion reaction is the one between  $\text{C}$  and  $\text{CO}$ , with an activation barrier of 136 kJ/mol. Coupling reactions of  $\text{CO}$  with  $\text{CH}$  or  $\text{CH}_2$  proceed with higher activation energies of 181

# C<sub>2</sub> hydrocarbon synthesis

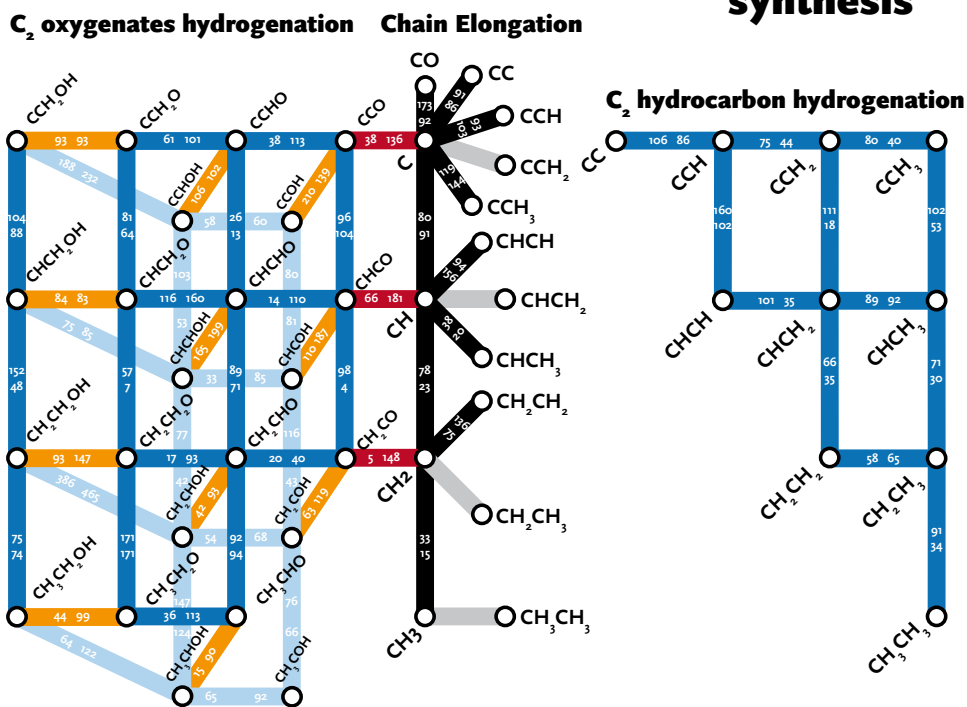


**Figure 4.5:** Forward and backward activation energies (kJ/mol) for the formation of C<sub>2</sub> intermediates and products from CO. The central black axis shows CH<sub>x</sub> + CH<sub>y</sub> coupling reactions to generate C<sub>2</sub> hydrocarbons (branches to the right) and CH<sub>x</sub> + CO coupling to generate C<sub>2</sub> oxygenates (branches to the left). The diagrams on the left and the right show the interconnected hydrogenation reactions for the C<sub>2</sub> oxygenates and C<sub>2</sub> hydrocarbons, respectively.

and 148 kJ/mol, respectively. Kapur *et al.* found that CH<sub>2</sub> + CO coupling has the lowest barrier,<sup>24</sup> although it should be noted that they did not study C + CO coupling.

## 4.3.8 CH<sub>x</sub>CH<sub>y</sub> HYDROGENATION

The formation of ethylene and ethane proceed by a series of hydrogenation reactions after the formation of the C–C bond. In total, there are 12 unique hydrogenation steps (Table 4.8). The locations of these hydrogenation reac-

**Table 4.7:**  $CH_x$ -CO coupling reactions on Rh(211). The reported forward and reverse energies are in relation to the most stable states found for the reactants and products and include zero-point-energy corrections.

| Index | Elementary reaction                  | Forward $E_{act}$<br>(kJ/mol) | Backward $E_{act}$<br>(kJ/mol) |
|-------|--------------------------------------|-------------------------------|--------------------------------|
| 29    | $C^* + CO^* \rightarrow CCO^*$       | 136                           | 38                             |
| 30    | $CH^* + CO^* \rightarrow CHCO^*$     | 181                           | 66                             |
| 31    | $CH_2^* + CO^* \rightarrow CH_2CO^*$ | 148                           | 5                              |

**Table 4.8:**  $CH_xCH_y$  hydrogenation reactions on Rh(211). The reported forward and reverse energies are in relation to the most stable states found for the reactants and products and include zero-point-energy corrections.

| Index | Elementary reaction                            | Forward $E_{act}$<br>(kJ/mol) | Backward $E_{act}$<br>(kJ/mol) |
|-------|--|-------------------------------|--------------------------------|
| 32    | $CC^* + H^* \rightarrow CCH^* + ^*$            | 106                           | 86                             |
| 33    | $CCH^* + H^* \rightarrow CCH_2^* + ^*$         | 75                            | 44                             |
| 34    | $CCH_2^* + H^* \rightarrow CCH_3^* + ^*$       | 80                            | 40                             |
| 35    | $CCH^* + H^* \rightarrow CHCH^* + ^*$          | 160                           | 102                            |
| 36    | $CCH_2^* + H^* \rightarrow CHCH_2^* + ^*$      | 111                           | 18                             |
| 37    | $CCH_3^* + H^* \rightarrow CHCH_3^* + ^*$      | 102                           | 53                             |
| 38    | $CHCH^* + H^* \rightarrow CHCH_2^* + ^*$       | 101                           | 35                             |
| 39    | $CHCH_2^* + H^* \rightarrow CHCH_3^* + ^*$     | 89                            | 92                             |
| 40    | $CHCH_2^* + H^* \rightarrow CH_2CH_2^* + ^*$   | 66                            | 35                             |
| 41    | $CHCH_3^* + H^* \rightarrow CH_2CH_3^* + ^*$   | 71                            | 30                             |
| 42    | $CH_2CH_2^* + H^* \rightarrow CH_2CH_3^* + ^*$ | 58                            | 65                             |
| 43    | $CH_2CH_3^* + H^* \rightarrow CH_3CH_3^* + ^*$ | 91                            | 34                             |

tions depend on the number of hydrogen atoms attached to the carbon atoms of the reacting intermediates. For instance, ethyl hydrogenation takes place at the step-edge, whereas earlier hydrogenation steps occur on the step. With the exception of  $CHCH_2$  hydrogenation to  $CHCH_3$

and  $CH_2CH_2$  hydrogenation to  $CH_2CH_3$ , all these elementary reaction steps are endothermic and proceed with forward activation energies below 120 kJ/mol. The notable exception is  $CCH$  hydrogenation to  $CHCH$ , which has a barrier of 160 kJ/mol.

**Table 4.9:**  $CH_xCH_yO_z$  hydrogenation reactions on Rh(211). The reported forward and reverse energies are in relation to the most stable states found for the reactants and products and include zero-point-energy corrections.

| Index | Elementary reaction                                | Forward $E_{act}$<br>(kJ/mol) | Backward $E_{act}$<br>(kJ/mol) |
|-------|--|-------------------------------|--------------------------------|
| 44    | $CCO^* + H^* \rightarrow CHCO^* + ^*$              | 96                            | 104                            |
| 45    | $CCO^* + H^* \rightarrow CCHO^* + ^*$              | 113                           | 38                             |
| 46    | $CCO^* + H^* \rightarrow CCOH^* + ^*$              | 210                           | 139                            |
| 47    | $CHCO^* + H^* \rightarrow CH_2CO^* + ^*$           | 98                            | 4                              |
| 48    | $CHCO^* + H^* \rightarrow CHCHO^* + ^*$            | 110                           | 14                             |
| 49    | $CHCO^* + H^* \rightarrow CHCOH^* + ^*$            | 187                           | 110                            |
| 50    | $CCHO^* + H^* \rightarrow CHCHO^* + ^*$            | 26                            | 13                             |
| 51    | $CCHO^* + H^* \rightarrow CCH_2O^* + ^*$           | 101                           | 61                             |
| 52    | $CCHO^* + H^* \rightarrow CCHOH^* + ^*$            | 102                           | 106                            |
| 53    | $CCOH^* + H^* \rightarrow CHCOH^* + ^*$            | 80                            | 81                             |
| 54    | $CCOH^* + H^* \rightarrow CCHOH^* + ^*$            | 60                            | 58                             |
| 55    | $CH_2CO^* + H^* \rightarrow CH_2CHO^* + ^*$        | 40                            | 20                             |
| 56    | $CH_2CO^* + H^* \rightarrow CH_2COH^* + ^*$        | 119                           | 63                             |
| 57    | $CHCHO^* + H^* \rightarrow CH_2CHO^* + ^*$         | 89                            | 71                             |
| 58    | $CHCHO^* + H^* \rightarrow CHCH_2O^* + ^*$         | 160                           | 116                            |
| 59    | $CHCHO^* + H^* \rightarrow CHCHOH^* + ^*$          | 199                           | 165                            |
| 60    | $CHCOH^* + H^* \rightarrow CH_2COH^* + ^*$         | 116                           | 43                             |
| 61    | $CHCOH^* + H^* \rightarrow CHCHOH^* + ^*$          | 85                            | 33                             |
| 62    | $CCH_2O^* + H^* \rightarrow CHCH_2O^* + ^*$        | 81                            | 64                             |
| 63    | $CCH_2O^* + H^* \rightarrow CCH_2OH^* + ^*$        | 93                            | 93                             |
| 64    | $CCHOH^* + H^* \rightarrow CHCHOH^* + ^*$          | 103                           | 53                             |
| 65    | $CCHOH^* + H^* \rightarrow CCH_2OH^*$              | 232                           | 188                            |
| 66    | $CH_2CHO^* + H^* \rightarrow CH_3CHO^* + ^*$       | 92                            | 94                             |
| 67    | $CH_2CHO^* + H^* \rightarrow CH_2CH_2O^* + ^*$     | 93                            | 17                             |
| 68    | $CH_2CHO^* + H^* \rightarrow CH_2CHOH^*$           | 93                            | 42                             |
| 69    | $CH_2COH^* + H^* \rightarrow CH_3COH^* + ^*$       | 76                            | 66                             |
| 70    | $CH_2COH^* + H^* \rightarrow CH_2CHOH^* + ^*$      | 67                            | 54                             |
| 71    | $CHCH_2O^* + H^* \rightarrow CH_2CH_2O^* + ^*$     | 57                            | 7                              |
| 72    | $CHCH_2O^* + H^* \rightarrow CHCH_2OH^* + ^*$      | 83                            | 84                             |
| 73    | $CHCHOH^* + H^* \rightarrow CH_2CHOH^* + ^*$       | 77                            | 42                             |
| 74    | $CHCHOH^* + H^* \rightarrow CHCH_2OH^* + ^*$       | 85                            | 75                             |
| 75    | $CCH_2OH^* + H^* \rightarrow CHCH_2OH^* + ^*$      | 104                           | 88                             |
| 76    | $CH_3CHO^* + H^* \rightarrow CH_3CH_2O^* + ^*$     | 113                           | 36                             |
| 77    | $CH_3CHO^* + H^* \rightarrow CH_3CHOH^* + ^*$      | 90                            | 15                             |
| 78    | $CH_3COH^* + H^* \rightarrow CH_3CHOH^* + ^*$      | 92                            | 63                             |
| 79    | $CH_2CH_2O^* + H^* \rightarrow CH_3CH_2O^* + ^*$   | 171                           | 171                            |
| 80    | $CH_2CH_2O^* + H^* \rightarrow CH_2CH_2OH^* + ^*$  | 147                           | 93                             |
| 81    | $CH_2CHOH^* + H^* \rightarrow CH_3CHOH^* + ^*$     | 147                           | 124                            |
| 82    | $CH_2CHOH^* + H^* \rightarrow CH_2CH_2OH^* + ^*$   | 465                           | 386                            |
| 83    | $CHCH_2OH^* + H^* \rightarrow CH_2CH_2OH^* + ^*$   | 152                           | 48                             |
| 84    | $CH_3CH_2O^* + H^* \rightarrow CH_3CH_2OH^* + ^*$  | 99                            | 44                             |
| 85    | $CH_3CHOH^* + H^* \rightarrow CH_3CH_2OH^* + ^*$   | 122                           | 64                             |
| 86    | $CH_2CH_2OH^* + H^* \rightarrow CH_3CH_2OH^* + ^*$ | 75                            | 74                             |

**Table 4.10:** Water formation reactions on Rh(211). The reported forward and reverse energies are in relation to the most stable states found for the reactants and products and include zero-point-energy corrections.

| Index | Elementary reaction   | Forward $E_{\text{act}}$<br>(kJ/mol) | Backward $E_{\text{act}}$<br>(kJ/mol) |
|-------|---|--------------------------------------|---------------------------------------|
| 87    | $\text{O}^* + \text{H}^* \rightarrow \text{OH}^* + *$                     | 156                                  | 142                                   |
| 88    | $\text{OH}^* + \text{OH}^* \rightarrow \text{H}_2\text{O}^* + \text{O}^*$ | 69                                   | 53                                    |
| 89    | $\text{OH}^* + \text{H}^* \rightarrow \text{H}_2\text{O}^* + *$           | 108                                  | 77                                    |

### 4.3.9 $\text{CH}_x\text{CH}_y\text{O}_z$ HYDROGENATION

Acetaldehyde and ethanol are formed by the hydrogenation of  $\text{CH}_x\text{CH}_y\text{O}_z$  intermediates. There are 43 unique elementary reaction steps, and the corresponding forward and backward activation energies are listed in Table 4.9. Similar to  $\text{CH}_x\text{CH}_y$  hydrogenation, the majority of the  $\text{CH}_x\text{CH}_y\text{O}_z$  hydrogenation steps are endothermic.  $\text{CH}_x\text{CH}_y\text{O}_z$  hydrogenation occurs either at the upper terrace or at the step-edge site depending on the number of hydrogen atoms attached to the carbon atoms of the reacting intermediate. The majority of the hydrogenation reactions have activation barriers between 80 and 120 kJ/mol. It is worth noting that very

high energy barriers are associated with the hydrogenation of

CCO to CCOH (210 kJ/mol), CHCO to CHCOH (187 kJ/mol), CHCHO to CHCHOH (199 kJ/mol), CCHOH to CCH<sub>2</sub>OH (232 kJ/mol), and CH<sub>2</sub>CHOH to CH<sub>2</sub>CH<sub>2</sub>OH (465 kJ/mol).

### 4.3.10 WATER FORMATION

Water formation can proceed via two different routes: the direct hydrogenation of O to OH and OH<sub>2</sub> or the reaction between two hydroxyl species (Table 10). The latter pathway, which involves proton migration between two hydroxyl groups, is preferred. This finding is similar to that reported for the stepped Ru(11 $\bar{1}$ 1) surface.<sup>28</sup>

## 4.4 CONCLUSION

All relevant elementary reaction steps for the hydrogenation of CO to methane, ethylene, formaldehyde, methanol, and

ethanol on the stepped Rh(211) surface were calculated using quantum chemical DFT calculations. The most important

findings of this study are:

- H-assisted CO dissociation has a much higher overall barrier than direct CO dissociation.
- In the methane formation pathway, C and CH hydrogenation are relatively difficult steps, whereas CH<sub>2</sub> and CH<sub>3</sub> hydrogenation are relatively facile steps. Analysis of the stability of the surface intermediates shows that CO, C and CH are the most stable C<sub>1</sub> reaction intermediates. This suggests that C+CO coupling is a candidate elementary reaction step for chain growth. The barrier of this reaction is favorable compared to those of CH+CO and CH<sub>2</sub>+CO coupling.
- Adsorbed CO can be hydrogenated to methanol. The pathway with

the lowest reaction barriers proceeds via formaldehyde, followed by its hydrogenation to CH<sub>3</sub>O to CH<sub>3</sub>OH. The final hydrogenation step to methanol was found to be very difficult ( $E_{\text{act}} = 183$  kJ/mol).

- The most facile CH<sub>x</sub>+CH<sub>y</sub> coupling reaction was C+C coupling. Although the forward barriers for C+CH and CH+CH coupling are similar, the former reaction will be more important because of the low CH surface coverage due to its lower stability than C.
- Water formation is preferred via proton migration between two hydroxyl species to form surface oxygen and water. ■

## 4.5 REFERENCES

- (1) Song, C. *Catal. Today* **2006**, *115*, 2.
- (2) Biloen, P.; Helle, J. N.; Sachtler, W. M. H. *J. Catal.* **1979**, *58*, 95.
- (3) Biloen, P.; Sachtler, W. M. H. In *Adv. Catal.*; D.D. Eley, H. P., Paul, B. W., Eds.; Academic Press: 1981; Vol. Volume 30, p 165.
- (4) Fischer, F.; Tropsch, H. *Brennst.-Chem* **1923**, *4*, 276.
- (5) Fischer, F.; Tropsch, H. *Brennst.-Chem* **1926**, *7*, 79.
- (6) van Santen, R. A.; Ciobica, I. M.; van Steen, E.; Ghouri, M. M. In *Adv. Catal.*; Bruce, C. G., Helmut, K., Eds.; Academic Press: 2011; Vol. Volume 54, p 127.
- (7) Spivey, J. J.; Egbeki, A. *Chem. Soc. Rev.* **2007**, *36*, 1514.
- (8) Choi, Y.; Liu, P. J. *Am. Chem. Soc.* **2009**, *131*, 13054.
- (9) Shetty, S. G.; van Santen, R. A.; Stevens, P. A.; Raman, S. J. *Mol. Cat. A* **2010**, *330*, 73.
- (10) Subramani, V.; Gangwal, S. K. *Energy & Fuels* **2008**, *22*, 814.
- (11) He, J.; Zhang, W.-n. *J. Zhejiang Univ. Sci. A* **2008**, *9*, 714.
- (12) Lu, J.; Liu, Y.; Li, N. J. *Nat. Gas Chem.* **2011**, *20*, 423.
- (13) Wang, H.; Liu, J.; Fu, J.; Wan, H.; Tsai, K. *Catal. Lett.* **1992**, *12*, 87.
- (14) Bhasin, M. M.; Bartley, W. J.; Ellgen, P. C.; Wilson, T. *P. J. Catal.* **1978**, *54*, 120.
- (15) Pan, X.; Fan, Z.; Chen, W.; Ding, Y.; Luo, H.; Bao, X. *Nat Mater* **2007**, *6*, 507.
- (16) Gronchi, P.; Marengo, S.; Mazzocchia, C.; Tempesti, E.; Del Rosso, R. *React. Kinet. Catal. Lett.* **1997**, *60*, 79.

- (17) Bowker, M. *Catal. Today* **1992**, *15*, 77.
- (18) Chen, G.; Guo, C.-Y.; Huang, Z.; Yuan, G. *Chem. Eng. Res. Des.* **2011**, *89*, 249.
- (19) Basu, P.; Panayotov, D.; Yates, J. T. J. *Am. Chem. Soc.* **1988**, *110*, 2074.
- (20) Zhang, Z. L.; Kladi, A.; Verykios, X. E. J. *Catal.* **1995**, *156*, 37.
- (21) Wong, T. T. T.; Stakheev, A. Y.; Sachtler, W. M. H. J. *Phys. Chem.* **1992**, *96*, 7733.
- (22) Lavalley, J. C.; Saussey, J.; Lamotte, J.; Breault, R.; Hindermann, J. P.; Kiennemann, A. J. *Phys. Chem.* **1990**, *94*, 5941.
- (23) Anderson, J. A.; Khader, M. M. J. *Mol. Catal. A: Chem.* **1996**, *105*, 175.
- (24) Kapur, N.; Hyun, J.; Shan, B.; Nicholas, J. B.; Cho, K. *J. Phys. Chem. C* **2010**, *114*, 10171.
- (25) Mavrikakis, M.; Bäumer, M.; Freund, H. J.; Nørskov, J. K. *Catal. Lett.* **2002**, *81*, 153.
- (26) Zhu, T. W.; van Grootel, P. W.; Filot, I. A. W.; Sun, S. G.; van Santen, R. A.; Hensen, E. J. M. *J. Catal.* **2013**, *297*, 227.
- (27) Grabow, L. C.; Mavrikakis, M. *ACS Catal.* **2011**, *1*, 365.
- (28) Filot, I. A. W.; van Santen, R. A.; Hensen, E. J. M. *Catal. Sci. Technol.* **2014**, *4*, 3129.
- (29) Filot, I. A. W.; van Santen, R. A.; Hensen, E. J. M. *Angew. Chem. Int. Ed.* **2014**, *53*, 47, 12746.
- (30) Filot, I. A. W.; Shetty, S. G.; Hensen, E. J. M.; van Santen, R. A. *J. Phys. Chem. C* **2011**, *115*, 14204.
- (31) van Grootel, P. W.; Hensen, E. J. M.; van Santen, R. A. *Langmuir* **2010**, *26*, 16339.
- (32) van Grootel, P. W.; van Santen, R. A.; Hensen, E. J. M. *J. Phys. Chem. C* **2011**, *115*, 13027.
- (33) Zhang, J.; Cao, X. M.; Hu, P.; Zhong, Z.; Borgna, A.; Wu, P. J. *Phys. Chem. C* **2011**, *115*, 22429.
- (34) Liu, Z.-P.; Hu, P. J. *Am. Chem. Soc.* **2002**, *124*, 11568.
- (35) Liu, Z.-P.; Hu, P. J. *Chem. Phys.* **2001**, *114*, 8244.
- (36) Wang, J.; Liu, Z.; Zhang, R.; Wang, B. *J. Phys. Chem. C* **2014**, *118*, 22691.
- (37) Stroppa, A.; Mittendorfer, F.; Andersen, J. N.; Parteder, G.; Allegretti, F.; Surnev, S.; Netzer, F. P. *J. Phys. Chem. C* **2009**, *113*, 942.
- (38) Chen, J.; Liu, Z.-P. *J. Am. Chem. Soc.* **2008**, *130*, 7929.
- (39) Chiu, C.-c.; Genest, A.; Rösch, N. *Top. Catal.* **2013**, *56*, 874.
- (40) Choi, Y.; Liu, P. *Catal. Today* **2011**, *165*, 64.
- (41) Guo, W.; Li, M.; Lu, X.; Zhu, H.; Li, Y.; Li, S.; Zhao, L. *Dalton Trans.* **2013**, *42*, 2309.
- (42) Li, M.; Guo, W.; Jiang, R.; Zhao, L.; Shan, H. *Langmuir* **2009**, *26*, 1879.
- (43) Blöchl, P. E. *Phys. Rev. B* **1994**, *50*, 17953.
- (44) Kresse, G.; Joubert, J. *Phys. Rev. B* **1999**, *59*, 1758.
- (45) Kresse, G.; Hafner, J. *J. Phys. Rev. B* **1994**, *49*, 14251.
- (46) Kresse, G.; Furthmüller, J. *J. Comput. Mater. Sci.* **1996**, *6*, 15.
- (47) Perdew, J. P.; Burke, K.; Ernzerhof, M. *Phys. Rev. Lett.* **1996**, *77*, 3865.
- (48) Henkelman, G.; Jónsson, H. *J. Chem. Phys.* **2000**, *113*, 9978.
- (49) Kittel, C. *Introduction to solid state physics*; John Wiley and Sons Inc.: New York, London, Sydney, 1966; Vol. 3rd ed.
- (50) Mavrikakis, M.; Bäumer, M.; Freund, H.-J.; Nørskov, J. K. *Catal. Lett.* **2002**, *81*, 153.
- (51) Shetty, S.; van Santen, R. A. *Catal. Today* **2011**, *171*, 168.
- (52) Shetty, S. G.; Jansen, A. P. J.; van Santen, R. A. *J. Phys. Chem. C* **2008**, *112*, 14027.
- (53) Joos, L.; Filot, I. A. W.; Cottenier, S.; Hensen, E. J. M.; Waroquier, M.; Van Speybroeck, V.; van Santen, R. A. *J. Phys. Chem. C* **2014**, *118*, 5317.

## Abstract

Based on kinetic parameters determined by density functional theory for all relevant elementary reactions for CO hydrogenation on Rh model surfaces, microkinetics simulations were carried out to determine the activity (CO and H<sub>2</sub> conversion rate) and selectivity (methane, ethylene, ethane, formaldehyde, methanol, acetaldehyde and ethanol) as a function of temperature. The reaction network and the elementary reaction steps that control the CO consumption rate and the product selectivities were analyzed. The degree of selectivity control concept was introduced to identify elementary reaction steps that control product selectivity. The CO conversion rate on Rh(211) surface is much higher than on Rh(111) and Rh(100) because of the very high barriers for CO dissociation on the terraced surfaces. The microkinetics simulations shows that formaldehyde is the dominant product at low temperature, ethanol at intermediate temperature, and methane at high temperature. The preference for ethanol over long hydrocarbon formation on Rh catalysts is due to the lower barrier for C + CO coupling compared to CH<sub>x</sub> + CH<sub>y</sub> coupling. The CCO intermediate is hydrogenated via a complex sequence of hydrogenation and dehydrogenation reactions to form ethanol. The simulations show that ethanol formation competes with methane formation at intermediate temperatures. The rate controlling steps are O hydrogenation to create vacancies for the dehydrogenation steps in the reaction sequence leading to ethanol, CH<sub>x</sub>CH<sub>y</sub>O hydrogenation for ethanol formation, and CH<sub>2</sub> and CH<sub>3</sub> hydrogenation for methane formation. CO dissociation does not control the overall reaction rate on Rh. The most important reaction steps that control the selectivity for ethanol over methane are CH<sub>2</sub> and CH<sub>3</sub> hydrogenation as well as CHCH<sub>3</sub> dehydrogenation.

★ *To most people, solutions mean finding the answers. But to chemists, solutions are things that are still all mixed up.* ★

**FIRST-  
PRINCIPLES-  
BASED  
MICROKINETICS  
SIMULATIONS  
OF CO  
HYDROGENATION  
ON RHODIUM**



**5**

## 5.1 INTRODUCTION

The dwindling supply of easy fossil resources and concerns about climate change due to their combustion are drivers for the exploration of alternative energy sources. The conversion of synthesis gas, derived from coal, residual oil, natural gas, or waste products, to long-chain hydrocarbons in the Fischer-Tropsch (FT) process provides an economically feasible alternative to crude oil refining.<sup>1,2</sup> The catalysts most commonly studied in FT synthesis have been based on Fe, Co, and Ru. These metals are known for their high activity and selectivity towards longer hydrocarbons in syngas conversion.<sup>3,4</sup> The study of syngas conversion over Rh catalysts is of academic interest, due to its propensity to form methanol, higher oxygenates, and hydrocarbons.<sup>5-7</sup> Understanding the unique product selectivity in CO hydrogenation over Rh catalysts provides a better understanding of the FT mechanism.

Many experimental works have focused on optimizing the ethanol yield of Rh catalysts.<sup>8-18</sup> In addition to methanol and ethanol, small amounts of olefins (primarily ethylene) and oxygenates such as acetaldehyde and acetic acid are obtained with these catalysts. The formation of C<sub>2</sub>-oxygenates by Rh catalysts is usually explained by its intermediate activity in CO dissociation.<sup>5,19</sup>

Pertinent questions concerning CO hydrogenation on Rh catalysts relate to the manner of CO dissociation, the reaction pathway to ethanol, and how ethanol formation competes with other products such as methane, higher hydrocarbons, and methanol. Several theoretical studies have been carried out to study some of the elementary reaction steps relevant to these issues; planar Rh(111) and stepped Rh(211) surfaces have been the subjects of most of these investigations.<sup>20-29</sup> However, a complete mechanistic study of CO hydrogenation on Rh that clarifies the abovementioned issues for Rh catalysts is lacking.

The use of first principles kinetic parameters in microkinetics simulations provides insight into the dependence of catalyst sensitivity on the structure of the catalytic surface and the composition of the adsorbed layer under reaction conditions.<sup>22,25,30</sup> With advances in computing power, it is currently possible to carry out comprehensive studies for increasingly complex catalytic reactions such as the Fischer-Tropsch reaction.<sup>31,32</sup> In our recent work, we resolved important issues related to the Fischer-Tropsch reaction involving catalytic site requirements, the nature of chain propagation, and the effect of the reactivity of the transition metal.<sup>32</sup> The active sites for

the Fischer-Tropsch reaction are step-edge sites on the surfaces of sufficiently reactive transition metals that catalyze long-chain hydrocarbon formation.

We constructed a microkinetic model using the kinetic parameters derived from the DFT calculations shown in the previous chapter. This model allows the calculation of overall reaction rates and kinetic parameters such as apparent activation energies and reaction orders. We conducted a detailed analysis of the reaction network leading to methane and

ethanol. In order to analyze the most important steps that control the CO consumption rate, we used the degree of rate control (DRC) concept developed by Campbell and co-workers.<sup>33,34</sup> In the present study, we expanded on this concept by using the degree of selectivity control, which provides insight into the key elementary reaction steps that control product selectivity. To the best of our knowledge, this is the first comprehensive first principles-based microkinetics study of CO hydrogenation on Rh.

## 5.2 COMPUTATIONAL METHOD

The activation barriers and corresponding vibrational frequencies of the initial, transition, and final states were used to compute forward and backward rate constants for the elementary reaction steps relevant to CO hydrogenation. For this purpose, the rate constant of each elementary surface reaction step was determined using the Eyring equation:

$$k = \frac{k_b T}{h} \frac{Q^\ddagger}{Q} \exp\left(\frac{-\Delta E_{\text{act}}}{k_b T}\right) \quad (5.1)$$

where  $k$  is the rate constant in mol/s,  $k_b$  is the Boltzmann constant,  $T$  is the temperature in K,  $h$  is Planck's constant,  $Q^\ddagger$  is the partition function of the transition state complex,  $Q$  is the partition function of the complex in the pre-activated (initial) state, and  $E_a$  is

the electronic activation energy.<sup>35,36</sup> The partition functions for the activated and pre-activated complexes were taken as the products of the translational, rotational, and vibrational partition functions corresponding to the configurational degrees of freedom of the surface complexes.<sup>35,36</sup> It is worthwhile to note that by following the definition of the vibrational partition function given by Fowler *et. al.*<sup>37</sup>, the zero point energy (ZPE) correction is included in the electronic activation energy.

To account for the entropy of the rotating methyl groups, the partition function of the classical expression for a hindered rotor ( $q_{\text{HR}}$ ) was used. For a methyl group, the partition function becomes:

$$q_{\text{HR}} = \frac{(2\pi)^{\frac{3}{2}} R}{h} \sqrt{3k_b T m_{\text{H}}} \quad (5.2)$$

where  $R$  is the C–H bond length and  $m_H$  is the mass of a hydrogen atom.

For non-activated molecular adsorption, it was assumed that the complex loses one translational degree of freedom with respect to the gas phase in the transition state. The changes in the rotational degrees of freedom were neglected. Accordingly, the following expression was employed for the rate of molecular adsorption:

$$k_{\text{ads}} = \frac{PA}{\sqrt{2\pi mk_b T}} S \quad (5.3)$$

where  $P$  is the partial pressure of the adsorbate in the gas phase,  $A$  is the surface area of the adsorption site,  $m$  is the mass of the adsorbate, and  $S$  is the sticking coefficient.<sup>38-41</sup>

For desorption, it was assumed that the complex has three rotational degrees of freedom and two translational degrees of freedom in the activated state, while it has only vibrational degrees of freedom in the adsorbed state. Accordingly, the rate of desorption is given by:

$$k_{\text{ads}} = \frac{k_b T^3}{h^3} \frac{A(2\pi mk_b)}{\sigma \theta_{\text{rot}}} \cdot \exp\left(\frac{-\Delta E_{\text{des}}}{k_b T}\right) \quad (5.4)$$

where  $\sigma$  is the symmetry number,  $\theta_{\text{rot}}$  is the characteristic temperature for rotation, and  $E_{\text{des}}$  is the desorption energy.<sup>38-41</sup>

The approach for the microkinetics simulations was as follows. Differential equations for all surface reaction intermediates were constructed using the rate constants of the elementary steps. Given a system of  $N$  elementary reaction steps,  $2N$  rate expressions (i.e., both forward and backward reactions) were obtained with the form:

$$r_j = k_j \prod_i c_i^{\nu_i} \quad (5.5)$$

where  $c_i$  is the concentration of species  $i$  in the elementary reaction step  $j$  on the surface, and  $\nu_i$  is the stoichiometric coefficient of species  $i$  in elementary reaction step  $j$ . These rate expressions were used to derive an ordinary differential equation for each component on the surface with the form:

$$\frac{\partial c_i}{\partial t} = \sum_j \nu_{i,j} r_j \quad (5.6)$$

where  $c_i$  is the concentration of species  $i$  on the surface, and  $\nu_{i,j}$  is the stoichiometric coefficient of species  $i$  in elementary reaction step  $j$ .

The in-house developed C++ program MKMCXX was employed to determine the steady-state coverages by integrating this set of ordinary differential equations with respect to time using the backward differentiation formula method.<sup>42-45</sup> The steady-state surface coverage values were used to compute the rates of the individual elementary reaction steps and the

overall rate per surface atom.

## 5.3 RESULTS

### 5.3.1 OVERALL KINETICS

Microkinetics simulations were performed to predict the CO consumption rate and selectivity as a function of temperature. The kinetic parameters are based on the DFT-computed values of activation energies and pre-exponential factors. The pressure in our simulations was 20 atm, and the H<sub>2</sub> to CO ratio was 2. Figure 5.1 shows the normalized turnover frequencies for CO and H<sub>2</sub> consumption and product (hydrocarbons and water) formation as a function of temperature. The optimum CO consumption rate is observed around 1050 K. The decrease in the CO consumption rate at high temperatures is caused by the rapid decrease in the surface CO coverage with temperature. The selectivity trends as functions of temperature are given in Figure 5.1, as well. At relatively low temperatures ( $T < 600$  K), the dominant product is formaldehyde. This is expected because the rates of CO dissociation at these temperatures are very low, and only CO can be hydrogenated. The hydrogenation of formaldehyde to methanol on this surface is difficult. With increasing temperature, the selectivity for ethanol is strongly increased, and small amounts of acet-

aldehyde are simultaneously present in the product mixture. Consistent with the overall exothermicity of the hydrogenation reactions, the ratio of acetaldehyde to ethanol increases slightly with temperature. The optimum ethanol yield occurs at 700 K; at this temperature, the combined yield of C<sub>2</sub>-oxygenates (ethanol and acetaldehyde) is also the highest. When the temperature is further increased, the selectivity for methane increases at the expense of C<sub>2</sub>-oxygenates. Ethylene is also formed in small amounts at intermediate temperatures. Our simulations show that ethane is not formed under the given reaction conditions. Above 900 K, methane is the dominant product, and ethylene and formaldehyde appear as side products.

The formation of longer olefins was not included in the current microkinetic model. To determine if this assumption introduced significant error, we carried out additional simulations of chain-growth reactions for hydrocarbons containing up to 10 carbon atoms. The activation barriers for the carbon-carbon forming steps leading to C<sub>n</sub> surface intermediates with  $n > 2$  were similar to those for C<sub>2</sub> formation from C<sub>1</sub> surface intermediates. The results of these simu-

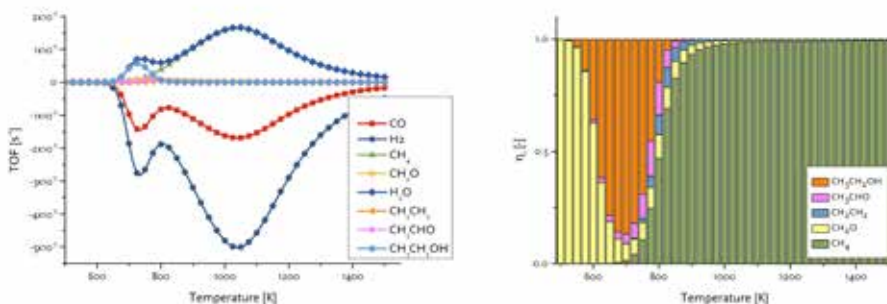


**Figure 5.1:** Figure 1: (left) Production (positive) and uptake (negative) of  $C_1$  and  $C_2$  components as well as  $H_2$  and  $CO$  in the microkinetics simulations of the Fischer–Tropsch reaction on  $Rh(211)$  ( $p = 20$  atm,  $H_2/CO$  ratio = 2); and (right) product selectivity as a function of temperature (right).

lations demonstrated that the selectivity for olefins with more than two carbon atoms was negligible. The chain-growth probability for  $C_{2+}$ -hydrocarbons was around  $10^{-7}$ . These results are in line with experimental data showing that selectivity for hydrocarbons with more than two carbon atoms is very low on Rh nanoparticle catalysts.

The analysis of the steady-state surface coverages in these microkinetics simulations (Figure 5.2) shows that the surface is fully covered with CO at low temperatures. At intermediate temperatures, the appearance of surface vacancies leads to an increase in the rate of CO dissociation. In addition, the surface contains H and O atoms along with small amounts of  $CH_x$  fragments. The temperature dependence of kinetic parameters (reaction orders with respect to CO and  $H_2$  and the apparent activation energies)

are also given (Figure 5.2). At low temperatures, the reaction order in CO is strongly negative, because adsorbed CO self-poisons its dissociation. As vacancies become available with increasing temperature, the CO reaction order increases. At high temperature, the CO reaction order is close to 0.5, and the reaction order with respect to  $H_2$  is always above unity. These data suggest that  $CH_x$  hydrogenation steps are the rate-controlling steps for methane formation. We also verified that the CO consumption rate on  $Rh(111)$  is negligible compared with the rate on  $Rh(211)$  due to the very high barrier for CO dissociation on the  $Rh(111)$  surface.

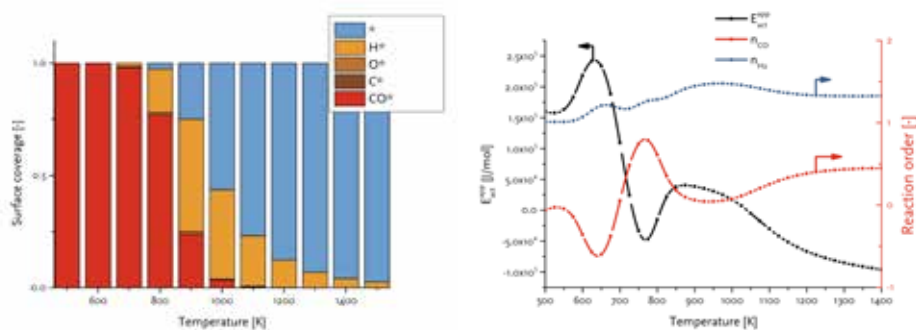


**Figure 5.2:** (left) : Surface coverage as a function of temperature. Only species with a surface coverage higher than 1% have been depicted.; and (right) reaction order (left axis) and apparent activation energy (right axis) as a function of temperature for the microkinetics simulation on Rh(211).

### 5.3.2 REACTION NETWORK ANALYSIS: RATE AND SELECTIVITY CONTROL

In the following section, we discuss in detail the reaction network that leads to the formation of the various hydrocarbon and oxygenate products. In particular, we identify elementary steps that control the overall CO consumption rate and the product selectivity and study how these steps change with reaction temperature. The elementary reaction steps that control the rate of CO consumption and the formation of the various products are identified by determining the degree of rate control (DRC) for all elementary reaction steps.<sup>33,34</sup> The DRC of a chemical reaction is defined as the relative change in the rate as a result of the relative change in the rate constant of a particular elementary reaction step while keeping

the equilibrium constant the same:

$$\chi_{c,i} = \left( \frac{\partial r_c / r_c}{\partial k_i / k_i} \right)_{k_{j \neq i}, K_i} = \left( \frac{\partial \ln(r_c)}{\partial \ln(k_i)} \right)_{k_{j \neq i}, K_i} \quad (5.7)$$

In Eq. 7,  $\chi_{c,i}$  is the DRC parameter of the elementary reaction step  $i$  for the key component  $c$ ,  $r_c$  is the overall reaction rate for key component  $c$ , and  $k_i$  and  $K_i$  are the rate and equilibrium constants for the elementary reaction step  $i$ , respectively. The condition that the equilibrium constant does not change implies that only the location of the transition state of a particular step is changed on the potential energy surface, affecting the forward and backward rate constants. The sum of all DRC values is unity.<sup>22,23</sup> It is customary to determine DRC values for the reactant as the key component. A positive DRC value for a particular elementary reaction

step then indicates that this step limits the reaction rate. A decrease in the activation energy for the transition state of this elementary reaction step would increase the overall rate. Negative values, on the other hand, point to rate-inhibiting elementary reaction steps; that is, lowering the barrier to the transition state of such a step decreases the overall reaction rate.

As we are mainly interested in selectivity issues for CO hydrogenation on Rh nanoparticle catalysts, we employ here the degree of selectivity control (DSC). The DSC quantifies the extent to which a particular elementary reaction step influences the selectivity for certain products. We determine the sensitivity of the absolute change in selectivity as a result of the relative change in the rate constant of a particular elementary reaction step. We use the absolute instead of the relative change, because we are interested in understanding selectivity issues when competition exists between two or more products. Thus, the degree of selectivity control for a particular key component is defined in the following manner:

$$\varepsilon_{c,i} = \left( \frac{\partial \eta_c}{\partial k_i / k_i} \right)_{k_{j \neq i}, K_i} = \left( \frac{\partial \eta_c}{\partial \ln(k_i)} \right)_{k_{j \neq i}, K_i} \quad (5.8)$$

where  $\varepsilon_{c,i}$  is the DSC of product  $c$  due to a change in the kinetics of elementary reaction step  $i$ , and  $\eta_c$  is the selectivity towards a key product component.

We again impose that the equilibrium constant of the elementary considered reaction step does not change. The products considered in the present study are formaldehyde, ethanol, acetaldehyde, ethylene, and methane. We can simply Equation 8 to a form that depends only on the DRC value of the reactant and the product whose DSC value is to be determined:

$$\varepsilon_{c,i} = \eta_c (\chi_{c,i} - \chi_{\text{reactant},i}) \quad (5.9)$$

In the present study, the reactant is CO.

DRC values based on CO as the key reactant as a function of temperature are shown in Figure 5.3, and the DSC values for the products are listed in Figure 5.4. For clarity, Figure 5.4 also contains the selectivity for each product as a function of temperature. It should be noted that in Figures 5.3 and 5.4, the elementary reaction steps are only given for steps with DRC and DSC values greater than 0.01. Thus, only 37 elementary reaction steps are relevant to the discussion of rate and selectivity control.

We first illustrate the use of these parameters for the low temperature regime (500-700 K), in which there is a change in the selectivity from exclusive formaldehyde formation to predominant ethanol formation. It follows that it is useful to introduce another parameter correlating

# $\chi_{CO}$

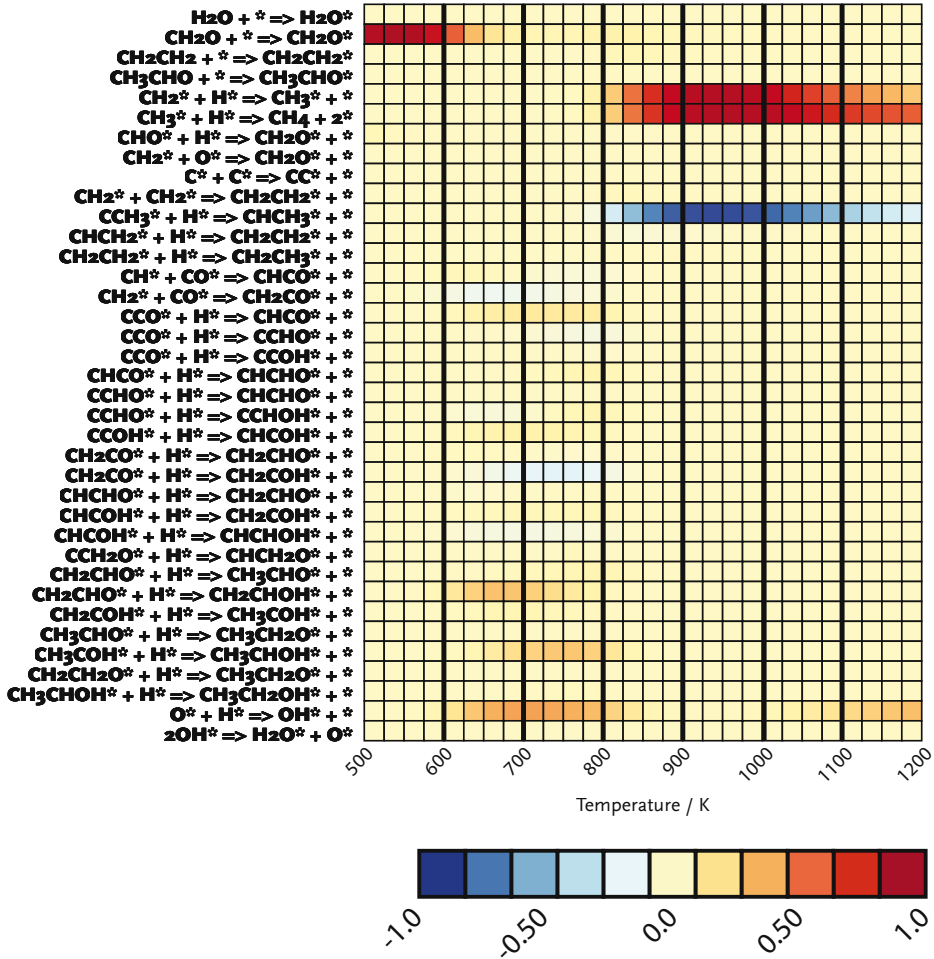
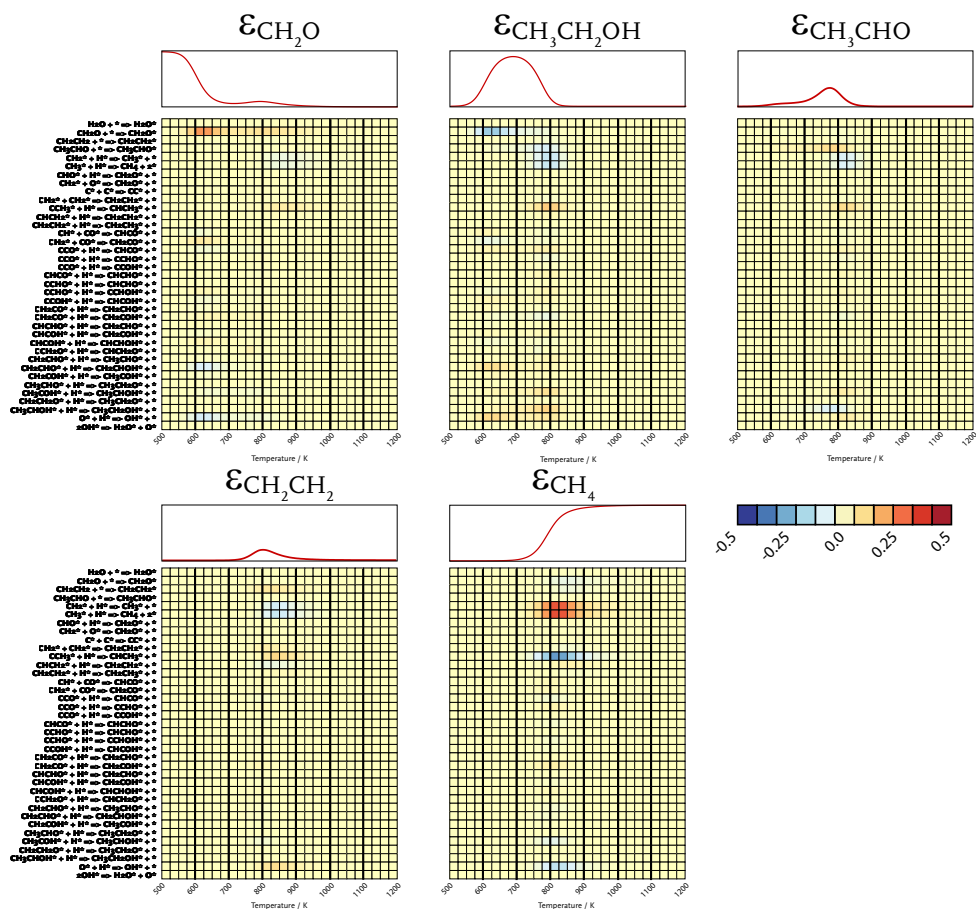


Figure 5.3: Degree of rate control analysis with CO as the key component as a function of temperature. Only elementary reaction steps with an absolute degree of rate control value larger than 0.01 have been included.

the DSC parameters of two products. Figure 5.4 shows that at temperatures below 600 K, formaldehyde desorption controls the overall CO consumption rate. Our simulations predict that methanol cannot

be formed due to the high barrier for the hydrogenation of adsorbed  $CH_2O$ . The desorption of  $CH_2O$  is preferred over its hydrogenation. Experimentally, methanol is observed as the dominant  $C_1$ -oxygenate



**Figure 5.4:** Degree of rate control analysis with CO as the key component as a function of temperature. Only elementary reaction steps with an absolute degree of rate control value larger than 0.01 have been included.

product.<sup>46</sup> We expect that formaldehyde can re-adsorb on other surface planes that are able to hydrogenate formaldehyde.

Figure 5.4 shows that as long as the selectivity for formaldehyde is high, all DSC values are close to zero. Also note that the sum of the DSC values of all elementary reaction steps for a single product equals zero.

When the temperature is raised from 575 K to 675 K, the selectivity shifts from formaldehyde to ethanol. In this regime, the DSC values of  $\text{CH}_2\text{O}$  for the  $\text{CH}_2\text{O}$  desorption step are positive, while those of  $\text{CH}_3\text{CH}_2\text{OH}$  are negative. The DSC values for these two products are strongly and inversely correlated in this temperature regime. This can be understood in the

following way. When the  $\text{CH}_2\text{O}$  desorption energy is decreased (i.e., when formaldehyde desorbs more easily), ethanol selectivity decreases because  $\text{CH}_2\text{O}$  formation consumes CO from the surface, which is needed for the formation of the C–CO bond that leads to ethanol (see below). Two examples of elementary reaction steps that decrease formaldehyde selectivity and increase ethanol selectivity when their activation barriers are lowered are: (i) the hydrogenation of  $\text{CH}_2\text{CHO}$  to  $\text{CH}_2\text{CHOH}$ ; and (ii) the hydrogenation of O to OH. These two reactions control the overall rate of CO consumption to a significant extent once ethanol selectivity becomes dominant. The importance of the first hydrogenation reaction to ethanol formation is evident. The second O hydrogenation step removes O from the surface. In the reaction sequence that leads to water, the O hydrogenation step is the most difficult step. The influence of this step on ethanol selectivity is discussed below in more detail.

The above discussion shows that it is useful to determine the elementary reaction steps for which the DSC parameters of two particular products are correlated. For the purpose of identifying such correlations, we define a correlation coefficient  $\rho_{c_1,c_2,i}$  that is based on the DSC parameters of two products  $c_1$  and  $c_2$  for a particular reaction step  $i$  in the following manner:

$$\rho_{c_1,c_2,i} = \varepsilon_{c_1,i} \cdot \varepsilon_{c_2,i} \quad (5.10)$$

Based on the five products considered in the present study, we need to compute ten different correlation coefficients for every elementary reaction step. Again, we limit ourselves to those reactions that have correlation coefficients larger than 0.01. As we correlate DSC values that are smaller than unity, only few steps have correlation coefficients larger than 0.01. The resulting data are presented in Figure 5.5. For the case of  $\text{CH}_2\text{O}$  vs.  $\text{CH}_3\text{CH}_2\text{OH}$  formation, we see that the three reaction steps discussed above lead to negative correlation coefficients. The influence of formaldehyde desorption is greater than those of the other two steps (indicated in red in Figure 5.5). For all of these three reaction steps, the correlations are negative. A negative correlation coefficient implies that the elementary reaction step under consideration controls the formation of the two products in a competitive manner. This competition is controlled by the concentration of a common reaction intermediate. As we show below, there are two further cases to be considered. In both cases, the correlation is positive, indicating that the changes in selectivity for the two considered products caused by a change in the kinetics of a particular elementary reaction step are in the same direction. There are two

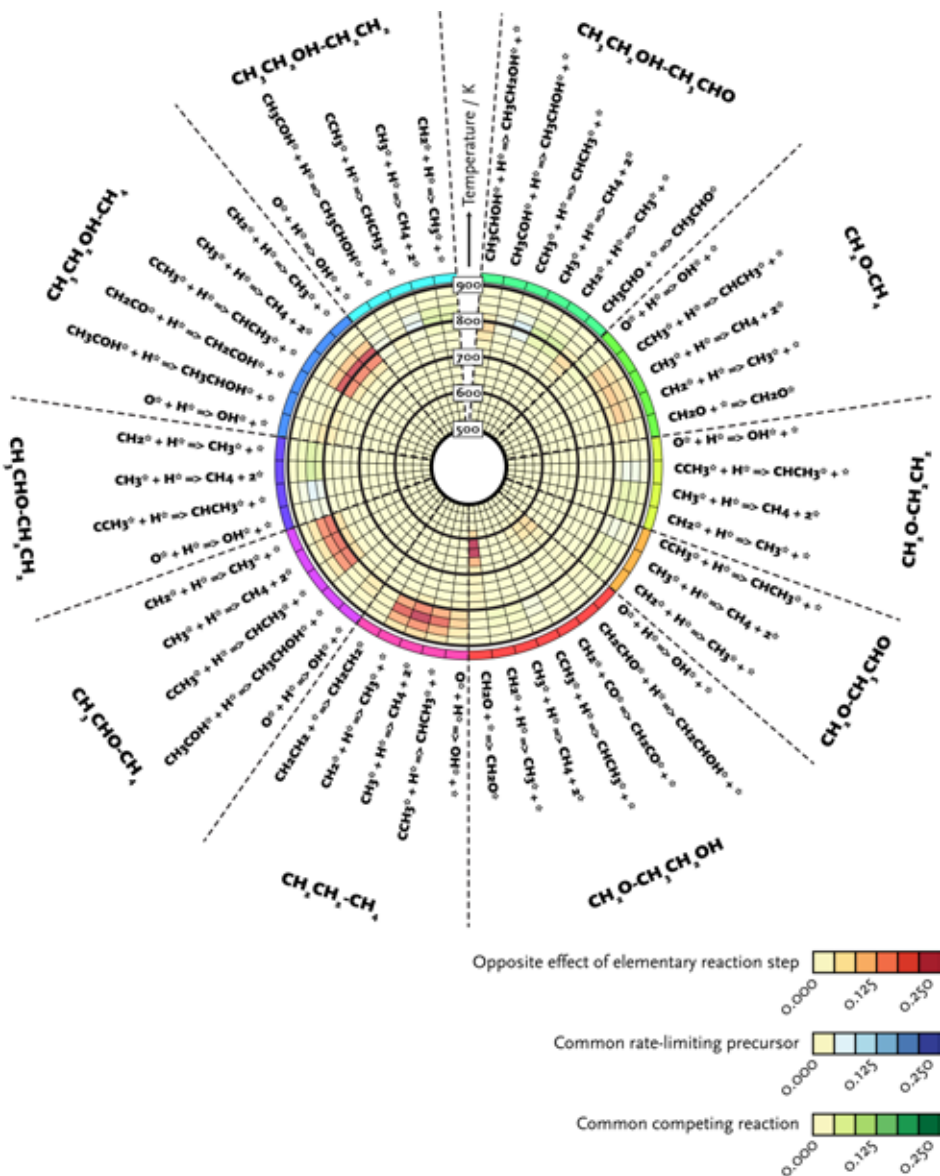


**Figure 5.5:** Cross-correlation graph of the degree of selectivity control for all possible combinations of products. Red indicates that the elementary reaction step results in an opposite effect between the two products, green indicates that the products have a common competing reaction, and blue indicates that the two products have a common precursor that is rate-limiting. For example, the green elements in the  $\text{CH}_3\text{CH}_2\text{OH}-\text{CH}_2\text{CH}_2$  section above  $T=800\text{K}$  indicate that  $\text{CH}_2 + \text{H} \rightarrow \text{CH}_3$  is a common competing reaction for ethanol and ethylene formation, as this reaction leads to a higher yield of methane and a lower yield of both ethanol and ethylene.

possibilities: lowering the barrier of a particular reaction step may either cause a decrease in the selectivity for the two products (indicated in green in Figure 5.5) or an increase in the selectivity for both products (indicated in blue in Figure 5.5).

We now use these DRC and DSC values along with the DSC correlations to discuss three regimes characterized by: (I) selective ethanol formation (675–725 K); (II) the transition from selective ethanol formation to selective methane formation (725–900 K); and (III) selective methane formation (900 K and higher).

*Regime I: Selective ethanol formation*  
(675–725 K)

Figure 5.6 shows the reaction network relevant to ethanol formation from CO and H<sub>2</sub>. The molar rate data are for a reaction temperature of 700 K, the optimum temperature of C<sub>2</sub>-oxygenates selectivity. Adsorbed CO is dissociated to C and O adatoms. The rates of indirect CO dissociation pathways involving CHO or COH surface intermediates are negligible. The preferred CH<sub>x</sub> + CO coupling reaction is the one between C and CO, which yields a strongly adsorbed CCO intermediate. Ethanol formation involves a complex series of surface reactions. First, CCO is hydrogenated to CH<sub>2</sub>CHOH in four steps via CHCO, CHCHO, and CH<sub>2</sub>CHO. Some of the CHCO surface

intermediates dissociate to form CH and CO. The CH<sub>2</sub>CHOH surface fragment is dehydrogenated to CHCHOH, CCHOH, and then to CCOH. Ethanol is then obtained by the sequential hydrogenation of CCOH to CHCOH, CH<sub>2</sub>COH, CH<sub>3</sub>COH, CH<sub>3</sub>CHOH, and finally CH<sub>3</sub>CH<sub>2</sub>OH. The preference for this particular reaction sequence can be explained as follows. The O atom of adsorbed CCO is very strongly bound; the activation energy for its hydrogenation to CCOH is over 200 kJ/mol. When the two carbon atoms in CCO are partially hydrogenated, the O atom is less strongly bound and is more easily hydrogenated. The activation barrier for O hydrogenation in adsorbed CH<sub>2</sub>CHO is less than 100 kJ/mol. When CCOH is obtained, the terminal C atom is first hydrogenated. The resulting CH<sub>3</sub>COH intermediate binds to the surface only via the carbonyl C atom and is then hydrogenated to adsorbed ethanol, which can desorb with an energy of 15 kJ/mol.

Figure 5.3 shows that the following elementary reaction steps control the rate of CO consumption (in decreasing order of DRC values): O hydrogenation > CH<sub>2</sub>CHO hydrogenation to CH<sub>2</sub>CHOH > CCO hydrogenation to CHCO > CH<sub>3</sub>COH hydrogenation to CH<sub>3</sub>CHOH. O hydrogenation is slow because of the strong binding of the O adatom to the stepped surface. As the surface is still mainly covered with CO in this temperature regime, the

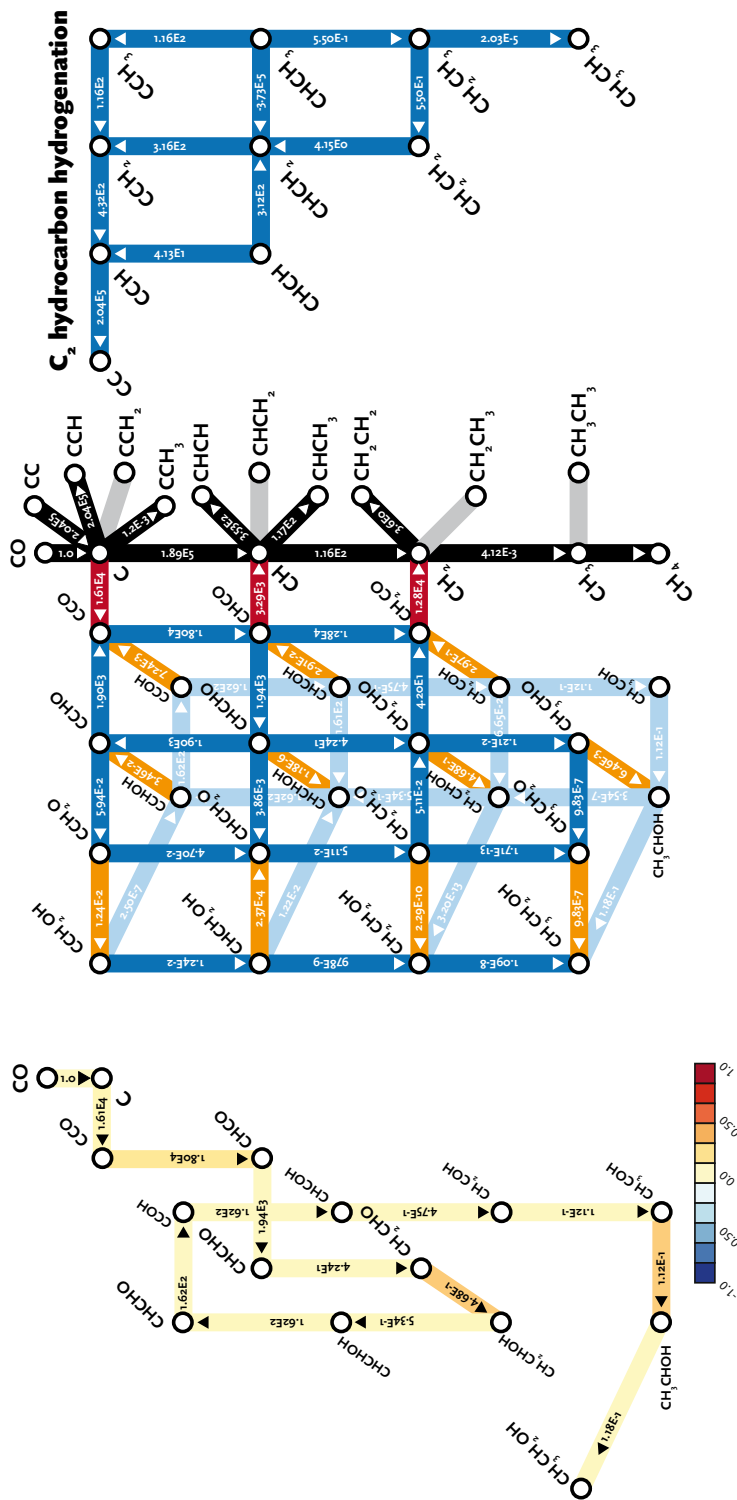


**Figure 5.6:** Reaction pathways for CO hydrogenation to  $\text{C}_2$  productsethanol on Rh(211) ( $p = 20$  atm,  $T = 700$  K,  $\text{H}_2/\text{CO}$  ratio = 2). Only the relevant elementary reaction steps leading to formation of ethanol are shown. The color of the lines corresponds to the degree of rate control (DRC) value. The elementary reaction steps for the hydrogenation of  $\text{CCO}$ ,  $\text{CH}_2\text{CHO}$  and  $\text{CH}_3\text{CHO}$  have an appreciable DRC value. (right) Reaction pathways for CO hydrogenation to  $\text{C}_2$  products on Rh(211) ( $p = 20$  atm,  $T = 700$  K,  $\text{H}_2/\text{CO}$  ratio = 2). The  $\text{C}_2$  hydrocarbon nodes (black lines) are part of the  $\text{C}_2$  hydrogenation network. The grey lines indicate C–C coupling reactions where no transition state could be identified; (right) overview of the main reaction pathway leading to the formation of ethanol from CO and  $\text{H}_2$ .



removal of O by lowering its barrier will lead to more vacancies. The overall CO consumption rate increases, because the increased number of vacancies facilitates the dehydrogenation reactions in the reaction sequence of CCO to ethanol. Rate-inhibiting reactions also occur; for example,  $\text{CH}_2 + \text{CO} \rightarrow \text{CH}_2\text{CO}$  inhibits the reaction rate because lowering the barrier of this step leads to the decomposition of the  $\text{CH}_2\text{CO}$  intermediate. This shifts the  $\text{CHCO} + \text{H} \rightarrow \text{CH}_2\text{CO}$  equilibrium to the right hand side, resulting in a decrease in CHCO coverage. CHCO is an important reaction intermediate in the formation of ethanol; therefore,  $\text{CH}_2\text{CO}$  formation is a rate-inhibiting step.

The detailed inspection of the molar fluxes in the reaction network shown in Figure 5.6 reveals that there are many surface reactions that occur at much higher rates than the overall CO consumption rate. For example, the rate of  $\text{CH}_2\text{CO}$  dissociation to  $\text{CH}_2$  and CO is four orders of magnitude higher than the rate of CO consumption. Likewise, adsorbed C reacts with CCH at a very high rate followed by its dehydrogenation to CC and the dissociation of CC back to two C adatoms. The DRC values for these surface reactions are negligible. As such reactions are not relevant to the formation of the product (ethanol in this temperature regime), we refer to these reactions as spectator reactions. It should

also be stressed that the surface coverages of CCH and CC adsorbates are very low compared with the coverages of adsorbed C and CH.

*Regime II: Transition from selective ethanol to selective methane formation (725–900 K)*

When the temperature is increased from 725 K to 900 K, the selectivity for methane increases strongly at the expense of ethanol. At the same time, the selectivities for ethylene and acetaldehyde also increase. The competition between ethanol and methane formation is of particular interest, because experimentally, methane is the main competing product in ethanol production from CO hydrogenation by Rh-based catalysts.<sup>46</sup> The shift in product selectivity occurs together with a shift in the rate-controlling steps of regime I to those of regime III (mainly  $\text{CH}_2$  and  $\text{CH}_3$  hydrogenation). Figure 5.4 shows that in the temperature range of 750–850 K, the following steps contribute most significantly to the negative correlation between these two products:

$$\text{CH}_2 + \text{H} \rightarrow \text{CH}_3, \text{CH}_3 + \text{H} \rightarrow \text{CH}_4 \text{ and}$$

$$\text{CCH}_3 + \text{H} \rightarrow \text{CHCH}_3.$$

The importance of the first two steps for methane formation is evident. The latter step also contributes to methane formation, because the dehydrogenation of the  $\text{CHCH}_3$  intermediate formed upon  $\text{CH} + \text{CH}_3$  coupling

results in  $CCH_3$  that can decompose to  $C + CH_3$ . The  $CCH_3 + H \rightarrow CHCH_3$  reaction step also exhibits a negative DSC correlation for ethylene and methane, because  $CHCH_3$  is an intermediate in ethylene formation (vide infra). To a lesser extent, a negative correlation also exists for the O hydrogenation step because vacancies are needed to facilitate the dehydrogenation steps for ethanol formation, while these vacancies are not relevant for  $CH_4$  formation.

Ethanol formation also competes with ethylene and acetaldehyde formation. Our analysis reveals that the only elementary reaction controlling the selectivity of ethanol versus that of ethylene is the hydrogenation of  $CH_3CHO$  to  $CH_3CHOH$ . This step is important in the reaction sequence that leads to ethanol. Likewise, there are only two reactions that control the selectivity of ethanol versus that of acetaldehyde. The ethanol selectivity increases when the energy of the transition state for  $CH_3CHOH$  hydrogenation to  $CH_3CH_2OH$  is lowered. This hydrogenation step precedes ethanol desorption, and if it is made more difficult, the selectivity for acetaldehyde increases. The acetaldehyde selectivity also increases when the desorption energy for acetaldehyde decreases, which negatively affects ethanol selectivity.

There is no competition between acetaldehyde and ethylene formation in the

current mechanism. Our analysis shows that a decrease in the barriers for  $CH_2$  and  $CH_3$  hydrogenation decreases the selectivity for acetaldehyde and ethylene. In addition, both selectivities increase when the barrier of O or  $CCH_3$  hydrogenation to  $CHCH_3$  is lowered.

We note that ethylene can be obtained in two different manners: via  $CH_2 + CH_2$  coupling and via  $CH + CH_3$  coupling. For the latter route, the resulting  $CHCH_3$  intermediate is hydrogenated to  $CH_2CH_3$  and then dehydrogenated to  $CH_2CH_2$ . The former pathway is more important than the latter. This chain-growth reaction is different from the preferred coupling step on a stepped Ru surface ( $CH + CH \rightarrow CHCH$ ).<sup>29</sup> The predominance of  $CH_2 + CH_2$  coupling over  $CH + CH$  coupling explains why the chain-growth probability for hydrocarbons on Rh(211) is very low.

#### Regime III: Selective methane formation (900 K and above)

At temperatures above 900 K, methane is the dominant reaction product. Ethylene and acetaldehyde are also produced in small amounts. The rate-controlling steps are  $CH_2$  and  $CH_3$  hydrogenation. The hydrogenation reaction of  $CCH_3$  to  $CHCH_3$  is rate-inhibiting, because this elementary reaction step facilitates the production of ethylene at

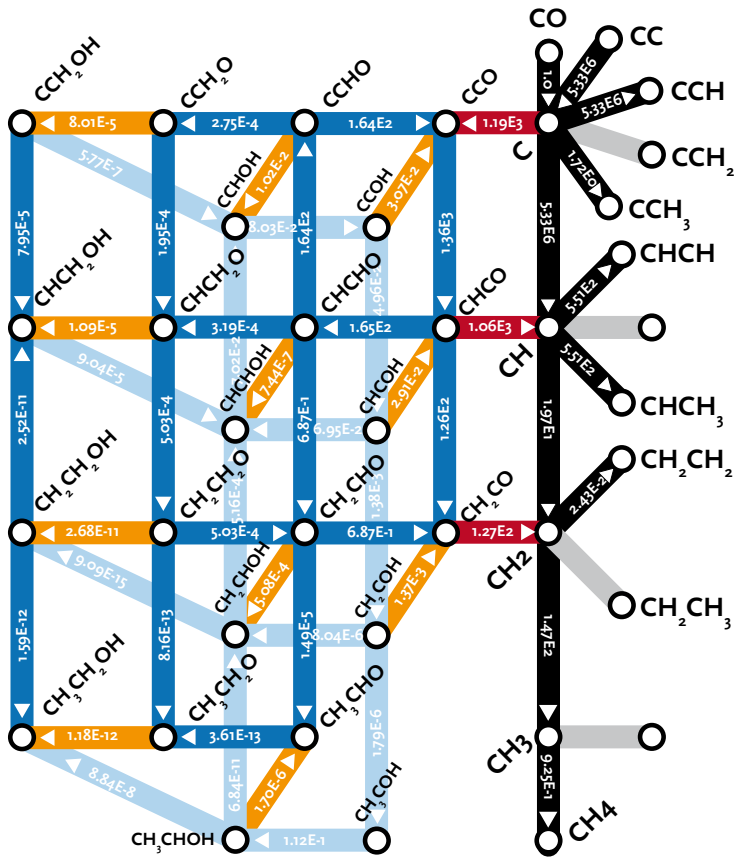


**Figure 5.8:** Reaction pathways for CO hydrogenation to  $C_2$  products on Rh(211) ( $p = 20$  atm,  $T = 1000$  K,  $H_2/CO$  ratio = 2)

the expense of  $CH_4$  formation. The reaction network is analyzed in more detail in Figures 5.7 and 5.8. Methane is formed by direct CO dissociation followed by sequential hydrogenation of the C intermediate. Figure 5.7 shows that none of the  $C_1$ -oxygenate pathways are relevant for methane formation. Figure 5.8 shows that under conditions of predominant methane formation, the rate of  $C + CO$

coupling remains very high compared with the overall CO consumption rate. These reactions do not lead to ethanol formation because of the high rates of  $CHCO$  and  $CH_2CO$  dissociation to  $CH_x$  and CO as well as the endothermicity of the hydrogenation reactions of  $CH_xCO$  intermediates that lead to ethanol.

### 5.3.3 GENERAL DISCUSSION

A key finding of these microkinetics simulations is that CO dissociation is not rate-limiting in the CO hydrogenation reaction on Rh(211). In many studies, slow CO dissociation has been suggested as the main cause for ethanol formation on Rh catalysts.<sup>12,13,46,47</sup> At temperatures below 600 K, the dominant product is formaldehyde, because the rate of CO dissociation is very low. Desorption of formaldehyde is preferred over hydrogenation to methanol. We expect that the hydrogenation of formaldehyde to methanol occurs on the less reactive planar surfaces. Ethanol can be obtained at intermediate temperatures with reasonable selectivity on the stepped Rh surface because of the intermediate Rh-carbon bond strength. On a terraced Rh surface, the Rh–C bond is weak and the CO dissociation barrier is consequently very high, leading to high methanol selectivity. High methanol selectivity has been observed when the Rh nanoparticle size is decreased,<sup>68</sup> which is related to the absence of step-edge sites on very small particles. On the step-edge site of Rh(211), the barrier for C + CO coupling of 136 kJ/mol competes favorably with the value of 156 kJ/mol for the CH + CH coupling reaction. In comparison, the CH + CH coupling reaction is strongly favored kinetically over the C + CO reaction on the step-edge site of Ru(11 $\bar{1}$ ). Thus,

the step-edge sites of Ru and Co catalyze CH + CH (and CH + CR, with R being an alkyl group) coupling reactions towards long-chain hydrocarbons,<sup>31,32</sup> and Rh(211) catalyzes the formation of ethanol via the formation of CCO and its hydrogenation. The barriers for the cleavage of the C–O bonds in CH<sup>x</sup>CO intermediates are very high ( $E_{\text{act}} > 180$  kJ/mol); thus, the formation of ethylene or higher hydrocarbons via this Pichler–Schulz-type pathway is kinetically hindered. As discussed above, the chain-growth probability via CH<sub>x</sub> insertion reactions (carbide mechanism) is also very low.

The formation of ethanol from the CCO intermediate involves a complex sequence of hydrogenation and dehydrogenation steps. In addition to some of these hydrogenation steps, O hydrogenation controls the formation rate of ethanol due to the need for vacancies for the dehydrogenation reactions relevant to hydrogenation of the terminal C and O atoms in the CCO intermediate.

At higher temperatures, the CO consumption rate increases as the surface becomes empty, and methane formation starts to compete with ethanol production. Ethylene, formaldehyde, and acetaldehyde are produced as side products. The rate of formation of higher hydrocarbons remains negligible. This is the regime that is relevant to many experimental studies.<sup>32,48</sup> Our kinetic analysis

shows that  $\text{CH}_2$  and  $\text{CH}_3$  hydrogenation reactions are the main steps that control the selectivity for ethanol. This provides a guiding principle for the design of Rh

catalysts with improved ethanol selectivity. An increase in the C bond strength will lower the rate of C hydrogenation, resulting in increased ethanol selectivity.

## 5.4 CONCLUSIONS

The first principles microkinetics model for CO hydrogenation presented herein shows how ethanol can be formed on a stepped Rh surface. In addition to ethanol, methane, ethylene, ethane, formaldehyde, methanol, and acetaldehyde are also formed. The reaction network and the elementary reaction steps that control the rate and the selectivities were analyzed as a function of temperature. This work provides detailed insights into the complex nature of the surface reactions that lead to the formation of the various products and into the competition between these products. We introduced a novel concept (the degree of selectivity control) that helps identify the elementary reaction steps that most significantly control product selectivities.

The reaction takes place on the Rh(211) surface, because the CO dissociation barriers on the terraced surfaces of Rh are too high. The model predicts the formation of formaldehyde at low temperature, ethanol at intermediate temperature, and methane at high temperature. At low temperature, formaldehyde is the main product because the rate of

CO dissociation is low. At intermediate temperatures, ethanol is formed by C + CO coupling followed by its hydrogenation to acetaldehyde and ethanol. C + CO coupling is preferred over  $\text{CH}_x + \text{CH}_x$  coupling on Rh, which explains the high ethanol selectivity. A small amount of ethylene is formed by  $\text{CH}_2 + \text{CH}_2$  coupling. Longer hydrocarbon chains with three or more C atoms are not formed because of the preference for C+CO coupling and the high barrier for C–O bond cleavage in  $\text{CH}_x\text{CO}$  surface intermediates. At high temperature, C is rapidly hydrogenated to methane.

The microkinetics simulations show that at intermediate temperatures, ethanol formation competes with methane formation. The rate controlling steps are O hydrogenation, which is required to create vacancies for the dehydrogenation steps in the reaction sequence leading to ethanol,  $\text{CH}_x\text{CH}_y\text{O}$  hydrogenation steps for ethanol formation, and  $\text{CH}_2$  and  $\text{CH}_3$  hydrogenation steps for methane formation. The most important reaction steps that control the selectivity for ethanol versus methane are  $\text{CH}_2$  and  $\text{CH}_3$

hydrogenation and CHCH<sub>3</sub> dehydrogenation. ■

## 5.5 REFERENCES

- (1) Colley, S. E.; Copperthwaite, R. G.; Hutchings, G. J.; Terblanche, S. P.; Thackeray, M. M. *Nature* **1989**, *339*, 129.
- (2) van Santen, R. A.; Ciobica, I. M.; van Steen, E.; Ghouri, M. M. In *Adv. Catal.*; Bruce, C. G., Helmut, K., Eds.; Academic Press: 2011; Vol. Volume 54, p 127.
- (3) Higman, C.; Tam, S. *Chem. Rev.* **2013**, *114*, 1673.
- (4) Bezemer, G. L.; Bitter, J. H.; Kuipers, H. P. C. E.; Oosterbeek, H.; Holewijn, J. E.; Xu, X.; Kapteijn, F.; van Dillen, A. J.; de Jong, K. P. *J. Am. Chem. Soc.* **2006**, *128*, 3956.
- (5) den Breejen, J. P.; Radstake, P. B.; Bezemer, G. L.; Bitter, J. H.; Frøseth, V.; Holmen, A.; Jong, K. P. d. *J. Am. Chem. Soc.* **2009**, *131*, 7197.
- (6) Loveless, B. T.; Buda, C.; Neurock, M.; Iglesia, E. *J. Am. Chem. Soc.* **2013**, *135*, 6107.
- (7) Markvoort, A. J.; van Santen, R. A.; Hilbers, P. A. J.; Hensen, E. J. M. *Angew. Chem. Int. Ed.* **2012**, *9*, 9012.
- (8) Spivey, J. J.; Egbeki, A. *Chem. Soc. Rev.* **2007**, *36*, 1514.
- (9) Choi, Y.; Liu, P. *J. Am. Chem. Soc.* **2009**, *131*, 13054.
- (10) Lu, J.; Liu, Y.; Li, N. *J. Nat. Gas Chem.* **2011**, *20*, 423.
- (11) Wang, H.; Liu, J.; Fu, J.; Wan, H.; Tsai, K. *Catal. Lett.* **1992**, *12*, 87.
- (12) Bhasin, M. M.; Bartley, W. J.; Ellgen, P. C.; Wilson, T. *P. J. Catal.* **1978**, *54*, 120.
- (13) Pan, X.; Fan, Z.; Chen, W.; Ding, Y.; Luo, H.; Bao, X. *Nat Mater* **2007**, *6*, 507.
- (14) Bowker, M. *Catal. Today* **1992**, *15*, 77.
- (15) Chen, G.; Guo, C.-Y.; Huang, Z.; Yuan, G. *Chem. Eng. Res. Des.* **2011**, *89*, 249.
- (16) Basu, P.; Panayotov, D.; Yates, J. T. *J. Am. Chem. Soc.* **1988**, *110*, 2074.
- (17) Zhang, Z. L.; Kladi, A.; Verykios, X. E. *J. Catal.* **1995**, *156*, 37.
- (18) Wong, T. T. T.; Stakheev, A. Y.; Sachtler, W. M. H. *J. Phys. Chem.* **1992**, *96*, 7733.
- (19) Anderson, J. A.; Khader, M. M. *J. Mol. Catal. A: Chem.* **1996**, *105*, 175.
- (20) Kapur, N.; Hyun, J.; Shan, B.; Nicholas, J. B.; Cho, K. *J. Phys. Chem. C* **2010**, *114*, 10171.
- (21) Mavrikakis, M.; Bäumer, M.; Freund, H. J.; Nørskov, J. *K. Catal. Lett.* **2002**, *81*, 153.
- (22) Zhu, T. W.; van Grootel, P. W.; Filot, I. A. W.; Sun, S. G.; van Santen, R. A.; Hensen, E. J. M. *J. Catal.* **2013**, *297*, 227.
- (23) Grabow, L. C.; Mavrikakis, M. *ACS Catal.* **2011**, *1*, 365.
- (24) Filot, I. A. W.; van Santen, R. A.; Hensen, E. J. M. *Catal. Sci. Technol.* **2014**, *4*, 3129.
- (25) Filot, I. A. W.; van Santen, R. A.; Hensen, E. J. M. *Angew. Chem. Int. Ed.* **2014**, DOI: 10.1002/anie.201406521.
- (26) Filot, I. A. W.; Shetty, S. G.; Hensen, E. J. M.; van Santen, R. A. *J. Phys. Chem. C* **2011**, *115*, 14204.
- (27) Zhang, J.; Cao, X. M.; Hu, P.; Zhong, Z.; Borgna, A.; Wu, P. *J. Phys. Chem. C* **2011**, *115*, 22429.
- (28) Liu, Z.-P.; Hu, P. *J. Am. Chem. Soc.* **2002**, *124*, 11568.
- (29) Liu, Z.-P.; Hu, P. *J. Chem. Phys.* **2001**, *114*, 8244.
- (30) Wang, J.; Liu, Z.; Zhang, R.; Wang, B. *J. Phys. Chem. C* **2014**, *118*, 22691.
- (31) Chen, J.; Liu, Z.-P. *J. Am. Chem. Soc.* **2008**, *130*, 7929.

- (32) Chiu, C.-c.; Genest, A.; Rösch, N. *Top. Catal.* **2013**, *56*, 874.
- (33) Choi, Y.; Liu, P. *Catal. Today* **2011**, *165*, 64.
- (34) Guo, W.; Li, M.; Lu, X.; Zhu, H.; Li, Y.; Li, S.; Zhao, L. *Dalton Trans.* **2013**, *42*, 2309.
- (35) Li, M.; Guo, W.; Jiang, R.; Zhao, L.; Shan, H. *Langmuir* **2009**, *26*, 1879.
- (36) Stegelmann, C.; Andreasen, A.; Campbell, C. T. *J. Am. Chem. Soc.* **2009**, *131*, 8077.
- (37) Blöchl, P. E. *Phys. Rev. B* **1994**, *50*, 17953.
- (38) Kresse, G.; Joubert, J. *Phys. Rev. B* **1999**, *59*, 1758.
- (39) Kresse, G.; Hafner, J. *J. Phys. Rev. B* **1994**, *49*, 14251.
- (40) Kresse, G.; Furthmüller, J. *J. Comput. Mater. Sci.* **1996**, *6*, 15.
- (41) Perdew, J. P.; Burke, K.; Ernzerhof, M. *Phys. Rev. Lett.* **1996**, *77*, 3865.
- (42) Henkelman, G.; Jónsson, H. *J. Chem. Phys.* **2000**, *113*, 9978.
- (43) Kittel, C. *Introduction to solid state physics*; John Wiley and Sons Inc.: Newyork, London, Sydney, 1966; Vol. 3rd ed.
- (44) Mavrikakis, M.; Bäumer, M.; Freund, H.-J.; Nørskov, J. K. *Catal. Lett.* **2002**, *81*, 153.
- (45) Joos, L.; Filot, I. A. W.; Cottenier, S.; Hensen, E. J. M.; Waroquier, M.; Van Speybroeck, V.; van Santen, R. A. *J. Phys. Chem. C* **2014**, *118*, 5317.
- (46) Cheng, J.; Hu, P.; Ellis, P.; French, S.; Kelly, G.; Lok, M. C. J. *Phys. Chem. C* **2008**, *112*, 6082.
- (47) Corral Valero, M.; Raybaud, P. *Catal. Lett.* **2013**, *143*, 1.
- (48) Hanaoka, T.; Arakawa, H.; Matsuzaki, T.; Sugi, Y.; Kanno, K.; Abe, Y. *Catal. Today* **2000**, *58*, 271.
- (49) Mei, D.; Rousseau, R.; Kathmann, S. M.; Glezakou, V.-A.; Engelhard, M. H.; Jiang, W.; Wang, C.; Gerber, M. A.; White, J. F.; Stevens, D. J. *J. Catal.* **2010**, *271*, 325.
- (50) Van Santen, R. A.; Markvoort, A. J.; Filot, I. A. W.; Ghouri, M. M.; Hensen, E. J. M. *Phys. Chem. Chem. Phys.* **2013**, *15*, 17038.



## Abstract

Density functional theory calculations were conducted to study  $N_2$  adsorption on various Rh surfaces and clusters with the aim to establish whether IR spectroscopy of  $N_2$  adsorbed on Rh nanoparticles can help to identify step-edge sites. Catalytic performance studies on zirconia-supported Rh nanoparticles and IR spectroscopy of  $N_2$  adsorbed on these nanoparticles were used to determine the active site for CO dissociation. The computational results show that the experimentally observed IR absorption band can be correlated to the presence of low-coordinated surfaces such as occur on step-edge sites. Steady-state isotopic transient kinetic analysis (SSITKA) data is combined with microkinetics simulations of CO hydrogenation on the stepped Rh(211) surface to rationalize the observed trends in catalytic activity and selectivity. Based on the SSITKA results, the microkinetics simulations point out that only the Rh(211) surface is able to catalyze the product formation as found in experiment. The barrier for CO dissociation on the terraced Rh(111) is too high to form higher oxygenates.

★ « *These are the dark matter engines I invented. They allow my starship to travel between galaxies in mere hours.* »

« *That's impossible. You can't go faster than the speed of light.* »

« *Of course not. That's why scientists increased the speed of light in 2208.* » ★

From Futurama, A Clone of My Own

**PROBING  
THE ACTIVE  
SITES FOR CO  
DISSOCIATION  
BY N<sub>2</sub> IR  
SPECTROSCOPY**



**6**

## 6.1 INTRODUCTION

Fischer-Tropsch synthesis is an attractive route for the valorization of natural gas into synthetic fuels and chemicals.<sup>1,2</sup> The exact nature of the reaction mechanism and especially the identification of the rate-limiting step(s) and the active site remain a topic of considerable debate.<sup>3-13</sup> From experiment, it is well known that catalytic activity strongly depends on the particle size.<sup>14-18</sup> This kind of structure sensitivity is usually understood in terms of the sensitive dependence of the rate of elementary reaction steps on the surface termination. Nanoparticles expose terraces, edges, corners and step-edges. The coordinative unsaturation of the surface atoms in these sites varies, which leads to different chemical reactivity. For the cleavage of  $\sigma$ -bonds (e.g., C-H bonds in alkanes), low-coordinated metal atoms (typically edge or corner atoms) are necessary. For the dissociation or formation of a  $\pi$ -bond such as in CO, a step-edge site is necessary that facilitates the overlap of the transition metal d-orbitals with the molecular  $\pi$ -bonds.<sup>9,19-21</sup> One predicts strong dependence of CO conversion on the particle size. Below a critical size, nanoparticles cannot stabilize step-edges anymore and, accordingly, such particles will only expose edge and corner atoms. Particles of intermediate size expose, in addition to edge and corner atoms, the

highest density of step-edge sites. The surfaces of very large particles will be dominated by terraces.<sup>9,12,17</sup>

Experimentally, the particle size dependence of the FT reaction has been well established. The group of De Jong<sup>16,17</sup> has shown that the optimal Co particle size for the FT reaction lies around 6 nm. Below this size, the activity of CO dissociation strongly decreases. Fierro and co-workers showed that Ru nanoparticles displayed a similar size dependence in the FT reaction.<sup>22</sup> Others have also explored the FT reaction in the aqueous phase. Xiao *et al.* showed a very pronounced particle size dependency for unsupported Ru nanoparticles.<sup>23</sup> On the contrary, Quek *et al.* showed that the particle size dependence for unsupported Ru nanoparticles is quite similar<sup>24</sup> to trends observed in conventional FT synthesis using supported Ru nanoparticles.<sup>22</sup> These data also pointed out the critical dependence of the chain-growth probability and the product (oxygenates vs. hydrocarbons) selectivity on the nanoparticle size.<sup>15</sup> A recent study points to the considerable disorder and corrugation of Ru nanoparticles as a function of their particle size.<sup>14</sup>

The importance of step-edge sites in heterogeneous reactions catalyzed by transition metals has been well esta-

blished in the work of Ertl.<sup>25</sup> Nørskov and co-workers have provided strong support for the importance of step-edges for N<sub>2</sub> activation on Ru surfaces.<sup>26</sup> Suggestions that such step-edges may be relevant to the activation of diatomic molecules such as N<sub>2</sub> have been made by Van Hardeveld and Van Montfoort.<sup>27</sup> These authors proposed that the surface of nanoparticles will contain so-called B<sub>5</sub> sites, that are ensembles of surface atoms arranged in a fashion that a step-edge is obtained. Based on geometric considerations, they argued that such sites occur most frequently on the surface of ~ 2 nm particles.<sup>20</sup>

Despite the apparent relevance of step-edge sites to metal catalysis, no experimental technique exists that can titrate these sites. The group of Chorkendorff has used isotopic scrambling between <sup>12</sup>C<sup>16</sup>O and <sup>13</sup>C<sup>18</sup>O on Ru nanoparticles to probe CO dissociation sites.<sup>28</sup> Van Hardeveld and Van Montfoort employed infrared spectroscopy of adsorbed N<sub>2</sub> on Ni, Pd and Pt.<sup>27,29</sup> The strong shift of the N-N absorption band compared to the gas-phase value was interpreted as a sig-

nature for the relatively strong adsorption of N<sub>2</sub> in the step-edge.

In the present work, we carried out a computational study of N<sub>2</sub> adsorption on various Rh surfaces and clusters with the aim to establish whether IR spectroscopy of N<sub>2</sub> adsorbed on Rh nanoparticles can help to identify step-edge sites. The work is complementary to existing catalytic performance data of zirconia-supported Rh nanoparticle catalysts that display structure sensitive behavior in CO hydrogenation. IR spectroscopy of N<sub>2</sub> adsorbed on reduced Rh catalysts shows a distinct band at 2205 cm<sup>-1</sup>, whose intensity correlates with catalytic performance. The computational data show that this IR band can be correlated to the presence of low-coordinated surface atoms. It will be argued that the strong correlation with the catalytic performance points to the presence of step-edge sites. Finally, steady-state isotopic transient kinetic analysis (SSITKA) data is combined with microkinetics simulations of the CO hydrogenation on the stepped Rh(211) surface to explain trends in the catalytic activity and product selectivity.

## 6.2 COMPUTATIONAL METHOD

In order to investigate the frequency and intensity of N<sub>2</sub> adsorption on different surface sites and in different adsorption modes, plane-wave density

functional theory calculations were performed. All calculations were performed using the Perdew-Burke-Ernzerhof (PBE) exchange-correlation functional<sup>30</sup> as

implemented in VASP.<sup>31,32</sup> To describe the interaction between the nuclei and the core electrons, the projector-augmented wave (PAW) method<sup>33</sup> was used. For the valence electrons, a plane-wave basis set with an energy cut-off of 500 eV was used. For the nanoparticles, the Brillouin zone sampling was restricted to the  $\gamma$  point. For the stepped surfaces, a Brillouin zone sampling of  $5 \times 5 \times 1$   $k$ -points was used. To include the Van der Waals (vdW) corrections, we have employed the semi-empirical DFT-D2 method of Grimme.<sup>34,35</sup> The electronic convergence criterion was set to  $10^{-5}$  eV, and geometries were converged to  $10^{-4}$  eV/Å using a conjugate-gradient algorithm that uses trial and corrector steps to converge the energy and the forces. In order to avoid spurious interactions between the images of the system, a vacuum layer of at least 10 Å was added in each direction for the nanoparticles, and along the  $z$ -axis perpendicular to the directions of the periodicity for the stepped surface. All frequencies were calculated using the finite-difference approach. The calculated  $N_2$  stretching frequency differed from the

experimental  $N_2$  stretching frequency by 2.8%. Because we are mainly interested in trends, we did not scale the calculated frequencies.

The infrared intensities of the vibrational modes were calculated using the method previously employed by Preuss and coworkers.<sup>36</sup> The intensity  $|I|$  of a normal mode is linearly correlated to the change in the dipole moment as function of a perturbation in the direction of the normal mode as given by equation 1.

$$I_\nu \propto \left| \frac{\partial \bar{\mu}}{\partial q_i} \right|^2 \quad (6.1)$$

where  $\mu$  is the dipole moment vector and  $q_i$  is the normal mode. It should be noted that for the slab calculations, the absolute values of the calculated in-plane dipole moment components are less useful due to the periodic boundary conditions and, therefore, we have only taken the change in the dipole moment in the direction perpendicular to the surface of the slab (i.e., the  $z$ -direction) for the calculation of the intensities.

## 6.3 RESULTS

We will first discuss the experimental results for CO conversion and IR measurements of  $N_2$  adsorption on the Rh nanoparticles that served as the starting

point to this computational modeling study. Then, we will discuss the DFT calculations to determine the  $N_2$  frequency and intensity as a function of surface to-

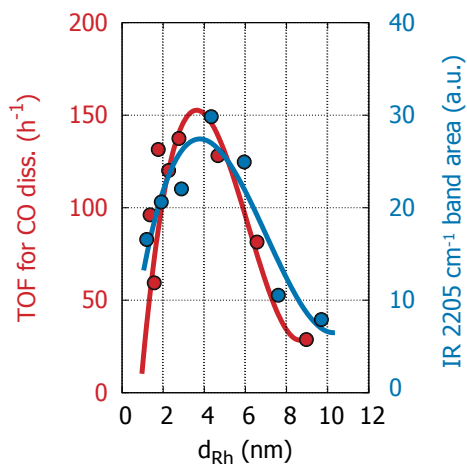


**Figure 6.1:** Turn over frequency (TOF) for CO as a function of the particle size. Intensity of the 2205  $cm^{-1}$  IR absorption band as a functional of particle size.

pology. Finally, the results are combined in an attempt to link the computational understanding about IR absorption by  $N_2$  molecules to the catalytic data.

### 6.3.1 FISCHER-TROPSCH CATALYSIS OVER ZIRCONIA-SUPPORTED RH NANOPARTICLES

A series of zirconia-supported Rh catalysts were prepared by pore volume impregnation of aqueous solutions of Rh-nitrate. The Rh particle size was varied by changing the Rh loading and the calcination/ageing procedure of the final catalyst, in an analogous manner as done in previous work.<sup>9</sup> The phase of the zirconia support was monoclinic in all

cases. The average Rh particle size was determined from TEM images as well as  $H_2$ -chemisorption.<sup>9</sup> Prior to activity measurements, the catalysts were reduced in  $H_2$  at 723 K. The catalytic activity was measured at 548 K at a  $H_2/CO$  ratio of 2. The turnover frequencies (TOFs) of CO dissociation were calculated on a carbon basis from products formed by CO dissociation.

The TOF of CO dissociation for this set of catalysts shows a strong particle size dependence (Figure 6.1). Optimum performance is observed for particles of about 4.7 nm. Catalytic performance data including hydrocarbon selectivities for a limited set of catalysts are given in Table 6.1. The main product of CO hydrogenation for these catalysts under the given reaction conditions is methane. The methanol selectivity is much lower than the ethanol selectivity. Optimum ethanol selectivity occurs at approximately the same particle size as the optimum particle size for CO dissociation.

SSITKA experiments were carried out in a setup described elsewhere.<sup>37</sup> The plug-flow microreactor was loaded with the catalyst diluted with SiC, and then pretreated in  $H_2$  at 723 K. After cooling to 548 K, the catalyst was exposed to the feed mixture of  $^{12}CO/H_2 = 1/2$  at a total pressure of 5 bar. At steady-state conditions, the feed composition was switched to a feed with  $^{13}CO/H_2 = 1/2$ . From the

**Table 6.1:** Turn-over-frequency (TOF), CO and CH<sub>x</sub> coverage as a function of particle diameter for CO hydrogenation over Rh/ZrO<sub>2</sub><sup>1</sup> Catalysts are denoted by Rh(x, aT) with x the metal loading (wt.%), a optionally indicating an ageing treatment and T the final catalyst treatment temperature (°C) followed by the support reference.

| Catalyst                            | d <sub>av</sub><br>nm | TOF<br>s <sup>-1</sup> | v <sub>CO</sub><br>s | v <sub>CHX</sub><br>s | θ <sub>CO</sub><br>% | θ <sub>CHx</sub><br>% |
|-------------------------------------|-----------------------|------------------------|----------------------|-----------------------|----------------------|-----------------------|
| Rh(2, 600)/ZrO <sub>2</sub> (600)   | 2.7                   | 0.014                  | 1.1                  | 1.2                   | 45                   | 1.3                   |
| Rh(2, a750)/ZrO <sub>2</sub> (600)  | 4.7                   | 0.024                  | 1.5                  | 1.8                   | 62                   | 3.0                   |
| Rh(2, a1000)/ZrO <sub>2</sub> (600) | 7.8                   | 0.011                  | 2.2                  | 2.5                   | 52                   | 2.3                   |

<sup>1</sup> reaction conditions: 275 °C , 5 bar

**Table 6.2:** Effect of Rh particle size on CO hydrogenation over Rh/ZrO<sub>2</sub><sup>1</sup> Catalysts are denoted by Rh(x, aT) with x the metal loading (wt.%), a optionally indicating an ageing treatment and T the final catalyst treatment temperature (°C) followed by the support reference.

| Catalyst                            | d <sub>av</sub> [nm] | Selectivity (%) |      |      |                           |
|-------------------------------------|----------------------|-----------------|------|------|---------------------------|
|                                     |                      | CH <sub>4</sub> | MeOH | EtOH | Total C <sub>2+</sub> Oxy |
| Rh(2, 600)/ZrO <sub>2</sub> (600)   | 2.7                  | 69              | 3.4  | 13   | 15                        |
| Rh(2, a750)/ZrO <sub>2</sub> (600)  | 4.7                  | 67              | 2.8  | 17   | 21                        |
| Rh(2, a1000)/ZrO <sub>2</sub> (600) | 7.8                  | 76              | 3.4  | 9    | 10                        |

<sup>1</sup> reaction conditions: 275 °C , 5 bar

mass spectrometry signals during the following backswitch, the surface residence times were calculated according to established procedures.<sup>37</sup> The residence times were corrected for the gas phase hold-up with the use of the Ne inert tracer; these values were then used as input to calcu-

late the number of reversibly adsorbed CO and CH<sub>x</sub> species and the CO and CH<sub>x</sub> surface coverages. Table 6.2 reports the results from SSITKA measurements carried out at a lower total pressure of 5 bar. It was verified in separate experiments that the particle size dependence of the

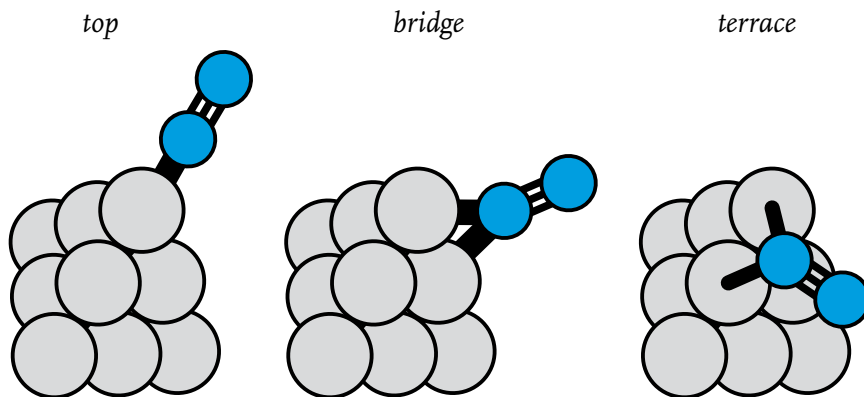


**Figure 6.2:** Geometries of top, bridge and terrace adsorption of  $N_2$  on a tetrahedral  $Rh_{10}$  cluster.

reaction rate and product selectivity was similar as in the experiments carried out at 20 bar. At 5 bar, optimum activity in CO dissociation also occurs for the catalyst containing on average 4.7 nm particles. The surface coverages of CO and  $CH_x$  are seen to depend on the particle size. The CO coverage is highest for the most active catalyst. The relatively strong variation of the CO coverage may point to differences in the CO adsorption strength as a function of the particle size. The  $CH_x$  surface coverage as measured by the  $CH_4$  transient is very low, consistent with SSITKA data for methanation on Co and Ru nanoparticle catalysts.<sup>22,39</sup> Also, the  $CH_x$  surface coverage display a maximum at the intermediate particle size for which optimum performance is observed.

Infrared experiments of adsorbed  $N_2$  were recorded on a Bruker IFS113v Fourier transform IR spectrometer. The

sample was pressed into a self-supporting wafer and placed in a controlled environment transmission IR cell with  $CaF_2$  windows. After reduction in hydrogen, the sample was cooled in vacuum to 90 K. Increasing amounts of  $N_2$  were admitted to the cell until saturation of the bands. In addition to a band due to weakly adsorbed  $N_2$  on the zirconia support, a distinct band at  $2205\text{ cm}^{-1}$  is visible for the reduced  $Rh/ZrO_2$  catalysts. This band was absent when  $N_2$  was adsorbed on a zirconia support without Rh metal. The intensity of this perturbed  $N_2$  adsorption band was determined and normalized to the Rh dispersion. The resulting values are shown as a function of the particle size in Figure 6.1. The intensity of the N-N stretching band at  $2205\text{ cm}^{-1}$  is seen to correlate with the TOF for CO dissociation. Accordingly, we speculated that the sites probed by IR spectroscopy

**Table 6.3:** Frequency and intensity of the different adsorption sites and modes of  $N_2$  on  $Rh_{10}$  clusters,  $Rh_{20}$  clusters and  $Rh(211)$  surfaces.

| Position             | Adsorption energy (kJ/mol) | N-N stretching frequency ( $cm^{-1}$ ) | N-N bond distance (Å) | N-N stretching intensity (arb. units) |
|----------------------|----------------------------|--|-----------------------|---------------------------------------|
| $Rh_{10}$ Top        | 80                         | 2216                                   | 1.13                  | 17                                    |
| $Rh_{10}$ Bridge     | 83                         | 2019                                   | 1.15                  | 4.5                                   |
| $Rh_{10}$ Terrace    | 45                         | 1928                                   | 1.18                  | 1.8                                   |
| $Rh_{20}$ Top (CN=3) | 101                        | 2195                                   | 1.13                  | 26                                    |
| $Rh_{20}$ Top (CN=9) | 68                         | 2212                                   | 1.13                  | 3.2                                   |
| $Rh_{20}$ Bridge     | 78                         | 2014                                   | 1.15                  | 12                                    |
| $Rh_{20}$ Terrace    | Migrates to top            |  |                       |                                       |
| $Rh(211)$ Top        | 89                         | 2205                                   | 1.13                  | 5.1                                   |
| $Rh(211)$ Bridge     | 47                         | 2065                                   | 1.14                  | 1.0                                   |
| $Rh(211)$ Bidentate  | 58                         | 1730                                   | 1.18                  | 1.4                                   |
| $Rh(211)$ Terrace    | Migrates to top            |  |                       |                                       |

of adsorbed  $N_2$  are the same as the sites involved in CO dissociation.

### 6.3.2 DFT CALCULATIONS

DFT calculations will be presented for three different Rh systems: tetrahedral  $Rh_{10}$  and  $Rh_{20}$  clusters and the stepped  $Rh(211)$  surface. These three systems

were chosen as they contain a variety of low-coordinated corner and edge sites ( $Rh_{10}$  and  $Rh_{20}$  clusters) as well as step, step-edge and terrace sites ( $Rh(211)$  surface). For each system,  $N_2$  was adsorbed on different adsorption sites in a variety of adsorption modes. The N-N stretching frequencies and intensities were calculated for all of these adsorption modes.

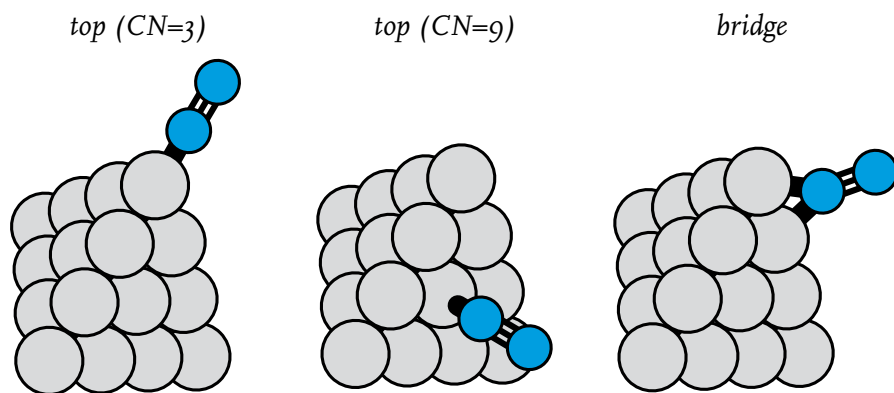


**Figure 6.3:** Geometries of top (CN=3), top (CN=9) and bridge adsorption of  $N_2$  on a tetrahedral  $Rh_{20}$  cluster.

Three different adsorption sites were studied for the  $Rh_{10}$  cluster. These sites are shown in Figure 6.2. The computed frequencies and intensities are collected in Table 6.3. Top adsorption was studied on a Rh atom with a coordination number (CN) of 3, bridge adsorption between two Rh atoms with CNs of 3 and 6 and threefold adsorption between three Rh atoms with CNs of 3, 6 and 6. For top and bridge adsorption, the adsorption energies were around 80 kJ/mol. The adsorption energy on the threefold site was significantly lower (45 kJ/mol). The N-N stretching frequency decreases when  $N_2$  is adsorbed in increasingly higher coordination sites. The increased coordination with the surface results in an increase of the N-N bond distance. Together these changes point to weakening of the N-N bond. The calculated IR intensities decreased going from top ( $I_v = 17$ ) to bridge

(4.5) and threefold (1.8) adsorption.

The three different adsorption sites for the  $Rh_{20}$  cluster are shown in Figure 3. When  $N_2$  was adsorbed on a threefold site, the adsorbate migrated to one of the top positions. The surface atoms of the threefold site on the  $Rh_{20}$  tetrahedral nanoparticle have a higher coordination number than those on the  $Rh_{10}$  tetrahedral nanoparticle. This finding shows that  $N_2$  adsorption on high-coordination sites involving Rh atoms with high metal coordination number is unlikely. It is consistent with the preference for  $N_2$  adsorption in top and bridge sites over threefold one on the  $Rh_{10}$  tetrahedral cluster.

Two different top adsorption modes were identified, involving Rh surface atoms with CN = 3 and CN = 9. One bridged adsorption geometry was found involving two Rh atoms with CN = 3 and 6. Top adsorption of  $N_2$  on the more

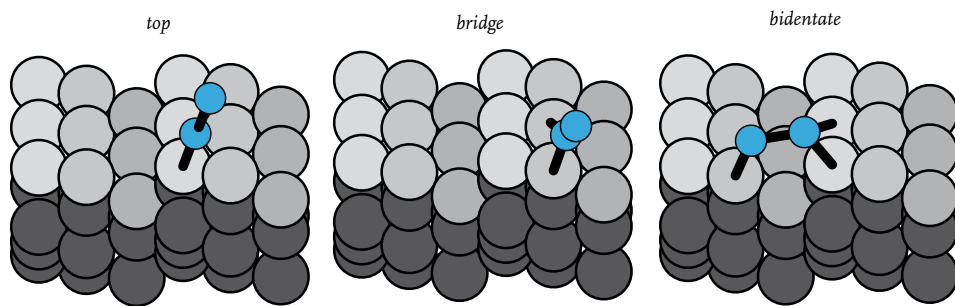


**Figure 6.4:** Geometries of top, bridge, bidentate and threefold adsorption of  $N_2$  on a stepped  $Rh(211)$  surface.

coordinatively saturated Rh atom (CN=9) was weaker (68 kJ/mol) than top adsorption on the Rh atom with CN = 3 (101 kJ/mol). The N-N stretching frequencies for the two top adsorptions were very similar (2195  $cm^{-1}$  and 2212  $cm^{-1}$  for CN = 3 and CN = 9, respectively). The N-N bond distances were 1.13 Å for both these adsorption geometries. The adsorption energy for the bridge configuration of  $N_2$  was 78 kJ/mol. The N-N frequency and the N-N bond distance in this case were 2014  $cm^{-1}$  and 1.15 Å. These results are in qualitative agreement with those for the  $Rh_{10}$  cluster. Similar to the trend seen for the  $Rh_{10}$  tetrahedral cluster, top adsorption on the Rh atom with CN = 3 had the highest intensity followed by bridge adsorption and top adsorption on a Rh atom with CN = 9.

Four different adsorption sites were investigated for the stepped  $Rh(211)$

surface (Figure 6.4). Among the systems studied, this surface is the only one that can bind  $N_2$  in a bidentate fashion. The other adsorption modes are top, bridge and threefold adsorption. The threefold adsorption site is on the terrace adjacent to the step-edge site. In line with the results above, threefold coordination of  $N_2$  to Rh atoms with CN = 9 led to its migration to the step-edge atom with CN = 7. In this adsorption mode, the  $N_2$  adsorption energy was 89 kJ/mol. This adsorption energy is intermediate to the values for top adsorption on Rh surface atoms with CN = 6 (101 kJ/mol) and with CN = 9 (68 kJ/mol). The adsorption energies for bridge and bidentate adsorption were 47 kJ/mol and 58 kJ/mol, respectively. The calculated  $N_2$  stretching frequencies are comparable to values for similar adsorption geometries computed for the  $Rh_{10}$  and  $Rh_{20}$  clusters.

## 6.4 DISCUSSION

The computational modeling results show the following trends for  $N_2$  adsorption on different surface sites. The N-N stretching lies around  $2200\text{ cm}^{-1}$  when  $N_2$  is adsorbed on top sites. When  $N_2$  adsorbs in higher coordination sites, the frequency shifts to lower values, i.e.  $2050\text{ cm}^{-1}$  for bridge adsorption,  $1950\text{ cm}^{-1}$  for terrace adsorption and  $1730\text{ cm}^{-1}$  for bidentate adsorption. The differences in the N-N stretching frequencies can be rationalized with the Dewar-Chatt-Duncanson model.<sup>39,40</sup> Adsorption in high coordination sites result in larger overlap between the *d*-orbitals of the metal atoms and the  $\pi$ -orbitals of the  $N_2$  adsorbate than on top adsorption. The stronger donation of electron density from the metal to the anti-bonding orbitals of  $N_2$  weakens the N-N bond and, accordingly, lowers the N-N stretching frequency.

The computed intensities of the adsorption geometries strongly correlate with the coordination number of the metal atom to which  $N_2$  adsorbs. For example, the intensity of the N-N stretching band in top adsorption increases with a decrease of the coordination number of the Rh atom to which  $N_2$  binds. This trend in the intensity can be explained as follows. Whereas  $N_2$  in the gas phase is not infrared-active due to its center of inversion,  $N_2$  adsorbed on a

metal surface will become infrared-active because the two N atoms are chemically different for the adsorption modes considered in this study. The interaction of the Rh atom with N increases when the metal-metal coordination number of Rh decreases. This will lead to a stronger difference between the two N atoms in adsorbed  $N_2$ . The resulting greater change in the dipole moment results in higher intensity of the corresponding IR band. The stronger interaction of  $N_2$  with lower coordinated metal atoms can also be seen from the adsorption energies that tend to be higher for more reactive surface atoms.

Comparing these computational data to the experimental IR spectra, we can conclude that the experimentally observed band at  $2205\text{ cm}^{-1}$  can be assigned to  $N_2$  molecules adsorbed on top sites. The intensity of the IR band depends on the nature of the Rh surface atoms. The computational results predict that the intensity will be higher for Rh atoms with a lower coordination number. Therefore, one expects that a decrease of the size of nanoparticles will increase the intensity of the  $2205\text{ cm}^{-1}$ , because smaller particles contain an increasing fraction of corner atoms. Our calculations, however, show that top adsorption on a Rh atom with CN = 3 in a  $Rh_{10}$  cluster results in a

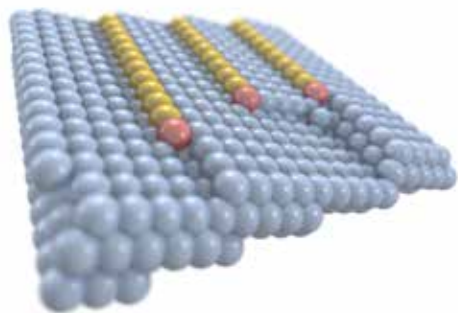


**Figure 6.5:** *Cartoon representation of a stepped surface. The yellow atoms are the step-edge atoms. Rows of these step-edge atoms are terminated by low-coordinated corner atoms, depicted in red.*

less intense IR band than top adsorption on a Rh atom in a  $\text{Rh}_{20}$  cluster. The different trend observed in Fig. 6.1 indicates that particles of intermediate size contain much more low-coordinated surface atoms than very small nanoparticles. We attribute this particular trend to the presence of step-edge sites. Firstly, top adsorption on the step-edge atom with  $\text{CN} = 7$  contributes more to the intensity than top adsorption on terrace surface sites. Secondly, we argue that with increasing Rh particle size the surface will be able to accommodate Rh metal overlayers. As exemplified in Fig. 5, these overlayers will contain corner atoms with a  $\text{CN}$  lower than 7.  $\text{N}_2$  adsorption on these sites will significantly contribute to the intensity of the  $\text{N}_2$  stretching band.

Thus, the trend in the  $\text{N}_2$  IR intensity with particle size can be explained

as follows. Very small particles contain low-coordinated Rh atoms that will adsorb  $\text{N}_2$ , however, contributing little to the overall intensity. With increasing particle size, step-edge sites can be stabilized. This will lead to a rapid increase of the number of low-coordinated Rh atoms, namely the step-edge sites themselves with  $\text{CN} = 7$  and atoms at the corners of the metal overlayers that develop on the terraces of the nanoparticles with a lower coordination number. The decrease of the IR intensity for particles larger than 4.7 nm suggests that these particles contain less step-edge sites, presumably because they contain less metal overlayers. Although we cannot provide a solid explanation for the disappearance of the metal overlayers on particles larger than 5 nm, we speculate that this might have to do with metal-support interactions. The corrugated shape of the relatively small nanoparticles may relate to the Rh-zirconia support interactions. When the particles become very large, the influence of these interactions with the support will be much smaller and the particles can attain shapes enclosed by surfaces with low surface free energies. Qualitatively, TEM images support this reasoning as the very large particles are clearly more faceted than the smaller ones.

Following this reasoning, we may then argue that the optimum in CO dissociation turnover frequency occurs

**Table 6.3:** Comparison of product selectivity between theory and experiment. The microkinetics simulations were conducted at  $T=800\text{K}$  and  $p=20\text{ atm}$ .

| Catalyst                           | Selectivity (%) |                        |                        |                       |                                   |                         |           |                           | Surface Coverage |               |
|------------------------------------|-----------------|------------------------|------------------------|-----------------------|-----------------------------------|-------------------------|-----------|---------------------------|------------------|---------------|
|                                    | $\text{CH}_4$   | $\text{C}_2\text{H}_4$ | $\text{CH}_3\text{OH}$ | $\text{CH}_2\text{O}$ | $\text{CH}_3\text{CH}_2\text{OH}$ | $\text{CH}_3\text{CHO}$ | Other Oxy | Total $\text{C}_{2+}$ Oxy | CO               | $\text{CH}_x$ |
| Rh(2, a750)/ZrO <sub>2</sub> (600) | 67              |                        | 2.8                    |                       | 17                                |                         |           | 21                        | 62               | 3.1           |
| Microkinetics Rh(211)              | 51.4            | 8.7                    | 0.0                    | 10.3                  | 16.2                              | 13.2                    | 10.3      | 29.4                      | 58.0             | 2.5           |
| Microkinetics Rh(111)              | 0.0             | 0.0                    | 0.0                    | 100                   | 0.0                               | 0.0                     | 100       | 0.0                       | 98.0             | 0.0           |

for the 4.7 nm Rh nanoparticles, because these particles contain the highest density of metal overlayers and, consequently, the highest density of step-edge sites. The strong correlation between the CO dissociation rate and the density of step-edge sites is supported by the preference for CO dissociation on step-edge sites ( $E_{\text{act}} = 167\text{ kJ/mol}$  for Rh(211)) as opposed to planar surfaces (e.g.  $300\text{ kJ/mol}$  for Rh(111) and  $205\text{ kJ/mol}$  for Rh(100)).<sup>41</sup>

Earlier in this thesis, the kinetics and mechanism of CO hydrogenation on the stepped Rh(211) surface has been explored by a combination of DFT calculations (chapter 4) and microkinetics simulations (chapter 5). A key step in the mechanism is the dissociation of adsorbed CO. Based on DFT-computed values, it was assumed that the rate of CO dissociation on the close-packed surface would be negligible. To confirm this,

we replaced the relatively low barrier for CO dissociation on Rh(211) of  $167\text{ kJ/mol}$  by the one computed for the Rh(111) surface, using the DFT values for all other reactions for the stepped surface. The model also included H-assisted CO dissociation on the Rh(111) surface, whose barrier of  $266\text{ kJ/mol}$ <sup>41</sup> is slightly more favorable than the value of  $300\text{ kJ/mol}$  without H-assistance. The resulting rates were four orders of magnitude lower than those predicted for the stepped surface.

Table 6.4 reports the product selectivities for 4.7 nm Rh nanoparticles on zirconia and results of microkinetics simulations carried out for the Rh(211) and Rh(111) surfaces at a temperature of  $800\text{ K}$ . This particular temperature was chosen, because the CO surface coverage was close to the CO coverage determined by SSITKA measurements. For the simulated Rh(111) data, formaldehyde

was the only product of CO conversion independent of the temperature. This is the consequence of the very high CO dissociation barrier. Qualitatively, the product distribution predicted by our Rh(211) microkinetics simulations agrees with the experimental data. In the simulations, formaldehyde is the main product because its hydrogenation on the stepped surface is difficult. In experiment, formaldehyde is rapidly hydrogenated, which is likely due to hydrogenation on terrace sites that more weakly interact with formaldehyde. Consistent with this, the simulated data also predict a higher acetaldehyde/ethanol ration than observed in experiment. The predicted selectivities for methane and higher hydrocarbons (in the simulations exclusively ethylene) are in very good agreement with the experimental data.

The microkinetics simulations described in chapter 5 showed that CO dissociation is not the rate-controlling step in CO hydrogenation for the stepped Rh(211) surface. This conclusion is not contradicted by the experimental observation that the TOF for CO dissociation scales with the number of step-edge sites. As the barrier for CO dissociation on other surfaces is very high, these sites will not contribute to the CO dissociation. Therefore, the rate of CO dissociation is

proportional to the number of step-edge sites.

Experimentally, it is observed that optimum C<sub>2</sub>-oxygenates selectivity occurs for 4.7 nm Rh nanoparticles. The SSITKA measurements show that these particles contain a higher surface coverage of CO and CH<sub>x</sub> surface intermediates. That the highest CO surface coverage is found for the particles with the highest density of step-edge sites is in line with the higher adsorption energy of CO on such sites than on terrace sites. The difference is about 30 kJ/mol. As CO dissociation is not controlling the overall rate of formation of methane nor ethanol, we predict that a change of the ratio of step-edge over planar surface sites will lead to changes in the CH<sub>x</sub> and CO coverage. The microkinetics simulations show that, under conditions that methane and ethanol are the main products, the most stable CH<sub>x</sub> surface intermediates are C and CH. As particles of intermediate size have relatively high CH<sub>x</sub> surface coverage, and also the highest CO surface coverage, we can understand that the relative rate of C+CO coupling, the elementary reaction steps that leads to C<sub>2</sub>-oxygenate), over that of CH<sub>x</sub> hydrogenation is highest. This will shift the product distribution to C<sub>2</sub>-oxygenates over that of methane, in line with the experimental data.

## 6.5. CONCLUSION

DFT calculations were carried out to predict  $N_2$  IR absorption spectra on Rh surfaces and clusters. On the basis of these calculations, the surface topology of zirconia-supported Rh nanoparticles could be predicted. It was shown that the smallest Rh nanoparticles mainly contain kink and edge sites. Particles of intermediate size expose steps and step-edges and large Rh nanoparticles predominantly contain low-index facets. The strong correlation between the catalytic performance at intermediate particle size and the high number of step-edge sites at this particle size then points out that step-edge sites are necessary for CO dissociation.

This reasoning is in line with the results from the SSITKA measurements as well as the microkinetics simulations.

The highest CO surface coverage found at maximum CO turnover rates is rationalized by the higher adsorption energy of CO on the Rh(211) surface than on Rh(111) terraces. As the  $CH_x$  coverage is relatively high as well, we reason that this leads to efficient C+CO coupling, that is a relevant step in the formation of higher oxygenates. From microkinetics simulations it is found that Rh(111) terraces cannot catalyze the formation of higher oxygenates due to the very high barrier for CO dissociation. These surfaces mainly produce the hydrogenated products of nondissociated CO. As only the step-edge sites are able to dissociate CO, the rate of CO dissociation has to scale with the number of these step-edge sites. ■

## 6.6 REFERENCES

- (1) Fischer, F.; Tropsch, H. *Brennst.-Chem* **1923**, *4*, 276.
- (2) Fischer, F.; Tropsch, H. *Brennst.-Chem* **1926**, *7*, 79.
- (3) Biloen, P.; Sachtler, W. M. H. In *Adv. Catal.*; D.D. Eley, H. P., Paul, B. W., Eds.; Academic Press: 1981; Vol. Volume 30, p 165.
- (4) Bowker, M. *Catal. Today* **1992**, *15*, 77.
- (5) Pilot, I. A. W.; van Santen, R. A.; Hensen, E. J. M. *Catal. Sci. Technol.* **2014**, *4*, 3129.
- (6) Pilot, I. A. W.; van Santen, R. A.; Hensen, E. J. M. *Angew. Chem. Int. Ed.* **2014**, DOI: 10.1002/anie.201406521.
- (7) Kellner, C. S.; Bell, A. T. J. *Catal.* **1981**, *70*, 418.
- (8) Kölbel, H.; Engelhardt, F. *Chem. Ing. Tech.* **1950**, *22*, 97.
- (9) Ligthart, D. A. J. M.; van Santen, R. A.; Hensen, E. J. M. *J. Catal.* **2011**, *280*, 206.
- (10) Ojeda, M.; Nabar, R.; Nilekar, A. U.; Ishikawa, A.; Mavrikakis, M.; Iglesia, E. *J. Catal.* **2010**, *272*, 287.
- (11) Ponec, V. *Catal. Rev.* **1978**, *18*, 151.

- (12) van Santen, R. A.; Ciobica, I. M.; van Steen, E.; Ghouri, M. M. In *Adv. Catal.*; Bruce, C. G., Helmut, K., Eds.; Academic Press: 2011; Vol. Volume 54, p 127.
- (13) Van Santen, R. A.; Markvoort, A. J.; Filot, I. A. W.; Ghouri, M. M.; Hensen, E. J. M. *Phys. Chem. Chem. Phys.* **2013**, *15*, 17038.
- (14) Quek, X.-Y.; Filot, I. A. W.; Pestman, R.; van Santen, R. A.; Petkov, V.; Hensen, E. J. M. *Chem. Commun.* **2014**.
- (15) Quek, X.-Y.; Pestman, R.; van Santen, R. A.; Hensen, E. J. M. *Catal. Sci. Technol.* **2014**, *4*, 3510.
- (16) Bezemer, G. L.; Bitter, J. H.; Kuipers, H. P. C. E.; Oosterbeek, H.; Holewijn, J. E.; Xu, X.; Kapteijn, F.; van Dillen, A. J.; de Jong, K. P. *J. Am. Chem. Soc.* **2006**, *128*, 3956.
- (17) den Breejen, J. P.; Radstake, P. B.; Bezemer, G. L.; Bitter, J. H.; Frøseth, V.; Holmen, A.; Jong, K. P. d. *J. Am. Chem. Soc.* **2009**, *131*, 7197.
- (18) Van Santen, R. A. *Acc. Chem. Res.* **2008**, *42*, 57.
- (19) Santen, R. A. v.; Neurock, M.; Shetty, S. G. *Chem. Rev.* **2009**, *110*, 2005.
- (20) Van Hardeveld, R.; Hartog, F. *Surf. Sci.* **1969**, *15*, 189.
- (21) van Hardeveld, R.; Hartog, F. In *Adv. Catal.*; D.D. Eley, H. P., Paul, B. W., Eds.; Academic Press: 1972; Vol. Volume 22, p 75.
- (22) Carballo, J. M. G.; Yang, J.; Holmen, A.; García-Rodríguez, S.; Rojas, S.; Ojeda, M.; Fierro, J. L. G. *J. Catal.* **2011**, *284*, 102.
- (23) Xiao, C. X.; Cai, Z.; Wang, T.; Kou, Y.; Yan, N. *Angew. Chem. Int. Ed.* **2008**, *47*, 746.
- (24) Quek, X.-Y.; Guan, Y.; van Santen, R. A.; Hensen, E. J. M. *ChemCatChem* **2011**, *3*, 1735.
- (25) Zambelli, T.; Wintterlin, J.; Trost, J.; Ertl, G. *Science* **1996**, *273*, 1688.
- (26) Díaz, C.; Vincent, J. K.; Krishnamohan, G. P.; Olsen, R. A.; Kroes, G. J.; Honkala, K.; Nørskov, J. K. *J. Chem. Phys.* **2006**, *125*.
- (27) van Hardeveld, R.; van Montfoort, A. *Surf. Sci.* **1966**, *4*, 396.
- (28) Strebel, C.; Murphy, S.; Nielsen, R. M.; Nielsen, J. H.; Chorkendorff, I. *Phys. Chem. Chem. Phys.* **2012**, *14*, 8005.
- (29) Van Hardeveld, R.; Van Montfoort, A. *Surf. Sci.* **1969**, *17*, 90.
- (30) Perdew, J. P.; Burke, K.; Ernzerhof, M. *Phys. Rev. Lett.* **1996**, *77*, 3865.
- (31) Kresse, G.; Furthmüller, J. *J. Comput. Mater. Sci.* **1996**, *6*, 15.
- (32) Kresse, G.; Hafner, J. *Phys. Rev. B* **1994**, *49*, 14251.
- (33) Kresse, G.; Joubert, J. *Phys. Rev. B* **1999**, *59*, 1758.
- (34) Grimme, S. *J. Comput. Chem.* **2006**, *27*, 1787.
- (35) Bućko, T. s.; Hafner, J. r.; Lebègue, S. b.; Ángyán, J. n. *G. J. Phys. Chem. A* **2010**, *114*, 11814.
- (36) Preuss, M.; Bechstedt, F. *Phys. Rev. B* **2006**, *73*, 155413.
- (37) van Dijk, H. A. J., Ph.D. thesis, Eindhoven University of Technology, 2001.
- (38) van Dijk, H. A. J.; Hoebink, J. H. B. J.; Schouten, J. C. *Top. Catal.* **2003**, *26*, 111.
- (39) Dewar, M. J. S. *Bull. Soc. Chim. Fr.* **1951**, *18*, C71.
- (40) Chatt, J.; Duncanson, L. A. *J. Chem. Soc.* **1953**, 2939.
- (41) Filot, I. A. W.; Shetty, S. G.; Hensen, E. J. M.; van Santen, R. A. *J. Phys. Chem. C* **2011**, *115*, 14204.



## Abstract

A comprehensive Density Functional Theory study of the Fischer-Tropsch mechanism on the corrugated Ru(11 $\bar{2}$ 1) surface has been carried out. Elementary reaction steps relevant to the carbide mechanism and the CO insertion mechanism are considered. Activation barriers and reaction energies were determined for CO dissociation, C hydrogenation, CH<sub>x</sub>+CH<sub>y</sub> and CH<sub>x</sub>+CO coupling, CH<sub>x</sub>CH<sub>y</sub>-O bond scission and hydrogenation reactions, which lead to formation of methane and higher hydrocarbons. Water formation that removes O from the surface was studied as well. The overall barrier for chain growth in the carbide mechanism (preferred path CH+CH coupling) is lower than that for chain growth in the CO insertion mechanism (preferred path C+CO coupling). Kinetic analysis predicts that the chain-growth probability for the carbide mechanism is close to unity, whereas within the CO insertion mechanism methane will be the main hydrocarbon product. The main chain propagating surface intermediate is CH via CH+CH and CH+CR coupling (R = alkyl). A more detailed electronic analysis shows that CH+CH coupling is more difficult than coupling reactions of the type CH+CR because of the  $\pi$ -donating effect of the alkyl substituent. These chain growth reaction steps are more facile on step-edge sites than on terrace sites. The carbide mechanism explains the formation of long hydrocarbon chains for stepped Ru surfaces in the Fischer-Tropsch reaction.

---

THIS CHAPTER HAS BEEN PUBLISHED AS:

Filot, I. A. W., van Santen, R. A., Hensen, E. J. M.,

*Catal. Sci. Technol.* 2014, 4, 3129-3140.



---

★ *Doing is a quantum leap from imagining.* ★

Barbera Sher

**QUANTUM  
CHEMISTRY OF  
THE FISCHER-  
TROPSCH  
REACTION  
CATALYZED  
BY A STEPPED  
RUTHENIUM  
SURFACE**



**7**

## 7.1 INTRODUCTION

The limited supply of readily available petroleum stimulates the search for alternative energy sources.<sup>1</sup> Due to its abundance, natural gas is increasingly considered as a valuable alternative feedstock for the synthesis of fuels and chemicals. Synthesis gas (a mixture of CO and H<sub>2</sub>), which can be obtained from natural gas by autothermal or steam reforming, can be used to produce long-chain hydrocarbons in the Fischer-Tropsch (FT) reaction.<sup>2-4</sup> Several mechanistic proposals for this chain-growth reaction have been reviewed elsewhere.<sup>5</sup> They can be distinguished by the assumption of the inserting species in the growing chain. The inserting species is either a CH<sub>x</sub> monomer derived from surface CO dissociation in the carbide mechanism or an intermediate with the C-O bond intact in the CO insertion mechanism. The carbide mechanism involves dissociation of adsorbed CO, hydrogenation of the carbon adatom to a CH<sub>x</sub> building block and its insertion into the growing hydrocarbon chains on the surface. The chain reaction is terminated by desorption of the hydrocarbon chain from the surface as an alkene or alkane. An alternative termination pathway involves CO insertion, that results in aldehyde and alcohol products. In the CO insertion mechanism, chain propagation proceeds via insertion of a CO moiety and

the C-O bond scission therefore occurs after C-C coupling. This is in contrast to the carbide mechanism, where C-O bond scission occurs prior to C-C coupling. Oxygen is predominantly removed from the surface as water.<sup>5-8</sup> The competing reaction is complete hydrogenation of the CH<sub>x</sub> surface intermediate to methane, which is an undesired by-product.

Good FT catalysts should exhibit high selectivity towards long-chain hydrocarbons<sup>4,9</sup> which requires facile CO dissociation and slow chain-growth termination.<sup>10,11</sup> Formation of methane, the undesired by-product of the FT reaction, should be minimized. The self-organization of monomeric C<sub>i</sub> species into growing chains can be seen as a simple polymerization process and the molecular weights of the hydrocarbon products tend to follow the Anderson-Schulz-Flory (ASF) distribution.<sup>12,13</sup> Experimentally, it is usually found that the C<sub>1</sub> and C<sub>2</sub> product selectivities deviate from the ASF distribution.<sup>12,14-20</sup>

Two important schools of thought exist about the nature of the catalytically active surface. On the one hand, it is assumed that the close-packed surfaces (terraces) are the active sites.<sup>21,22</sup> Although metal atoms with low coordination numbers are in principle more reactive, it has been argued that these more reactive

low-coordinated sites become blocked due to their strong interaction with the adsorbed species and, in particular, with carbon adatoms. On the other hand, the high reactivity of low-coordinated sites, especially for CO bond dissociation over stepped sites, is considered to be crucial to provide sufficient monomer building blocks to maintain a high rate of chain growth.<sup>11,23-26</sup>

The mechanism of CO dissociation on metallic surfaces has recently been elucidated. Experimental observations<sup>27,28</sup> and theoretical calculations<sup>24,29,30</sup> agree on the importance of ensembles of surface metal atoms arranged in such a way that a stepped site is obtained for facile CO dissociation. These sites are usually called  $B_5$  sites. On such stepped sites of Co and Ru surfaces, the direct dissociation of CO is favoured over the hydrogen-assisted alternative involving the formyl (CHO) intermediate.<sup>23,24,31,32</sup> Although the discovery of the Fischer-Tropsch reaction is almost a century ago, many open questions remain about the reactions that lead to chain growth and chain-growth termination.

A large number of candidate reaction steps have been proposed for chain growth relevant to carbide and CO insertion mechanisms. Originally, Fischer and Tropsch proposed that surface  $\text{CH}_2$  couples with surface  $\text{CH}_3$ .<sup>2,33</sup> Modern insights about surface reactivity and

theoretical chemistry advances now learn us that this proposal is incorrect, because the predicted barrier for this coupling step is very high<sup>30</sup> and, also, because the surface coverage of  $\text{CH}_2$  and  $\text{CH}_3$  is predicted to be low.<sup>34-36</sup> Hu and coworkers<sup>37</sup> have explored various coupling reactions for a range of transition metal surfaces using Density Functional Theory (DFT). Their analysis stresses the importance of the surface abundance of particular  $\text{CH}_x$  species and, also, indicates that stepped sites are preferred for C-C bond formation reactions for Ru surfaces, with  $\text{C}+\text{CH}$  and  $\text{CH}+\text{CH}$  coupling being the most favourable pathways. On Co surfaces, however,  $\text{CH}_2+\text{CH}_2$  coupling and  $\text{C}+\text{CH}_3$  coupling are more likely candidates for chain growth. Saeys and co-workers have studied the CO insertion pathway on flat  $\text{Co}(0001)$  surfaces.<sup>38,39</sup>  $\text{CH}_2+\text{CO}$  coupling was found to be the most favourable pathway.<sup>38</sup> The group of Maitlis has performed extensive studies on the mechanistic aspects employing a model system composed using a Co homogeneous catalyst.<sup>40-42</sup> They found that the  $\text{CH}_2$  insertion into a surface alkyl is the dominant mechanism. Water formation, which is required to remove O originating from CO dissociation, was also studied recently by DFT.<sup>43-46</sup> It is generally proposed that, following OH formation, formation of adsorbed water occurs more favourably through proton

migration between two hydroxyl adsorbates than via direct hydrogenation of the hydroxyl intermediate.

In the present theoretical study, we employed DFT to investigate all elementary reaction steps from syngas following the carbide as well as the CO insertion mechanism that lead to formation of ethylene and ethane on a stepped Ru(11 $\bar{2}$ 1) surface. These reactions include the already well-studied CO dissociation and CH<sub>4</sub> formation, because our aim is to build a database of kinetic parameters for all reaction steps relevant to the FT reaction at the same computational accuracy. We also study the hydrogenation of

the surface intermediates towards olefinic and paraffin products and include formation of water, which removes O atoms from the surface. We rationalize the experimentally observed lower C<sub>2</sub> selectivity in the ASF distribution by considering how the reactivity of C<sub>3</sub> surface intermediates will differ from that of C<sub>2</sub> intermediates. We explain the different kinetics of coupling reactions occurring on terraces and step-edge sites. Finally, we elaborate on the most likely FT pathway by comparing the different FT reaction routes comprising both the carbide and the CO insertion mechanism.

## 7.2 METHOD

Density Functional Theory (DFT) calculations were performed using the Vienna Ab Initio simulation package (VASP).<sup>47,48</sup> The Perdew-Burke-Ernzerhof (PBE) exchange-correlation functional was employed for all calculations.<sup>49</sup> To describe the interaction between nuclei and core electrons, the projector-augmented wave (PAW) method was used.<sup>50,51</sup> For the valence electrons a plane-wave basis set with an energy cut-off of 400 eV and a Brillouin zone sampling of 5x5x1 *k*-points were used. All elementary reactions were investigated on a stepped Ru(11 $\bar{2}$ 1) surface model (Figure 7.1). The model for the stepped site consists of a slab with a

thickness of at least 5 atomic layers and using a *p*(2x2) unit cell. To confirm that the thickness of the slab was sufficient, it was verified that the energy with respect to the number of layers in the slab was converged. The Ru(11 $\bar{2}$ 1) surface contains terrace and step-edge sites and is accordingly representative for a dual reaction centre mechanism as explored earlier.<sup>10</sup> In order to avoid spurious interactions between the images of the system, a vacuum layer of at least 10 Å was added along the *z*-axis. To confirm that the vacuum layer was large enough, it was verified that the electron density approached zero at the border of the unit cell. To avoid

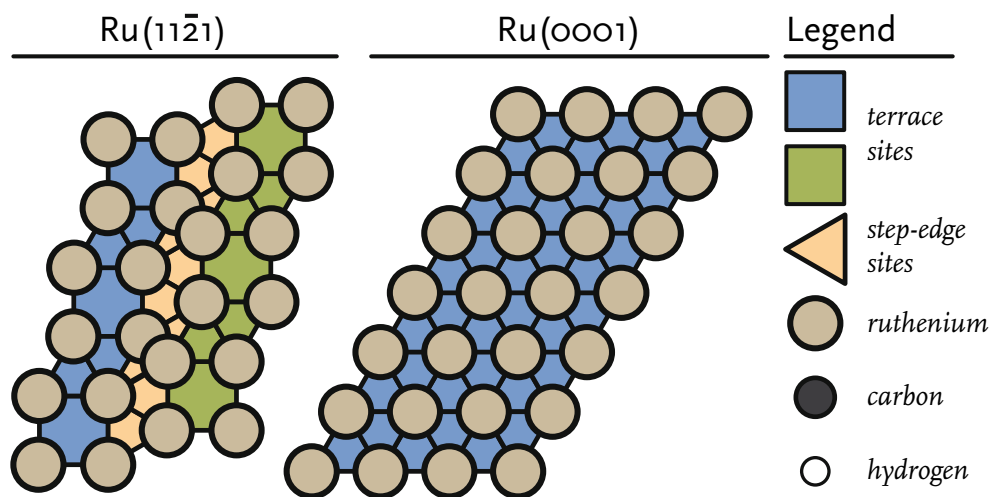


**Figure 7.1:** Schematic representation of (left) the corrugated Ru( $11\bar{2}1$ ) surface and (right) the close-packed Ru(0001) terrace surface.

dipole–dipole interactions between the super cells, adsorbates were placed on both sides of the surface retaining an inversion centre.

Ionic relaxation was carried out by the conjugate gradient method. During geometry optimization, all the degrees of freedom of the atoms in the slab as well as the adsorbed species were relaxed. To determine transition states, the nudged elastic band (NEB) method as developed by Jónsson *et al.* was employed.<sup>52</sup> The initial images between the optimized initial and final states were obtained via linear interpolation. The transition state was confirmed to be a saddle point on

the electronic energy surface by means of frequency analysis. Within VASP, this frequency analysis is performed by constructing a Hessian matrix using the finite difference approach. We only considered the frequencies of the adsorbed species within this analysis as the contribution of the metal atoms can be neglected. Prior to investigating the location and properties of the transition states, the structure and energetics of a large number of adsorption models of reactants, intermediates and products were determined. Based on these results, the initial guesses for the transition states were constructed.

**Table 7.1:** Methanation pathway of synthesis gas on Ru(11 $\bar{2}$ 1). The reported forward and reverse energies are in relation to the most stable states found for the reactants and products.

| Index | Elementary reaction                            | Forward E <sub>act</sub><br>(kJ/mol) | Backward E <sub>act</sub><br>(kJ/mol) |
|-------|--|--------------------------------------|---------------------------------------|
| 1     | CO* + * → C* + O*                              | 65                                   | 90                                    |
| 2     | C* + H* → CH* + *                              | 40                                   | 39                                    |
| 3     | CH* + H* → CH <sub>2</sub> * + *               | 75                                   | 37                                    |
| 4     | CH <sub>2</sub> * + H* → CH <sub>3</sub> * + * | 57                                   | 47                                    |
| 5     | CH <sub>3</sub> * + H* → CH <sub>4</sub> + 2*  | 94                                   | 57                                    |

## 7.3 RESULTS AND DISCUSSION

### 7.3.1 DFT CALCULATIONS

DFT calculations will be presented for the elementary reaction steps relevant to the carbide as well as the CO insertion mechanism of the Fischer-Tropsch reaction. The main groups of reactions studied are (i) CO dissociation, (ii) C hydrogenation to CH<sub>x</sub> intermediate and CH<sub>4</sub>, (iii) CH<sub>x</sub>-CH<sub>x</sub> coupling, (iv) CH<sub>x</sub>-CH<sub>x</sub> hydrogenation, (v) CH<sub>x</sub>-CO coupling, (vi) CH<sub>x</sub>CH<sub>y</sub>-O hydrogenation, (vii) CH<sub>x</sub>-CH<sub>y</sub>-O scission and (viii) O hydrogenation to H<sub>2</sub>O. For the carbide mechanism, reactions of groups (i), (ii), (iii), (iv) and (viii) are relevant. The CO insertion mechanism is covered by reaction of groups (i), (v), (vi), (vii) and (viii). We did not explore oxygen removal via CO<sub>2</sub> formation, because the CO<sub>2</sub> selectivity for Ru catalysts in the FT reaction is low.<sup>13,53,54</sup>

#### 7.3.1.1 CO DISSOCIATION

The energy barriers for CO dissociation are given in Table 7.1 and correspond well with values reported before for the stepped Ru(11 $\bar{2}$ 1) surface.<sup>23</sup> Direct dissociation of CO is the preferred route, because the hydrogen-assisted route involves the thermodynamically unfavourable formyl intermediate, resulting in a much higher overall barrier for CH formation.

#### 7.3.1.2 C HYDROGENATION TO CH<sub>4</sub>

Hydrogenation of adsorbed C to CH<sub>4</sub> has been investigated for the Ru(11 $\bar{2}$ 1) surface before.<sup>36</sup> Here, we carried out these calculations at the same computational accuracy as for the other elementary reaction steps. The forward and backward activation energies for the con-

**Table 7.2:** Methanation pathway of synthesis gas on Ru(11 $\bar{2}$ 1). The reported forward and reverse energies are in relation to the most stable states found for the reactants and products.

| Index | Elementary reaction                             | Forward $E_{act}$<br>(kJ/mol) | Backward $E_{act}$<br>(kJ/mol) |
|-------|---|-------------------------------|--------------------------------|
| 6     | $C^* + C^* \rightarrow CC^* + ^*$               | 138                           | 144                            |
| 7     | $C^* + CH^* \rightarrow CCH^* + ^*$             | 129                           | 75                             |
| 8     | $C^* + CH_2^* \rightarrow CCH_2^* + ^*$         | not found                     |                                |
| 9     | $C^* + CH_3^* \rightarrow CCH_3^* + ^*$         | 92                            | 116                            |
| 10a   | $CH^* + CH^* \rightarrow CHCH^* + ^*$ (terrace) | 149                           | 117                            |
| 10b   | $CH^* + CH^* \rightarrow CHCH^* + ^*$ (step)    | 86                            | 55                             |
| 11    | $CH^* + CH_2^* \rightarrow CHCH_2^* + ^*$       | not found                     |                                |
| 12    | $CH^* + CH_3^* \rightarrow CHCH_3^* + ^*$       | not found                     |                                |
| 13    | $CH_2^* + CH_2^* \rightarrow CH_2CH_2^* + ^*$   | 54                            | 60                             |
| 14    | $CH_2^* + CH_3^* \rightarrow CH_2CH_3^* + ^*$   | not investigated              |                                |
| 15    | $CH_3^* + CH_3^* \rightarrow CH_3CH_3^* + ^*$   | not investigated              |                                |

secutive hydrogenation steps of  $CH_x$  ( $x = 0-3$ ) to  $CH_y$  ( $y = 1-4$ ) are listed in Table 7.1.

The activation energies are with respect to the most stable adsorption site of the reacting surface adsorbates. In analogy with results for other transition metals, C hydrogenation to CH is relatively facile. For Ru(11 $\bar{2}$ 1), it is slightly endothermic. Further hydrogenation to  $CH_2$  (methylidene) is more difficult ( $E_{act} = 75$  kJ/mol) and endothermic by 38 kJ/mol. This implies that at reasonable reaction temperatures surface  $CH_2$  and its hydrogenation products are much less abundant than C and CH surface intermediates. The barrier for the endothermic  $CH_3$  (methyl) formation is 57 kJ/mol. The barrier for  $CH_4$  formation, which

involves a single elementary reaction step recombining  $CH_3$  and H over a single Ru atom, has the highest barrier among the  $CH_x$  hydrogenation steps (94 kJ/mol).

### 7.3.1.3 $CH_x + CH_y$ COUPLING REACTIONS

A total of 10 reactions between  $CH_x$  species were considered for carbon-carbon bond formation to describe chain growth in the carbide mechanism of the Fischer-Tropsch reaction (Table 7.2).

Reactions between  $CH_2$  and  $CH_3$  and between two  $CH_3$  (reactions 14 and 15) were not investigated, because it is well known that the interaction of the spatially extended C-H bonds in  $CH_3$  adsorbates

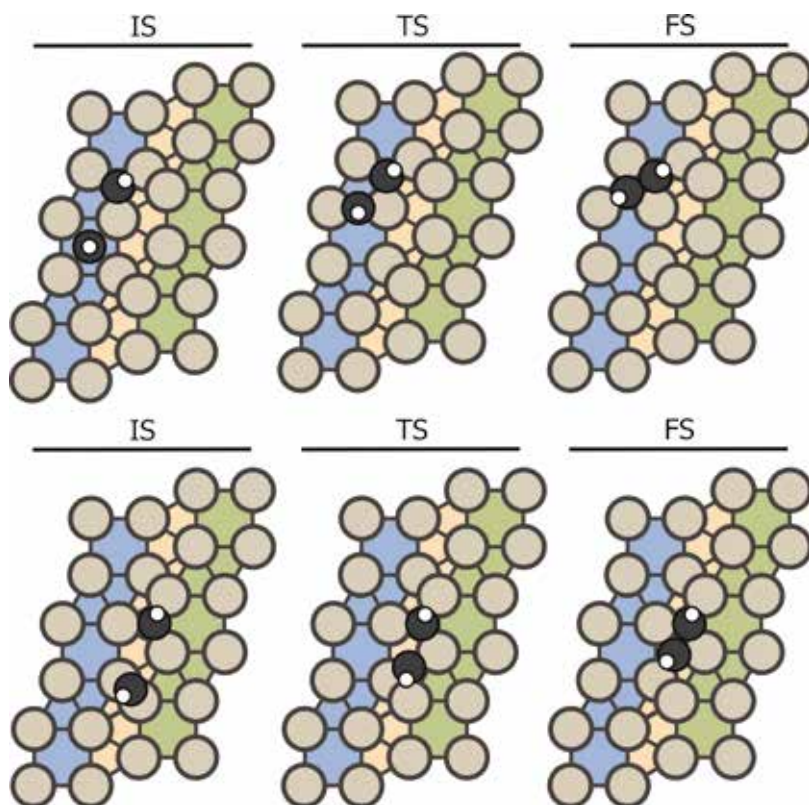


**Figure 7.2:** Schematic representation of the two CH+CH coupling pathways on the Ru(111) surface. The coupling of two CH moieties on (top) a terrace site and (bottom) a step-edge site. The black and white spheres represent carbon and hydrogen atoms, respectively.

results in repulsion, precluding C-C bond formation.<sup>55</sup> Despite considerable efforts, we could not identify transition states for the following reactions: C+CH<sub>2</sub>, CH+CH<sub>2</sub> and CH+CH<sub>3</sub> coupling. We assume that these reaction will not occur on the Ru(111) surface. It should be noted that these reactions have been reported to be feasible on terrace surfaces.<sup>56</sup> For the remaining five coupling steps C+C, C+CH, CH+CH, CH<sub>2</sub>+CH<sub>2</sub> and C+CH<sub>3</sub> coupling, we identified six unique transition states.

For the CH+CH coupling step, two different pathways were found (see Figure 7.2).

The analogous coupling reaction involving longer chains adsorbed on the surface are of the CH+CR type with R being an alkyl group. Therefore, we investigated this latter reaction step for R = CH<sub>3</sub> in more detail in Section 7.3.2. Table 7.2 shows that the barrier for CH+CH coupling is substantially lower on the step-edge site than on the terrace surface. This preference for coupling on

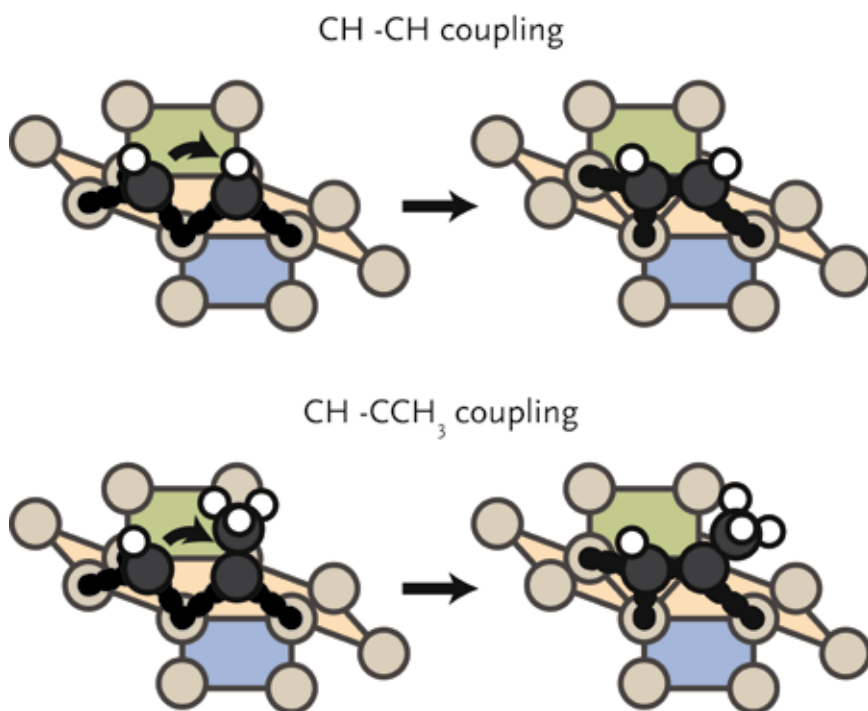


**Figure 7.3:** Schematic representation of hydrogenation of adsorbed acetylene to ethane.

the step-edge site is in accordance with several other works.<sup>37,57,58</sup> Based on this insight, we investigated the other coupling reactions (reactions 6, 7, 9 and 13) on the stepped surface as well. The most facile coupling reaction occurs between two methylidene species with a barrier of 54 kJ/mol (reaction 6). The barrier for the other coupling reactions are higher: 86 kJ/mol for CH+CH, 92 kJ/mol for C+CH<sub>3</sub>, 129 kJ/mol for C+CH and 138 kJ/mol for coupling of two carbon adatoms (C+C).

#### 7.3.1.4 CH<sub>x</sub>CH<sub>y</sub> HYDROGENATION REACTIONS

After formation of carbon-carbon bonds, higher hydrocarbons may leave the surface as olefins or paraffins (see Figure 7.3). We investigated such chain-growth termination steps for CH<sub>x</sub>-CH<sub>y</sub> species. From CCH, a large number of hydrogenation routes to ethylene and ethane needs to be considered. These possibilities and the results of a reaction energy analysis are given in Table 7.3.

Hydrogenation of CCH to CCH<sub>2</sub> (reaction 17) and CHCH to CHCH<sub>2</sub> (reaction 19) have very similar forward activation

**Table 7.3:** Hydrogenation reactions of  $C_2$  surface intermediates and their forward and backward activation energies for Ru(111̄1).

| Index | Elementary reaction                            | Forward $E_{act}$<br>(kJ/mol) | Backward $E_{act}$<br>(kJ/mol) |
|-------|--|-------------------------------|--------------------------------|
| 16    | $CC^* + H^* \rightarrow CCH^* + ^*$            | 104                           | 72                             |
| 17    | $CCH^* + H^* \rightarrow CCH_2^* + ^*$         | 82                            | 129                            |
| 18    | $CCH_2^* + H^* \rightarrow CCH_3^* + ^*$       | 19                            | 4                              |
| 19    | $CHCH^* + H^* \rightarrow CHCH_2^* + ^*$       | 83                            | 46                             |
| 20    | $CHCH_2^* + H^* \rightarrow CHCH_3^* + ^*$     | 62                            | 34                             |
| 21    | $CCH^* + H^* \rightarrow CHCH^* + ^*$          | 140                           | 162                            |
| 22    | $CCH_2^* + H^* \rightarrow CHCH_2^* + ^*$      | 82                            | 21                             |
| 23    | $CCH_3^* + H^* \rightarrow CHCH_3^* + ^*$      | 82                            | 8                              |
| 24    | $CHCH_2^* + H^* \rightarrow CH_2CH_2^* + ^*$   | 45                            | 42                             |
| 25    | $CHCH_3^* + H^* \rightarrow CH_2CH_3^* + ^*$   | 19                            | 23                             |
| 26    | $CH_2CH_2^* + H^* \rightarrow CH_2CH_3^* + ^*$ | 58                            | 34                             |
| 27    | $CH_2CH_3^* + H^* \rightarrow CH_3CH_3 + 2^*$  | 112                           | 71                             |

barriers around 82 kJ/mol. While  $CCH_2$  formation is exothermic,  $CHCH_2$  formation is endothermic. Subsequent hydrogenation to  $CCH_3$  (reaction 18) and  $CHCH_3$  (reaction 20) proceeds with barriers of 19 and 62 kJ/mol, respectively.

Comparatively, hydrogenation of CCH to CHCH and the reverse dehydrogenation of CHCH to CCH (reaction 21) are kinetically hindered with barriers of 140 and 162 kJ/mol, respectively. Hydrogenation of  $CCH_2$  to  $CHCH_2$  (reaction 22) and of  $CCH_3$  to  $CHCH_3$  (reaction 23) have barriers of 82 kJ/mol. The reverse dehydrogenation reactions are very facile with barriers of 21 and 8 kJ/mol, respectively. This implies that  $CCH_x$  intermediates

are significantly more stable than the corresponding  $CHCH_x$  intermediates. This difference draws similarity to the higher stability of adsorbed CH over  $CH_2$ . Finally, we consider reactions that lead to formation of ethylene (reaction 24) and ethane (reactions 25, 26 and 27). Whereas ethylene formation proceeds with an activation energy of 45 kJ/mol and is almost thermodynamically neutral, the hydrogenation of  $CHCH_3$  to  $CH_2CH_3$  and, finally,  $CH_3CH_3$  is endothermic. Although the first hydrogenation step to  $CH_2CH_3$  is facile and slightly exothermic, the second hydrogenation step toward ethane has to overcome a relatively high barrier of 112 kJ/mol. It is endothermic by 41 kJ/mol.

**Table 7.4:**  $CH_x+CO$  coupling reactions and their forward and backward activation energy.

| Index | Elementary reaction                      | Forward $E_{act}$<br>(kJ/mol) | Backward $E_{act}$<br>(kJ/mol) |
|-------|--|-------------------------------|--------------------------------|
| 28    | $C^* + CO^* \rightarrow CCO^* + *$       | 138                           | 61                             |
| 29    | $CH^* + CO^* \rightarrow CHCO^* + *$     | 148                           | 44                             |
| 30    | $CH_2^* + CO^* \rightarrow CH_2CO^* + *$ | 155                           | 36                             |
| 31    | $CH_3^* + CO^* \rightarrow CH_3CO^* + *$ | not investigated              |                                |

Alternatively, adsorbed ethylene can be further hydrogenated to  $CH_2CH_3$  (reaction 26). Although this reaction is facile with an activation barrier of 58 kJ/mol, the reverse reaction is more favourable with an activation energy of 34 kJ/mol.

### 7.3.1.5 $CH_x+CO$ COUPLING

Three different reactions between  $CH_x$  species and CO were considered for chain propagation in the CO insertion mechanism (Table 7.4). These reactions all involve the migration of adsorbed CO to a site adjacent to the  $CH_x$  adsorption site followed by C-C bond formation.

Both carbon atoms in the final coupled  $CH_x$ -CO species coordinate to surface Ru atoms. This strongly differs from mechanisms proposed based on homogeneous mononuclear coordination complexes for CO insertion or migration.<sup>59</sup>

The reaction between  $CH_3$  and CO (reaction 30) was not considered due to the expected steric repulsion. The most facile CO insertion reaction is the C+CO cou-

pling reaction (reaction 28) with a barrier of 138 kJ/mol. The barrier for CH+CO coupling (reaction 29) and  $CH_2+CO$  coupling (reaction 30) are somewhat higher at 148 kJ/mol and 155 kJ/mol, respectively. From comparison with the data in Table 7.2, it is immediately clear that the barriers for CO insertion are significantly higher than those for  $CH_x+CH_y$  coupling (Table 7.2). Moreover, all CO insertion reactions are strongly endothermic by at least 77 kJ/mol, implying that the rate constants for the reverse reactions are substantially higher.

### 7.3.1.6 $CH_x$ -CO HYDROGENATION

After CO insertion, the resulting  $CH_x$ -CO moiety can be hydrogenated to form a  $CH_xCH_yO$  species. We did not consider formation of oxygenated products that can leave the surface, because their yield is usually very low under practical FT conditions. For each  $CH_xCO^*$  intermediate, the hydrogenation of either carbon atom was considered. This results in five

**Table 7.5:** Hydrogenation reactions of  $\text{CH}_x\text{CO}$  surface intermediates and their forward and backward activation energies for  $\text{Ru}(\text{11}\bar{1}\bar{1})$ .

| Index | Elementary reaction   | Forward $E_{\text{act}}$<br>(kJ/mol) | Backward $E_{\text{act}}$<br>(kJ/mol) |
|-------|---|--------------------------------------|---------------------------------------|
| 32    | $\text{CCO}^* + \text{H}^* \rightarrow \text{CHCO}^* + *$                     | 104                                  | 77                                    |
| 33    | $\text{CCO}^* + \text{H}^* \rightarrow \text{CCHO}^* + *$                     | not found                            |                                       |
| 34    | $\text{CHCO}^* + \text{H}^* \rightarrow \text{CH}_2\text{CO}^* + *$           | 95                                   | 41                                    |
| 35    | $\text{CHCO}^* + \text{H}^* \rightarrow \text{CHCHO}^* + *$                   | 68                                   | 7                                     |
| 36    | $\text{CH}_2\text{CO}^* + \text{H}^* \rightarrow \text{CH}_2\text{CHO}^* + *$ | 63                                   | 4                                     |

**Table 7.6:**  $\text{CH}_x\text{CH}_y\text{-O}$  bond scission and their forward and backward activation energies.

| Index | Elementary reaction  | Forward $E_{\text{act}}$<br>(kJ/mol) | Backward $E_{\text{act}}$<br>(kJ/mol) |
|-------|--|--------------------------------------|---------------------------------------|
| 37    | $\text{CCO}^* + * \rightarrow \text{CC}^* + \text{O}^*$                | 52                                   | 127                                   |
| 38    | $\text{CHCO}^* + * \rightarrow \text{CCH}^* + \text{O}^*$              | 92                                   | 163                                   |
| 39    | $\text{CH}_2\text{CO}^* + * \rightarrow \text{CCH}_2^* + \text{O}^*$   | 77                                   | 248                                   |
| 40    | $\text{CHCHO}^* + * \rightarrow \text{CHCH}^* + \text{O}^*$            | 72                                   | 225                                   |
| 41    | $\text{CH}_2\text{CHO}^* + * \rightarrow \text{CHCH}_2^* + \text{O}^*$ | 65                                   | 234                                   |

different hydrogenation reactions (Table 7.5).

We could not identify a transition state for  $\text{CCO}^*$  hydrogenation (reaction 33). The orientation of the  $\text{CCO}^*$  moiety in the step-edge site prevents hydrogenation of the carbon atom of the CO group. The most difficult hydrogenation step is that of  $\text{CCO}^*$  to  $\text{CHCO}^*$  (reaction 32), which involves an activation energy of 104 kJ/mol. The other reactions, i.e. the hydrogenation of  $\text{CHCO}^*$  to  $\text{CH}_2\text{CO}$ , that of  $\text{CHCO}^*$  to  $\text{CHCHO}^*$  and finally the hydrogenation of  $\text{CH}_2\text{CO}^*$  to  $\text{CH}_2\text{CHO}^*$

proceed with lower activation energies of 95, 68 and 63 kJ/mol, respectively. All  $\text{CH}_x\text{CO}$  hydrogenation reactions are endothermic.

### 7.3.1.7 $\text{CH}_x\text{CH}_y\text{-O}$ BOND SCISSION

For chain growth to proceed, the C-O bond in the  $\text{CH}_x\text{CH}_y\text{O}$  surface intermediate must first cleave. Five such elementary reaction steps were considered for which results are listed in Table 7.6.

Among these reactions, it is most easy to cleave the C-O bond in  $\text{CCO}^*$  with

**Table 7.7:** Elementary reaction steps leading to removal of water including their forward and backward activation energies.

| Index | Elementary reaction   | Forward $E_{\text{act}}$<br>(kJ/mol) | Backward $E_{\text{act}}$<br>(kJ/mol) |
|-------|---|--------------------------------------|---------------------------------------|
| 42    | $\text{O}^* + \text{H}^* \rightarrow \text{OH}^* + *$                         | 97                                   | 49                                    |
| 43    | $\text{OH}^* + \text{H}^* \rightarrow \text{H}_2\text{O}^* + *$               | 89                                   | 15                                    |
| 44    | $\text{OH}^* + \text{OH}^* \rightarrow \text{H}_2\text{O}^* + \text{O}^* + *$ | 54                                   | 11                                    |

an activation energy of 52 kJ/mol. The C-O bond cleavage barriers for the other reactions are higher. All reactions are strongly exothermic, especially those for the partially hydrogenated fragments.

### 7.3.1.8 WATER FORMATION

In the FT reaction, the surface oxygen atoms deriving from CO dissociation are predominantly removed as water. Water formation can proceed via two mechanisms, both involving intermediate OH formation from O and H (reaction 42) followed by either direct hydrogenation of OH to  $\text{H}_2\text{O}$  (reaction 43) or via proton migration between two OH species to form  $\text{H}_2\text{O}$  and O (reaction 44). The first hydrogenation step to produce adsorbed OH has a relatively high barrier of 97 kJ/mol. The barrier for water formation via OH hydrogenation is 89 kJ/mol. Comparatively, the reaction between two hydroxyl groups is much more facile with a barrier of 54 kJ/mol. This suggests that water formation by reaction of two OH groups

to  $\text{H}_2\text{O}$  and adsorbed O is preferred.

### 7.3.2 ELECTRON DENSITY DIFFERENCE ANALYSIS

To understand the differences in activation energies of the various elementary reaction steps, we investigated electron density differences of selected reactions. Since the use of atomic charges is not preferred as it is difficult to assign electrons to a specific atom and chemical bonding typically involves contributions of several molecular orbitals, it is more instructive to map electron density differences in space. We focus here on three important issues relevant for the FT reaction. Firstly, we address the different reactivities of terrace and stepped sites. In particular, we focus on the coupling step with the lowest activation barrier, i.e. CH+CH coupling. Secondly, we will compare CH coupling with CH and  $\text{CCH}_3$  on stepped sites, because the latter reaction is relevant for formation of  $\text{C}_3$  products. Finally, we will highlight the different adsorption

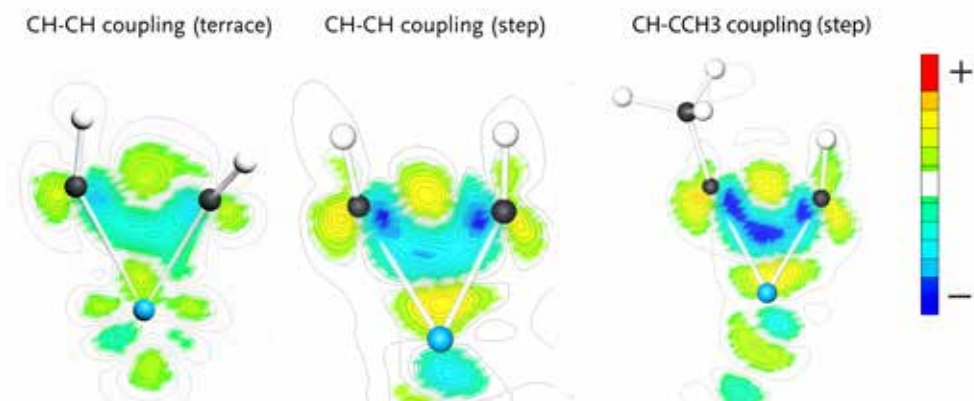


**Figure 7.4a:** Electron density difference plots of the transition state for CH+CH coupling on the terrace (left), step-edge (middle) and of CH+CCH<sub>3</sub> coupling on the step-edge (right) of the Ru(111) surface. These plots were generated by subtracting the electron density of the individual CH moieties on the surface from the electron density of the complex. Note that the electron density difference for the step-edge site is larger than for the terrace site.

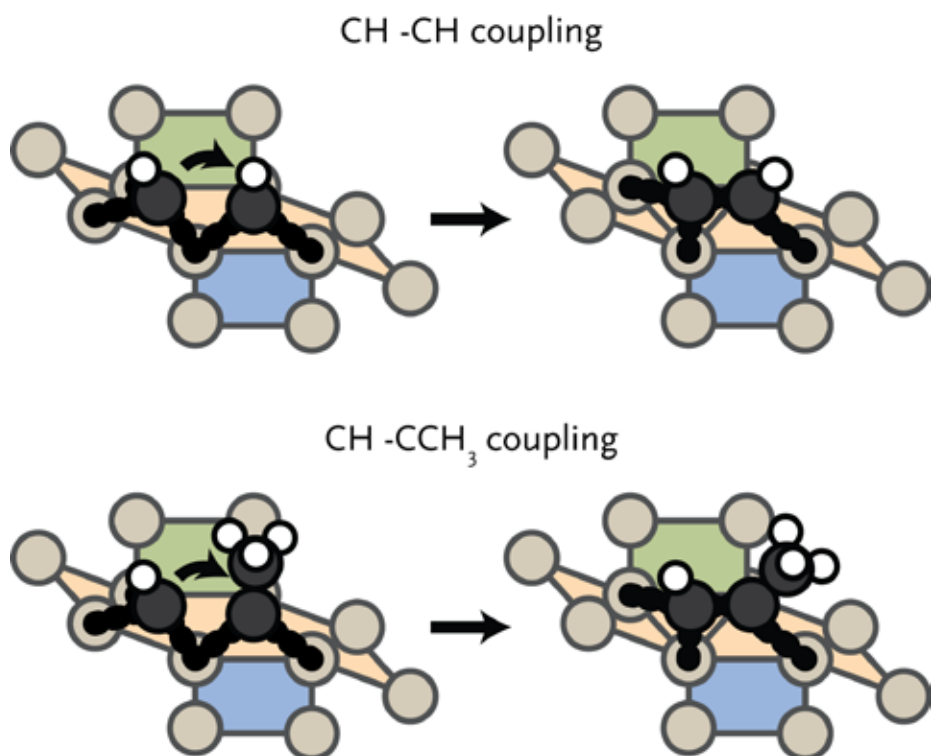


**Figure 7.4b:** Schematic representation of CH-CH and CH-CCH<sub>3</sub> coupling on a step-edge site of the Ru(111) surface. The initial and final state of reaction are displayed.

strengths of ethylene and propylene on stepped sites, which explains the lower than expected C<sub>2</sub> selectivity observed during the FT reaction.

### 7.3.2.1 CH+CH COUPLING

The barriers for CH+CH coupling on stepped and terrace sites of the Ru(111̄1) (Figure 7.2) are 86 and 149 kJ/mol, respectively. Figure 7.4a shows the electron density shifts that result from the formation of C-C bonds between two CH surface species in the corresponding transition state complexes. To determine these, the electron density distributions of the two separate CH fragments and the empty surface were subtracted from the electron density distribution of the transition state complex. It is seen that in the transition state for the stepped site the electron density between the two C atoms is lowered and shifts to the metal atom. The corresponding shift in electron density for the transition state formation on the terrace site is smaller. There are two reasons for this difference. Firstly, it relates to the specific geometry of the transition state complex on the stepped site, which results in increased overlap between the bonding C-C orbitals and the metal d-band. Secondly, the coordinative unsaturation of the surface metal atoms is higher for the stepped than for the terrace surface. The decrease in electron

density between the two CH fragments by electron donation to the metal center results in decreased Pauli repulsion and, accordingly, in lower activation energy for coupling.

### 7.3.2.2 CH+CH vs. CH+CCH<sub>3</sub> COUPLING

We found that methylidyne (CH) coupling to the CCH<sub>3</sub> surface intermediate (Figure 7.4b) proceeds with lower barrier than CH coupling to another CH species (65 vs. 86 kJ/mol). In Figure 7.4a, the electron density shifts for C-C bond formation are shown. It can be seen that in the transition state for CH+CCH<sub>3</sub> coupling more electron density is shifted from between the CH and CCH<sub>3</sub> species to the metal atom relative to the CH-CH case. This difference is caused by the σ-donating effect of the methyl group. Consequently, the Pauli repulsion between CH and CCH<sub>3</sub> is lower than between two CH fragments, explaining why the barrier for coupling of the former two fragments is lower.

### 7.3.2.4 ETHYLENE VS. PROPYLENE DESORPTION

Ethylene and propylene adsorb 'side-on' on a single Ru atom through interaction with their C=C double bonds. The adsorption energies of ethylene and

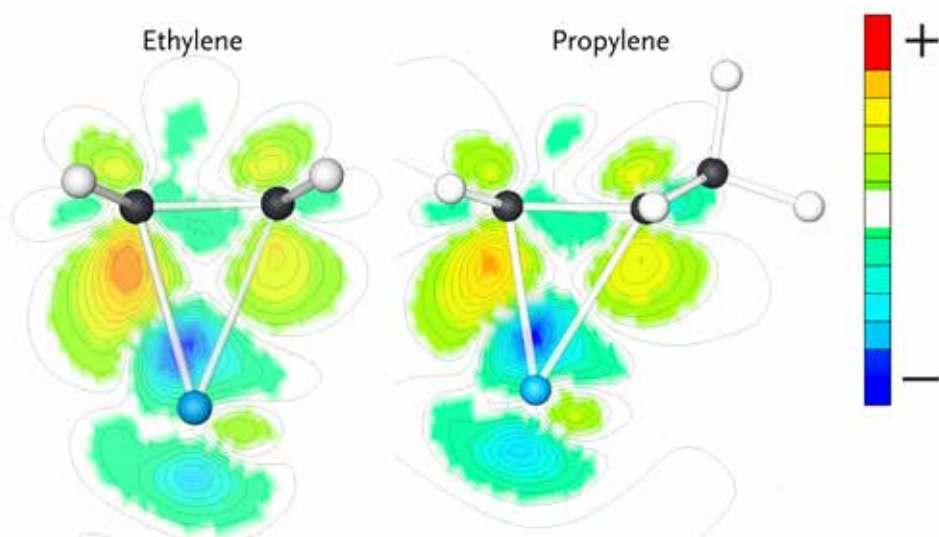


**Figure 7.5:** Electron density difference plots of the adsorbed states of ethylene (left) and propylene (right) on the  $Ru(11\bar{1}1)$  surface. These plots were generated by subtracting the electron density of the individual complexes in vacuum and empty surface from the electron density of the complex. Note that the electron density difference for ethylene is larger than for propylene.

propylene are 120 and 100 kJ/mol, respectively. The electron density shifts upon olefin adsorption are shown in Figure 7.5. Here, the electron density difference is determined by subtracting the electron density of the adsorbate in the geometry it has in the adsorbed state and the empty surface from the electron density of the surface-adsorbate complex. The difference in electron density for ethylene is larger than for propylene. The reason for the decreased electron density shift of the double bond in adsorbed propylene is the  $\pi$ -accepting nature of the  $CH_3$  substituent. This results in weaker adsorption of propylene as compared to ethylene. We

expect that the stronger interaction of ethylene will result in increased surface residence time of this fragment, which increases the probability of its chain growth relative to desorption and hydrogenation as compared with that of its higher carbon number analogues.

### 7.3.3 REACTION ENERGY DIAGRAMS

We constructed reaction energy diagrams based on the elementary reaction steps explored in the DFT study (Tables 7.2-7.6). Figure 7.6 shows the reaction energy diagram for formation of ethylene



and water from CO and H<sub>2</sub> in the carbide mechanism. For comparison, this diagram also contains the reaction pathway that leads to methane and water from synthesis gas. The ZPE (zero-point energy)-corrected overall reaction energies for ethylene and methane formation are -212 and -217 kJ/mol, respectively, which are close to thermodynamic data.

Figure 7.7 shows that the preferred pathway for formation of adsorbed CH<sub>2</sub>CH<sub>2</sub> involves CH+CH coupling followed by hydrogenation to CH<sub>2</sub>CH<sub>2</sub>. The C+CH coupling reaction is very unfavourable with a forward barrier of 129 kJ/mol. The overall barrier for C+CH<sub>3</sub> coupling is also unfavourable, because CH<sub>3</sub> formation is endothermic and the barrier for its coupling to C is also relatively high. Further reaction of CCH<sub>3</sub> to CH<sub>2</sub>CH<sub>2</sub> would involve the endothermic dehydrogenation to CCH<sub>2</sub>, followed by the endothermic hydrogenation to CHCH<sub>2</sub> ( $E_{\text{act}} = 61$  kJ/mol) and the nearly thermoneutral hydrogenation step to adsorbed CH<sub>2</sub>CH<sub>2</sub> with a barrier of 45 kJ/mol. Although coupling of two CH<sub>2</sub> fragments is facile, their formation is strongly endothermic. As C and CH are the most stable surface intermediates yet coupling reactions between C adsorbates are unfavourable, CH is predicted to be the dominant chain propagation surface intermediate. The desorption energy of adsorbed ethylene is 120 kJ/mol. The further hydrogenation of

ethylene to ethane is included in Figure 7.6. The most difficult step towards ethane formation is the hydrogenative desorption of CH<sub>2</sub>CH<sub>3</sub> to CH<sub>3</sub>CH<sub>3</sub> with an activation energy of 112 kJ/mol.

Figure 7.8 summarizes the pathways relevant to the CO insertion mechanism leading towards CHCH\* formation in a reaction energy diagram. Similar to the carbide mechanism, the growing chain is initiated from adsorbed C\*, which requires CO dissociation. The most favourable path involves C+CO coupling followed by CC formation and its hydrogenation to CHCH. As CH together with C are the most stable CH<sub>x</sub> surface intermediates, we also considered CH+CO coupling. The overall barrier to CCH\* formation via this route is higher because of the relatively low stability of the CHCO intermediate. This pathway is nevertheless relevant to the CO insertion mechanism, because only the first coupling (i.e., C<sub>2</sub> formation) can proceed via C+CO. Growth beyond C<sub>2</sub> surface species will proceed via CR+CO with R being an alkyl group, for which the barrier of the CH+CO coupling is a reasonable estimate. Although the barrier for CH<sub>2</sub>+CO coupling is only slightly higher than for the other considered coupling reactions, the lower surface stability of CH<sub>2</sub> vs. C and CH results in a substantially higher overall barrier towards the product without the O atom, namely CH<sub>2</sub>C. The

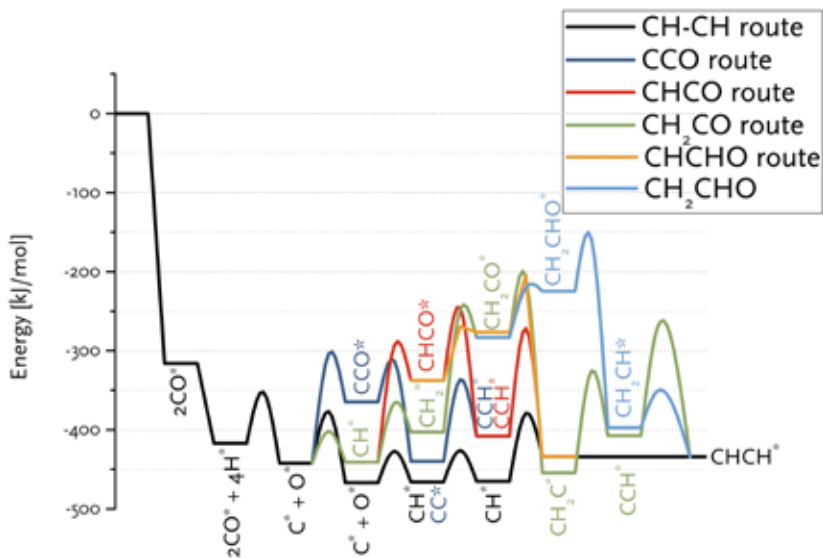


**Figure 7.8:** Reaction energy diagram for CHCH\* formation from CO and H<sub>2</sub>. The various routes in the CO insertion mechanism are compared to the CH-CH route in the carbide mechanism.

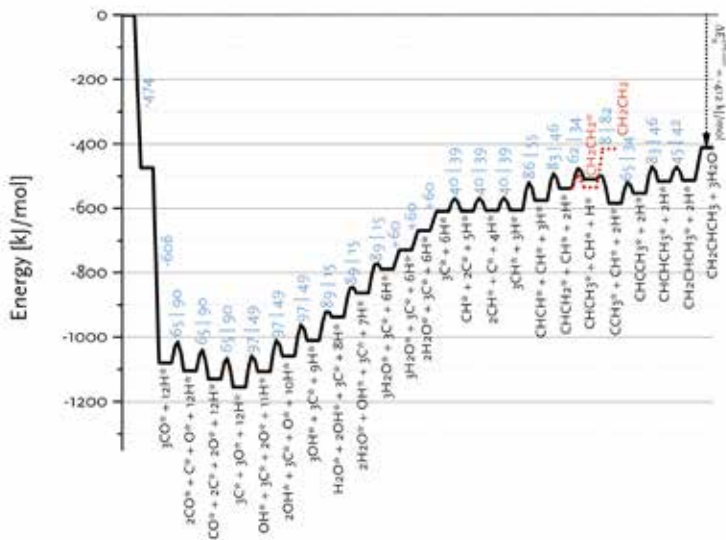


**Figure 7.9:** Reaction energy diagram for propylene from carbon monoxide and hydrogen. All data are for the Ru(11 $\bar{2}$ 1) surface.

alternative pathway via  $\text{CH}_2\text{CHO}$  is even less favourable.

Comparison of these paths with that of chain growth via  $\text{CH}+\text{CH}$  coupling (Figure 7.8) clearly shows that the overall barrier for  $\text{CHCH}$  formation via the carbide mechanism (63 kJ/mol) is substantially lower than the preferred pathway via  $\text{CO}$  insertion (138 kJ/mol). The  $\text{CO}$  insertion route is unfavourable because of the endothermicity of the  $\text{CH}_x+\text{CO}$  coupling (Table 7.4) as well as of subsequent  $\text{CH}_x\text{CO}$  hydrogenation reactions (Table 7.5).

Figure 7.9 shows the reaction energy diagram for propylene formation within the carbide mechanism. This diagram involves  $\text{CH}$  as the main inserting species in view of the low barrier for  $\text{CH}$  insertion into  $\text{CCH}_3$  species as compared to the most favourable  $\text{CH}+\text{CH}$  pathway for  $\text{C}_2$  formation. Figure 7.9 also shows that further growth of the  $\text{CHCH}_2$  surface intermediate is favoured over formation and desorption of ethylene. This already indicates that the computed kinetics are conducive to formation of long chain hydrocarbon products on this surface. Compared to the  $\text{C}_2$  case, there will be less competition between chain growth of a  $\text{C}_3$  intermediate and desorption of propylene, because the desorption energy of propylene is lower than that of ethylene. We expect that the adsorption energy of longer olefins will be very similar to that

of propylene. Qualitatively, the different balances between chain growth and product desorption for  $\text{C}_2$  and higher carbon number surface intermediates explains the experimentally observed  $\text{C}_2$  selectivity below that of the ASF distribution for the higher hydrocarbon products.<sup>12</sup>

### 7.3.4 CARBIDE VS. CO INSERTION MECHANISM

An important prerequisite for obtaining long hydrocarbon chains in the Fischer-Tropsch reaction is fast chain growth rate vs. chain-growth termination rate. This condition will lead to high values for the chain-growth probability  $\alpha$ , defined as

$$\alpha = \frac{\theta_i}{\theta_{i-1}} \quad (7.1)$$

where  $\theta_i$  is the concentration of growing hydrocarbon chains with length  $i$ .

We have earlier deduced explicit expressions for the chain-growth probability within the framework of lumped-sum kinetics for both the carbide and the  $\text{CO}$  insertion mechanism.<sup>25,26,60</sup> For the carbide mechanism, the expression is

$$\alpha_c = \frac{k_p \theta_{C_1}}{k_p \theta_{C_1} + k_t} \quad (7.2)$$

where  $\alpha_c$  is the chain-growth probability in the carbide mechanism,  $k_p$  the rate

**Table 7.8:** Rate constants computed at  $T = 220^\circ\text{C}$  for chain-propagation and –chain-growth termination for the most favourable routes in carbide and CO insertion mechanisms.

| Route                           | Mechanism    | chain propagation<br>[mol/s] | chain-growth<br>termination [mol/s] |
|---------------------------------|--------------|------------------------------|-------------------------------------|
| CHCH                            | Carbide      | $6.79 \cdot 10^2$            | $5.88 \cdot 10^{-4}$                |
| CCH <sub>3</sub>                | Carbide      | $4.51 \cdot 10^{-1}$         | $5.88 \cdot 10^{-4}$                |
| CH <sub>2</sub> CH <sub>2</sub> | Carbide      | $3.94 \cdot 10^{-2}$         | $5.88 \cdot 10^{-4}$                |
| CHCO                            | CO insertion | $1.74 \cdot 10^{-8}$         | $5.88 \cdot 10^{-4}$                |
| CHCHO                           | CO insertion | $1.00 \cdot 10^{-12}$        | $5.88 \cdot 10^{-4}$                |
| CH <sub>2</sub> CO              | CO insertion | $3.80 \cdot 10^{-13}$        | $5.88 \cdot 10^{-4}$                |
| CH <sub>2</sub> CHO             | CO insertion | $5.84 \cdot 10^{-17}$        | $5.88 \cdot 10^{-4}$                |

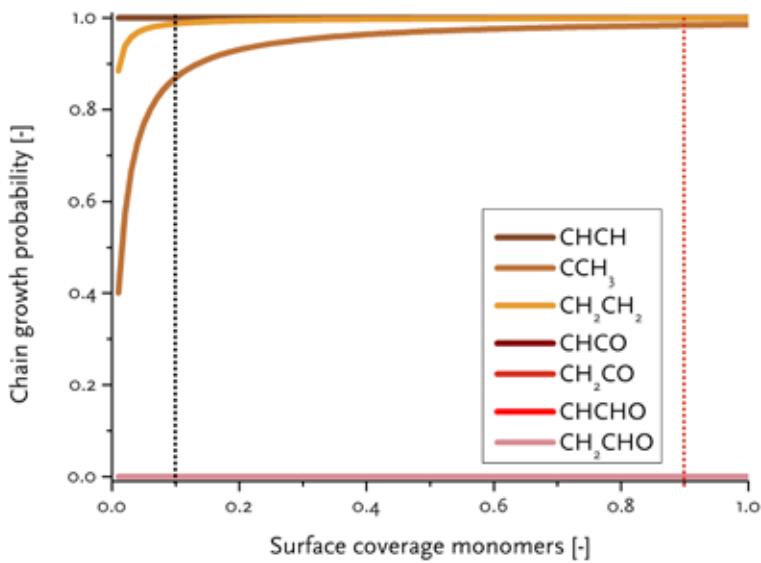


**Figure 7.10:** Computed chain-growth probability ( $\alpha$ ) as a function of the surface coverage of the chain propagating surface intermediate (CH in the carbide mechanism and CO in the CO insertion mechanism). The black and red dotted lines indicate typical respective  $C_1$  and CO coverage encountered under typical FT reaction conditions.

constant for  $\text{CH}_x+\text{CH}_y$  coupling,  $\theta_{\text{C}_1}$  the surface concentration of  $\text{C}_1$  monomers and  $k_t$  the rate for chain-growth termination. For the CO insertion mechanism, we have deduced the expression

$$\alpha_{\text{CO}} = \frac{k_p \theta_{\text{CO}}}{k_p \theta_{\text{CO}} + k_t} \quad (7.3)$$

where  $\alpha_{\text{CO}}$  is the chain-growth probability in the CO insertion mechanism and  $\theta_{\text{CO}}$  the surface concentration of CO. These formulas imply that a high  $\alpha$ -value is obtained when the rate constant for chain propagation ( $k_p$ ) is significantly higher than the rate constant for chain-growth termination ( $k_t$ ).

To determine the reaction rate constants for the chain growth steps in Eqs. 7.2 and 7.3, we determined the highest overall barrier along the reaction pathway with respect to the energy of the monomeric building block. These building blocks are surface CH and CO adsorbates, respectively, for the carbide and CO insertion mechanisms. The rate constants are listed in Table 7.8. Equations 7.2 and 7.3 show that the chain-growth probability

will also depend on the surface coverage of the chain propagating intermediate. To understand whether the proposed mechanisms can lead to desired Fischer-Tropsch products, we simply determined the chain-growth probability as a function of these surface coverages. The  $\text{C}_1$  coverage is reported to be below 10% under FTS conditions, whereas the CO surface coverage may be assumed to be 90% or higher.<sup>11,26,60</sup> Figure 7.10 shows that the chain-growth probability for the CO insertion mechanism is negligible irrespective of the CO coverage. This analysis implies that  $\text{CH}_x$  hydrogenation to methane is strongly preferred over chain propagation with CO as the building block. On the contrary, all three pathways with reasonable overall barrier for chain growth in the carbide mechanism, that is  $\text{CH}+\text{CH}$  coupling (96 kJ/mol),  $\text{CH}_2+\text{CH}_2$  coupling (126 kJ/mol) and  $\text{C}+\text{CH}_3$  coupling (136 kJ/mol) give greater than zero values for the chain-growth probability. At typical  $\text{C}_1$  coverage below 10%, the chain-growth probability is highest for the  $\text{CH}+\text{CH}$  coupling pathway.

## 7.4 CONCLUSIONS

DFT calculations were carried out for elementary reaction steps of carbide and CO insertion mechanisms relevant to the Fischer-Tropsch reaction on the stepped

$\text{Ru}(11\bar{1}1)$  surface. Activation barriers and reaction energies were determined for CO dissociation, C hydrogenation,  $\text{CH}_x+\text{CH}_y$  and  $\text{CH}_x+\text{CO}$  coupling, hydrogenation

reactions of the surface intermediates,  $\text{CH}_x\text{CH}_y\text{-O}$  bond scission and O hydrogenation, which lead to formation of methane, higher hydrocarbons including olefins and alkanes and water. The preferred path for propagation in the carbide mechanism is CH+CH coupling. Higher hydrocarbons are formed by CH insertion into a  $\text{CCH}_3$  (or  $\text{C}(\text{CH}_2)_n\text{CH}_3$  equivalents) intermediate, which is formed via a sequence of hydrogenation-dehydrogenation steps of adsorbed CHCH. Coupling reactions of the type CH+CCH<sub>3</sub> are more favorable than CH+CH coupling, which is attributed to the  $\sigma$ -donating effect of the alkyl substituent. CH+CH coupling is much more favorable on the stepped site of the Ru(11 $\bar{1}$ ) surface than on the terrace site. The difference originates from the stronger overlap of the forming  $\pi$ -bonds between the CH fragments with the partially empty d-orbitals of the more reactive metal surface atoms, resulting in decreased Pauli repulsion. The preferred

coupling pathway in the CO insertion mechanism involves the reaction between C and CO followed by facile C-O bond cleavage in CCO. All the  $\text{CH}_x\text{CO}$  intermediates are relatively unstable on the surface as compared to  $\text{CH}_x$  and CO, so that the overall barriers for chain-growth via CO-insertion are much higher than those via CH+CH coupling. The kinetic consequence of this difference is that high chain-growth rate constants are predicted for the carbide mechanism, whereas these are very low for the CO insertion mechanism. This kinetic analysis predicts methane to be the main product during CO hydrogenation within the CO insertion mechanism. With kinetic parameters computed for the carbide mechanism, high chain-growth probability is predicted. The carbide mechanism explains the formation of long hydrocarbon chains on the stepped Ru surface. ■

## 7.5 REFERENCES

- (1) Song, C. *Catal. Today* **2006**, *115*, 2.
- (2) Fischer, F.; Tropsch, H. *Brennst.-Chem* **1923**, *4*, 276.
- (3) Somorjai, G. A. *Introduction to Surface Chemistry and Catalysis*; Wiley: New York, 1994.
- (4) Anderson, R. B. *The Fischer-Tropsch Synthesis*; Academic Press: New York, 1984.
- (5) van Santen, R. A.; Ciobica, I. M.; van Steen, E.; Ghouri, M. M. In *Adv. Catal.*; Bruce, C. G., Helmut, K., Eds.; Academic Press: 2011; Vol. Volume 54, p 127.
- (6) Biloen, P.; Sachtler, W. M. H. In *Adv. Catal.*; D.D. Eley, H. P., Paul, B. W., Eds.; Academic Press: 1981; Vol. Volume 30, p 165.
- (7) Bell, A. T. *Catal. Rev.* **1981**, *23*, 203.

- (8) van Santen, R. A.; Ghouri, M. M.; Shetty, S.; Hensen, E. J. M. *Catal. Sci. Technol.* **2011**, *1*, 891.
- (9) Steynberg, A. P. In *Stud. Surf. Sci. Catal.*; André, S., Mark, D., Eds.; Elsevier: 2004; Vol. Volume 152, p 1.
- (10) Markvoort, A. J.; van Santen, R. A.; Hilbers, P. A. J.; Hensen, E. J. M. *Angew. Chem. Int. Ed.* **2012**, *9*, 9012.
- (11) van Santen, R. A.; Markvoort, A. J.; Ghouri, M. M.; Hilbers, P. A. J.; Hensen, E. J. M. *J. Phys. Chem. C* **2013**, *117*, 4488.
- (12) Van Der Laan, G. P.; Beenackers, A. A. C. M. *Catal. Rev.* **1999**, *41*, 255.
- (13) Claeys, M.; van Steen, E. In *Stud. Surf. Sci. Catal.*; André, S., Mark, D., Eds.; Elsevier: 2004; Vol. Volume 152, p 601.
- (14) Novak, S.; Madon, R. J.; Suhl, H. J. *Catal.* **1982**, *77*, 141.
- (15) Iglesia, E.; Reyes, S. C.; Madon, R. J.; Soled, S. L. In *Adv. Catal.*; D.D. Eley, H. P., Paul, B. W., Eds.; Academic Press: 1993; Vol. Volume 39, p 221.
- (16) Kuipers, E. W.; Vinkenburg, I. H.; Oosterbeek, H. J. *Catal.* **1995**, *152*, 137.
- (17) Kuipers, E. W.; Scheper, C.; Wilson, J. H.; Vinkenburg, I. H.; Oosterbeek, H. J. *Catal.* **1996**, *158*, 288.
- (18) Wojciechowski, B. W. *Catal. Rev.* **1988**, *30*, 629.
- (19) Abbot, J.; Wojciechowski, B. W. *Can. J. Chem. Eng.* **1988**, *66*, 817.
- (20) Sarup, B.; Wojciechowski, B. W. *Can. J. Chem. Eng.* **1989**, *67*, 620.
- (21) Ojeda, M.; Nabar, R.; Nilekar, A. U.; Ishikawa, A.; Mavrikakis, M.; Iglesia, E. *J. Catal.* **2010**, *272*, 287.
- (22) Loveless, B. T.; Buda, C.; Neurock, M.; Iglesia, E. J. *Am. Chem. Soc.* **2013**, *135*, 6107.
- (23) Shetty, S.; van Santen, R. A. *Catal. Today* **2011**, *171*, 168.
- (24) Shetty, S. G.; Jansen, A. P. J.; van Santen, R. A. J. *Phys. Chem. C* **2008**, *112*, 14027.
- (25) Van Santen, R. A.; Markvoort, A. J.; Filot, I. A. W.; Ghouri, M. M.; Hensen, E. J. M. *Phys. Chem. Chem. Phys.* **2013**, *15*, 17038.
- (26) van Santen, R. A.; Markvoort, A. J. *ChemCatChem* **2013**, *5*, 3384.
- (27) Zubkov, T.; Morgan Jr, G. A.; Yates Jr, J. T. *Chem. Phys. Lett.* **2002**, *362*, 181.
- (28) Mavrikakis, M.; Bäumer, M.; Freund, H. J.; Nørskov, J. K. *Catal. Lett.* **2002**, *81*, 153.
- (29) Hammer, B.; Nørskov, J. K. In *Adv. Catal.*; Bruce C. Gates, H. K., Ed.; Academic Press: 2000; Vol. Volume 45, p 71.
- (30) Liu, Z.-P.; Hu, P. *J. Am. Chem. Soc.* **2002**, *124*, 11568.
- (31) Ciobica, I. M.; van Santen, R. A. J. *Phys. Chem. B* **2003**, *107*, 3808.
- (32) Shetty, S.; Jansen, A. P. J.; van Santen, R. A. J. *Am. Chem. Soc.* **2009**, *131*, 12874.
- (33) Fischer, F.; Tropsch, H. *Brennst.-Chem* **1926**, *7*, 79.
- (34) Gong, X.-Q.; Raval, R.; Hu, P. *J. Chem. Phys.* **2005**, *122*, 024711.
- (35) Ciobica, I. M.; Frechard, F.; van Santen, R. A.; Kleyn, A. W.; Hafner, J. J. *Phys. Chem. B* **2000**, *104*, 3364.
- (36) Shetty, S. G.; Jansen, A. P. J.; van Santen, R. A. J. *Phys. Chem. C* **2010**, *114*, 22630.
- (37) Cheng, J.; Hu, P.; Ellis, P.; French, S.; Kelly, G.; Lok, M. C. J. *Phys. Chem. C* **2008**, *112*, 6082.
- (38) Zhuo, M.; Tan, K. F.; Borgna, A.; Saeys, M. J. *Phys. Chem. C* **2009**, *113*, 8357.
- (39) Zhuo, M.; Borgna, A.; Saeys, M. J. *Catal.* **2013**, *297*, 217.
- (40) Maitlis, P. M.; Long, H. C.; Quyoum, R.; Turner, M. L.; Wang, Z.-Q. *Chem. Commun.* **1996**, *1*.

- (41) Quyoum, R.; Berdini, V.; Turner, M. L.; Long, H. C.; Maitlis, P. M. J. *Catal.* **1998**, *173*, 355.
- (42) Turner, M. L.; Marsih, N.; Mann, B. E.; Quyoum, R.; Long, H. C.; Maitlis, P. M. J. *Am. Chem. Soc.* **2002**, *124*, 10456.
- (43) Gong, X.-Q.; Raval, R.; Hu, P. *Surf. Sci.* **2004**, *562*, 247.
- (44) Gong, X.-Q.; Raval, R.; Hu, P. *Mol. Phys.* **2004**, *102*, 993.
- (45) Michaelides, A.; Alavi, A.; King, D. A. *J. Am. Chem. Soc.* **2003**, *125*, 2746.
- (46) Zhu, T. W.; van Grootel, P. W.; Filot, I. A. W.; Sun, S. G.; van Santen, R. A.; Hensen, E. J. M. *J. Catal.* **2013**, *297*, 227.
- (47) Kresse, G.; Furthmüller, J. *J. Comput. Mater. Sci.* **1996**, *6*, 15.
- (48) Kresse, G.; Hafner, J. *Phys. Rev. B* **1994**, *49*, 14251.
- (49) Perdew, J. P.; Burke, K.; Ernzerhof, M. *Phys. Rev. Lett.* **1996**, *77*, 3865.
- (50) Blöchl, P. E. *Phys. Rev. B* **1994**, *50*, 17953.
- (51) Kresse, G.; Joubert, J. *Phys. Rev. B* **1999**, *59*, 1758.
- (52) Henkelman, G.; Jónsson, H. *J. Chem. Phys.* **2000**, *113*, 9978.
- (53) Lunde, P. J.; Kester, F. L. *Ind. Eng. Chem. Process Des. Dev.* **1974**, *13*, 27.
- (54) Pendyala, V.; Shafer, W.; Davis, B. *Catal. Lett.* **2013**, *143*, 895.
- (55) Zheng, C.; Apeloig, Y.; Hoffmann, R. *J. Am. Chem. Soc.* **1988**, *110*, 749.
- (56) Chen, Z.-X.; Aleksandrov, H. A.; Basaran, D.; Rösch, N. *J. Phys. Chem. C* **2010**, *114*, 17683.
- (57) Chen, J.; Liu, Z.-P. *J. Am. Chem. Soc.* **2008**, *130*, 7929.
- (58) Cheng, J.; Gong, X.-Q.; Hu, P.; Lok, C. M.; Ellis, P.; French, S. *J. Catal.* **2008**, *254*, 285.
- (59) van Leeuwen, P. W. N. M. In *Homogeneous Catalysis*; Springer Netherlands: 2004, p 125.
- (60) van Santen, R. A.; Ghouri, M.; Hensen, E. M. J. *Phys. Chem. Chem. Phys.* **2014**, *16*, 10041.

## Abstract

Microkinetics simulations are presented based on DFT-determined elementary reaction steps of the Fischer-Tropsch (FT) reaction. Long-chain hydrocarbon formation occurs on stepped Ru surfaces with CH as the inserting monomer, whereas planar Ru only produces methane due to slow CO activation. By varying surface reactivity descriptors three reactivity regimes are identified with rates being controlled by CO dissociation, chain-growth termination or water removal. Predicted surface coverages are dominated by CO, C or O, respectively. Optimum FT performance occurs at the interphase of CO dissociation and chain-growth termination limited regimes. Current FT catalysts are suboptimal limited by CO activation and/or O removal.

---

THIS CHAPTER HAS BEEN PUBLISHED AS:

Pilot, I.A.W., van Santen, R.A., Hensen, E.J.M., 2014,  
*Angew. Chem. Int. Ed.*, 53, (47), 12746-12750



---

★ *For the record: Quantum mechanics does not deny the existence of objective reality. Nor does it imply that mere thoughts can change external events. Effects still require causes, so if you want to change the universe, you need to act on it.*★

Lawrence M. Krauss

# THE OPTIMALLY PERFORMING FISCHER- TROPSCH CATALYST



# 8

## 8.1 INTRODUCTION

The Fischer-Tropsch (FT) process that converts synthesis gas into longer hydrocarbons has become the subject of an intensive research effort driven by the increasing value of liquid energy carriers compared to the ample supply of natural gas.<sup>1,2</sup> The heterogeneous Fischer-Tropsch reaction is mechanistically complex. Unravelling the relation between the surface chemical reactions and the composition of the adsorbed layer poses a great challenge. The mechanism essentially combines a polymerization type surface reaction, that produces mainly linear hydrocarbons with the in-situ generation of monomers containing a single C atom. Many uncertainties exist on the nature of the reaction intermediates and hence also on the relative rates of the elementary reaction steps.

Advances in computational catalysis enable detailed studies of surface reactions at the molecular level, generating important new and comprehensive information about the relation between the relative stability of surface intermediates and their rate of formation and conversion as function of catalyst composition and structure.

With respect to the important question of selectivity of the FT reaction, according to one school of thought small particles are not reactive since strongly

adsorbed CO inhibits chain growth<sup>3-6</sup>, according to others step-edge sites are required that are not stable on small particles.<sup>7-9</sup> This explains the observation that selectivity to methane strongly increases and CO consumption rate decreases for smaller transition metal nanoparticles.<sup>8,10</sup> Microkinetics simulations based on computed molecular reactivity data provide a unique opportunity to resolve such debates. Rate controlling steps can be deduced<sup>11,12</sup> and hence one can identify the nature of particular relevant surface intermediates at reaction conditions.

The present microkinetics simulation make use of DFT quantum-chemical data of the elementary reaction rates of the many reaction intermediates proposed in FT-catalysis.<sup>1,2,13-24</sup> Few of such complete studies exist that not only consider methane formation<sup>25,26</sup> but also include formation of longer hydrocarbon chains. Earlier microkinetics studies using approximate molecular reactivity data are available.<sup>9,27-32</sup> Data for the Ru(11 $\bar{2}$ 1) surface will be compared with predictions for the Ru(0001) surface. The DFT results have been discussed elsewhere.<sup>33</sup>

The stepped Ru(11 $\bar{2}$ 1) surface is chosen because its reactive centers have a low barrier for CO activation and bind reaction intermediates strongly.<sup>34-36</sup> Because the metal-carbon interaction energy is

relatively strong, we expect it to have a low rate of methane formation compared to production of longer hydrocarbons. Comparison with the dense Ru(0001) surface is made, because this surface has a high barrier for CO activation and therefore can be expected to have high selectivity to methane. These expectations are amongst others based on our previous work with approximate and sometimes estimated values of reaction intermediate data.<sup>9,27-29</sup>

The microkinetics simulation data on the Ru(11 $\bar{2}$ 1) surface will show that under the condition of optimum C<sub>20+</sub> yield, the reaction rate is controlled by the rate of water formation. This causes the CO consumption rate to be slow with the surface predominantly covered by O atoms. We

## 8.2 METHOD

Our model, which takes into account both the carbide as well as the CO insertion mechanism<sup>45</sup>, is defined in detail in chapter 7. All elementary reactions steps, i.e. direct and hydrogen activated CO dissociation, CH<sub>x</sub> hydrogenation, CH<sub>x</sub>-CH<sub>y</sub> coupling, CH<sub>x</sub>-CO coupling, CH<sub>x</sub>C-O bond scission as well as hydrocarbon chain desorption as olefins and paraf-

have extended these results to other catalyst material reactivity regimes by varying the computed reaction intermediate reactivity parameters using scaling rules<sup>37</sup> relating the stability of surface species with adsorption energies of atomic C and O as reactivity performance parameters. By using in addition Brønsted-Evans-Polanyi (BEP) relations<sup>38-43</sup> we have constructed a two-dimensional volcano plot<sup>22,44</sup> of CO consumption rate, selectivity and other relevant kinetic parameters. Three different reactivity regimes can be identified, i.e. previously proposed<sup>27-29</sup> monomer formation and chain-growth termination limited regimes as well as a regime where oxygen removal is limiting. The CO consumption rate maximum is located in between these regimes.

ins are taken into account. To partially account also for the lateral interactions, the CO adsorption energy is taken as a function of the surface coverage. Microkinetics simulations have been conducted as well. Details about the microkinetics implementation can be found in chapter 2 and chapter 5.

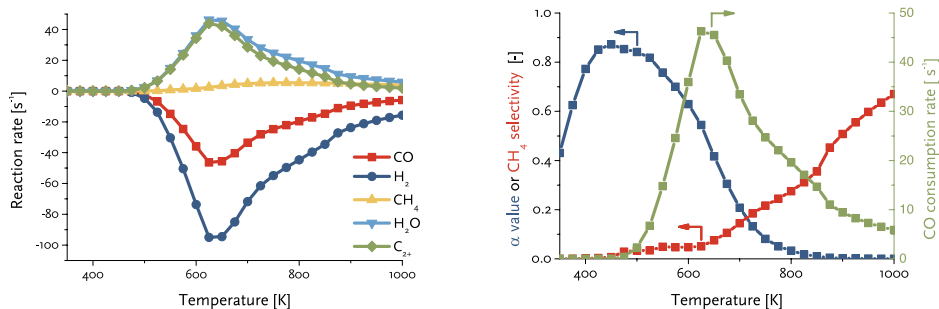


**Figure 8.1:** Microkinetics simulations for the Ru(111) surface ( $p = 20 \text{ atm}$ ;  $\text{H}_2/\text{CO} = 2$ ): (left panel) FT CO consumption rate (green), chain-growth probability (blue) and methane selectivity (red); (right panel) CO (red) and  $\text{H}_2$  (dark blue) consumption rates (negative) and  $\text{CH}_4$  (yellow),  $\text{H}_2\text{O}$  (light blue) and  $\text{C}_{2+}$  (green) production rates (positive) as a function of temperature.

## 8.3 RESULTS AND DISCUSSION

Figure 8.1 shows the predicted FT catalytic performance as a function of reaction temperature at a  $\text{H}_2/\text{CO}$  ratio of 2 and a total pressure of 20 atm. Consumption rates of CO and  $\text{H}_2$  and production rates of methane, higher hydrocarbons and water are given in Figure 8.1 (left). The chain-growth probability  $\alpha$  and the methane selectivity as a function of the reaction temperature are shown in Figure 8.1 (right). The CO consumption rate ( $r_{\text{CO}}$ ) goes through a maximum with temperature. At relatively low temperatures, predominantly higher hydrocarbons are formed with very little methane. With increasing temperature the yield of methane increases and it becomes the dominant product at higher temperatures. The maximum in  $\text{C}_{2+}$  production rate around

600 K is below that of maximum methane product rate ( $\sim 675 \text{ K}$ ). The chain-growth probability in Figure 8.1b also goes through a maximum around 475 K. At lower temperatures, the chain-growth probability decreases because of the low rate of CO dissociation, resulting in low surface coverage with  $\text{C}_1$  building blocks (surface coverages as function of temperature are shown in Figure 8.2 (right)). The decrease of the chain-growth probability goes together with a strong increase of the methane selectivity. The decreasing chain-growth probability at higher temperatures is the consequence of the low coverage with  $\text{C}_1$  building blocks on the surface.

Predicted  $\text{C}_1$  and  $\text{C}_2$  selectivities deviate from the Anderson-Schulz-Flory

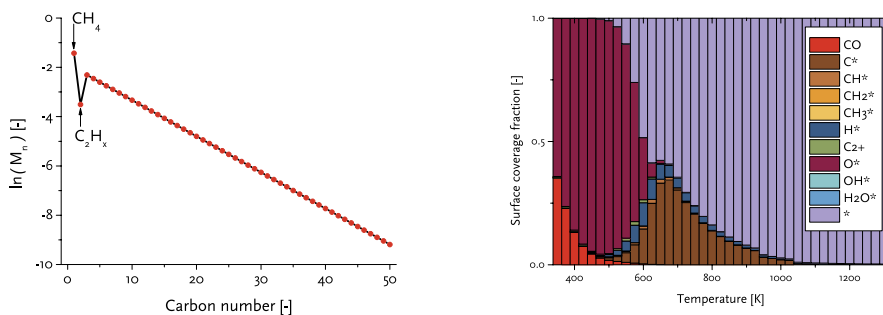


**Figure 8.2:** (left) Hydrocarbon product selectivity at a temperature of 500 K. The chain growth probability for hydrocarbons with more than two carbon atoms under these conditions is 0.83. Note the deviations of the C<sub>1</sub> and C<sub>2</sub> from the Anderson-Schulz-Flory distribution. (right) : Steady-state surface coverage as a function of the reaction temperature for the Ru(11 $\bar{1}$ 1) surface ( $p = 20$  bar; H<sub>2</sub>/CO = 2).

(ASF) distribution in line with experiment (Figure 2 (left)). The lower C<sub>2</sub> selectivity is due to stronger binding and easier chain growth of ethylene compared to higher olefins.<sup>33</sup> The low CH<sub>4</sub> selectivity on this surface is consistent with the lower overall barrier for chain growth compared to the overall barrier for methane formation. Only at high temperature CH<sub>4</sub> formation is preferred.

To elucidate the salient details of the FT reaction for the Ru(11 $\bar{1}$ 1) surface, the reaction path from CO and H<sub>2</sub> to hydrocarbons and water products was analyzed in detail in a calculated reaction intermediate flow scheme at the level of the elementary reaction steps (Figure 8.3). This analysis was performed at T = 500 K, as we found that at this particular temperature the selectivity toward C<sub>20+</sub> hydrocarbons was maximum (see Figure

8.4). In industrial practice, formation of long-chain hydrocarbons with minimum CH<sub>4</sub> formation is the preferred condition. Figure 8.4 indicates the relative participation of intermediates in particular reaction steps. As CO conversion to longer hydrocarbons proceeds exclusively by insertion of CH<sub>x</sub> intermediates, we omitted CO insertion pathways. The rate of CO insertion is very low because of the high barrier of CO insertion as previously discussed.<sup>33</sup> The reaction path analysis shows the importance of CH as the main inserting surface intermediate. The main chain-growth pathway involves insertion of CH into adsorbed CR (R = H or alkyl) growing chains. The resulting surface intermediate CHCR is then hydrogenated to CHCHR. It turns out to be preferred to first dehydrogenate the  $\alpha$ -C atom of this fragment before hydrogenating the  $\beta$ -CH

group, so that the reaction sequence is  $\text{CHCHR}^* + * \rightarrow \text{CCHR}^* + \text{H}^*$  and  $\text{CCHR}^* + \text{H}^* \rightarrow \text{CCH}_2\text{R}^* + *$ . The latter species is represented in Figure 8.3 by CR. This sequence represents the main chain-growth mechanism. The predominance of chain growth according to the carbide mechanism<sup>45</sup> with CH is in line with predictions of Cheng et al.<sup>24</sup>

The resulting CR species can undergo two hydrogenation reactions of the  $\alpha$ -C atom and one dehydrogenation reaction of the  $\beta$ - $\text{CH}_2\text{R}$  group to produce the adsorbed olefin  $\text{CH}_2\text{CHR}^*$ . This  $\text{CH}_2\text{CHR}^*$  intermediate can either desorb from the surface as the 1-olefin or undergo another dehydrogenation of the  $\alpha$ -C atom to form  $\text{CHCHR}^*$ , which is an intermediate in the chain propagation route. The high chain-growth probability at intermediate temperature stems from the higher rate of dehydrogenation compared to desorption. Oxygen removal through water formation predominantly proceeds via proton migration between two hydroxyl groups.

To underpin the importance of the stepped surface for facile CO dissociation, we carried out additional calculations for the less reactive dense Ru(0001) surface. We used data from literature for CO dissociation on this surface.<sup>46,47</sup> Because of the high direct CO dissociation barrier ( $>200$  kJ/mol)<sup>36,47</sup> the route via formyl (overall barrier 146 kJ/mol)<sup>47</sup> dominates.

To model the FT reaction for Ru(0001) we employed for all other elementary reactions kinetic data determined for the Ru(11 $\bar{2}$ 1) surface. Under conditions that predict good FT performance for Ru(11 $\bar{2}$ 1) the planar Ru(0001) surface only produces methane. Besides difficult CO dissociation, this is also due to more facile methane formation from adsorbed C on Ru(0001) (21 kJ/mol) compared with Ru(11 $\bar{2}$ 1) (86 kJ/mol). The CO consumption rate is much lower than for the stepped surface.

Optimal catalytic performance conditions were then analyzed by evaluating the consequences of variations in the activation energies of the elementary reaction steps. These can be related to the interaction energies of the transition metal surface with C and O adatoms using BEP and scaling law principles.<sup>37,38</sup> Relevant to the discussion below, we exemplify this by the dependence of the activation barrier for CO dissociation on the metal-C ( $\Delta E_C$ ) and -O ( $\Delta E_O$ ) bond strength via

$$\Delta(\Delta E_a^{\text{CO}}) = \alpha(\Delta E_C + \Delta E_O) \quad (8.1)$$

Figure 8.5 shows the CO consumption rate as function of these interaction energies. Microkinetics simulations were performed at  $T = 500$  K,  $p = 20$  atm and  $\text{H}_2/\text{CO} = 2$ , because it represents the important case that wax production is maximized. The CO consumption rate

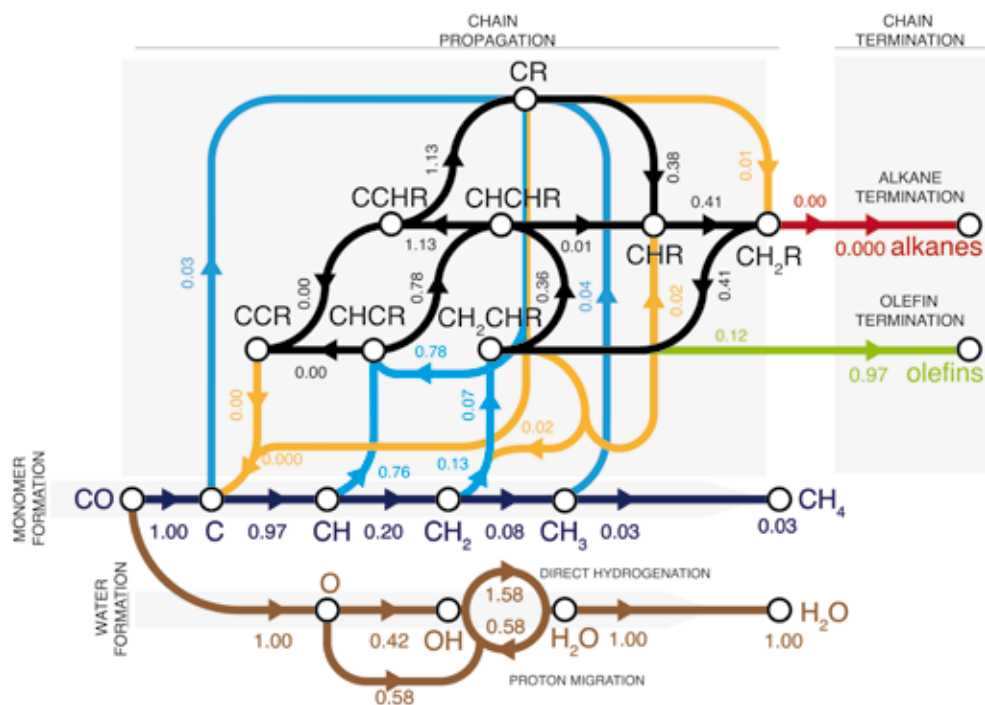


**Figure 8.3:** Reaction path analysis for the FT reaction on  $Ru(11\bar{1}1)$  ( $T = 500\text{ K}$ ;  $p = 20\text{ bar}$ ;  $H_2/CO = 2$ ). The nodes represent reactants, surface intermediates and products, the lines between them the elementary reaction steps and the numbers molar rates.

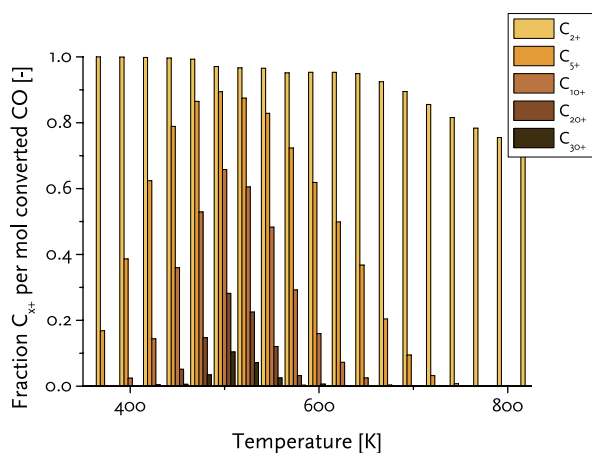


**Figure 8.4:** Fraction of  $C_{x+}$  hydrocarbons as a function of temperature. At  $T = 500\text{ K}$  the optimum selectivity toward  $C_{20+}$  chains is found.

strongly depends on the adatom bond strengths and exhibits a Volcano-type behavior. The predicted rate for the Ru(11 $\bar{2}$ 1) surface is close to the optimum.

Three distinct regimes can be distinguished in Figure 8.5 on the basis of differences in the rate-controlling step for the overall FT reaction. These regimes will be discussed below. To facilitate the discussion, Figure 8.5 also contains contour plots for the most important kinetic parameters for the FT reaction as function of  $\Delta E_c$  and  $\Delta E_o$ .

In regime I, the CO consumption rate is controlled by the rate of CO dissociation. The reaction order with respect to CO is positive in this regime. The H<sub>2</sub> reaction order is slightly negative, because increasing H coverage lowers the CO dissociation rate. The apparent activation energy is close to the activation energy for CO dissociation. It can be seen that decreasing reactivity of the metal surface (going to the top right hand corner of the contour plots) will result in lower chain-growth probability  $\alpha$ . A low reactive metal such as Ni combines low rate of CO dissociation with facile CH<sub>4</sub> formation.<sup>48-50</sup> With increasing metal reactivity the chain-growth probability strongly increases. In regime I, the FT reaction proceeds in the monomer-formation limit, as earlier discussed by us in a lumped kinetics analysis.<sup>28</sup>

In regime II, the rate is limited by the

rates of chain growth and chain-growth termination (chain-growth termination limit)<sup>28</sup>. Under these conditions the surface is nearly fully covered with C and CH intermediates. Consistent with this, a degree of rate control ( $\chi_{DRC}$ ) analysis (Figure 8.6) reveals that the two reaction steps with the greatest  $\chi_{DRC}$  are hydrogenation of CHCR ( $\chi_{DRC} = 0.7$ ) and desorption of olefins ( $\chi_{DRC} = 0.3$ ). The most difficult step is CHCR hydrogenation to CHCHR, which is an essential step in the chain-growth mechanism, i.e. in the formation of CCH<sub>2</sub>R, the intermediate into which the next CH building block can insert. The slightly positive CO reaction order in this regime stems from the inhibiting effect of the C-CR decoupling step ( $\chi_{DRC} = -0.5$ ), which requires free sites. With increasing CO partial pressure, the fraction of free sites decreases and, accordingly, also the rate of decoupling decreases. This increases the overall CO consumption rate. The H<sub>2</sub> reaction order is strongly positive, because chain growth requires several hydrogenation steps. Typically, the apparent activation energies in this regime are small or can even take negative values. The apparent activation energy is negative when with increasing temperature vacancies are created due to product desorption. The increased vacancy concentration increases the C-CR decoupling rate, which lowers the overall CO consumption rate. Figure 8.5 shows

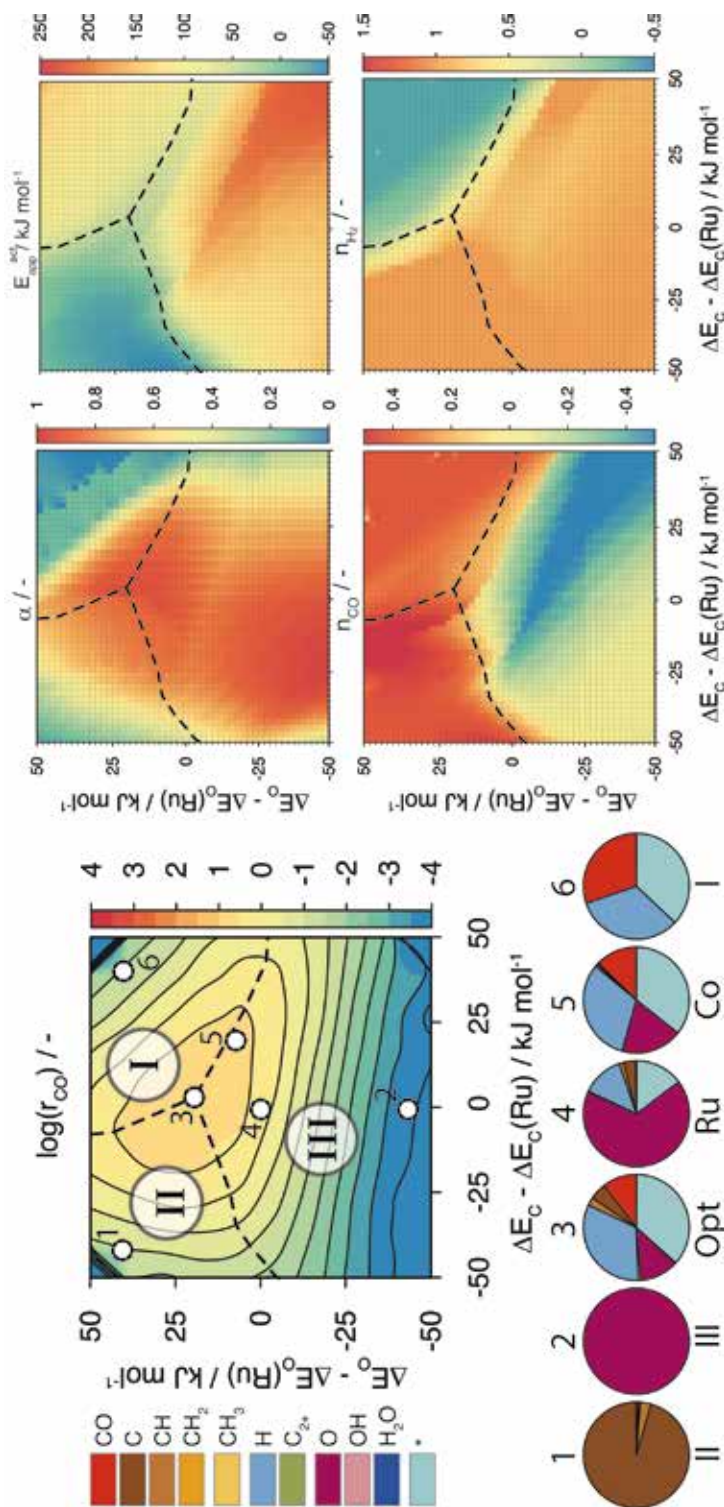


**Figure 8.5:** (left) CO consumption rate and steady-state surface coverages (the numbers in the graph refer to the numbers above the pie charts) as a function of the metal-carbon and metal-oxygen bond strength ( $T = 500$  K;  $p = 20$  bar;  $H_2/CO = 2$ ). The activation barriers for all elementary reaction steps were scaled to the metal-carbon and metal-oxygen bond strengths. Three regimes are distinguished based on the nature of the rate-controlling step, i.e. CO dissociation (regime I), chain growth and chain-growth termination (regime II) and water formation (regime III). The positions of Ru and Co metals are indicated on the basis of their metal-carbon and metal-oxygen bond strengths; (right) simulated kinetic parameters for the FT reaction ( $T = 500$  K;  $p = 20$  bar;  $H_2/CO = 2$ ) as a function of  $\Delta E_C$  and  $\Delta E_O$  relative to the respective values for Ru(11 $\bar{2}$ ): (left-top) the chain-growth probability, (right-top) the apparent activation energy (kJ/mol), (left-bottom) reaction order with respect to CO and (right-bottom) reaction order with respect to  $H_2$ .

that chain-growth probability strongly decreases with increasing  $\Delta E_C$ , which leads to high activation barriers for the hydrogenation reactions. Whereas methane formation requires hydrogenation of one C atom, chain growth also involves hydrogenation of the growing chain next to C hydrogenation to CH for insertion. Consequently, methane formation will become preferred over chain growth at high metal-C interaction energy.

Regime III is representative for surfaces to which oxygen binds strongly. Then water removal can become the rate-controlling step. Candidate rate-controlling elementary reaction steps are OH hydrogenation to  $H_2O$  and proton migration between two OH species to form O and  $H_2O$ . This is consistent with O being the most abundant surface intermediate. High  $\Delta E_O$  implies that the barrier for CO dissociation is low. Consequently, the CO reaction order is negative. For relatively low  $\Delta E_C$  the apparent activation energy is very high because the O atom needs to be removed from the surface. When the metal-C interaction energy increases the surface adsorbed layer will contain an increasing amount of C and CH intermediates as well as growing chains instead of O. This results in an increase of the CO consumption rate, the chain-growth probability and a decrease of the apparent activation energy. For high  $\Delta E_C$  the CO consumption rate and the chain-growth

probability decrease again, because C hydrogenation becomes difficult.

The maximum CO consumption rate at  $T = 500$  K and  $p = 20$  atm is obtained for  $\Delta E_C = 2.1$  and  $\Delta E_O = 20.2$  kJ/mol. Consistent with the Sabatier principle,<sup>38,45</sup> this maximum is the result of the competition of several competing elementary reaction steps. In this case, OH hydrogenation ( $\chi_{DRC} = 0.47$ ), CO dissociation ( $\chi_{DRC} = 0.19$ ),  $CH_2 + CHR$  coupling ( $\chi_{DRC} = 0.12$ ), C+CR coupling ( $\chi_{DRC} = 0.078$ ) and CHCHR hydrogenation ( $\chi_{DRC} = 0.045$ ) determine the The maximum CO consumption rate at  $T = 500$  K and  $p = 20$  atm is obtained for  $\Delta E_C = 2.1$  and  $\Delta E_O = 20.2$  kJ/mol. Consistent with the Sabatier principle,<sup>38,45</sup> this maximum is the result of the competition of several competing elementary reaction steps. In this case, OH hydrogenation ( $\chi_{DRC} = 0.47$ ), CO dissociation ( $\chi_{DRC} = 0.19$ ),  $CH_2 + CHR$  coupling ( $\chi_{DRC} = 0.12$ ), C+CR coupling ( $\chi_{DRC} = 0.078$ ) and CHCHR hydrogenation ( $\chi_{DRC} = 0.045$ ) determine the CO consumption rate maximum. The surface coverages at this optimum are  $\theta_{CO} \approx 0.11$ ,  $\theta_O \approx 0.12$ ,  $\theta_H \approx 0.33$ ,  $\theta_C \approx 0.05$ ,  $\theta_{CH} \approx 0.02$ ,  $\theta_{C_2+} \approx 0.01$  and  $\theta^* \approx 0.37$ . The CO and  $H_2$  reaction orders are 0.30 and 0.66, respectively, and the apparent activation energy is 37 kJ/mol. The chain-growth probability is high at 0.92. The reaction order in CO is higher than typically found in experiment, whereas the apparent activation

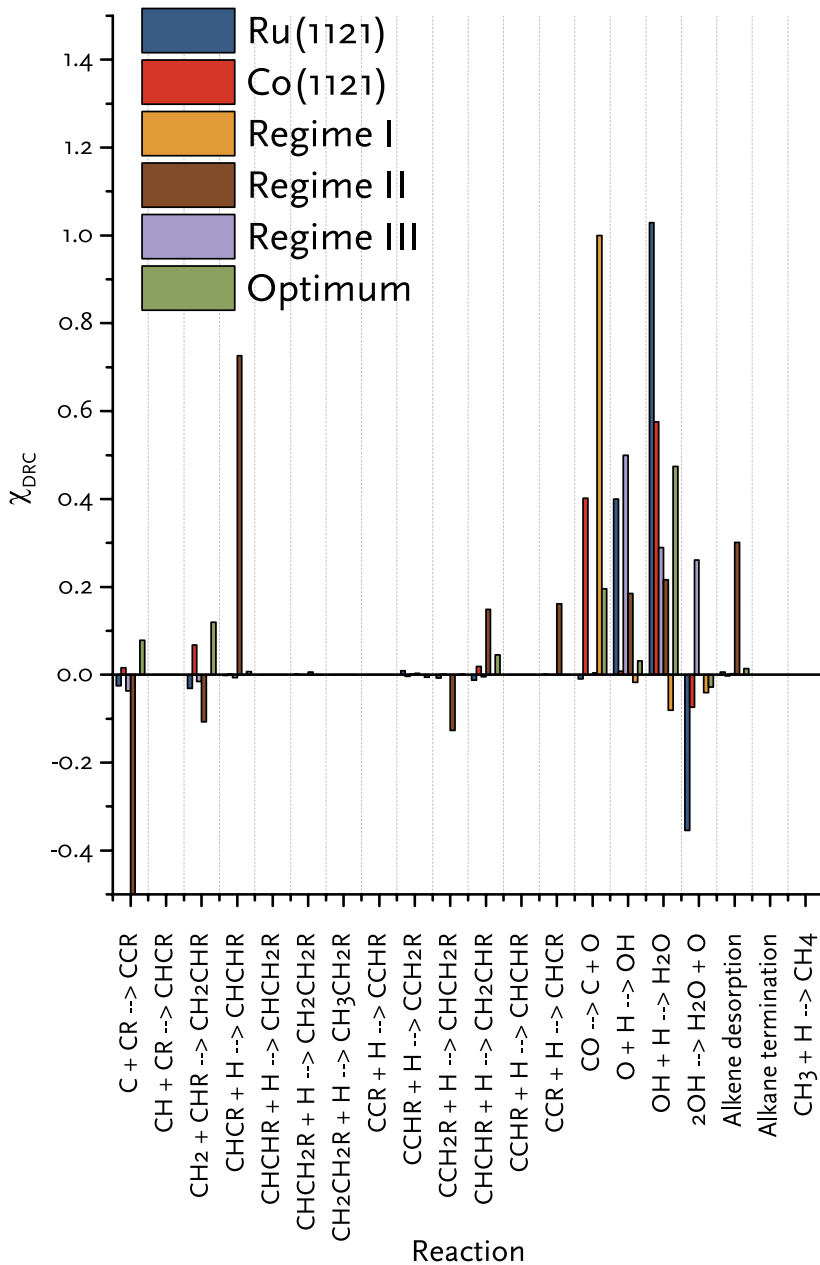


**Figure 8.6:** Sensitivity analysis of the three kinetic regimes as well as for optimum CO consumption rate ( $T = 500$  K;  $p = 20$  bar;  $H_2/CO = 2$ )

energy is lower.<sup>17,51-53</sup> This indicates that FT synthesis using Ru or Co catalysts is not conducted at optimum performance potential. Although the simulated catalyst optimum depends on the chosen pa-

## 8.4 CONCLUSION

By comparing the simulated reaction orders and activation energies with experimental data<sup>17,51-55</sup>, we deduce that current FT catalysts operate somewhere between regimes I and II. The FT reaction on Ru metal proceeds in the chain-growth limit with a surface partially poisoned by O adatoms, whereas on Co surfaces the reaction occurs in the monomer-formation limit. In this case, CO dissociation is controlling the rate, consistent with the general assumption in kinetic studies for the Co-catalyzed FT reaction.<sup>15,17,18,52</sup> Another important aspect of our findings is that in these regimes the coordinative unsaturated surface metal atoms in the step-edge site are not poisoned by C adatoms<sup>3,5</sup> that are formed upon CO dissociation. Our analysis shows that this is because of rapid CH

rameters for the CO adsorption energy, increasing or decreasing the adsorption energy of CO to simulate different CO coverages does not alter this finding (see Figure 8.7).

intermediate formation, the key chain-growth monomer. The present work also shows that production of long-chain hydrocarbons is consistent with high CO coverage, as even at relatively high CO coverage a high rate of chain growth can be maintained. Increasing the CO adsorption energy does not change this result, but leads to a shift of the reaction maximum to higher temperatures. Thirdly, this study identifies sites with a low barrier for CO dissociation as the locus of the FT reaction. This implies that the FT reaction with low methane selectivity will take place on a relatively small part of the surface of the catalytic nanoparticles.<sup>56</sup> Low-reactive dense surface are the locus of CO hydrogenation to methane.

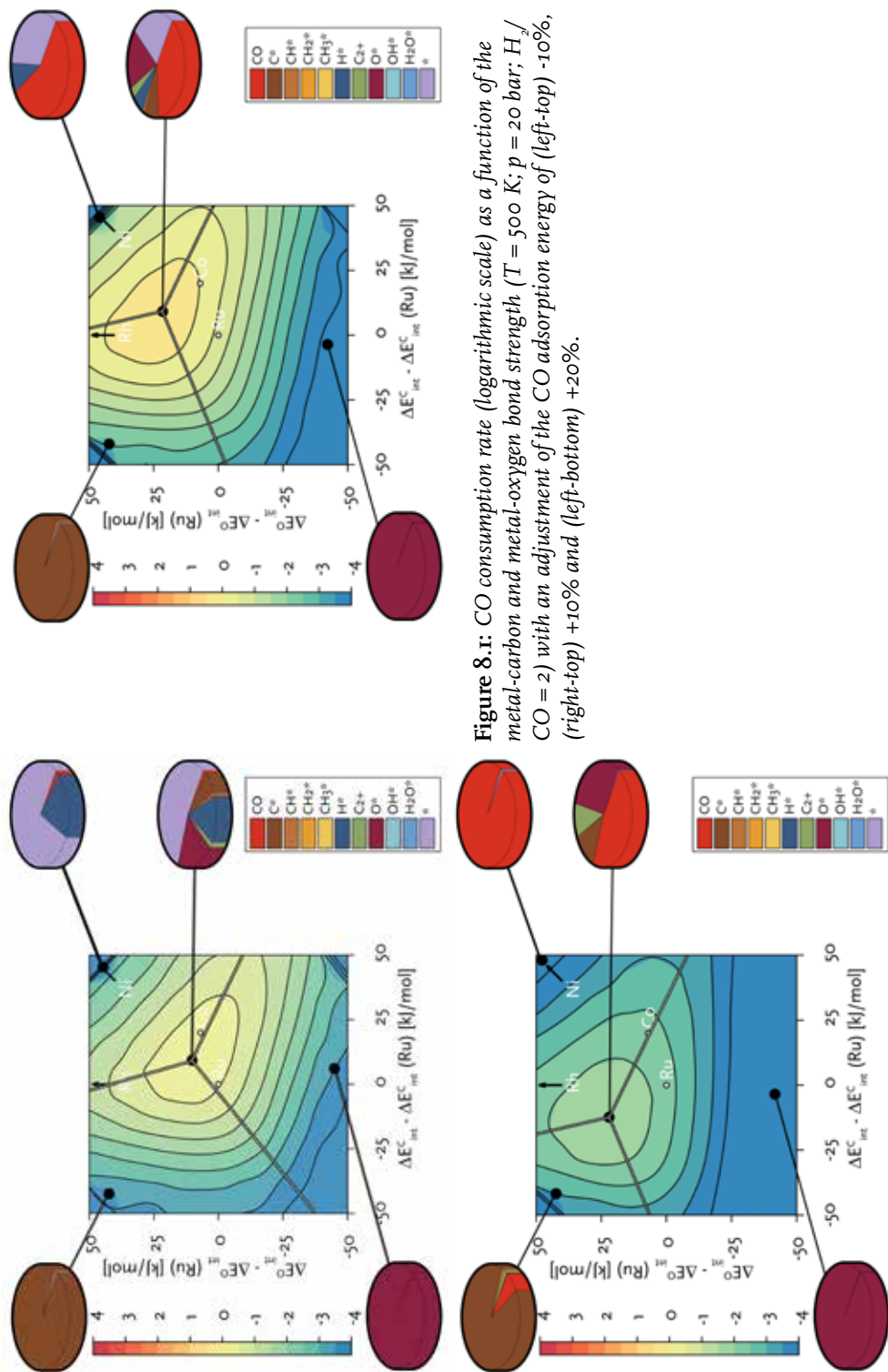


**Figure 8.1:** CO consumption rate (logarithmic scale) as a function of the metal-carbon and metal-oxygen bond strength ( $T = 500$  K;  $p = 20$  bar;  $H_2/CO = 2$ ) with an adjustment of the CO adsorption energy of (left-top) -10%, (right-top) +10% and (left-bottom) +20%.

## 8.5 REFERENCES

- (1) Fischer, F.; Tropsch, H. *Brennst.-Chem* **1923**, *4*, 276.
- (2) Fischer, F.; Tropsch, H. *Brennst.-Chem* **1926**, *7*, 79.
- (3) Fei Tan, K.; Xu, J.; Chang, J.; Borgna, A.; Saeys, M. J. *Catal.* **2010**, *274*, 121.
- (4) Saeys, M.; Tan, K. F.; Chang, J.; Borgna, A. *Ind. Eng. Chem. Res.* **2010**, *49*, 11098.
- (5) Moodley, D. J.; van de Loosdrecht, J.; Saib, A. M.; Overett, M. J.; Datye, A. K.; Niemantsverdriet, J. W. *Applied Catalysis A: General* **2009**, *354*, 102.
- (6) Lee, D.-K.; Lee, J.-H.; Ihm, S.-K. *Applied Catalysis* **1988**, *36*, 199.
- (7) Quek, X.-Y.; Filot, I. A. W.; Pestman, R.; van Santen, R. A.; Petkov, V.; Hensen, E. J. M. *Chem. Commun.* **2014**.
- (8) Van Santen, R. A. *Acc. Chem. Res.* **2008**, *42*, 57.
- (9) van Santen, R. A.; Ghouri, M. M.; Shetty, S.; Hensen, E. J. M. *Catal. Sci. Technol.* **2011**, *1*, 891.
- (10) den Breejen, J. P.; Radstake, P. B.; Bezemer, G. L.; Bitter, J. H.; Frøseth, V.; Holmen, A.; Jong, K. P. d. J. *Am. Chem. Soc.* **2009**, *131*, 7197.
- (11) Stegelmann, C.; Andreasen, A.; Campbell, C. T. J. *Am. Chem. Soc.* **2009**, *131*, 8077.
- (12) Campbell, C. T. J. *Catal.* **2001**, *204*, 520.
- (13) Biloen, P.; Helle, J. N.; Sachtler, W. M. H. J. *Catal.* **1979**, *58*, 95.
- (14) Biloen, P.; Sachtler, W. M. H. In *Adv. Catal.*; D.D. Eley, H. P., Paul, B. W., Eds.; Academic Press: 1981; Vol. Volume 30, p 165.
- (15) Outi, A.; Rautavuoma, I.; van der Baan, H. S. *Applied Catalysis* **1981**, *1*, 247.
- (16) Anderson, R. B. *The Fischer-Tropsch Synthesis*; Academic Press: New York, 1984.
- (17) Wojciechowski, B. W. *Catal. Rev.* **1988**, *30*, 629.
- (18) Yates, I. C.; Satterfield, C. N. *Energy & Fuels* **1991**, *5*, 168.
- (19) Liu, Z.-P.; Hu, P. J. *Am. Chem. Soc.* **2002**, *124*, 11568.
- (20) Cheng, J.; Gong, X.-Q.; Hu, P.; Lok, C. M.; Ellis, P.; French, S. J. *Catal.* **2008**, *254*, 285.
- (21) Gong, X.-Q.; Raval, R.; Hu, P. J. *Chem. Phys.* **2005**, *122*, 024711.
- (22) Cheng, J.; Hu, P. J. *Am. Chem. Soc.* **2008**, *130*, 10868.
- (23) Cheng, J.; Hu, P.; Ellis, P.; French, S.; Kelly, G.; Lok, C. M. *Top. Catal.* **2010**, *53*, 326.
- (24) Cheng, J.; Hu, P.; Ellis, P.; French, S.; Kelly, G.; Lok, M. C. J. *Phys. Chem. C* **2008**, *112*, 6082.
- (25) Ojeda, M.; Nabar, R.; Nilekar, A. U.; Ishikawa, A.; Mavrikakis, M.; Iglesia, E. J. *Catal.* **2010**, *272*, 287.
- (26) Loveless, B. T.; Buda, C.; Neurock, M.; Iglesia, E. J. *Am. Chem. Soc.* **2013**, *135*, 6107.
- (27) Markvoort, A. J.; van Santen, R. A.; Hilbers, P. A. J.; Hensen, E. J. M. *Angew. Chem. Int. Ed.* **2012**, *9*, 9012.
- (28) van Santen, R. A.; Markvoort, A. J.; Ghouri, M. M.; Hilbers, P. A. J.; Hensen, E. J. M. *J. Phys. Chem. C* **2013**, *117*, 4488.
- (29) Van Santen, R. A.; Markvoort, A. J.; Filot, I. A. W.; Ghouri, M. M.; Hensen, E. J. M. *Phys. Chem. Chem. Phys.* **2013**, *15*, 17038.
- (30) Storsæter, S.; Chen, D.; Holmen, A. *Surf. Sci.* **2006**, *600*, 2051.
- (31) Lozano-Blanco, G.; Thybaut, J. W.; Surla, K.; Galtier, P.; Marin, G., B. *Oil & Gas Science and Technology - Rev. IFP* **2006**, *61*, 489.
- (32) Lozano-Blanco, G.; Thybaut, J. W.; Surla, K.; Galtier, P.; Marin, G. B. *Ind. Eng. Chem. Res.* **2008**, *47*, 5879.
- (33) Filot, I. A. W.; Santen, R. A. v.; Hensen, E. J. M. **2014**.
- (34) Shetty, S. G.; Jansen, A. P. J.; van Santen, R. A. J. *Phys. Chem. C* **2008**, *112*, 14027.

- (35) Shetty, S.; Jansen, A. P. J.; van Santen, R. A. *J. Am. Chem. Soc.* **2009**, *131*, 12874.
- (36) Shetty, S.; van Santen, R. A. *Catal. Today* **2011**, *171*, 168.
- (37) Abild-Pedersen, F.; Greeley, J.; Studt, F.; Rossmeisl, J.; Munter, T. R.; Moses, P. G.; Skúlason, E.; Bligaard, T.; Nørskov, J. K. *Phys. Rev. Lett.* **2007**, *99*, 016105.
- (38) Santen, R. A. v.; Neurock, M.; Shetty, S. G. *Chem. Rev.* **2009**, *110*, 2005.
- (39) Hammer, B.; Nørskov, J. K. In *Adv. Catal.*; Bruce C. Gates, H. K., Ed.; Academic Press: 2000; Vol. Volume 45, p 71.
- (40) Michaelides, A.; Liu, Z. P.; Zhang, C. J.; Alavi, A.; King, D. A.; Hu, P. J. *Am. Chem. Soc.* **2003**, *125*, 3704.
- (41) Bligaard, T.; Nørskov, J. K.; Dahl, S.; Matthiesen, J.; Christensen, C. H.; Sehested, J. *J. Catal.* **2004**, *224*, 206.
- (42) Pallassana, V.; Neurock, M. *J. Catal.* **2000**, *191*, 301.
- (43) Nørskov, J. K.; Bligaard, T.; Logadottir, A.; Bahn, S.; Hansen, L. B.; Bollinger, M.; Benggaard, H.; Hammer, B.; Slijivancanin, Z.; Mavrikakis, M.; Xu, Y.; Dahl, S.; Jacobsen, C. J. H. *J. Catal.* **2002**, *209*, 275.
- (44) Lausche, A. C.; Medford, A. J.; Khan, T. S.; Xu, Y.; Bligaard, T.; Abild-Pedersen, F.; Nørskov, J. K.; Studt, F. *J. Catal.* **2013**, *307*, 275.
- (45) van Santen, R. A.; Ciobic , I. M.; van Steen, E.; Ghouri, M. M. In *Adv. Catal.*; Bruce, C. G., Helmut, K., Eds.; Academic Press: 2011; Vol. Volume 54, p 127.
- (46) Ciobica, I. M.; Frechard, F.; van Santen, R. A.; Kleyn, A. W.; Hafner, J. *J. Phys. Chem. B* **2000**, *104*, 3364.
- (47) Ciobica, I. M.; van Santen, R. A. *J. Phys. Chem. B* **2003**, *107*, 3808.
- (48) Sehested, J.; Dahl, S.; Jacobsen, J.; Rostrup-Nielsen, J. R. *The Journal of Physical Chemistry B* **2004**, *109*, 2432.
- (49) Andersson, M. P.; Abild-Pedersen, F.; Remediakis, I. N.; Bligaard, T.; Jones, G.; Engbæk, J.; Lytken, O.; Horch, S.; Nielsen, J. H.; Sehested, J.; Rostrup-Nielsen, J. R.; Nørskov, J. K.; Chorkendorff, I. *J. Catal.* **2008**, *255*, 6.
- (50) Mueller, J. E.; van Duin, A. C. T.; Goddard, W. A. *J. Phys. Chem. C* **2009**, *113*, 20290.
- (51) Van Der Laan, G. P.; Beenackers, A. A. C. M. *Catal. Rev.* **1999**, *41*, 255.
- (52) Zennaro, R.; Tagliabue, M.; Bartholomew, C. H. *Catal. Today* **2000**, *58*, 309.
- (53) Sarup, B.; Wojciechowski, B. W. *Can. J. Chem. Eng.* **1989**, *67*, 620.
- (54) Claeys, M.; van Steen, E. In *Stud. Surf. Sci. Catal.*; André, S., Mark, D., Eds.; Elsevier: 2004; Vol. Volume 152, p 601.
- (55) van Steen, E.; Schulz, H. *Applied Catalysis A: General* **1999**, *186*, 309.
- (56) Shetty, S. G.; Ciobica, I. M.; Hensen, E. J. M.; van Santen, R. A. *Chem. Commun.* **2011**, *47*, 9822.

## Abstract

Fischer–Tropsch synthesis is an attractive process to convert alternative carbon sources, such as biomass, natural gas, or coal, to fuels and chemicals. Deactivation of the catalyst is obviously undesirable, and for a commercial plant it is of high importance to keep the catalyst active as long as possible during operating conditions. In this study, the reactivity of CO on carbon-covered cobalt surfaces has been investigated by means of density functional theory (DFT). An attempt is made to provide insight into the role of carbon deposition on the deactivation of two cobalt surfaces: the closed packed Co(0001) surface and the corrugated Co(11 $\bar{2}$ 1) surface. We also analyzed the adsorption and diffusion of carbon atoms on both surfaces and compared the mobility. Finally, the results for Co(0001) and Co(11 $\bar{2}$ 1) are compared, and the influence of the surface topology is assessed.

---

THIS CHAPTER HAS BEEN PUBLISHED AS:

Joos, L., Filot, I.A.W., Cottenier, S., Hensen, E.J.M.,  
Waroquier, M., van Speybroeck, V., van Santen, R.A.,  
*J. Phys. Chem. C*, 2014, 118, 10, 5317-5327



---

★ *The fundamental laws necessary for the mathematical treatment of a large part of physics and the whole of chemistry are thus completely known, and the difficulty lies only in the fact that application of these laws leads to equations that are too complex to be solved.* ★

Paul Dirac

**REACTIVITY OF  
CO ON CARBON-  
COVERED  
COBALT  
SURFACES  
IN FISCHER-  
TROPSCH  
SYNTHESIS**



**9**

## 9.1 INTRODUCTION

High petroleum prices, geopolitical conflicts, oil spills, energy dependence... there are a myriad of reasons for companies and countries to look for alternative carbon sources, such as natural gas, biomass, or coal. Fischer–Tropsch synthesis (FTS) is an attractive process that can convert syngas, derived from these alternative feedstock, to diesel fuels and basic chemicals. Cobalt is commonly used as a catalyst, due to its high selectivity, high activity, and relatively low cost. However, a lot of research has also focused on other metals, such as iron or ruthenium.<sup>1</sup> As the number of commercial FTS plants increases, the need for a full mechanistic understanding of the elementary reactions is now bigger than ever.<sup>2,3</sup>

The FTS process was patented in 1923<sup>4</sup> and has been investigated extensively ever since. The reactions in FTS are highly complex, and a fundamental understanding of the different phenomena is desired, both to optimize the industrial process and to gain information on surface chemistry in general. Computational methods may contribute to this fundamental understanding by elucidating the reactions on an atomic scale.

It is remarkable that to date, decades after the discovery of the reaction, there is still no agreement on the underlying mechanism of FTS.<sup>5</sup> Fischer and Tropsch

first proposed the carbene mechanism, which starts with direct dissociation of CO in atomic carbon and oxygen. Carbon atoms are subsequently hydrogenated to CH<sub>x</sub> species that then couple to hydrocarbon chains. In order to produce long chains, it is crucial that dissociation of CO proceeds faster than the coupling and hydrogenation reactions.<sup>6,7</sup> On the closed-packed Co(0001) surface however, the barrier for direct CO dissociation is very high (218 kJ/mol at a CO coverage of 1/9 of a monolayer (ML)).<sup>8</sup>

This high CO dissociation barrier led to the rise of alternative mechanisms. In the hydroxycarbene mechanism, CO is first hydrogenated to CHO, after which the HC–O bond is broken.<sup>9–11</sup> Then C/C coupling and CH<sub>x</sub> hydrogenation take place. At a 1/4 ML CO coverage on Co(0001), both the CO hydrogenation barrier (126 kJ/mol) and the HC–O cleavage barrier (96 kJ/mol) are lower than that of direct CO dissociation (272 kJ/mol at 1/4 ML of CO) but are still rather high. Moreover, the CHO species is extremely unstable on cobalt surfaces.<sup>12</sup> In the CO insertion mechanism, CO is first inserted in the growing hydrocarbon chain and only then the C–O bond is cleaved.<sup>13,14</sup>

In search of lower CO dissociation barriers, Ge and Neurock performed periodic DFT calculations to find out to what

extent defect sites could affect the barrier.<sup>8</sup> The presence of a zigzag channel on Co(11 $\bar{2}$ 0) enhances the reactivity by reducing the barrier for CO dissociation to 195 kJ/mol for a CO coverage of 1/8 ML. More stepped surfaces Co(10 $\bar{1}$ 2) and Co(11 $\bar{2}$ 4) succeed in decreasing the barrier more significantly to 123 and 89 kJ/mol, respectively. Even lower barriers are found for direct CO dissociation on the Co(10 $\bar{1}$ 0) B surface (B refers to the specific surface cut)<sup>15</sup> where the activation barrier is only 68 kJ/mol, whereas the overall barrier for the hydroxycarbene (HCO) mechanism is 105 kJ/mol on the same surface. Other computational studies also indicate that the carbene mechanism is indeed the preferred route on stepped and corrugated metal surfaces such as ruthenium,<sup>7,16-20</sup> rhodium,<sup>21</sup> and cobalt.<sup>22</sup> An ideal active site for FTS should not only have low barriers for CO dissociation but also allow for a propagation cycle to take place that can sustain itself. On Ru(11 $\bar{2}$ 1), such a cycle was determined, with CO dissociation and CH-CH coupling occurring on different sites.<sup>7</sup>

This catalytic cycle is obviously an idealized situation because, in practice, unwanted side reactions are inevitable. Several deactivation mechanisms are occurring in industrial catalysts. Deposition of carbon species on the cobalt surface was identified as one of the main deactivation mechanisms.<sup>23-25</sup> The problem

is 2-fold: carbon species can block active sites and thus hinder the adsorption and dissociation of CO, but they will also influence the catalytic activity in neighboring sites.<sup>26</sup> It has been confirmed by a recent DFT study of Li *et al.* that both carburization of the cobalt surface and site blockage by surface carbon deposition are indeed deactivating the cobalt catalysts.<sup>27</sup>

Locally or during short periods, the surface might be hydrogen lean so that carbon atoms cannot participate in the catalytic cycle. A DFT study showed that when carbon atoms couple to oligomeric species they are more stable than the individual atoms.<sup>28</sup> These oligomers can further grow to cyclic species and – ultimately - graphene sheets that significantly alter the electronic structure of the surface.<sup>29</sup> This is possible on flat surfaces, although steps in the surface are usually considered as nucleation sites for carbon fragments.<sup>30-33</sup> Formation of graphene and carbon nanotubes on metal surfaces has been investigated because of the unique properties of these materials, but during FTS, their presence is undesirable.<sup>24,25</sup>

The presence of subsurface carbon under typical FTS conditions is still open to discussion. Generally, it is accepted that a surface carbide can form during FTS conditions and that the thermodynamical driving force increases with increasing carbon coverage.<sup>34</sup> Carbon atoms

under the surface significantly influence the electronic structure of the surface and, therefore, also the reactions taking place at that surface.<sup>35</sup>

In this study, the effect of carbon deposition on the adsorption and dissociation of CO is under investigation using DFT calculations. Although the FTS mechanism is still under discussion, the

direct CO dissociation is certainly attractive as an important and simple model step. Since the reaction strongly depends on the surface structure the effect of carbon deposition will be investigated for two surfaces: the closed packed Co(0001) surface and the corrugated Co(11 $\bar{2}$ 1) surface.

## 9.2 COMPUTATIONAL METHOD

Calculations were performed with the periodic DFT code VASP (Vienna Ab initio Simulation Package).<sup>36,37</sup> This code uses projector-augmented wave pseudopotentials<sup>38,39</sup> and a plane wave basis set to describe the electron density. The exchange-correlation functional is expressed by the generalized gradient approximation with the Perdew-Burke-Ernzerhof parametrization.<sup>40</sup> As cobalt is a magnetic metal, calculations are spin polarized with a plane wave cutoff energy of 400 eV. Surfaces were modeled using a four-layer symmetric slab, in which all atoms were allowed to relax. A 3x3 and 2x2 unit cell was used for Co(0001) and Co(11 $\bar{2}$ 1), respectively, maintaining a vacuum of at least 10 Å. The *k*-point sampling of the first Brillouin zone is a gamma point sampling of (5x5x1) for both the Co(0001) and the Co(11 $\bar{2}$ 1) surfaces. Dipole-dipole interactions between adsorbing molecules on both sides of the slab

were avoided using a symmetric slab with adsorption on both sides of the surface. Electronic convergence was set to 10<sup>-5</sup> eV, and geometries are converged to 10<sup>-4</sup> eV using a conjugate-gradient algorithm that uses trial and corrector steps to converge both the energy of the structure as well as the forces on the ions. Transition states (TS) were identified using the climbing Nudged Elastic Band (cNEB) method as implemented in VASP 5.11. First, 30 ionic steps were calculated with the cNEB algorithm. Then, a frequency calculation was performed on the image with the highest energy. When frequency analysis showed one imaginary frequency in the direction of the reaction coordinate, the structure was further relaxed with a Newton-Raphson algorithm until the forces were smaller than 0.01 eV/Å. Finally, the transition state was confirmed using partial Hessian vibrational analysis with a step size of 0.02 Å. Zero-point energy

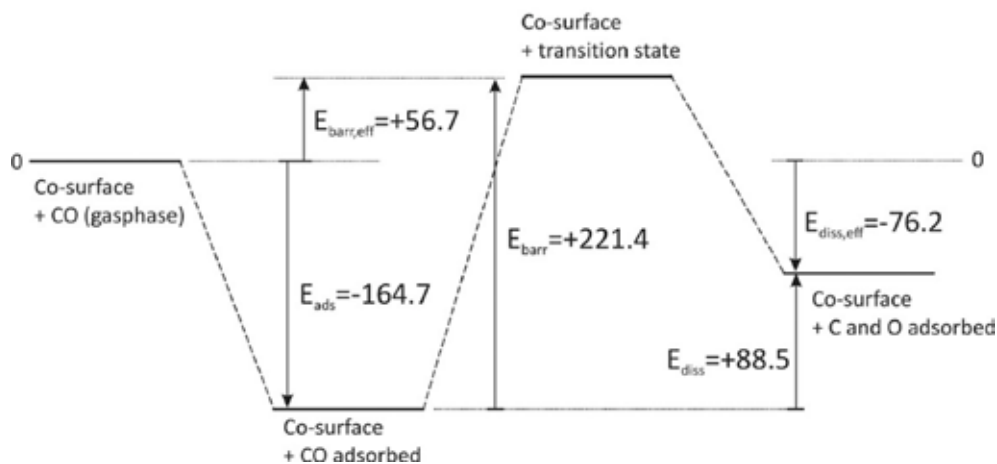


**Figure 9.1:** Energy profile for CO dissociation and graphical explanation of the definitions used in this manuscript. To give some indication, energy values (in kJ/mol) are given for CO dissociation on a flat Co(0001) cobalt surface without carbon deposition.

corrections are not included because they are small (less than 5 kJ/mol) and not essential for drawing conclusions from the results.

To model the deactivation by carbon deposition, one carbon atom is put on several positions of the surface and in the subsurface. Although the carbon coverage might be much higher in typical cobalt catalysts under FTS conditions, this approach is useful because it focuses only on the interaction between carbon and CO and not between different coadsorbed carbon atoms. Note that the symmetric slab approach implies that on the other side of the surface a second carbon atom is present. This symmetric approach reduces the computation time but can create repulsive effects between

two carbon atoms if they are adsorbed in the first or second subsurface layer. Still, concentrations of two carbon atoms per 36 or 48 cobalt atoms are sufficiently low to avoid unrealistic interactions. The stability of the carbon atom is given with respect to the reaction  $\text{CO} + \text{H}_2 \rightarrow \text{C} + \text{H}_2\text{O}$ . The so-called deposition energy is then defined as

$$E_{\text{depos}} = \frac{(E_{\text{slab+C}} + 2E_{\text{H}_2\text{O}} - E_{\text{slab}} - 2E_{\text{CO}} - 2E_{\text{H}_2})}{2} \quad (9.1)$$

The factor 2 in this equation is related to the symmetric slab approach. The energies that describe the adsorption and dissociation of CO are represented graphically in Figure 9.1. First, the CO adsorption energy can be expressed as

$$E_{\text{ads}} = (E_{\text{slab+CO}} - E_{\text{slab}} - 2E_{\text{CO}}) / 2 \quad (9.2)$$

Second, the energy of the transition state (TS) and final state (FS) can be reported with respect to two references.  $E_{\text{barr}}$  and  $E_{\text{diss}}$  represent the energy with respect to the initial state (IS), while  $E_{\text{barr,eff}}$  and  $E_{\text{diss,eff}}$  report the energy with respect to gas-phase CO, the so-called effective or apparent dissociation barrier or energy. The dissociation barrier can hence be written as

$$\ddot{u}_{\text{barr}} = (E_{\text{slab+(C-O)}^\ddagger} - E_{\text{slab+CO}}) / 2 \quad (9.3)$$

while the effective dissociation barrier is defined as

$$E_{\text{barr,eff}} = (E_{\text{slab+C-O}}^\ddagger - E_{\text{slab}} - 2E_{\text{CO}}) / 2 \quad (9.4)$$

In the expressions for  $E_{\text{diss}}$  and  $E_{\text{diss,eff}}$ ,  $E_{\text{slab+(C-O)}^\ddagger}$  is replaced with  $E_{\text{slab+C+O}}$ . Introduction of two reference states (the IS and gas-phase CO) has its merits, especially when considering different surfaces. Whether or not the CO dissociation takes place depends on the stability of the IS: if CO is too tightly bound to the metal surface, the dissociation barrier  $E_{\text{barr}}$  be-

comes too high, reducing the probability that dissociation will occur. On the other hand, the energy barrier with respect to a gas-phase CO molecule is also an important ingredient in the discussion. This is best illustrated with the example of CO dissociation on Co(0001) in Figure 9.1. Not only is the dissociation barrier very high (221.4 kJ/mol), the energy of the TS is also 56.7 kJ/mol higher than that of a gas-phase CO molecule. In other words, the probability that the CO molecule desorbs from the surface is larger than that it dissociates on the surface. Moreover, the dissociation energy is positive with 88.5 kJ/mol, but the final state is still 76.2 kJ/mol lower than gas-phase CO. Thus, the reaction is endothermic with respect to the IS but exothermic with respect to gas-phase CO. If the reaction is strongly exothermic, it is thermodynamically favored. It is an interplay of all these aspects that makes the CO dissociation feasible or not. In the next section, we will discuss how the energy of the TS and FS may shift when extra carbon atoms are present on the surface or in the subsurface.

## 9.3 RESULTS AND DISCUSSION

In this section, we will discuss the deposition of carbon atoms and the effect on the adsorption and dissociation of

CO. First, we consider the flat Co(0001) surface and then the corrugated Co(1121) surface. For both surfaces, we investi-

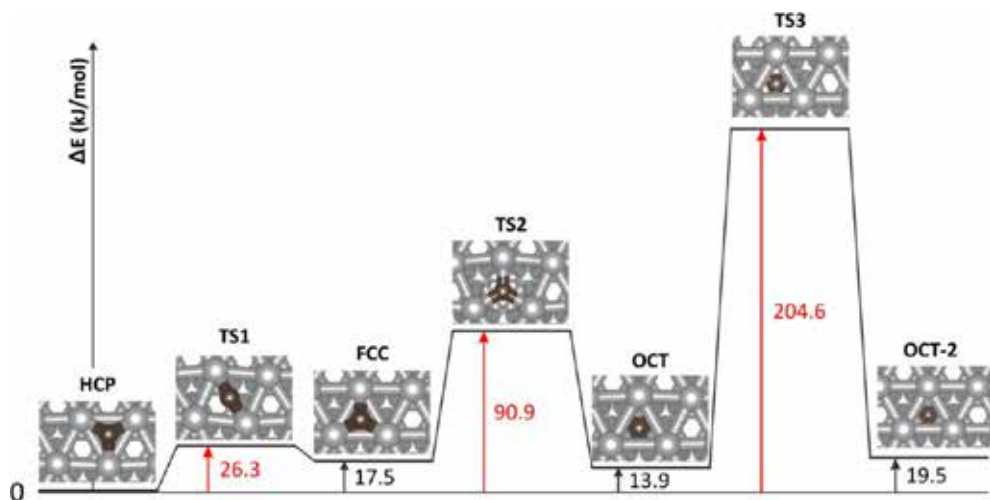


**Figure 9.2:** Profile for carbon diffusion on Co(0001) surface. Energies are reported with respect to the HCP adsorption site and are expressed in kJ/mol. Positions are described in the text.

gated the diffusion of carbon atoms and checked the influence of the carbon atom on the adsorption and dissociation of CO.

## 9.3.1 FLAT SURFACE

### 9.3.1.1 CARBON DIFFUSION

In Figure 9.2, a carbon diffusion profile at 1/9 ML on Co(0001) is presented. The most stable site for carbon adsorption on this surface is the HCP site, with a deposition energy of  $-87.8$  kJ/mol, which agrees fairly well with the value of  $-91.6$  kJ/mol reported by Swart *et al.* for the HCP site on the Co(111) surface.<sup>28</sup> The bridge site (TS1) is a transition state for diffusion to the FCC site. The barrier for this transition is low (26.3 kJ/mol),

and the energy of a carbon atom in the TS1 site is only slightly higher than in the FCC site (17.5 kJ/mol). The diffusion profile will likely depend on the carbon coverage, as a similar theoretical study at 1/4 ML coverage reported values of 40.1 and 26.1 kJ/mol for TS1 and FCC, respectively.<sup>41</sup>

From the FCC site, the carbon atom can diffuse in the subsurface octahedral site OCT. This subsurface site is 3.6 kJ/mol lower in energy than the surface FCC site, but a barrier of 73.4 kJ/mol has to be overcome. During diffusion, the surrounding Co–Co distances are elongated from 2.64 Å in the FCC geometry to 2.98 Å in the transition state (TS2), after which they relax to 2.73 Å in the OCT configuration. Diffusion into the second

subsurface layer has a barrier of 190.7 kJ/mol, more than twice as high as the diffusion into the first subsurface layer. In the transition state (TS<sub>3</sub>), the carbon pushes the three surrounding cobalt atoms away from each other to a distance of about 2.96 Å, compared to 2.57 Å in both OCT and OCT-2, which explains the high barrier. Consideration of the diffusion into the second subsurface layer attains the limit of the four-layers symmetric slab model. Moreover, the carbon encountered its counterpart at a relatively short distance, creating unphysical extra repulsive effects. Our results compare well with the results of Li *et al.*, although the latter used an asymmetric slab and a different functional for their calculations.<sup>27</sup> Our calculations predict a lower barrier and energy difference for diffusion from HCP to the FCC site, but both studies predict substantial energy barriers, preventing carbon atoms from diffusing into the second and deeper sublayers.

In this study, we did not investigate the influence of the coverage on the diffusion barriers, although it was demonstrated for Ni(111) that both the stability of carbon as well as the diffusion barriers vary widely with the surface and subsurface carbon coverage.<sup>42</sup> This aspect is certainly worth further investigation.

In the next section, the effect of extra carbon atoms on the adsorption and dissociation of CO is analyzed. Only the

two most stable sites for carbon are considered: the HCP site and the OCT site. A quick back-of-the-envelope calculation of the Boltzmann distribution shows that at 500 K and 1/9 ML coverage, only 3% of the carbon atoms are present in an OCT position; all other sites are even less likely to be occupied and will not be considered.

### 9.3.1.2 EFFECT OF CARBON DEPOSITION ON CO DISSOCIATION

To assess the influence of carbon on CO dissociation, an extra carbon atom is deposited on different positions with respect to the dissociating molecule. Figure 9.3 shows the selected cases and their geometries for initial state (IS), transition state (TS), and final state (FS). The first row is the reference case: carbon dissociation on a FLAT surface, without any extra carbon atoms. In the next five cases, the extra carbon on the surface resides in an HCP or OCT position. We did not scan all possible positions for the extra carbon atom, since conclusions can already be drawn from the data set displayed in Figure 9.3. To give an overall picture of the different cases, the results are also assembled in the energy profile in Figure 9.4, following the convention in Figure 9.1.

In the absence of any additional carbon (reference case FLAT), the CO disso-

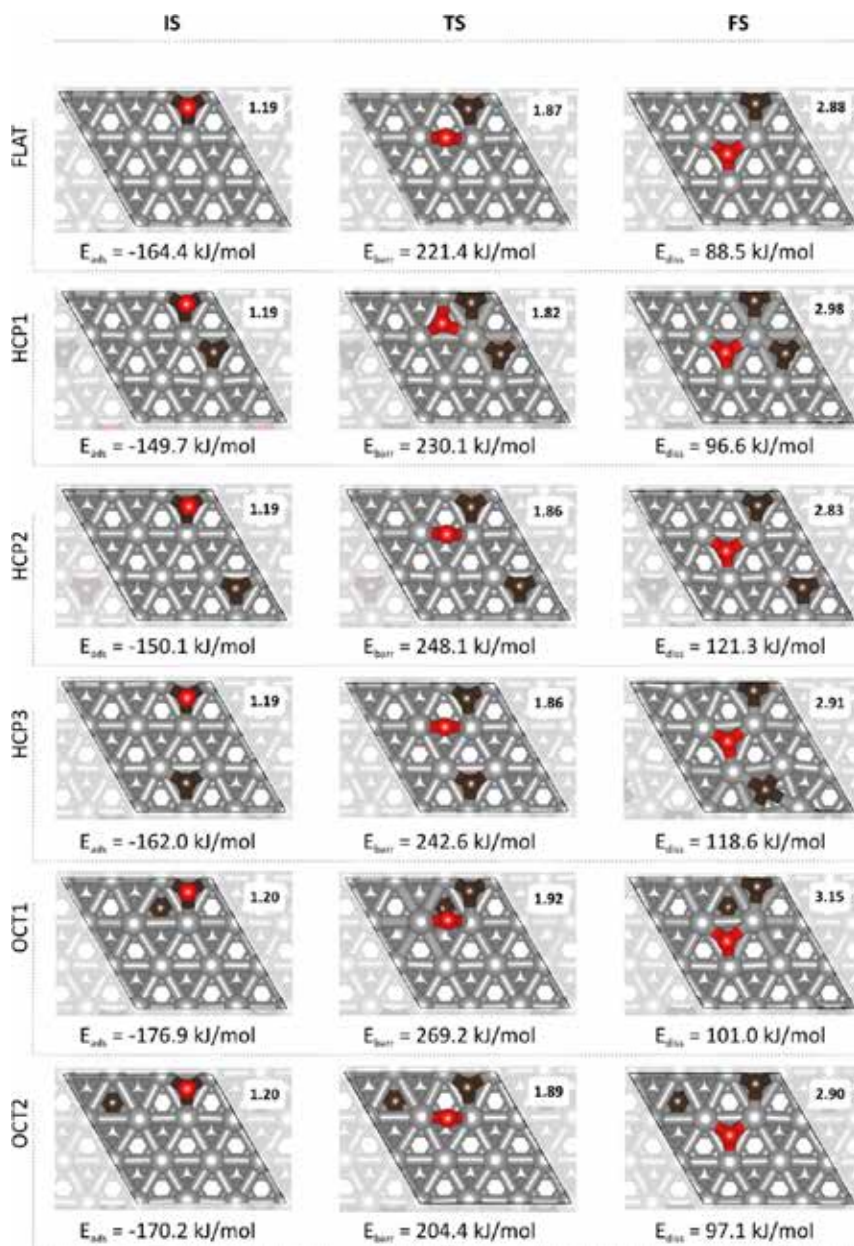


**Figure 9.3:** Influence of an extra carbon atom on CO dissociation on Co(0001). Different positions are considered for the extra carbon atom, and the dissociation profile is visualized along the row. In the FLAT case (first row), no extra carbon atom has been deposited on the cobalt surface. For each case the adsorption energy ( $E_{ads}$ ), the dissociation barrier ( $E_{barr}$ ), and the dissociation energy ( $E_{diss}$ ) are given in kJ/mol. C–O distance is written in the right corner in Å.

ciation path on Co(0001) starts with a CO molecule in the HCP site that dissociates in a carbon and an oxygen atom in two adjacent HCP sites. The adsorption energy is  $-164.7$  kJ/mol, in line with previous studies that report energies between  $-156$  and  $-175$  kJ/mol, depending on the CO coverage and the details of the methodology.<sup>8,13,43</sup> With respect to the IS, we find a barrier of  $221.4$  kJ/mol and a dissociation energy of  $88.5$  kJ/mol. These results correspond well with previous calculations from Ge and Neurock, which report  $218.0$  and  $76.5$  kJ/mol, respectively.<sup>8</sup>

The adsorption energy is less negative when a carbon atom is coadsorbed on the surface. If the extra carbon and the adsorbed molecule are one HCP site apart (situation HCP1 and HCP2),  $E_{\text{ads}}$  is almost  $15$  kJ/mol less negative than on the empty surface. In fact, the IS for HCP1 and HCP2 is identical due to the symmetry; the negligible difference of  $0.4$  kJ/mol is due to the accuracy of our method. In case they are two HCP sites apart (HCP3), the adsorption energy is more or less the same as in the FLAT geometry. This behavior can be explained by the lateral interaction between the CO molecule and the extra carbon atom: if the C–CO distance is shorter, the repulsive interaction is larger and the adsorption is weaker. In case a carbon atom is present in OCT1 or OCT2, the adsorption is stronger than for the empty surface.

Calculations confirm that the presence of extra carbon atoms on the surface have an influence on the adsorption energy, which varies in the range of  $20$  kJ/mol. More interesting is the question how the dissociation barrier is affected by extra carbon atoms. On the FLAT surface, CO dissociation has a barrier of  $221.4$  kJ/mol. In the case of a carbon atom coadsorbed on the surface, the dissociation barrier is higher due to the higher surface coverage. In HCP1, the extra carbon atom is located in the HCP site next to the dissociating CO molecule and shares the central cobalt atom around which the CO molecule dissociates. For HCP2 and HCP3, the carbon atom is located further away from the dissociation site. The increase in the barrier is lower for HCP1 than for HCP2 and HCP3, so it seems that the carbon and oxygen atoms prefer to cluster together on the surface. Moreover, the CO distance can be related to the stability of the TS: for HCP1 the CO distance is shorter than for HCP2 and HCP3 ( $1.82$  vs  $1.86$  Å), in line with the respective dissociation barriers ( $225.0$  vs  $242.9$  and  $237.9$  kJ/mol).

When carbon is present in the OCT1 position, right under the dissociating CO molecule, the barrier is almost  $50$  kJ/mol higher than on a FLAT surface. In this case, the higher barrier is a combination of stronger CO adsorption in the IS ( $E_{\text{ads}} = -176.9$  kJ/mol for OCT1,  $-164.7$

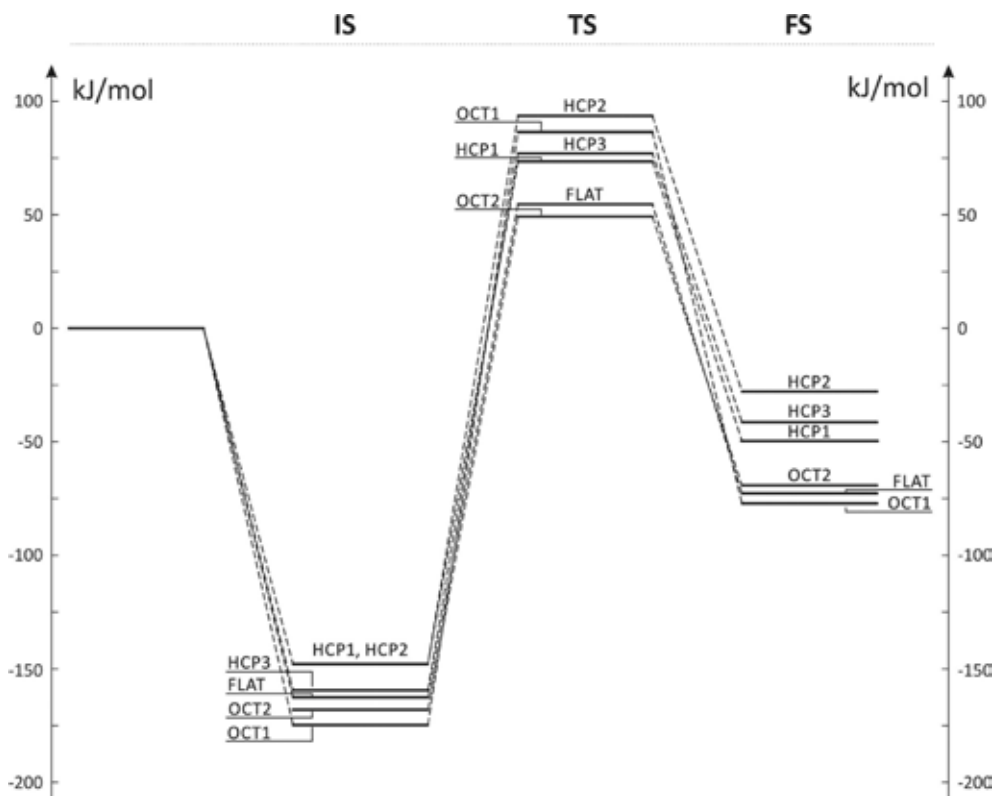


**Figure 9.4:** Energy profile for CO dissociation starting from various initial configurations characterized by carbon deposition at different positions on the cobalt surface. Energy scale in kJ/mol.

kJ/mol for FLAT) and a less stable TS ( $E_{\text{barr,eff}} = 92.3$  kJ/mol for OCT<sub>I</sub>, 56.7 kJ/mol for FLAT). This clearly illustrates the importance of the IS stability on the dissociation reaction. For the other subsurface position, OCT<sub>2</sub>, the barrier is surprisingly lower than in the reference case. Although the dissociation barrier is lowered, the TS still lies above the energy of gas-phase CO, implying that CO would likely desorb from the surface rather than dissociate on the surface. Second,

the chance of finding a carbon atom in the subsurface is small, as discussed in the previous section. It is therefore much more likely to find a surface carbon atom and hence a higher barrier.

Finally, we notice that the dissociation energy for carbon covered surfaces is systematically higher than in the FLAT reference case. For carbon coadsorbed on the surface, this can be rationalized by the lateral interaction between the dissociated C and O atom and the extra



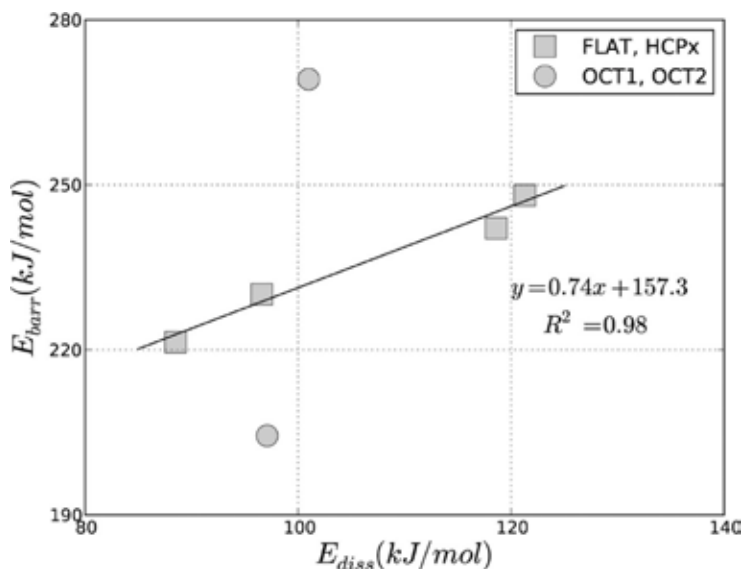


**Figure 9.5:** For surface carbon, there is a linear BEP correlation between the dissociation barrier and the dissociation energy.

carbon atom.

The energy profile displayed in Figure 9.4 suggests a Brønsted–Evans–Polanyi (BEP) relationship<sup>44,45</sup> between the dissociation barrier and the energy for the FLAT surface and for cases HCP<sub>1</sub>, HCP<sub>2</sub>, and HCP<sub>3</sub>, as shown in Figure 9.5. This BEP correlation is in line with the observation that CO dissociation has a late transition state on Co(0001).<sup>46</sup> It indicates that the influence of surface carbon is similar in the TS and FS and that there is a similarity in geometry or electronic effects between TS and FS. For OCT<sub>1</sub> and OCT<sub>2</sub>, however, the BEP correlation fails, so the effect of the extra carbon atom is no longer the same in the TS and FS. The dissociating oxygen atom might expe-

rience different electronic effects while dissociating on the surface just above the subsurface carbon atom. The similarity between TS and FS is no longer present, and hence, the BEP correlation fails.

### 9.3.2 CORRUGATED SURFACE

Apart from the flat Co(0001) surface, we also investigated the diffusion of carbon and the effect of carbon on the dissociation of CO on a corrugated surface, represented by Co(11 $\bar{2}$ 1) (Figure 9.6). The surface is characterized by two-dimensional trenches and ridges along the *b*-axis, and along that axis the cobalt atoms are positioned in a saw tooth profile. Overall, the cobalt atoms are on four

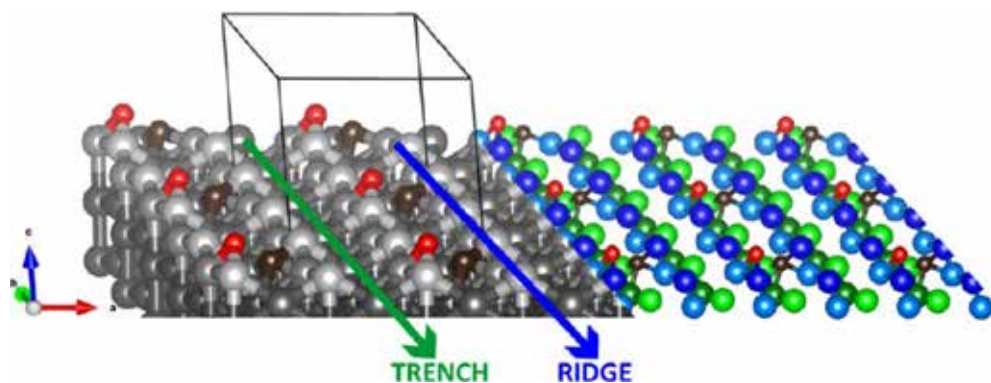


**Figure 9.6:** Two representations of the topology of the  $\text{Co}(11\bar{2}1)$  surface. The darker the shade of gray, the deeper the cobalt atom is located with respect to the  $c$  axis. Ridges (blue) and trenches (green) along the  $b$  axis are depicted. For clarity, the unit cell and axes are given as well as the transition state of a dissociating CO molecule, with the carbon atom in the 4-fold site and the oxygen molecule in a bridge position on the ridge.

different levels with respect to the  $c$  axis.

On the left in Figure 9.6, this is represented in four shades of gray: the deeper the atom, the darker its color. On the right, only surface atoms are displayed: those positioned on the ridges in blue and those in the trenches in green.

Surface cobalt coordination numbers are 6 and 7 on the ridge and 9 and 10 in the trench, in contrast with a coordination number of 9 on  $\text{Co}(0001)$ .  $\text{Co}(11\bar{2}1)$  is equivalent with the stepped  $\text{Co}(211)$  surface for cobalt with an FCC crystal structure. We considered a CO coverage of  $1/4$  ML (based on the primitive cell), corresponding to  $0.014 \text{ \AA}^{-2}$ , comparable with  $0.020 \text{ \AA}^{-2}$  for  $\text{Co}(0001)$ . During typical FTS conditions, the CO coverage might actually be higher, but a deeper analysis was outside the scope of this work.

### 9.3.2.1 CARBON DEPOSITION

In Figure 9.7, a diffusion profile for carbon on  $\text{Co}(11\bar{2}1)$  is presented.  $\text{Co}(11\bar{2}1)$  is represented schematically in this Figure. Cobalt atoms on the ridge are indicated in blue and those in the trench in green. The darker the color, the deeper the atom is located with respect to the  $c$  axis. The most stable site for carbon adsorption is the 4-fold (FF) site. Carbon is coordinated with four surface cobalt atoms and only  $2.13 \text{ \AA}$  from a fifth cobalt atom under the surface. In this FF site, the carbon has a deposition energy of  $-137.3 \text{ kJ/mol}$  and is hence significantly more strongly bound than in the HCP site on  $\text{Co}(0001)$  ( $E_{\text{depos}} = -87.8 \text{ kJ/mol}$ ).

From the FF site, the carbon atom can



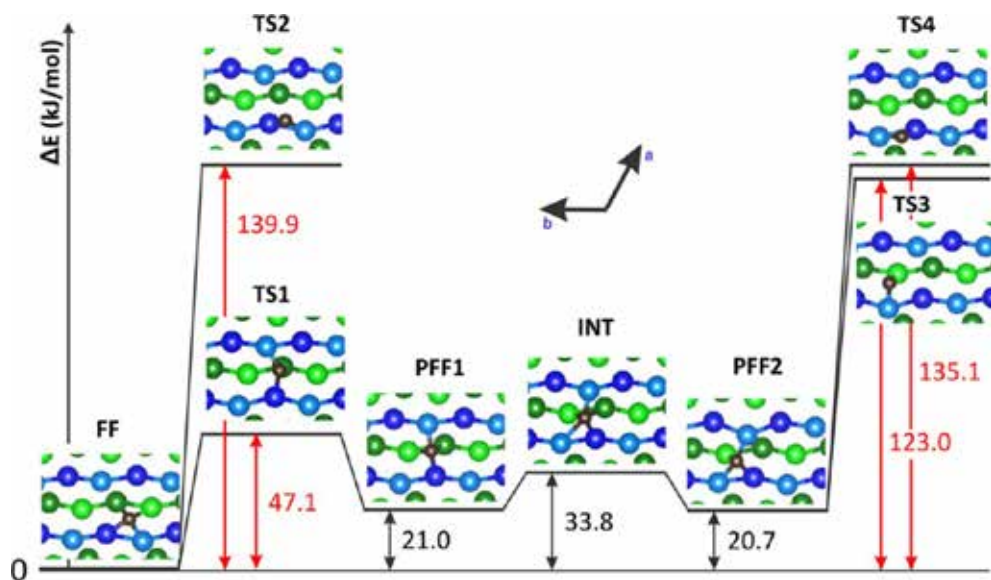


**Figure 9.7:** Diffusion profile for carbon on a corrugated  $\text{Co}(11\bar{2}1)$  surface, showing that barriers are much higher than on  $\text{Co}(0001)$ . To diffuse from one FF site to the next FF site in the same trench has an overall barrier of 123.0 kJ/mol; diffusion from one trench to the other has an even higher barrier (135.1 kJ/mol). Energies are with respect to the FF adsorption site and given in kJ/mol. Positions are described in the text.

diffuse in the trench along the  $b$  axis and reach the subsequent FF site after crossing local minima PFF<sub>1</sub> and PFF<sub>2</sub>. PFF<sub>1</sub> is a pseudo-4-fold site<sup>8,16</sup> where the carbon atom is in between two 3-fold sites, coordinated with four surface cobalt atoms in total. The PFF<sub>1</sub> site is 21.0 kJ/mol higher in energy than the FF site; the diffusion barrier is 47.1 kJ/mol.

Close to PFF<sub>1</sub>, a second pseudo-4-fold site is identified as a local minimum PFF<sub>2</sub> that has almost the same energy. No transition state could be constructed between PFF<sub>1</sub> and PFF<sub>2</sub>. Instead, an intermediate structure has been deter-

mined with an energy that is some 13 kJ/mol higher than the two neighboring local minima. The transition state for the PFF<sub>1</sub>–INT and INT–PFF<sub>2</sub> diffusion were not found, as well. During the PFF<sub>1</sub>–PFF<sub>2</sub> transition, carbon is keen to maintain its 4-fold cobalt coordination, thereby reshuffling the surface. Finally, the carbon can diffuse from PFF<sub>2</sub> in the next FF site. The transition state (TS<sub>3</sub>) for this move passes through a bridge configuration, where carbon is coordinated with only two cobalt atoms, explaining the high diffusion barrier (123 kJ/mol).

For diffusion into a neighboring

trench, the carbon atom can pass through two bridge positions (TS<sub>2</sub> and TS<sub>3</sub>). Starting from the FF site, the carbon can diffuse over the hill with an energy of 139.9 kJ/mol; from the PFF<sub>2</sub> site the barrier is 135.1 kJ/mol. For TS<sub>2</sub> and TS<sub>3</sub>,  $E_{\text{depos}}$  is 2.6 and -2.2 kJ/mol, respectively, much higher than -61.5 kJ/mol for the bridge site on Co(0001), all indicating that carbon is not likely to diffuse into neighboring trenches on Co(11 $\bar{2}$ 1).

In the next paragraph, we will also consider two subsurface sites, SUB<sub>1</sub> and SUB<sub>2</sub>, that were obtained by inserting carbon atoms into two adjacent subsurface positions under the active site, with carbon coordination numbers of 7 and 6, respectively. SUB<sub>1</sub> and SUB<sub>2</sub> are 70.5 and 36.5 kJ/mol higher in energy than the FF site, and unfortunately, we could not find transition states for the subsurface diffusion. However, from the stability of the subsurface species, it is clear that the diffusion in the subsurface is thermodynamically not favorable. Again, at high coverages, the presence of such subsurface carbon might become more likely.<sup>33,35</sup>

It is clear that carbon diffusion is completely different on Co(0001) and Co(11 $\bar{2}$ 1). On Co(0001), carbon diffusion has a barrier of only 26.3 kJ/mol, so surface carbon is very mobile on this surface. On the Co(11 $\bar{2}$ 1) surface, carbon atoms are more stable ( $E_{\text{depos}} = -137.3$  kJ/mol for FF,  $E_{\text{depos}} = -87.8$  kJ/mol for HCP), but dif-

fusion on this surface is kinetically hindered due to high barriers. Formation of extensive carbon clusters,<sup>28</sup> graphene, or nanotubes<sup>30</sup> on the corrugated Co(11 $\bar{2}$ 1) surface remains questionable, as CO dissociation can happen simultaneously in adjacent sites, and diffusion along the trench might not be the only route to form carbon clusters.

### 9.3.2.2 EFFECT OF CARBON DEPOSITION ON CO DISSOCIATION

The CO dissociation path on the Co(11 $\bar{2}$ 1) surface is visualized in Figure 9.8 and compared with that on the Co(0001) surface. On Co(11 $\bar{2}$ 1), dissociation starts with a CO molecule in the 4-fold site, adsorbed with an energy of -160.1 kJ/mol, similar to -164.4 kJ/mol on Co(0001). In the initial state on Co(11 $\bar{2}$ 1), the carbon is coordinated with four cobalt atoms and the oxygen with two cobalt atoms, as compared to three Co-C bonds in the HCP site on Co(0001). The longer C-O bond distance (1.32 versus 1.19 Å) already indicates that the CO molecule is preactivated in the 4-fold site.

In the transition state on the corrugated surface, the oxygen atom migrates over the ridge and ends in a 3-fold site in the adjacent trench. The carbon and oxygen atoms do not share any cobalt atoms in the TS. The dissociation barrier





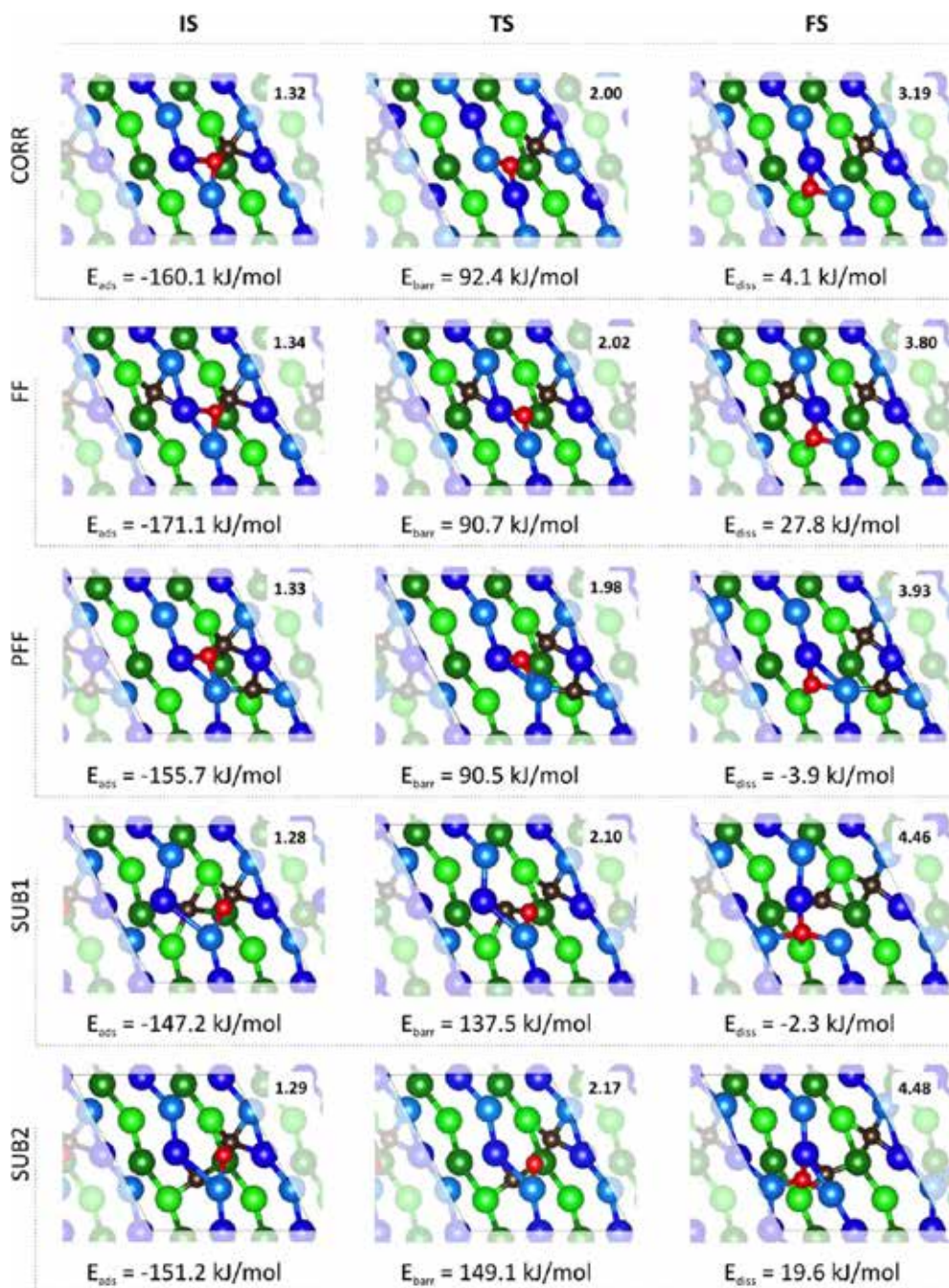


**Figure 9.9:** Influence of carbon on CO dissociation. C–O distance is printed in Å in the upper right corner. The influence of surface carbon is low, while subsurface species raise the barrier significantly.

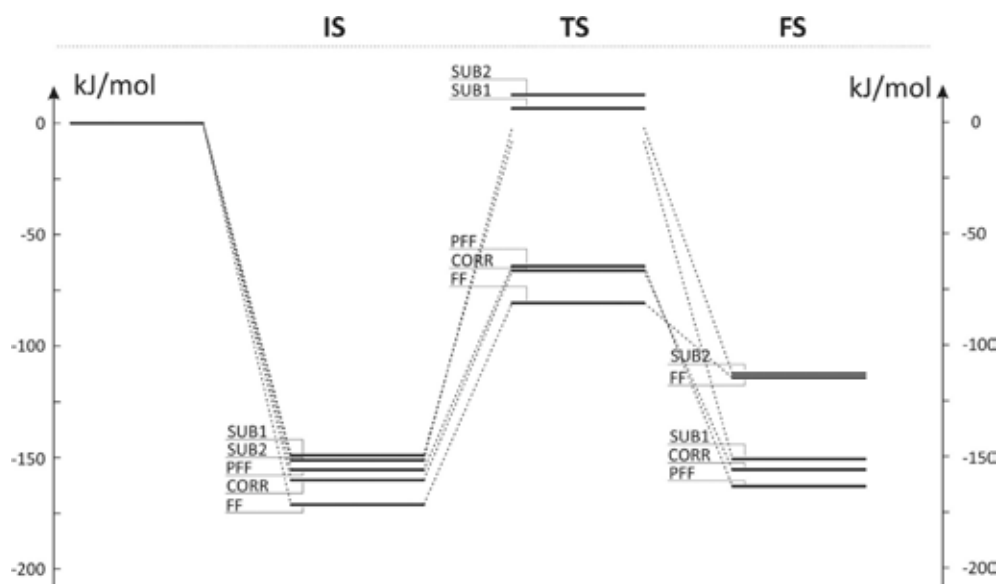


**Figure 9.10:** Energy profile for CO dissociation on  $Co(11\bar{2}1)$  starting from various initial configurations characterized by carbon deposition at different positions on the cobalt surface. Energy scale in kJ/mol.

at a FF site in a trench adjacent to the adsorption site of the CO molecule, the electron-withdrawing effect of carbon contributes to a stronger adsorption energy for CO,  $E_{\text{ads}} = -171.1$  kJ/mol. This effect also brings the oxygen closer to the cobalt atom that is shared between oxygen and the extra carbon (Co–O distance reduced from 2.27 to 2.07 Å). For a carbon in the PFF site, the adsorption energy is less negative, due to a repulsion between C and CO, which are here adsorbed in the same trench. The barrier for CO dissociation is only slightly affected by the presence of surface carbon species and actually lower for both FF and PFF. Finally, the dissociation energy is higher (27.8

kJ/mol) for FF as compared to CORR because of the repulsive interaction between the dissociated oxygen and the extra carbon atom, which are in the same trench after dissociation. PFF shows the opposite effect: in the FS, there is no longer repulsion between the oxygen atom and the extra carbon atom, now in an adjacent trench, resulting in a negative reaction energy of  $-3.9$  kJ/mol. In other words, in the FF case, there is more repulsion after CO dissociation than before, while for PFF, the opposite holds true.

An extra carbon atom embedded under the surface (SUB1 and SUB2) has a negative influence on the dissociation profile. The carbon restructures

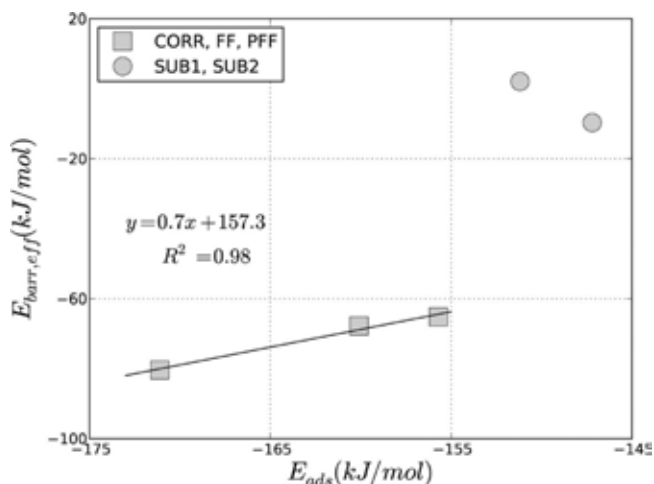


**Figure 9.11:** For surface carbon, there is a linear correlation between the effective dissociation barrier and the adsorption energy. For subsurface carbon, this correlation fails.

the surface around the CO adsorption site, significantly enlarging one of the Co–O distances (from 2.27 Å in CORR to 3.38 Å in SUB1 and 3.02 Å in SUB2). This rearrangement has its direct impact on the C–O distance, which becomes shorter (1.28 Å for SUB1 and 1.29 Å for SUB2), indicating a less activated C–O molecule. Indeed, the dissociation barriers are substantially raised with about 50 kJ/mol. The dissociation energy is negative for SUB1, where the oxygen atom assumes a 4-fold coordination due to reconstruction of the surface. Although a surface reconstruction is also seen in SUB2, it seems to be less favorable, resulting in a higher dissociation energy.

Finally, a striking feature of CO dissociation on the corrugated surface - apart from the lowering of the barrier with

more than 100 kJ/mol - is the dissociation energy, which drops to only 4.1 kJ/mol for the CORR surface. The presence of an extra carbon on the surface does not alter this substantial dropdown of the dissociation energy with regard to the flat surface. The most beneficial situation is that the dissociated oxygen and the extra carbon atom occupy adjacent trenches in the FS, leading to a dissociation energy of -4.4 kJ/mol.

Unlike on the Co(0001) surface, there is no BEP-like correlation between the FS and the TS for the Co(11 $\bar{2}$ 1) surface. Interestingly, we find a linear correlation between the adsorption energy (or the energy of the IS with respect to gasphase CO) and the effective dissociation barrier  $E_{barr,eff}$  (also relative to a gas-phase CO molecule), as long as the extra carbon is



located on the surface (Figure 9.11). This correlation suggests that the effects that stabilize the IS also determine the stability of the TS. As  $E_{\text{barr,eff}} - E_{\text{barr}} = E_{\text{ads}}$ , the observed linearity is also visible in a nearly constant barrier  $E_{\text{barr}}$  for CORR, FF, and PFF. This can be explained by the geometry of the dissociating CO molecule on the jagged Co(11 $\bar{2}$ 1) surface: in the IS and TS, the dissociating molecule is located on one side of the trench, while in the FS the oxygen is sitting in the adjacent trench after dissociation. It is

also reflected in the C–O distance, which in the TS (2.02 Å) is closer to the IS (1.34 Å) than to the FS (3.80 Å). These observations indicate an early transition state for CO dissociation on Co(11 $\bar{2}$ 1), and it would be worth investigating whether other corrugated or stepped surfaces show the same behavior. The correlation again fails for subsurface carbon, which is not surprising, as the geometry of the active site is significantly altered by the presence of these carbon species.

## 9.4 CONCLUSIONS

In this work, deposition of carbon on the flat Co(0001) and the corrugated Co(11 $\bar{2}$ 1) surface and the influence of this extra carbon on CO dissociation has been investigated by means of DFT quantum chemical calculations.

In a first part, the preferential positions of the extra carbon atom on the surfaces have been localized and migration of carbon on the surface was examined. We found a diffusion barrier of only 26.3 kJ/mol on Co(0001), providing evidence that carbon is very mobile on the flat surface. On Co(11 $\bar{2}$ 1), the carbon atom is more tightly bound and the diffusion barriers are much higher, especially when carbon has to diffuse over the ridge (with a barrier up to 139.9 kJ/mol). Subsurface positions are significantly less stable for

both cobalt surfaces.

Second, the surface topology significantly influences the dissociation profile, both for clean cobalt surfaces and for surfaces with an extra carbon atom. A corrugated surface displays a more favorable dissociation profile with barriers that are more than 100 kJ/mol lower than on the closed-packed Co(0001) surface. Moreover, an extra carbon atom on the surface only slightly affects the dissociation barrier for Co(11 $\bar{2}$ 1). A subsurface carbon has a stronger influence on both flat and corrugated surfaces, but subsurface carbon atoms are less stable than surface carbon species, so the probability that they occur is lower. Finally, dissociation is strongly endothermic on Co(0001) with respect to the IS, while  $E_{\text{diss}}$  is small or

even slightly negative on Co(11 $\bar{2}$ 1).

In conclusion, the topology of the surface has a significantly larger influence on CO dissociation than the presence of an extra carbon on the surface. The higher stability of carbon atoms on Co(11 $\bar{2}$ 1) in

combination with the lower CO dissociation barriers on this corrugated surface will likely give rise to a delicate balance between the stability and the activity of the active sites. ■

## 9.5 REFERENCES

- (1) Schulz, H.; Claeys, M. *Applied Catalysis A: General* **1999**, *186*, 91.
- (2) Leckel, D. *Energy & Fuels* **2009**, *23*, 2342.
- (3) van Steen, E.; Schulz, H. *Applied Catalysis A: General* **1999**, *186*, 309.
- (4) Fischer, F.; Tropsch, H. *Berichte der deutschen chemischen Gesellschaft (A and B Series)* **1923**, *56*, 2428.
- (5) Corral Valero, M.; Raybaud, P. *Catal. Lett.* **2013**, *143*, 1.
- (6) Ciobîca, I. M.; Kramer, G. J.; Ge, Q.; Neurock, M.; van Santen, R. A. *J. Catal.* **2002**, *212*, 136.
- (7) Shetty, S.; van Santen, R. A. *Catal. Today* **2011**, *171*, 168.
- (8) Ge, Q.; Neurock, M. *The Journal of Physical Chemistry B* **2006**, *110*, 15368.
- (9) Huo, C.-F.; Li, Y.-W.; Wang, J.; Jiao, H. *J. Phys. Chem. C* **2008**, *112*, 14108.
- (10) Ojeda, M.; Nabar, R.; Nilekar, A. U.; Ishikawa, A.; Mavrikakis, M.; Iglesia, E. *J. Catal.* **2010**, *272*, 287.
- (11) Loveless, B. T.; Buda, C.; Neurock, M.; Iglesia, E. *J. Am. Chem. Soc.* **2013**, *135*, 6107.
- (12) Inderwildi, O. R.; Jenkins, S. J.; King, D. A. *J. Phys. Chem. C* **2008**, *112*, 1305.
- (13) Zhuo, M.; Tan, K. F.; Borgna, A.; Saeys, M. *J. Phys. Chem. C* **2009**, *113*, 8357.
- (14) Zhuo, M.; Borgna, A.; Saeys, M. *J. Catal.* **2013**, *297*, 217.
- (15) Shetty, S.; van Santen, R. A. *Phys. Chem. Chem. Phys.* **2010**, *12*, 6330.
- (16) Shetty, S. G.; Jansen, A. P. J.; van Santen, R. A. *J. Phys. Chem. C* **2008**, *112*, 14027.
- (17) Shetty, S.; van Santen, R. *Top. Catal.* **2010**, *53*, 969.
- (18) Shetty, S. G.; Ciobica, I. M.; Hensen, E. J. M.; van Santen, R. A. *Chem. Commun.* **2011**, *47*, 9822.
- (19) van Santen, R. A.; Ghouri, M. M.; Shetty, S.; Hensen, E. J. M. *Catal. Sci. Technol.* **2011**, *1*, 891.
- (20) Tison, Y.; Nielsen, K.; Mowbray, D. J.; Bech, L.; Holse, C.; Calle-Vallejo, F.; Andersen, K.; Mortensen, J. J.; Jacobsen, K. W.; Nielsen, J. H. *J. Phys. Chem. C* **2012**, *116*, 14350.
- (21) Filot, I. A. W.; Shetty, S. G.; Hensen, E. J. M.; van Santen, R. A. *J. Phys. Chem. C* **2011**, *115*, 14204.
- (22) Liu, J.-X.; Su, H.-Y.; Li, W.-X. *Catal. Today* **2013**, *215*, 36.
- (23) Moodley, D. J.; van de Loosdrecht, J.; Saib, A. M.; Overett, M. J.; Datye, A. K.; Niemantsverdriet, J. W. *Applied Catalysis A: General* **2009**, *354*, 102.
- (24) Saib, A. M.; Moodley, D. J.; Ciobica, I. M.; Hauman, M. M.; Sigwebela, B. H.; Weststrate, C. J.; Niemantsverdriet, J. W.; van de Loosdrecht, J. *Catal. Today* **2010**, *154*, 271.
- (25) Tsakoumis, N. E.; Rønning, M.; Borg, Ø.; Rytter, E.; Holmen, A. *Catal. Today* **2010**, *154*, 162.
- (26) Teschner, D.; Révay, Z.; Borsodi, J.; Hävecker, M.;



- Knop-Gericke, A.; Schlögl, R.; Milroy, D.; Jackson, S. D.; Torres, D.; Sautet, P. *Angew. Chem. Int. Ed.* **2008**, *47*, 9274.
- (27) Li, B.; Zhang, Q.; Chen, L.; Cui, P.; Pan, X. *Phys. Chem. Chem. Phys.* **2010**, *12*, 7848.
- (28) Swart, J. C. W.; Ciobica, I. M.; van Santen, R. A.; van Steen, E. *J. Phys. Chem. C* **2008**, *112*, 12899.
- (29) Swart, J. C. W.; van Steen, E.; Ciobica, I. M.; van Santen, R. A. *Phys. Chem. Chem. Phys.* **2009**, *11*, 803.
- (30) Ramírez-Caballero, G. E.; Burgos, J. C.; Balbuena, P. B. *J. Phys. Chem. C* **2009**, *113*, 15658.
- (31) Fei Tan, K.; Xu, J.; Chang, J.; Borgna, A.; Saeys, M. J. *Catal.* **2010**, *274*, 121.
- (32) Saeys, M.; Tan, K. F.; Chang, J.; Borgna, A. *Ind. Eng. Chem. Res.* **2010**, *49*, 11098.
- (33) Tan, K. F.; Chang, J.; Borgna, A.; Saeys, M. J. *Catal.* **2011**, *280*, 50.
- (34) Sautet, P.; Cinquini, F. *ChemCatChem* **2010**, *2*, 636.
- (35) van Helden, P.; Ciobica, I. M. *ChemPhysChem* **2011**, *12*, 2925.
- (36) Kresse, G.; Hafner, J. *Phys. Rev. B* **1994**, *49*, 14251.
- (37) Kresse, G.; Furthmüller, J. *J. Comput. Mater. Sci.* **1996**, *6*, 15.
- (38) Blöchl, P. E. *Phys. Rev. B* **1994**, *50*, 17953.
- (39) Kresse, G.; Joubert, J. *Phys. Rev. B* **1999**, *59*, 1758.
- (40) Perdew, J. P.; Burke, K.; Ernzerhof, M. *Phys. Rev. Lett.* **1996**, *77*, 3865.
- (41) Balakrishnan, N.; Joseph, B.; Bhethanabotla, V. R. *Applied Catalysis A: General* **2013**, *462–463*, 107.
- (42) Xu, J.; Saeys, M. J. *Phys. Chem. C* **2008**, *112*, 9679.
- (43) Huo, C.-F.; Li, Y.-W.; Wang, J.; Jiao, H. *J. Phys. Chem. C* **2008**, *112*, 3840.
- (44) Bligaard, T.; Nørskov, J. K.; Dahl, S.; Matthiesen, J.; Christensen, C. H.; Sehested, J. *J. Catal.* **2004**, *224*, 206.
- (45) Viñes, F.; Vojvodic, A.; Abild-Pedersen, F.; Illas, F. J. *Phys. Chem. C* **2013**, *117*, 4168.
- (46) Santen, R. A. v.; Neurock, M.; Shetty, S. G. *Chem. Rev.* **2009**, *110*, 2005.



# SUMMARY AND OUTLOOK

---

## Quantum Chemical and microkinetic modeling of the Fischer-Tropsch reaction

---

### SUMMARY

The limited supply of readily available fossil resources stimulates the search for alternative energy sources. Due to the abundant supply of cheap natural gas, methane is increasingly considered as a valuable alternative feedstock for the synthesis of fuels and chemicals. Synthesis gas, a mixture of CO and H<sub>2</sub>, derived from natural gas by autothermal or steam reforming can be used to produce long-chain hydrocarbons in the Fischer-Tropsch process. Although the Fischer-Tropsch process is known for more than a century, the underlying mechanisms are still poorly understood.

The rapid increase in computing power provides a unique opportunity to study comprehensive chemical networks such as that of the Fischer-Tropsch reaction, by constructing microkinetics simulations based on computed molecular reactivity

data. Using such microkinetics simulations, kinetic parameters such as reaction orders and apparent activation energies can be derived and compared with experiment; elementary reaction steps that control the rate of chemical conversion in such chemical networks can then be identified.

Pertinent mechanistic questions in Fischer-Tropsch synthesis relate to the mode of CO dissociation, the dominant mechanism (the carbide versus the CO-insertion mechanism), the identification of the active site, and how the rates of the many elementary reaction steps influence CO conversion and product selectivity. In this thesis, the focus has been on Rh- (Chapters 3-6) and Ru-catalyzed (Chapters 7 and 8) Fischer-Tropsch synthesis. Ru is useful as a Fischer-Tropsch catalyst to produce long-chain hydrocar-

bons to be used as transportation fuels. Rh is known for its selectivity to produce  $C_2$ -oxygenates that may be used as chemical feedstock.

In Chapter 3, the effect of surface topology and system size on the dissociation of CO on Rh catalysts was studied. It was found that the major factors governing the reaction barriers are the sharing of metal atoms by carbon and oxygen in the transition state and the coordination of the metal atoms involved in the Rh-C bond in the transition state versus their coordination in the initial state. It was shown that the effect of site topology on CO dissociation is more prominent than the electronic effects due to a change in the catalytic particle size.

To construct a comprehensive microkinetics simulation for CO hydrogenation over Rh(211) surfaces, a database of all relevant elementary reaction steps involved in this chemical network was constructed in chapter 4 using density functional theory calculations. From these and the microkinetics simulations, it was found that CO dissociation proceeds in a direct (non-hydrogen-assisted) fashion. In contrast to common assumption in scientific literature, the rate of CO dissociation does not control the overall reaction rate. Due to the relatively low stability of CH on the Rh(211) surface versus that of CO, the overall reaction barrier for C+CO coupling is lower than the barrier

for CH+CH coupling. This rationalizes the experimentally observed high selectivity for ethanol versus that of hydrocarbons. Ethanol formation is always in competition with methane formation. We have shown that ethanol formation will be favored when the hydrogenation of  $CH_2$  and  $CH_3$  and the dehydrogenation of  $CHCH_3$  become inhibited.

In Chapter 6, a computational study of  $N_2$  adsorbed on various Rh surfaces and Rh nanoparticles is conducted with the aim to establish whether IR spectroscopy of  $N_2$  adsorbed on Rh nanoparticles can help to identify step-edge sites. This computational study and the microkinetics model of chapter 5 are combined with existing catalytic performance data of zirconia-supported Rh nanoparticles. The strong correlation between the catalytic performance and the number of step-edge sites as measured by the IR intensity of the  $N_2$  stretching frequency show that step-edge sites are necessary for CO dissociation.

In Chapter 7, a database of rate parameters was constructed for FT synthesis on the Ru(11 $\bar{1}$ 1) surface. All elementary reaction steps relevant to both the carbide as well as the CO-insertion mechanism were studied. The data indicate that the carbide mechanism will result in higher CO conversion rates than the CO-insertion mechanism. Only in the carbide mechanism long-chain hydrocarbons

are formed; the dominant product in the CO-insertion mechanism is methane due to the slow rate of  $\text{CH}_x + \text{CO}$  coupling. The locus for the  $\text{CH} + \text{CH}$  coupling reaction is the step-edge site. Here, the overlap of the d-band with the molecular orbitals is more favorable for the formation of  $\pi$ -bonds between the CH fragments.

The calculated rate parameters in Chapter 7 were used to construct a microkinetics model in Chapter 8. To extrapolate the results of the quantum chemical calculations of chapter 7 to other metals by means of two reactivity descriptors, scaling relations as well as Brønsted-Evans-Polanyi relations were used. From this analysis, three kinetic regimes were found that are characterized by the elementary reaction step that limits the overall reaction rate in these regimes. In the monomer formation limiting regime, the CO dissociation limits the rate. In the water-formation limiting regime, the hydrogenation of OH limits the reaction. In the chain-growth li-

miting regime, the hydrogenation of the growing chains is rate-limiting. Industrial catalysts operate at the boundary of the monomer formation and water removal limiting regimes and hence are suboptimal. By comparing corrugated  $\text{Ru}(11\bar{2}1)$  with the flat  $\text{Ru}(0001)$  surface, it was found that only the former surface efficiently catalyzes CO dissociation and hence produces long hydrocarbon products.

In Chapter 9, the effect of surface topology and co-adsorption of C on the CO dissociation over Co-catalysts was investigated. It was found that the topology of the surface has a significantly larger influence on CO dissociation than the presence of additional carbon atoms on the surface. The higher stability of carbon atoms on  $\text{Co}(11\bar{2}1)$  in combination with the lower CO dissociation barriers on this corrugated surface will likely give rise to a delicate balance between the stability and the intrinsic activity of the surface sites.

## OUTLOOK

Advances in simulation methodology and the rise in computing power have resulted in a wide variety of computational methods applicable to the field of catalysis. When several such methods are combined, catalytic phenomena of increasing complexity can be studied by

computational means. The connection between density functional theory calculations and microkinetics simulations is such a multiscale approach; it provides an essential tool to develop an atomistic understanding of catalytic performance. In this approach, the molecular properties

such as electronic energies are bridged with macroscale properties such as reaction kinetics. In this thesis, we have shown how DFT-based kinetic parameters can be used in microkinetics models that are able to elucidate many unresolved issues in Fischer-Tropsch catalysis. Despite these successes, these models contain assumptions that may influence the overall result.

The efficiency of carrying out microkinetics simulations lies in the mean-field approximation and the assumption that the catalytic surface on which adsorbents react is static. Though these simplifications enable the construction of an effective tool in the study of reaction mechanics, they prevent the modeling of catalytic systems whose mechanism is strongly influenced by the local configuration of the adsorbates. Such systems require detailed time-dependent topological information to properly describe the reaction kinetics. For example, in the work of Ertl, strong correlations between the adsorbed species gives rise to pattern formation.<sup>1</sup> Moreover, the assumption of a static catalytic surface is far from reality. The size and shape of catalytic nanoparticles have a profound effect on the composition of the adsorbed layer and, accordingly, the reaction rate. At the same time, the adsorbates affect the surface topology at the local scale and the particle size and shape at the nanoparticle scale.

In Fischer-Tropsch catalysis, one can identify many issues that relate to the dynamic changes occurring on the catalytic surfaces as the reaction evolves. The work of De Groot and Wilson has elegantly shown how the surface of a Co single crystal restructures under FT synthesis conditions.<sup>2</sup> A main question relates to the mechanism of these surface restructuring processes. Does such reconstruction occur due to strongly bound surface carbon atoms or adsorption of carbon monoxide? How do such adsorbate-induced reconstructions affect particle size and shape? What is the interaction between the different crystalline facets exposed on a nanoparticle? If this can be understood, it would be important to include these dynamic changes in kinetic models so that the effect of overlayer composition on the interrelated surface structure and catalytic activity and selectivity can be properly described. In this way, predictions can be made about the evolution of the catalyst on longer time scales, providing for instance insight into activation and deactivation phenomena.

To answer these questions, computational models that describe the dynamic evolution of atomic systems over time are needed. Molecular dynamics (MD) is the methodology of choice for such atomistic simulations. However, when the phenomena of interest occur over longer time scales, molecular dynamics become

computationally too expensive due to the small time steps necessary to properly evolve the system over time. Kinetic Monte Carlo (KMC) can in principle overcome such limitations by exploiting the fact that long-time dynamics typically consist of different jumps between states.<sup>3,4</sup>

To ensure proper chemical description of the larger systems, quantum chemical methods will be required. Although quantum chemical methods provide a high level of accuracy, they come at a high computational cost. This cost limits quantum calculations to relatively small system sizes and short time scales. Ideally, one would like to employ MD or KMC to simulate large systems at longer time scale. If it would be possible to connect the detailistic information obtained from quantum chemical calculations with the efficiency of MD and KMC, we would obtain an effective and powerful multiscale tool to study many of the open questions in FT synthesis.

One such approach is ReaxFF, as it essentially bridges the gap between the two computational realms (DFT versus MD/KMC) by providing a method that retains a high level of accuracy, while still being able to model the chemical interactions of the atoms and molecules in a relatively simple way. This is done by a detailed parametrization of the atomic,

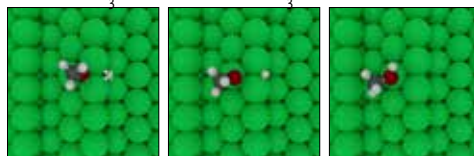
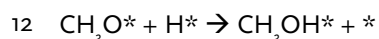
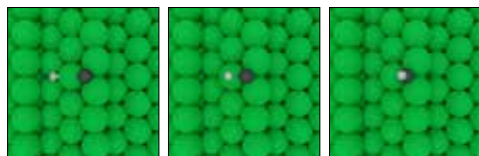
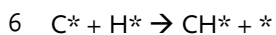
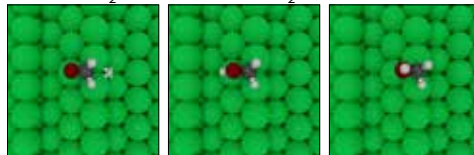
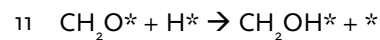
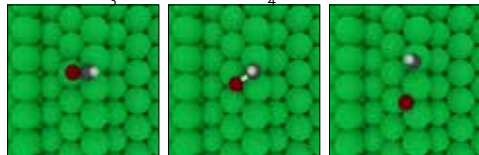
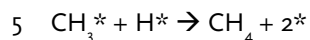
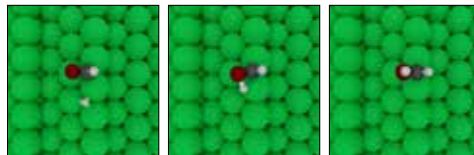
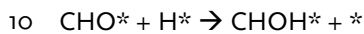
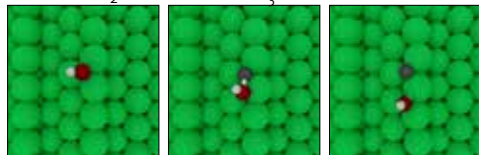
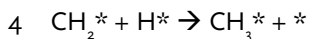
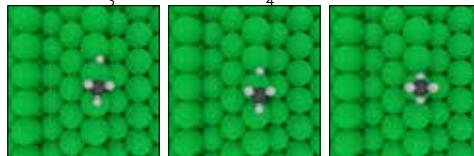
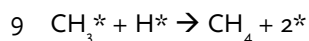
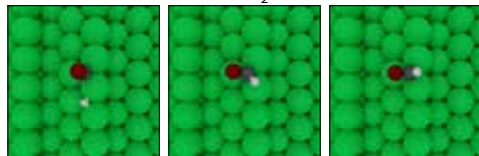
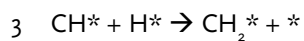
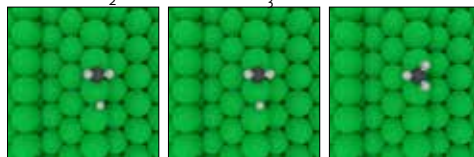
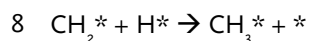
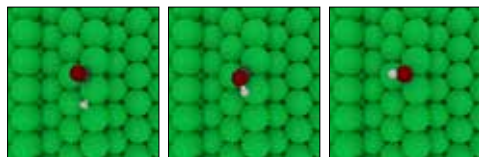
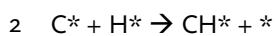
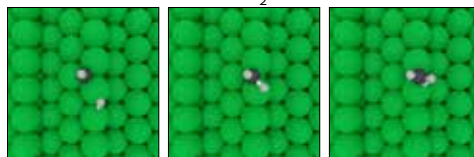
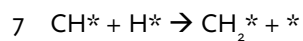
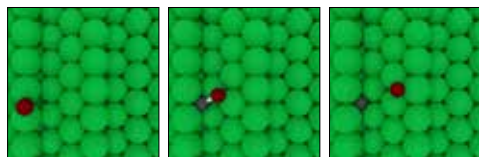
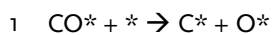
bonding, angle and torsion properties of each particle and interaction within the systems. This parametrization is done using quantum chemical data. Fitting such potentials requires specialized algorithms as standard fitting procedures such as line searches or Levenberg-Marquardt algorithms have too long convergence times or result in solutions that are local instead of global minima. Markov-Chain Monte-Carlo (MCMC), on the other hand, is an effective algorithm for fitting these large sets of parameters by using simulated annealing to find the global minimum.

With such an approach combining accurate DFT calculations to study adsorbate-induced surface reconstruction and elementary reaction steps, fitting of reactive force-fields and carrying out molecular dynamics using reactive force-fields it will become possible to study the transient behaviour of the Fischer-Tropsch reaction, essentially enabling the study of how the overlayer changes give rise to activation of the catalyst at the initial stages of its lifetime and, ultimately, its demise into an inactive state. When larger systems are within reach, also effects such as that of the support and promoter ions on the catalytic activity, selectivity and stability can be investigated. ■

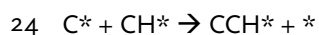
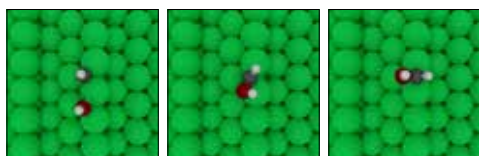
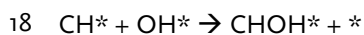
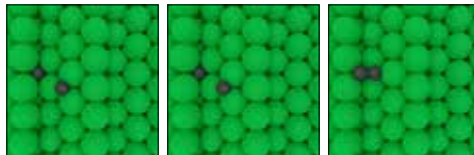
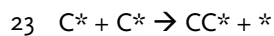
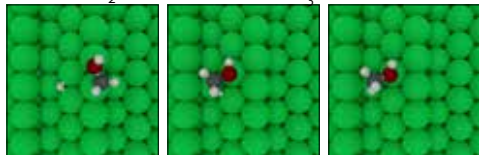
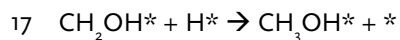
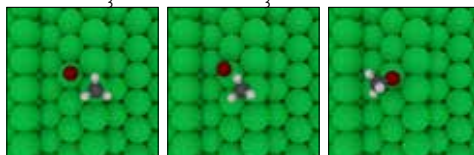
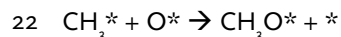
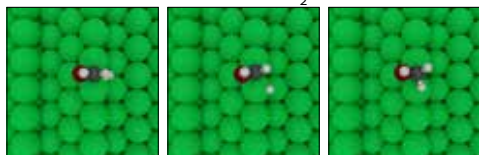
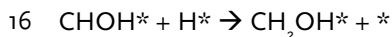
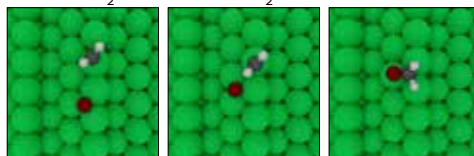
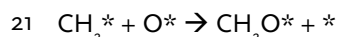
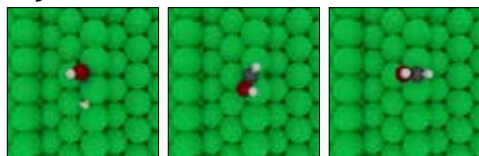
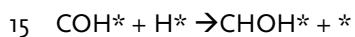
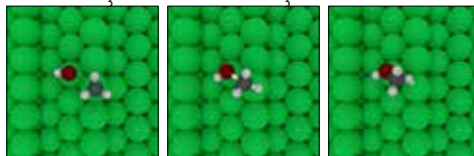
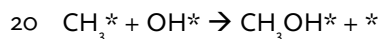
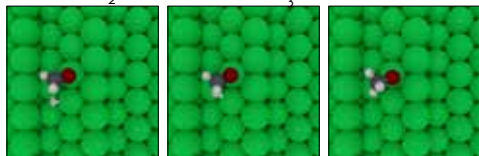
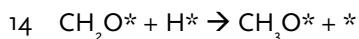
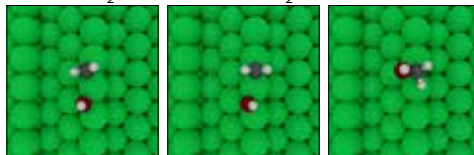
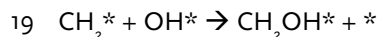
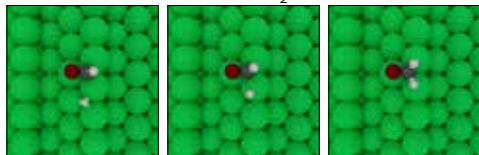
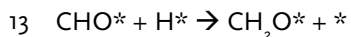
## REFERENCES

- (1) Cox, M. P.; Ertl, G.; Imbihl, R. *Phys. Rev. Lett.* **1985**, *54*, 1725.
- (2) Wilson, J.; de Groot, C. *The Journal of Physical Chemistry* **1995**, *99*, 7860.
- (3) Voter, A. In *Radiation Effects in Solids*; Sickafus, K., Kotomin, E., Uberuaga, B., Eds.; Springer Netherlands: 2007; Vol. 235, p 1.
- (4) Jansen, A. P. J. *An Introduction to Kinetic Monte Carlo Simulations of Surface Reactions*; Springer Berlin Heidelberg, 2012.

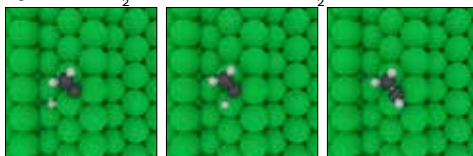
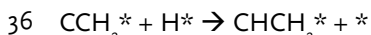
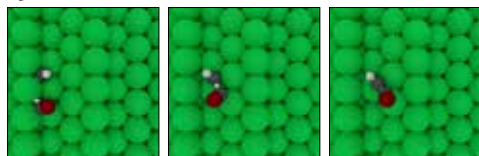
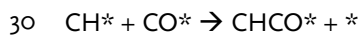
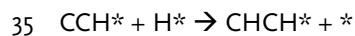
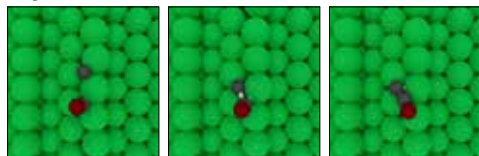
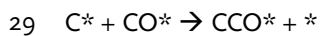
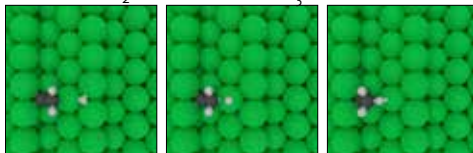
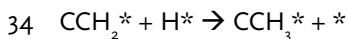
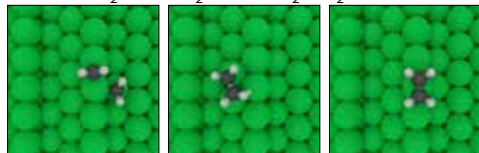
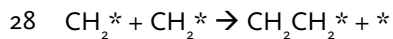
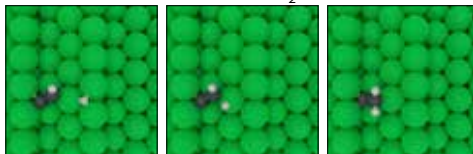
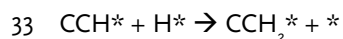
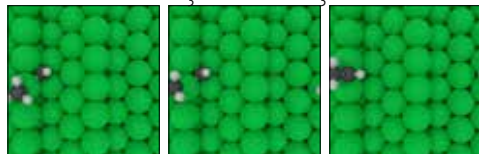
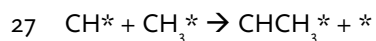
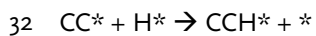
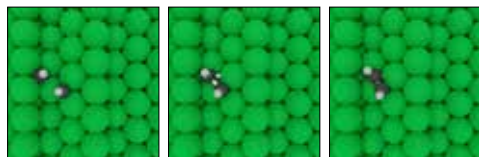
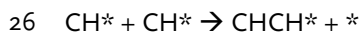
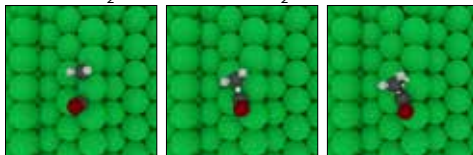
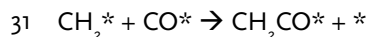
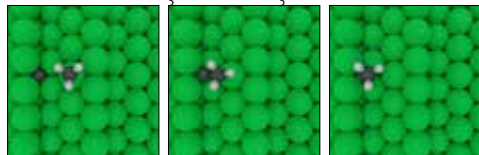
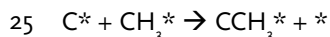
# APPENDIX A



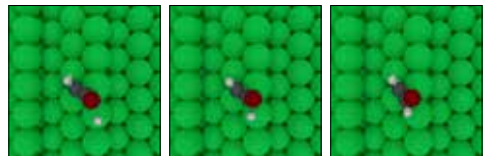
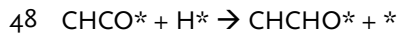
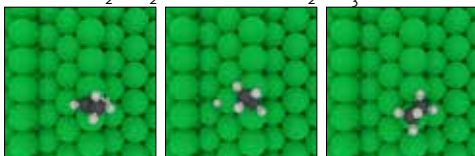
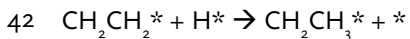
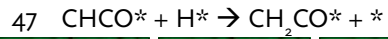
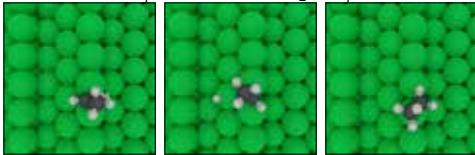
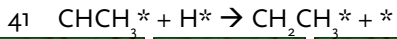
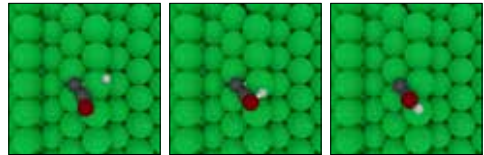
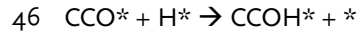
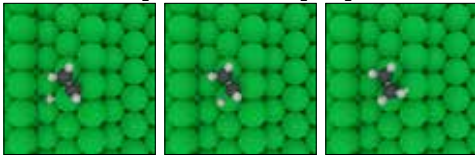
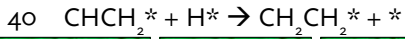
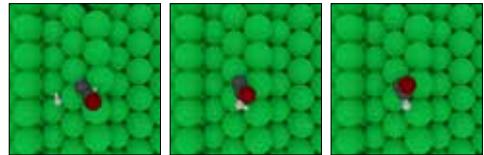
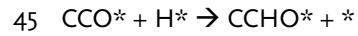
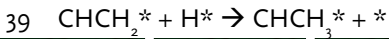
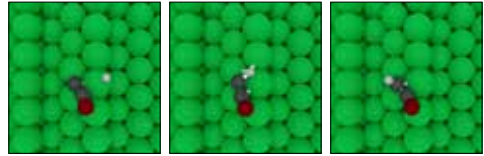
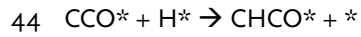
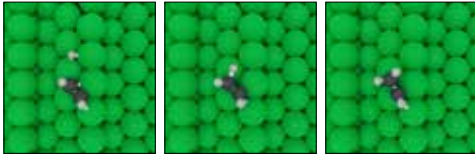
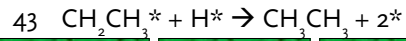
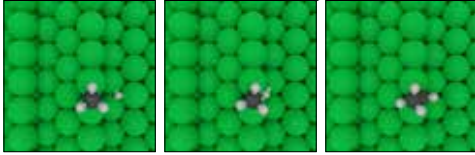
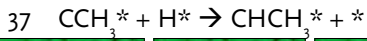
# GEOMETRIES OF ELEMENTARY REACTION STEPS ON RH(211)



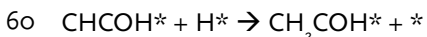
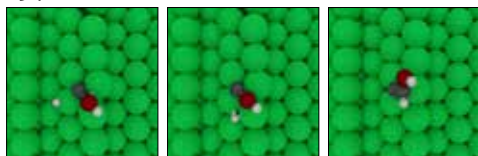
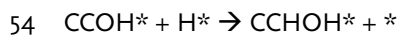
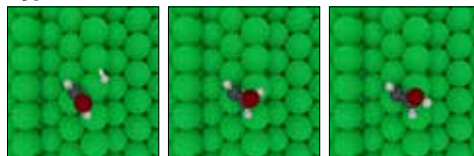
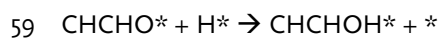
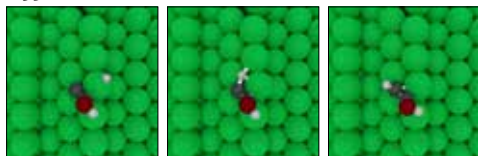
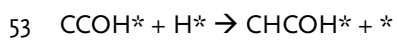
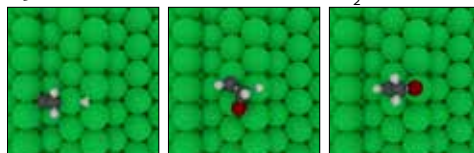
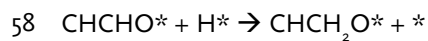
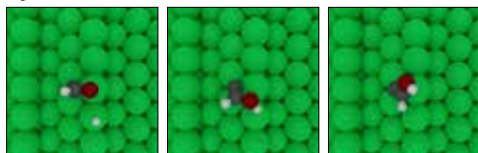
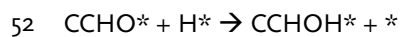
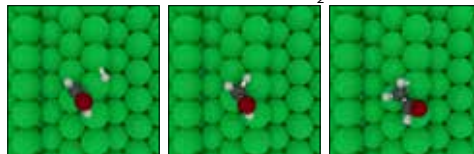
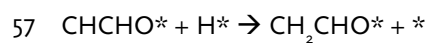
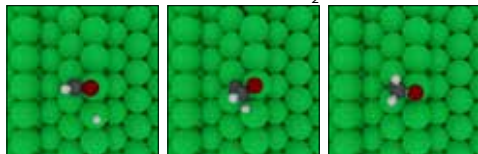
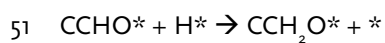
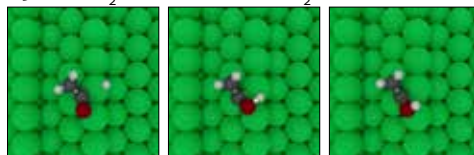
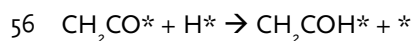
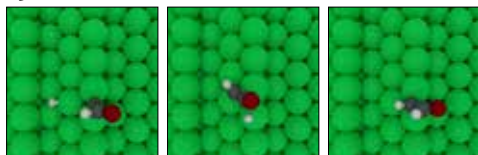
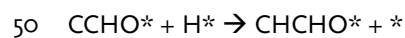
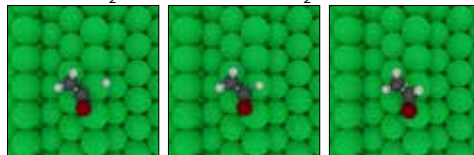
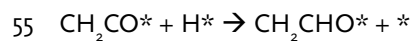
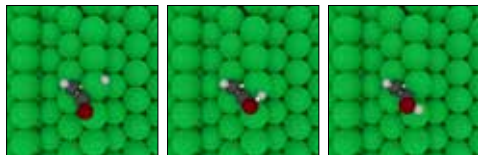
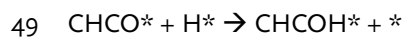
# APPENDIX A



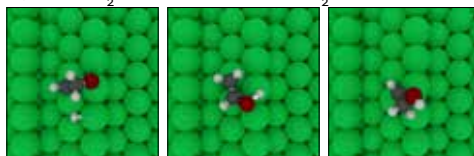
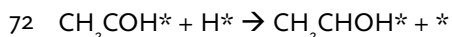
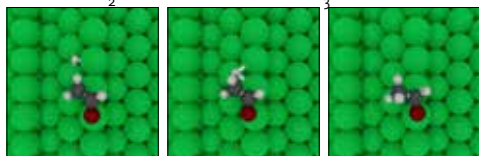
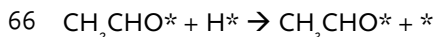
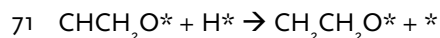
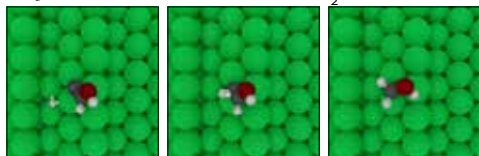
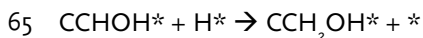
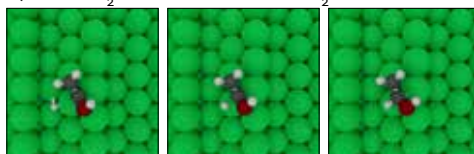
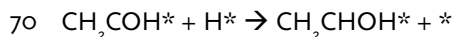
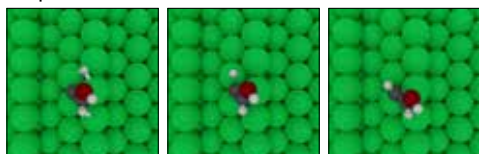
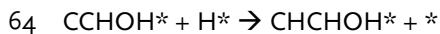
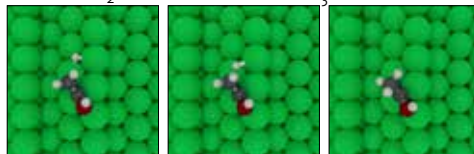
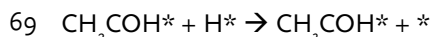
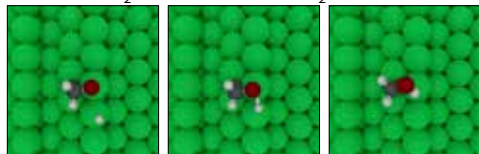
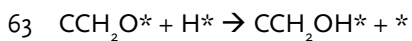
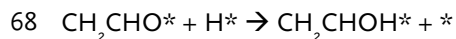
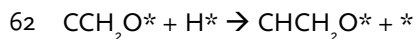
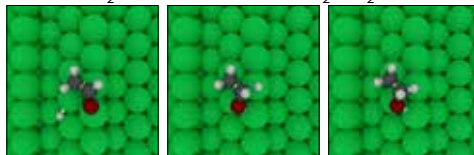
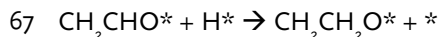
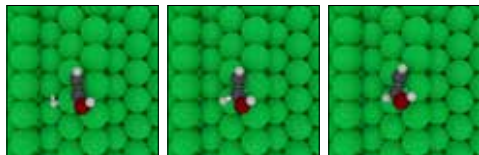
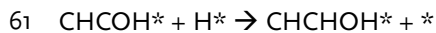
# GEOMETRIES OF ELEMENTARY REACTION STEPS ON RH(211)



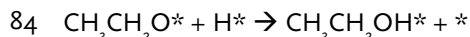
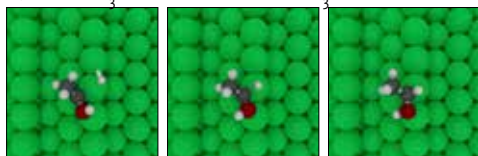
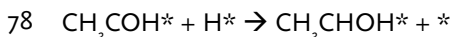
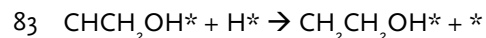
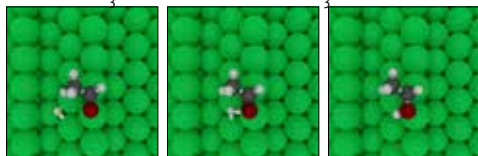
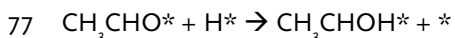
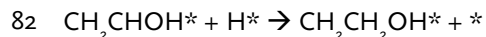
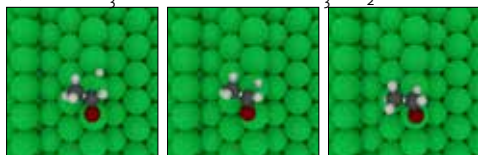
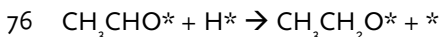
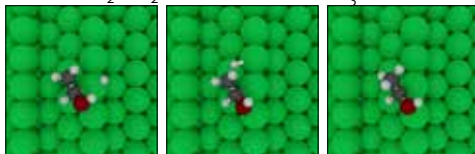
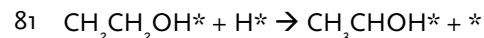
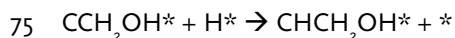
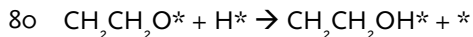
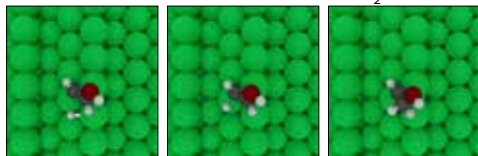
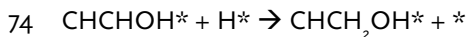
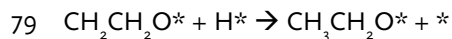
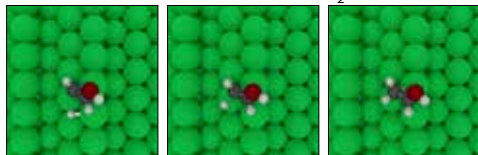
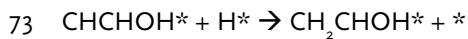
# APPENDIX A



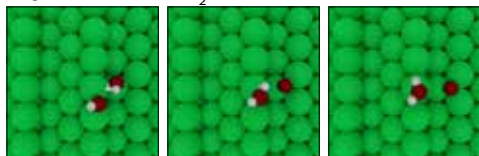
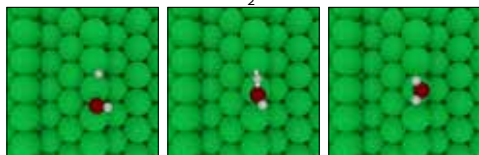
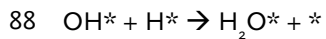
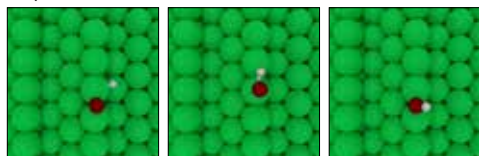
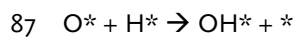
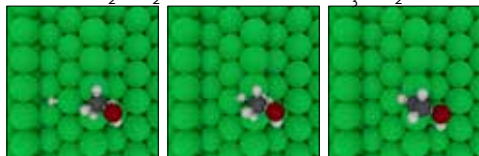
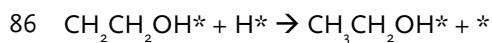
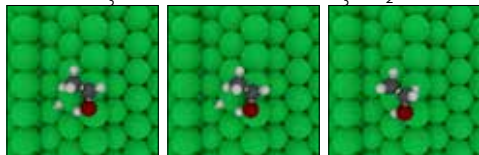
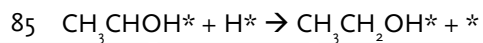
# GEOMETRIES OF ELEMENTARY REACTION STEPS ON RH(211)



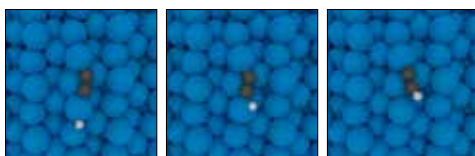
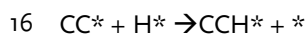
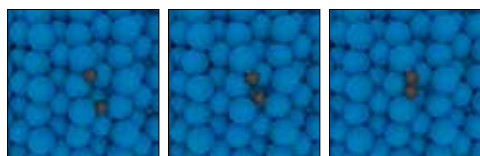
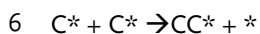
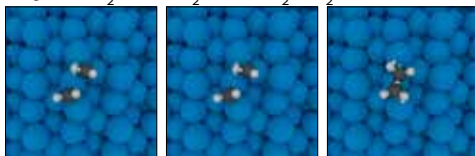
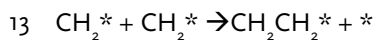
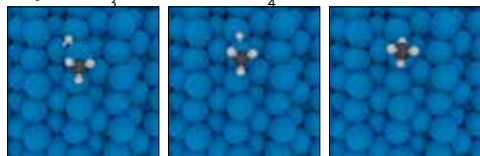
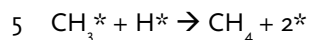
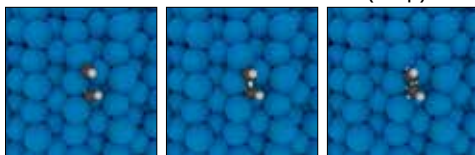
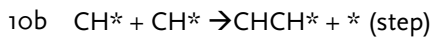
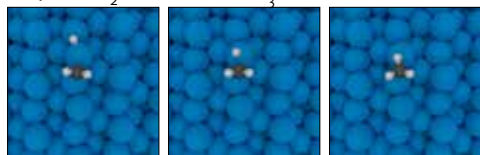
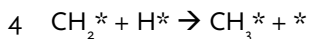
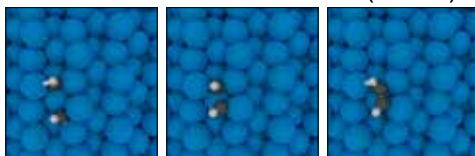
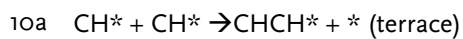
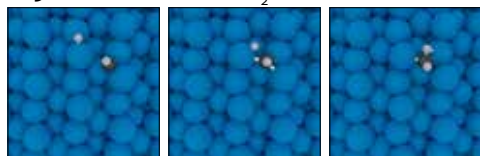
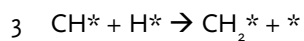
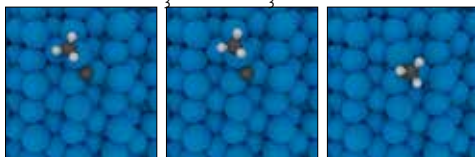
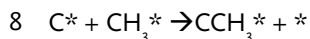
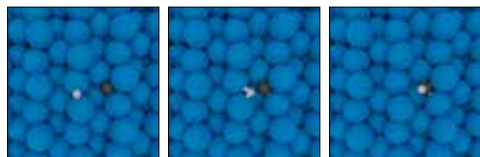
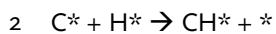
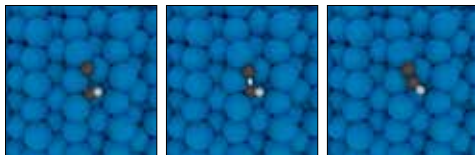
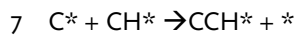
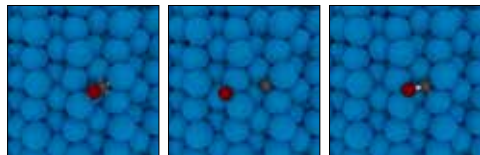
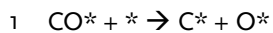
# APPENDIX A



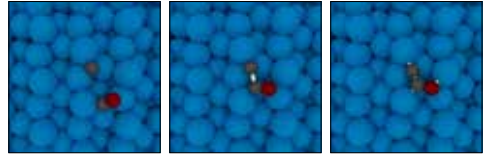
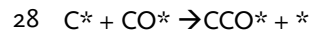
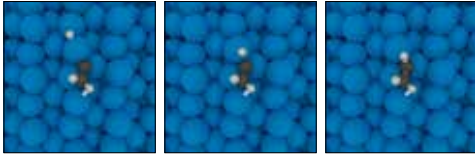
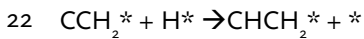
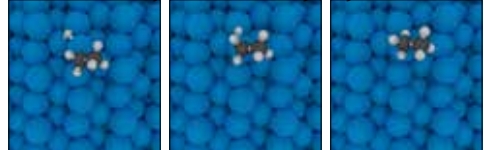
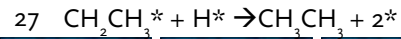
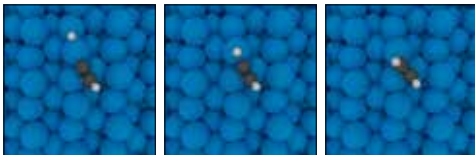
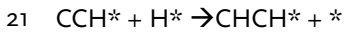
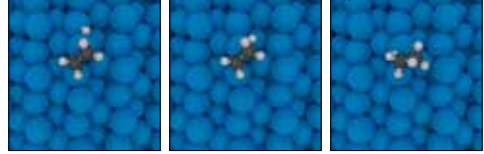
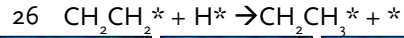
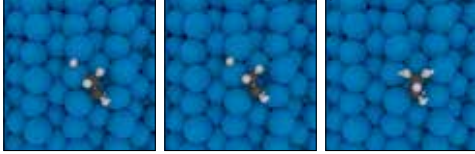
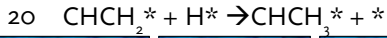
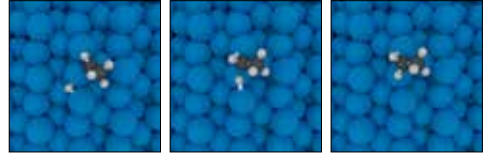
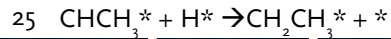
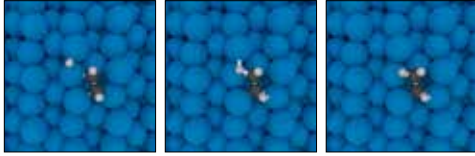
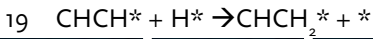
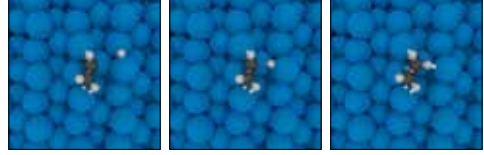
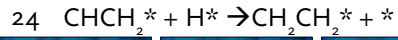
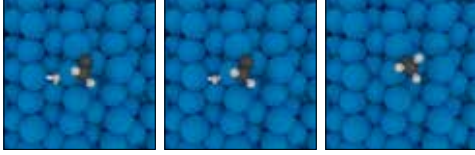
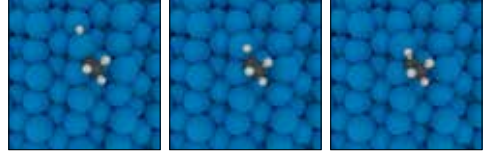
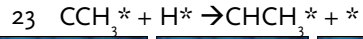
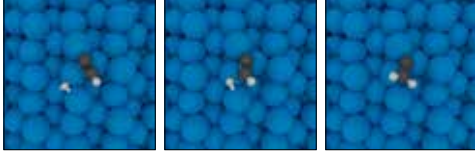
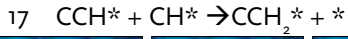
# GEOMETRIES OF ELEMENTARY REACTION STEPS ON RH(211)

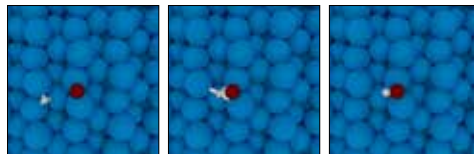
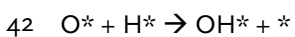
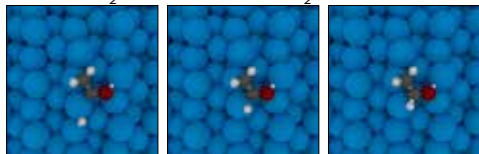
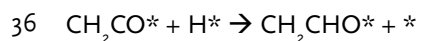
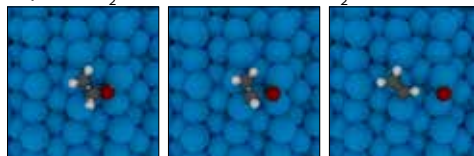
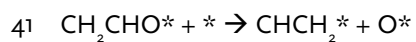
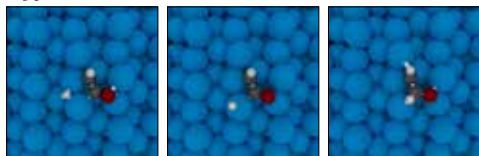
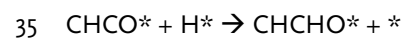
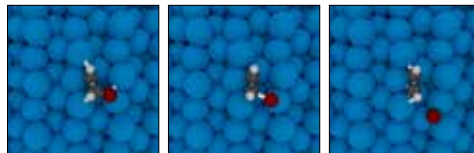
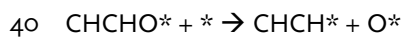
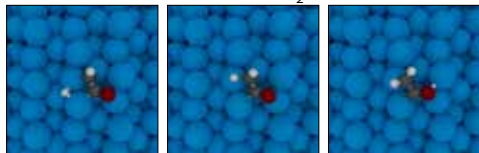
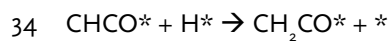
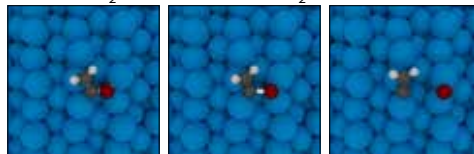
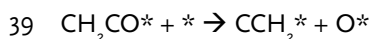
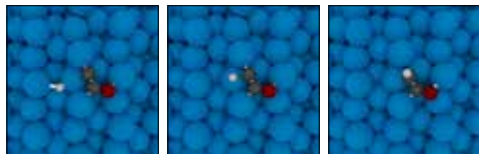
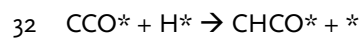
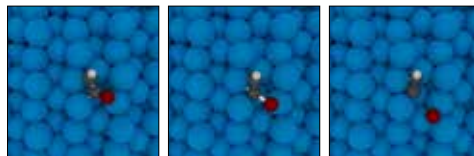
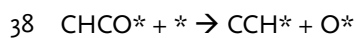
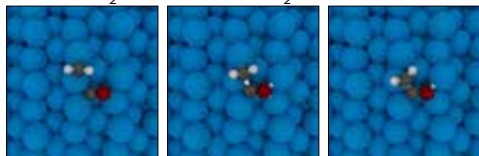
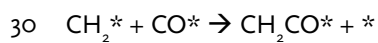
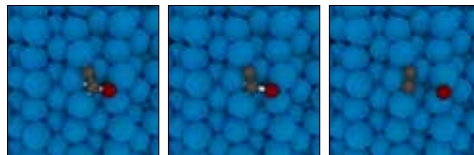
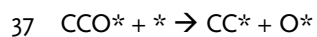
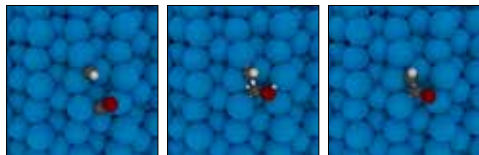


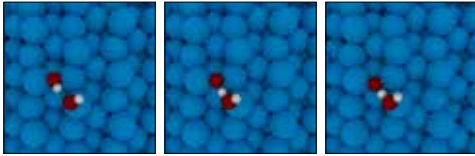
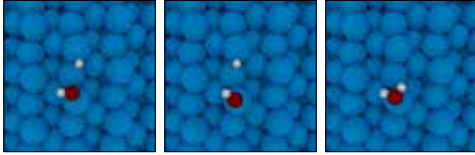
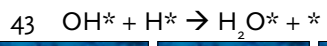
# APPENDIX B



# GEOMETRIES OF ELEMENTARY REACTION STEPS ON RU(11 $\bar{2}$ 1)







# CURRICULUM VITAE



Ivo Filot was born on the 28<sup>th</sup> of January, 1985 in Sittard. After having finished pre-university college at Trevianum Scholengroep in Sittard, he studied Chemical Engineering and Chemistry at the Eindhoven University of Technology.

During his Bachelor's program, he undertook extracurricular courses in physics, mathematics and computer sciences. In 2007, he obtained his Bachelor's Degree with the *judicium cum laude*.

He started his Master's program in the Molecular Engineering Track. His graduation project focused on the elucidation of the cooperativity effects in the stacking behavior of benzene-1,3,5-tricarboxamides under the supervision of prof.dr. Bert Meijer.

At the end of his Master's studies, he did an internship at Technip Zoetermeer where he optimized the insulation thickness of thermal cracking installations. In December 2009, he obtained his Master of Science degree with the *judicium cum laude*.

In January 2010, he started his Ph.D. research under the supervision of prof.dr.ir. Emiel Hensen. The results of this work are presented in this dissertation. In 2012, he was selected to participate in the 63<sup>rd</sup> Lindau Nobel Laureate Meetings. He has won the best lecture prize at the 14<sup>th</sup> Netherlands Chemistry and Catalysis conference as well as the best poster award at the 7<sup>th</sup> TOCAT conference in Kyoto, Japan.

At the end of 2011, he founded the company Zuidstijl, which provides services in the development and maintenance of web-based inventory management software and web content management systems.

Since 2015, he is employed as a university researcher in the group of Emiel Hensen.

# LIST OF PUBLICATIONS

## JOURNAL ARTICLES

-  « Microkinetic Modeling of the Oxygen Reduction Reaction at the Pt(111)/Gas Interface », Fantauzzi, D., Zhu, T., Mueller, J.E., Filot, I.A.W., Hensen, E.J.M., Jacob, T., 2014, *Catal. Lett.*, DOI: 10.1007/s10562-014-1448-5
-  « The Optimally Performing Fischer-Tropsch Catalyst », Filot, I.A.W., van Santen, R.A., Hensen, E.J.M., 2014, *Angew. Chem. Int. Ed.*, 53, (47), 12746-12750
-  « Quantum Chemistry of the Fischer-Tropsch reaction catalysed by a stepped ruthenium surface », Filot, I.A.W., van Santen, R.A., Hensen, E.J.M., 2014, *Catal. Sci. Technol.*, 4, (9), 3129-3140
-  « Correlating Fischer-Tropsch activity to Ru nanoparticle surface structure as probed by high-energy X-ray diffraction », Quek, X.Y., Filot, I.A.W., Pestman, R., van Santen, R.A., Petkov, V., Hensen, E.J.M., 2014, *Chem. Comm.*, 50, (45), 2005-2008
-  « Reactivity of CO on Carbon-Covered Cobalt Surfaces in Fischer-Tropsch Synthesis », Joos, L., Filot, I.A.W., Cottenier, S., Hensen, E.J.M., Waroquier, M., van Speybroeck, V., van Santen, R.A., 2014, 118, (10), 5317-5327
-  « Development of a benzimidazole-derived bidentate P,N-ligand for enantioselective iridium-catalyzed hydrogenations », Weemers, J.J.M., Sypaseuth, F.D., Bäuerlein, P.S., van der Graaff, W.N.P., Filot, I.A.W., Lutz, M., Müller, C., 2014, *Eur. J. Org. Chem.*, (2), 350-362
-  « Self-healing systems based on disulfide-thiol exchange reactions », Pepels, M.P.F., Filot, I.A.W., Klumperman, L., Goossens, J.G.P., *Polymer Chemistry*, 2013, 4, (18), 4955-4965

-  « Catalytic properties of extraframework iron-containing species in ZSM-5 for N<sub>2</sub>O decomposition », Li, G., Pidko, E.A., Filot, I.A.W., van Santen, R.A., Li, C., Hensen, E.J.M., *J. Catal.*, **2013**, 308, 386-397
-  « Conformational Analysis of Chiral Supramolecular Aggregates: Modeling the Subtle Difference between Hydrogen and Deuterium », Yoko, N., Markvoort, A.J., Cantekin, S., Filot, I.A.W., ten Eikelder, H.M.M., Meijer, E.W., Palmans, A.R.A., *J. Am. Chem. Soc.*, **2013**, 135, (44), 16497-16506
-  « Mechanism and microkinetics of the Fischer-Tropsch reaction », van Santen, R.A., Markvoort, A.J., Filot, I.A.W., Hensen, E.J.M., *Phys. Chem. Chem. Phys.*, **2013**, 15, (40), 17038-17063
-  « Microkinetics of steam methane reforming on platinum and rhodium metal surfaces », Zhu, T., van Grootel, P.W., Filot, I.A.W., Sun, S.G., van Santen, R.A., Hensen, E.J.M., *J. Catal.*, **2013**, 297, 227-235
-  « The origin of isotope-induced helical-sense bias in supramolecular polymers of benzene-1,3,5-tricarboxamides », Filot, I.A.W., Palmans, A.R.A., Hilbers, P.A.J., Hensen, E.J.M., de Greef, T.F.A., Pidko, E.A., *Phys. Chem. Chem. Phys.*, **2012**, 14, 13997-14002
-  « Size and Topological Effects of Rhodium Surfaces, Clusters and Nanoparticles on the Dissociation of CO », Filot, I.A.W., Shetty, S.G., Hensen, E.J.M., van Santen, R.A., *J. Phys. Chem. C*, **2011**, 115, 14204-14212
-  « Cooperative Two-Component Self-Assembly of Mono- And Ditopic Monomers », Smulders, M.M.J., Nieuwenhuizen, M.M.L., Grossman, M., Filot, I.A.W., Lee, C.C., de Greef, T.F.A., Schenning, A.P.H.J., Palmans, A.R.A., Meijer, E.W., *Macromolecules*, **2011**, 44 (16) , 6581-6587
-  « Dynamic Supramolecular Polymers Based on Benzene-1,3,5-tricarboxamides: The Influence of Amide Connectivity on Aggregate Stability and Amplification of Chirality », Stals, P.J.M., Everts, J.C., de Bruijn, R., Filot, I.A.W., Smulders, M.M.J., Martín-Rapún, R., Pidko, E.A., de Greef, T.F.A., Palmans, A.R.A., Meijer, E.W., *Chem. Eur. J.*, **2010**, 16 , 810-821

 « Tuning the Extent of Chiral Amplification by Temperature in a Dynamic Supramolecular Polymer », Smulders, M.M.J., [Filot, I.A.W.](#), Leender, J.M.A., van der Schoot, P., Palmans, A.R.A., Schenning, A.P.H.J., Meijer, E.W., *J. Am. Chem. Soc.*, **2010**, *126*, 611-619

 « Understanding Cooperativity in Hydrogen-Bond-Induced Supramolecular Polymerization: A Density Functional Theory Study », [Filot, I.A.W.](#), Palmans, A.R.A., Hilbers, P.A.J., van Santen, R.A., Pidko, E.A., de Greef, T.F.A., *J. Phys. Chem. B*, **2010**, *114*, 13667-13674

## **ORAL CONTRIBUTIONS**

 « Microkinetics investigation of CO hydrogenation on stepped Rh(211) surfaces. », [Filot, I.A.W.](#), Broos, R.J.P., van Rijn, J.P.M., van Heugten G.J.H.A., van Santen, R.A., Hensen, E.J.M., **2014**, The Graduate Course on Theoretical Chemistry and Spectroscopy, Han-sur-Lesse, Belgium

 « Predictive microkinetic modeling of complex catalytic reactions: the Fischer-Tropsch reaction. », [Filot, I.A.W.](#), van Santen, R.A., Hensen, E.J.M., **2014**, Chemistry as Innovating Science (CHAINS) 2014, Veldhoven, The Netherlands

 « Elucidation of the Fischer-Tropsch mechanism », [Filot, I.A.W.](#), van Santen, R.A., Hensen, E.J.M., **2014**, 15<sup>th</sup> International Conference on Theoretical Aspects of Catalysis, London, United Kingdom

 « Elucidation of the Fischer-Tropsch mechanism by Microkinetic Modeling », [Filot, I.A.W.](#), van Santen, R.A., Hensen, E.J.M., **2014**, Deutscher Katalyiker 47. Jahrestreffen, Weimar, Germany

 « Elucidation of the Fischer-Tropsch mechanism », [Filot, I.A.W.](#), van Santen, R.A., Hensen, E.J.M., **2014**, Netherlands Chemistry and Catalysis Conference XV, Noordwijkerhout, The Netherlands

- 🎧 « Elucidating the Fischer-Tropsch mechanism », [Filot, I.A.W.](#), van Santen, R.A., Hensen, E.J.M., 2014, NRSC-Catalysis Workshop, Utrecht, The Netherlands
- 🎧 « Towards a microkinetic model for the Fischer-Tropsch reaction », [Filot, I.A.W.](#), van Santen, R.A., Hensen, E.J.M., 2013, 23<sup>rd</sup> North American Catalysis Meeting, Louisville, United States of America
- 🎧 « Identification of sites for low barrier CO dissociation sites in the Fischer-Tropsch Synthesis reaction. », [Filot, I.A.W.](#), Ligthart, M.D.A.J., van Santen, R.A., Hensen, E.J.M., 2013, Netherlands Chemistry and Catalysis Conference XIV, Noordwijkerhout, The Netherlands (🏆 Lecture prize)
- 🎧 « Elucidating the Fischer-Tropsch mechanism », [Filot, I.A.W.](#), van Santen, R.A., Hensen, E.J.M., 2013, The Graduate Course on Theoretical Chemistry and Spectroscopy, Han-sur-Lesse, Belgium
- 🎧 « Towards a microkinetic model for the Fischer-Tropsch reaction », [Filot, I.A.W.](#), van Santen, R.A., Hensen, E.J.M., 2013, Deutscher Katalytiker 46. Jahrestreffen, Weimar, Germany
- 🎧 « Structure sensitivity of supported Rh nanoparticles », [Filot, I.A.W.](#), Ligthart M.D.A.J., Quek, X.-Y., van Grootel, P.W., Almutairi, A., Song, W., Popa, C., van Santen, R.A., Hensen, E.J.M., 2013, NRSC-Catalysis Workshop, Utrecht, The Netherlands
- 🎧 « Towards a microkinetic model of the Fischer-Tropsch synthesis reaction: Selectivity issues for the Ru FTS catalyst », [Filot, I.A.W.](#), Ligthart M.D.A.J., van Santen, R.A., Hensen, E.J.M., 2012, Netherlands Chemistry and Catalysis Conference XIII, Noordwijkerhout, The Netherlands
- 🎧 « Identifying the active site for Fischer-Tropsch catalysis by IR spectroscopy of adsorbed N<sub>2</sub>: a combined computational and experimental study. », [Filot, I.A.W.](#), Ligthart M.D.A.J., van Santen, R.A., Hensen, E.J.M., 2012, NRSC-Catalysis Workshop, Utrecht, The Netherlands
- 🎧 « Towards a microkinetic model of the Fischer-Tropsch synthesis reaction: Selectivity issues for the Ru FTS catalyst », [Filot, I.A.W.](#), Ligthart M.D.A.J., van Santen, R.A., Hensen, E.J.M., 2012, Syngas Conference, Cape Town, South Africa

🎤 « Size and topological effects of Rhodium Surfaces, Clusters and Nanoparticles on the dissociation of CO », [Filot, I.A.W.](#), Shetty, S., van Santen, R.A., Hensen, E.J.M., 2011, Netherlands Chemistry and Catalysis Conference XII, Noordwijkerhout, The Netherlands

## **POSTER PRESENTATIONS**

👁 « Elucidation of the Fischer-Tropsch Mechanism: Which is the dominant mechanism? », [Filot, I.A.W.](#), van Santen, R.A., Hensen, E.J.M., 2014, 7<sup>th</sup> Tokyo Conference on Advanced Catalytic Science and Technology (TOCAT7), Kyoto, Japan (🏆 Poster prize)

👁 « Elucidation of the Fischer-Tropsch Mechanism: Which is the dominant mechanism? », [Filot, I.A.W.](#), van Santen, R.A., Hensen, E.J.M., 2014, Symposium on Engineering for Sustainability, Eindhoven, The Netherlands

👁 « Towards a microkinetic model for the Fischer-Tropsch reaction », [Filot, I.A.W.](#), van Santen, R.A., Hensen, E.J.M., 2013, EuropaCat XI, Lyon, France

👁 « Identifying the active site for Fischer-Tropsch catalysis by IR spectroscopy of adsorbed N<sub>2</sub>: a combined computational and experimental study. », [Filot, I.A.W.](#), Ligthart M.D.A.J., van Santen, R.A., Hensen, E.J.M., 2012, Shell Symposium, Amsterdam, The Netherlands

👁 « Fischer-Tropsch synthesis; Pichler-Schulz versus carbide mechanism. A DFT study on Ru(111̄21) », [Filot, I.A.W.](#), Ligthart M.D.A.J., S., van Santen, R.A., Hensen, E.J.M., 2012, 14<sup>th</sup> International Conference on Theoretical Aspects of Catalysis, Vlissingen, The Netherlands

## **BOOK CHAPTERS**

📖 « The quantum chemistry of transition metal surface bonding and reactivity », van Santen, R.A., [Filot, I.A.W.](#), 2014, *The chemical bond : chemical bonding across the periodic table*, G. Frenking & S. Shaik (Eds.), Chichester: Wiley., 269-333

# ACKNOWLEDGEMENTS

I found the acknowledgement section always quite peculiar in the sense that it has the least scientific value, though it is the most well-read part of a dissertation. One's colleagues will check whether their names are mentioned in it and look for funny puns. Some read it line by line, most just look for their names in the section and read the lines before and after it. They perhaps read the whole paragraph. Nevertheless, it is a lot of fun to write, so here goes.

The process of undertaking a Ph.D., and all the things that have happened outside of it, has been one of the most personality shaping years of my life. With that in mind, I would like to thank a great many people, without whom this document could not exist.

First and foremost, I would like to thank my promotors. Emiel, I have sincerely enjoyed working in your group these past years. You were always very critical about my work (which I find a good thing!), you have a strong aspiration with regard to high-quality education and you have always motivated me to achieve more at my work. The many fruitful discussions, your help in structuring manuscripts and this dissertation and your support are highly appreciated. Thank you for providing me the opportunity to do my Ph.D. research in your group.

Rutger, I really enjoyed our discussions. Your knowledge and understanding of all the intricacies of computational catalysis is formidable to say the least. Often I had the feeling that I was not doing something novel, but that I was just re-discovering all your previous results. Luckily you comforted me that my research was indeed novel.

I am grateful to prof.dr.ir. Krijn de Jong, prof.dr.ir. Hans Kuipers, prof.dr. Philippe Sautet and dr.ir. Xander Nijhuis for taking part in my reading committee and attending my defense ceremony.

Arjan and Kees-Jan, thank you for being my paranymphs. Besides your support during my Ph.D. studies, I would like to thank you here (in advance) for your work during and after the ceremony.

Dr.ir. Tom de Greef and dr.ir. Anja Palmans are acknowledged for the nice collaboration for the research on benzene-tricarboxamides. Sometimes old research topics are hard to let go and I am very fortunate to have made some very nice publications together. Also I would like to thank prof.dr. Christiaan Müller for the nice collaboration and scientific discussions.

During my Ph.D. studies, I had the privilege of coaching some very talented students. In special I would like to thank Bart and Robin for their excellent scien-

tific work and for being awesome outside working hours as well. Bart, you have programmed some very critical parts of the MKMCXX program which has been used extensively in this thesis. Also many thanks for coping with me during all the conferences and graduate courses we went to together. Robin, you have performed an unprecedented amount of density functional theory calculations in a very short time. The amount of electricity consumed in this process could easily power a small village, though. Jeaphianne and Gert-Jan, a lot of thanks for your pioneering work. The outcome of your hard work and especially the things you discovered that we could never have imagined, have really boosted our research. Lennart Joos, I enjoyed working with you and it has resulted in a very nice thesis chapter. Joost and Erik, thanks for helping us out understanding the workings of the ADF software and for the development of some important pieces of coding. Thanks goes to Wilbert, Evi, Laura and Roderigh for some very interesting results in your Bachelor or research projects. I have learned a great deal from coaching you.

My awesome colleagues. A lot of thanks to you all. Thanks for helping me out. Thanks for supporting me. Thanks for keeping me company drinking beer. A few people I would like to thank in more detail. Evgeny, thank you for pointing out that two academic levels difference do

not mean anything, but the years of work earning two academic levels make all the difference. Sharan Shetty, thank you for coaching me in my first year. It was both inspiring as well as enjoyable. I would like to acknowledge Peter Vassilev for properly teaching me how to use VASP, Linux and OpenDX. You have showed me that reading the manual is really the shortest route to understanding software. William, vielen Dank, dass du mir hilfst, Deutsch fehlerfrei zu schreiben und zu sprechen sowie für dein allumfassendes Wissen über Geschichte und Kultur. Tobias, vielen Dank, für das Korrekturlesen dieses sowie des vorherigen Satzes. Arno and Lennart, thanks for helping out with the *semper excellentissimus* (S.E.) meetings this year. All other people attending these S.E. meeting, thank you for attending! To Arjan and Jos, thank you for motivating me to run faster every Friday during our weekly running tour around the Karpendonckse Plas. James and Jan, it was an utmost pleasure having dinners together. Michel, Abdulkarim and Wei-Chen, you three have supported me with a tremendous amount of highly valuable experimental results which was invaluable to me for validating all my models. Keep up the excellent work! My distinguished colleague Xian-Yang Quek, you showed me that it is perfectly acceptable to have a complete paragraph of laudatory phrases as the opening of an e-mail. Guanna,

thank you for teaching me the words 海狸 and 奶酪. Although I have much to learn in terms of pronunciation, they will sure come in handy. Weiyu, thanks for the many interesting discussions about DFT and quantum chemistry in general. Tianwei, thank you for extensively testing MKMCXX and pointing out some bugs in our coding. Georgy, thank you for your very original response when I mentioned (rather loudly) the abbreviation for N-acetylcysteine. Yi, your drawing skills are way beyond standard awesomeness. Never stop making your superb cartoons! Tiny is acknowledges for teaching me the word “epibreren” and Gijsbert for teaching me the etymology of that word. Remco, thank you for teaching me the strong difference between a question and something that can be interpreted as a question, and your support in the search for “haute cuisine” hamburgers.

Of course, Emma “the group mother” Eltink deserves her own paragraph in these acknowledgements. You are the best secretary I have had in all my working years. You have helped me a lot during my Ph.D. in filling out forms, navigating through the bureaucratic procedures and supporting me with firm and direct advice (exemplary lines are: “quit whining and just do your work” and “life is tough, deal with it”). You have proven to be a lifesaver considering my absent-mindedness.

Many thanks to my friends. Maartje and Rom, you have showed me that you can be elitist, hipster, unique but most of all extremely funny at the same time. AnnA en Bram, thank you for spending time chilling out on each other’s coaches watching Star Trek episodes with special beers (also another word of thanks for Maartje and Rom for joining these as well). Martijn, Tess and Ravi, it was a lot of fun visiting you in Munich during the Oktoberfest. The one liter *Maßkrug* (yes, this is a pleonasm) in my cupboard is a very nice reminder. Importantly, I would like to dedicate the caloric value of my thesis to Tom, who has shown me that everything can (and in his presence *will*) burn. Tom has also shown me the many uses of beer, such as its use as an anesthetic, aphrodisiac, antiseptic, laundry softener and as an excuse for being late at work. Juliën, I enjoyed the time brewing beer together and you teaching me how to properly sharpen a kitchen knife. Patrick and Müge, thanks for the great time at parties. Dannie, Ferdi, Yoran, Tom, Bart and Mark, geer zeet mich un sjoon stelke nutte koempeleers. Joep, Joyce, Christiaan, Menno, Tom en Nordin. Thanks for the awesome city-trips with “flying jaws” and other nonsense. To my fellow members at the Prometheus student association, I really enjoyed the time hanging out with the group and the many conversations we had on both serious as

well as non-serious topics.

Also thanks to the great people of Navigators Eindhoven and Kernteam for supporting me in spiritual terms. Cobi, Martin, Kees-Jan, Rianne, Peter, Rik, Gert-Jan, Klaas, Willemijn, Ruben van Gaalen, Sander, Bart, David, Eljakim, Joost, Kristen, Mariëlle, Robert, Ruben Tan and Sjoukje. Many blessing to you all.

I would like to thank my family for their support as well. You were always very interested in what I was doing. You were there for me when I needed you the most. Pap and mam, thank you for raising me to be what I am today. Anouk and Dannie, many thanks for your company and your great sense of humor. Also I would like to thank Rex for showing me repetitively how to thoroughly relax.

My dearest Sandra. A special word of thanks goes to you. You have spent a lot of time and effort in the last two weeks before the digital version of this booklet went to the printer reviewing all my chapters. This makes you one of those very few persons who has read the whole thesis and is not a committee members or yours truly. Thank you for pointing out the strange “Ivo-sentences”, for highlighting all the hyphenation errors of which there are most likely still 1,000 left in this thesis and for supporting me when I had strong urges to defenestrate my computer. Your humor, kindness and honesty

are very important to me and you inspire me to continue to be a better person.